

A Continual Learning-driven Model for Accurate and Generalizable Segmentation of Clinically Comprehensive and Fine-grained Whole-body Anatomies in CT

Dazhou Guo^{1†}, Zhanghexuan Ji^{1†}, Yanzhou Su^{1,3†}, Dandan Zheng^{2†}, Heng Guo^{1,3}, Puyang Wang⁴, Ke Yan^{1,3}, Yirui Wang¹, Qinji Yu¹, Zi Li^{1,3}, Minfeng Xu^{1,3}, Jianfeng Zhang^{1,3}, Haoshen Li¹, Jia Ge², Tsung-Ying Ho⁵, Bing-Shen Huang⁶, Tashan Ai⁷, Kuaile Zhao⁷, Na Shen⁸, Qifeng Wang⁹, Yun Bian¹⁰, Tingyu Wu¹¹, Peng Du¹¹, Hua Zhang¹², Feng-Ming Kong¹³, Alan L. Yuille¹⁴, Cher Heng Tan¹⁵, Chunyan Miao^{16,17}, Perry J. Pickhardt¹⁸, Senxiang Yan^{2*}, Ronald M. Summers^{19*}, Le Lu^{1*}, Dakai Jin^{1*}, Xianghua Ye^{2*}

¹DAMO Academy, Alibaba Group

²Department of Radiation Oncology, The first Affiliated Hospital, Zhejiang University, Hangzhou, China

³Hupan Laboratory, Hangzhou, China

⁴School of Medicine, Johns Hopkins University, Baltimore, United States of America

⁵Department of Nuclear Medicine, Chang Gung Memorial Hospital, LinKou, ROC

⁶Department of Radiation Oncology, Proton and Radiation Therapy Center, Chang Gung Memorial Hospital, LinKou, ROC

⁷Department of Radiation Oncology, Fudan University Shanghai Cancer Center, Shanghai, China

⁸Department of Otolaryngology-Head & Neck Surgery, Zhongshan Hospital, Fudan University, Shanghai, China

⁹Department of Radiation Oncology, Sichuan Cancer Hospital, Sichuan, China

¹⁰Department of Radiology, Shanghai Institution of Pancreatic Disease, Shanghai, China

¹¹Department of Colorectal and Anal Surgery, Xinhua Hospital Affiliated to Shanghai Jiaotong University School of Medicine, Shanghai, China

¹²Linking Med Inc., Beijing, China

¹³Department of Clinical Oncology, School of Clinical Medicine, LKS Faculty of Medicine, The University of Hong Kong and University of Hong Kong–Shenzhen Hospital, Hong Kong, China

¹⁴Department of Computer Science, Johns Hopkins University, Baltimore, United States of America

¹⁵Department of Diagnostic Radiology, Tan Tock Seng Hospital, Singapore

¹⁶Center of AI in Medicine, Nanyang Technological University, Singapore

¹⁷Alibaba-NTU Global e-Sustainability CorpLab (ANGEL), Nanyang Technological University, Singapore

¹⁸Radiology & Medical Physics, School of Medicine & Public Health, University of Wisconsin, Madison, United States of America

¹⁹Radiology and Imaging Sciences, National Institutes of Health Clinical Center, Bethesda, United States of America

† Daggers indicate first coauthors, they contributed equally

* Asterisks indicate co-corresponding authors

Abstract. Precision medicine in the quantitative management of chronic diseases and oncology would be greatly improved if the Computed Tomography (CT) scan of any patient could be segmented, parsed and analyzed in a precise and detailed way. However, there is no such fully annotated CT dataset with all anatomies (e.g., up to 235 organs and sub-organs) delineated for training because of the exceptionally high manual cost, the need for specialized clinical expertise, and the time required to finish the task. To this end, we proposed a novel continual learning-driven CT model that can segment complete anatomies presented using dozens of previously partially labeled datasets, dynamically expanding its capacity to segment new ones without compromising previously learned organ knowledge. Existing multi-dataset approaches are not able to dynamically segment new anatomies without catastrophic forgetting and would encounter optimization difficulty or infeasibility when segmenting hundreds of anatomies across the whole range of body regions. Our single unified CT segmentation model, CL-Net, can highly accurately segment a clinically comprehensive set of 235 fine-grained whole-body anatomies (including 73 new anatomies not available elsewhere, but with good clinical utility). Composed of a universal encoder, multiple optimized and pruned decoders, and a body-part-guided merging module, CL-Net is developed using 13,952 CT scans from 20 public (4,855) and 16 private (9,097) high-quality partially labeled CT datasets of various vendors, different contrast phases, and pathologies. Extensive evaluation demonstrates that CL-Net consistently outperforms the upper limit of an ensemble of 36 specialist nnUNets trained per dataset with the complexity of $\sim 5\%$ model size and significantly surpasses the segmentation accuracy of recent leading “segment anything”-style medical image foundation models by large margins ($>9.9\%$ Dice score). Our continual learning-driven CL-Net model (with 55.5MB parameters) would lay a solid foundation to facilitate many downstream tasks of oncology and chronic diseases using the most widely adopted CT imaging.

Contents

1 Introduction	4
2 Results	6
3 Discussion	18
4 Method	22
A1 Details of Datasets	39
A2 Details on Experimental Settings	40
A3 Continual Segmentation Results of Continual Learning Network (CL-Net) on Five Representative Public Datasets	44
A4 Details on Continual Learning Network (CL-Net) Implementation	47
A5 Details on Ablation Studies of General Encoder (General Encoder (GE))	52
A6 Details on Ablation Studies of Multi-path Decoding Heads	57
A7 Related Work and Reimplementation of Comparison Methods	60

Abbreviation	Definition	Abbreviation	Definition
ASD	Average Surface Distance	FL-Supporting	Feature Level Supporting
BPR	Body Part Regression	GE	General Encoder
CL-Net	Continual Learning Network	LTH	Lottery Ticket Hypothesis
CSS	Continual Semantic Segmentation	LN	Lymph Node
CT	Computed Tomography	LNS	Lymph Node Station
DDP	Distributed Data Parallel	NPC	Nasopharyngeal Carcinoma
DSC	Dice Similarity Coefficient	SAM	Segment Anything Model
EMA	Exponential Moving Average	SSL	Self-Supervised Learning

List of Abbreviation | All abbreviations used in the manuscript are presented in alphabetical order.

1 Introduction

Semantic image segmentation parses medical scans into spatially coherent and meaningful anatomical compartments that serve as an essential functionality to facilitate numerous downstream clinical tasks. Among all advanced cross-sectional imaging modalities, computed tomography (CT) is the most widely used in radiology and oncology due to its wide availability and effectiveness in cancer screening^{1,2}, disease diagnosis³, treatment planning and monitoring⁴. CT is widely used for a broad range of non-oncologic clinical indications, including unexplained abdominal pain and trauma, etc. For example, harness the rich cardiometabolic data embedded within CT scans that can add great clinical value and describe the rapidly growing field of “opportunistic CT screening”^{5,6}. 3D organ or lesion segmentation in CT has been a well-studied problem. With the emergence of many dedicatedly labeled organ imaging datasets⁷ and the rapid advancement of deep learning segmentation techniques, particularly the introduction of nnUNet⁸, 3D segmentation network models trained in specific datasets have achieved quantitative performance comparable to that of human experts⁹⁻¹¹, potentially suitable for real clinical practice. However, these models so far are restricted to segmenting only the types of anatomies present in the specific training datasets and training separate models would be required to handle any additional anatomies or datasets, which may be (highly) inconvenient and lack the scalability for wide clinical task deployment.

Segmenting all anatomies semantically and accurately from multiple or up to dozens of different training datasets using a single unified model faces the challenge of partial labeling problem, since all datasets are annotated for a specific organ/lesion or a limited group of organs/lesions, given the laborious nature of 3D volume annotation. To solve this issue, recent approaches have explored in-context learning¹²⁻¹⁴, various loss designs (marginal and exclusive losses)¹⁴⁻¹⁶, or re-mapping all labels with a unique ID across datasets and simply extending the last convolutional layer to produce output channels for all re-mapped labels¹⁷. Although partially effective, these methods are often applied to a specific body region and can only segment a limited number of anatomies¹²⁻¹⁶ (normally 3~30). Expanding the scope to cover a broader range of body regions and more anatomy types may lead to optimization difficulty or infeasibility and a tendency to be overfitted onto dominant classes. For example, the recent MultiTalent¹⁷ method, as a straightforward extension of nnUNet to handle multi-dataset scenarios, experiences (extremely) slow convergence and takes over 1,000 GPU hours when training on using only five datasets of 1,471 CT scans. Moreover, this approach does not produce a unique output for the same organs present in multiple datasets and would require post-merging or dataset ID to generate the final output.

With the recent emergence of the Segment Anything Model (SAM)¹⁸ in the natural 2D image, a growing number of SAM-style medical universal segmentation models have been developed¹⁹⁻²⁵. Benefiting from SAM’s core design principles of class-agnostic segmentation, multi-modality prompt encoding, and iterative training, SAM¹⁸ can learn from large and diverse image datasets, demonstrating impressive performance in promptable interactive segmentation and zero-shot generalizability in natural images. In the medical imaging domain, despite being promoted as foundation models learned from vast amounts of (public) data across various imaging modalities, SAM-style

segmentation models^{19,22-24} with text prompts or even bounding box prompts (which is a much easier scenario), still evidently and quantitatively underperform the dataset-specific trained segmentation models by substantial margins when evaluated fairly and rigorously. For example, the latest prompt-required BiomedParse²⁴ offers clearly inferior performance compared to the automated nnUNet⁸ model in organ segmentation using 3D CT scans (Table 3), potentially making it far from clinically useful. The underwhelming performance observed for SAM-style models in the medical domain can be attributed to the following factors: 1) Unlike natural images, where targets often display distinct visual features, medical image segmentation is challenging due to the difficulty in delineating ambiguous local boundaries. Anatomical targets in medical scans frequently exhibit a subtle visual contrast with adjacent structures or the background. Consequently, Transformer architectures (adopted in SAM), known for their exceptional ability to model long-range spatial dependencies, offer limited advantages in capturing local subtle visual differences and, meanwhile, are difficult to optimize effectively. 2) The dimensional gap between 3D medical scans and 2D natural images significantly hinders SAM’s transferability. Meanwhile, directly training SAM in 3D leads to a dramatic increase in model parameters, further exacerbating the optimization challenges. This raises the core question: *how to build an effective and accurate universal medical segmentation model that is capable of segmenting all clinically relevant anatomies of the human body on CT scans (the most prevalent imaging modality used in radiology/oncology), and consistently achieving comparable or even better segmentation performance in accuracy and speed than the dataset-specific trained state-of-the-art nnUNet⁸ models?*

To resolve all aforementioned problems, we propose to tackle universal segmentation in CT from a new perspective of continual learning and introduce a unified, scalable, and nonforgetting continuous learning method (CL-Net), capable of harnessing the synergies of a large number of partially labeled datasets to accurately segment the union of all anatomies present across all datasets. Continual learning is a sequential process that aims to dynamically adapt and extend the model to learn new targets or update existing targets without (re)access to previous training datasets²⁶⁻²⁹. Our Continual Learning Network (CL-Net) is an architectural-based framework, which comprises a shared/general encoder, a set of sequentially optimized and pruned light-weighted decoders (one decoder per organ or per group of organs) and a body-part-guided output merging module. The key characteristics of CL-Net include: 1) A trained then frozen general encoder coupled with sequentially added decoders for subsequent training datasets can extract sufficiently representative image features to segment new or update existing anatomies. The frozen encoder enables CL-Net to dynamically adapt and segment new anatomies, while preserving all previously acquired knowledge, even in the absence of access to prior training data. 2) By assigning each organ (that is, major anatomy) or group of relevant organs (e.g., rib instances) to independent decoders, multiple datasets containing specific organ groups can be used sequentially or simultaneously and integrated together to optimize the associated decoders, ensuring that more data variations (from all healthy and pathological subjects) are observed/captured by CL-Net. This decoder setup naturally handles the partial labeling in multi-dataset segmentation. 3) Optimizing each decoder with Lottery Ticket Hypothesis (LTH)-based pruning strategy^{30,31}, CL-Net only needs to maintain a very small fraction of effective parameters for each decoder (normally 1~3% model size of the

default full size decoder), ensuring its modeling scalability. 4) The body-part guided merging module, which combines outputs from all decoders, can effectively reduce distal false-positive segmentation from different decoders. A preliminary technical version³² appeared in ICCV-2023, and this work introduces substantial methodological extensions, together with entirely new and significantly much larger-scale experiments and analysis. For example, replacing the dataset-wise decoder design with organ-wise decoder substantially increases the model’s flexibility in managing partially labeled datasets and its scalability for learning from large-scale data and diverse anatomy types. Furthermore, the new LTH-based pruning strategy achieves a higher model compression rate compared to the knowledge distillation-based pruning in the original version³². Furthermore, the updated framework supports both continual segmentation (dataset sequentially accessible) and universal segmentation (dataset simultaneously accessible).

We build the CL-Net model using 13,952 CT scans from 20 public (4,855) and 16 private (9,097) high-quality partially labeled CT datasets of different vendors, different contrast phases and pathologies (based on a collection of our previous peer-reviewed work), which can automatically and accurately parse a set of 235 whole-body human anatomies, encompassing 193 organs, 33 lymph node stations, and 9 lesions. Compared to existing work, more fine-grained vessels, muscle substructures and glands are covered, as well as lymph node stations in head & neck and chest regions, to facilitate both oncologic and non-oncologic clinical diagnosis. In addition, our private datasets are primarily collected from pathological patient cohorts, which contain more disease-oriented organs as a valuable addition to the data diversity of public datasets. Through extensive comparison, CL-Net consistently outperforms or matches the performance of an ensemble of 36 specialist nnUNets⁸ trained on each dataset (Dice-Sørensen coefficient [DSC]: 86.1% vs 83.9%) and the nnUNet-extended universal model MultiTalent¹⁷ (+2.7% DSC), and significantly outperforms the latest leading SAM-style medical foundation models (on a subset of anatomies that appeared in their training data) by evidently large margins, e.g., VISTA3D²⁵ (+2.9% DSC), SAT-Pro²² (+9.9% DSC) and BiomedParse²⁴ (+67.0% DSC in 3D). We will make our CL-Net network model publicly available (for non-commercial use), providing scientists and physicians with the latest comprehensive and precise 235 whole-body CT anatomy segmentation tool as a useful routine clinical imaging semantic quantification and assessment tool.

2 Results

Overview of Datasets The goal of CL-Net is to train *continuously or simultaneously* a unified model capable of segmenting a comprehensive set of fine-grained whole-body anatomies with high precision on 3D CT scans. To accomplish this, 36 CT data sets are assembled for **model training and internal testing**, comprising 20 public and 16 private data sets in-house (a total of 13,952 CT scans, Fig. 1) of different institutions with various vendors, phases, and pathologies. These datasets cover the entire human body region, including head & neck, chest, abdomen, and pelvis, and contain a wide range of anatomies, such as major organs, bones, muscles, vessels, glands, lymph node stations, and lesions, etc. In total, there are 235 anatomy types (Supplementary Sec.

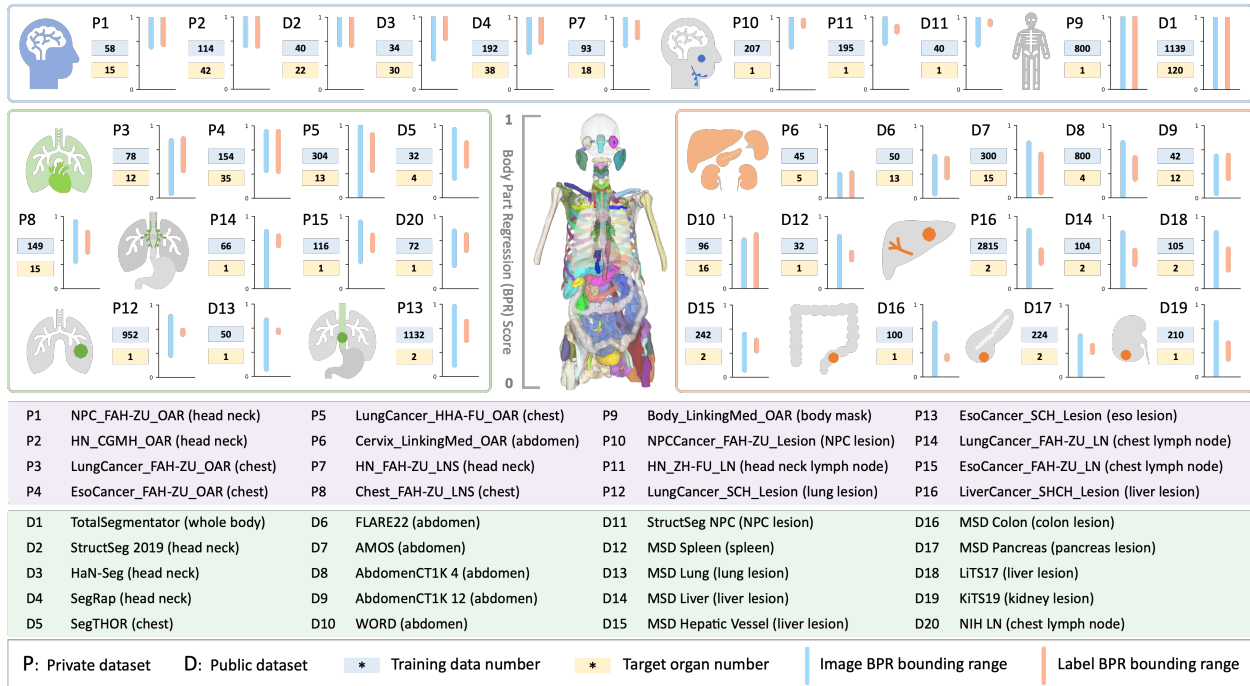


Fig. 1 | Dataset fingerprints. Overview of 36 datasets used for model development and internal validation, including 16 private (P) and 20 public (D) datasets. Datasets are categorized into head-neck (blue box), chest (green box), and abdomen (orange box) groups, based on the primary body region covered by their target organs, except for TotalSegmentator V2 and Body_LinkingMed_OAR, which span the entire body. For each dataset, the number of training CT scans, number of target organs, and vertical range of body part regression (BPR) scores of CT scans and foreground labels are provided. The BPR score represents the relative vertical position of each slice in a CT scan, normalized from the bottom of pelvis (0) to the top of head (1). Additional dataset fingerprint details are available in Supplementary Sec. A1.

A1, Table S1). The 20 public datasets contain 4,855 CT scans (35% of all data), which are divided to 3,904 for training and 951 for testing (detailed data split of each dataset in the Supplementary Table S1). Together, these datasets include 162 anatomical structures or substructures (Table S3). Our 16 private datasets, collected from multiple institutions, comprise a total of 9,097 CT scans (65% of the entire data), including 7,278 for training and 1,819 for testing (detailed data split of each data set in the Supplementary Table S1). These private datasets contain 125 anatomical structures (Table S2), including 52 overlapping and 73 additional fine-grained structures not present in the public data sets. Regarding the annotation process, anatomies in our private datasets have been carefully labeled by our clinical collaborators over the past several years and have been extensively used in our previous peer-reviewed work^{10,32-54}. We also collect seven datasets that did not appear in the model development for the **external testing** (Supplementary Table S4), which includes 1,979 CT scans of 43 anatomy types (39 organs and four lesions). Specifically, external testing covers 12 head & neck, 14 chest and 13 abdominal organs, and four lesions of various regions of the body. Moreover, we ensure that an external dataset of a specific body-part/lesion-type comes from an institution that does not provide training data of this body-part/lesion-type. For example, the HN_SMU_OAR consists of 268 CT scans of head & neck cancer patients obtained from a medical center in south China that is different from all sources of head & neck organ datasets used in training (NPC_FAH_ZU_OAR, HN_CGMH_OAR, StructSeg_2019, HaN-Seg and SegRap).

Two CL-Net Configurations CL-Net is designed to support both *Universal Segmentation (partial label learning)* and *Continual Segmentation* of large-scale whole-body anatomies in CT scans (Fig. 2). Its learning process begins with training a general encoder using one or multiple datasets (e.g., TotalSegmentator V2⁵⁵). Then, the general encoder is frozen in subsequent steps. In the **universal segmentation** configuration, CL-Net constructs individual decoders for each type of anatomy or group of relevant anatomy (e.g., rib instances) across the entire collection of datasets, as all datasets are available simultaneously for training. Each decoder is then sequentially trained using all data samples that contain the corresponding anatomy type(s). In the **continual segmentation** configuration, where only one dataset is accessible at a time, CL-Net is sequentially trained on each dataset. Using the available dataset at each step, CL-Net incrementally adds and trains new decoders for previously unseen anatomy types or fine-tunes existing decoders via Exponential Moving Average (EMA) for anatomy types already appearing in previous datasets. In both configurations, CL-Net facilitates accurate, efficient, and scalable segmentation of whole-body anatomies, accommodating sequential and simultaneous dataset availability, respectively.

2.1 Overview of Experimental Setting We perform extensive experimental evaluation in three dataset settings: 1) full internal evaluation using all 36 internal datasets, 2) comparative internal evaluation using five representative internal public datasets, and 3) external evaluation using seven external datasets. First, the **full internal evaluation** is performed by developing the CL-Net^{U₃₆} and CL-Net^{C₃₆} using 13,952 CT scans of the 36 internal datasets under both partial label (simultaneous access to the dataset) and continual training configurations (sequential access to the dataset). The detailed training and testing split of 36 datasets is summarized in the Supplementary Table S1. The complete internal evaluation provides comprehensive results for CL-Net across the entire

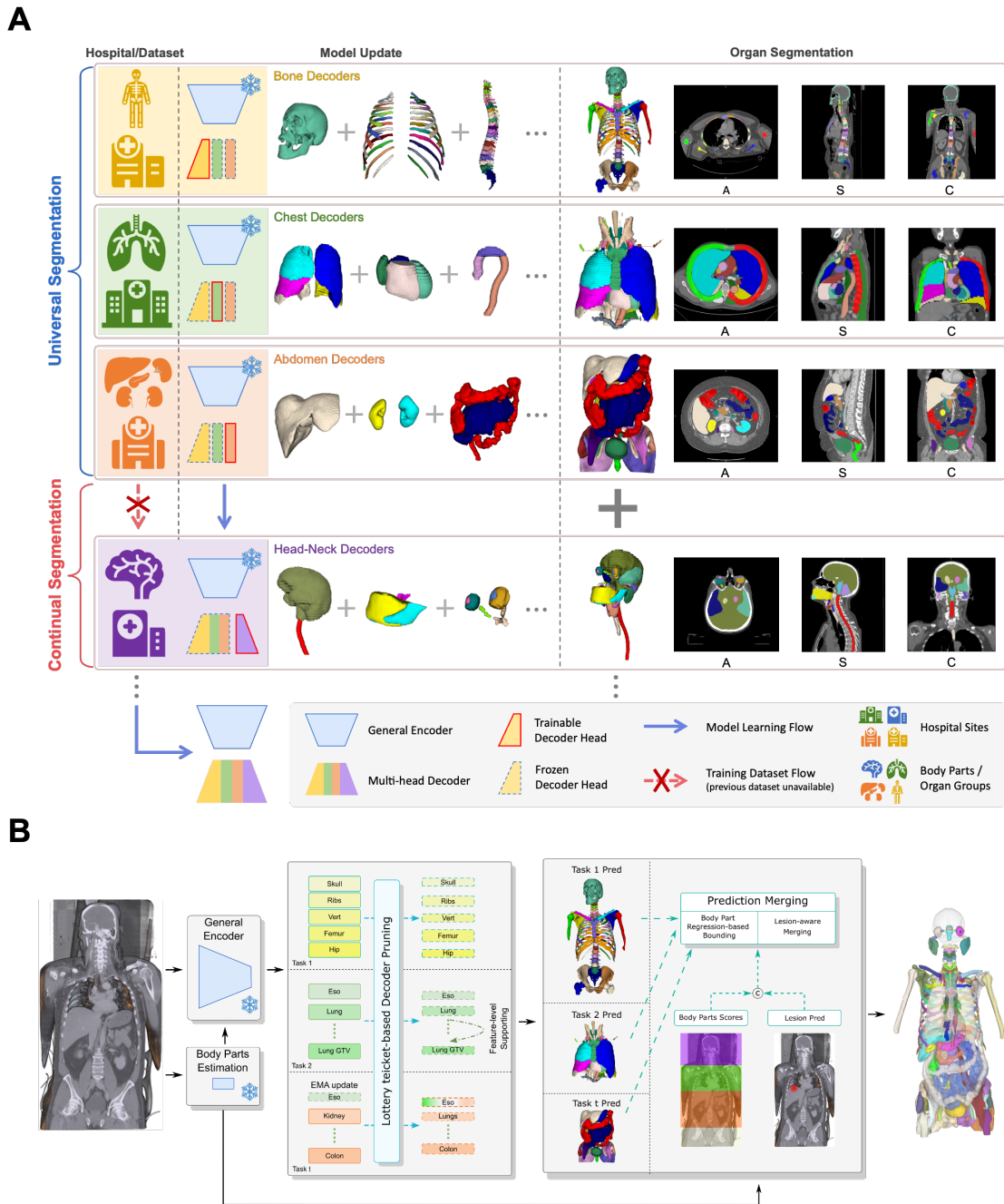


Fig. 2 | Illustration of the learning process and architecture of CL-Net. A. CL-Net can be trained or updated from both universal segmentation and continual segmentation settings, with the pre-trained General Encoder (GE) being frozen. In the partial label segmentation setting, with simultaneous access to datasets of different body parts, the model directly learns different decoders to segment whole-body organs. In the continual segmentation setting, with sequentially available new datasets and no access to previous ones, lightweight decoders of corresponding anatomy structures are added or updated, enabling segmentation of all learned organs without forgetting. B. An overview of the CL-Net framework: a GE for feature extraction, multiple decoders for organ-wise segmentation, a LTH-based decoder pruning module, and a prediction merging module.

set of 235 whole-body anatomies, and compares to the performance of fully optimized ¹ 36-nnUNet ⁸ specialists ensemble (nnUNet^{E₃₆}), which should be considered as the true state-of-the-art segmentation results. We also evaluate the impact of decoder pruning by comparing CL-Net^{U₃₆} with its original unpruned counterpart model (CL-Net^{U₃₆_{unpruned}}).

Next, the **internal comparative evaluation** is conducted on five representative public datasets (a total 1,471 CT scans and 137 anatomy types), including TotalSegmentator V2 (whole-body) ⁵⁵, StructSeg19 (head & neck) ⁵⁶, SegThor (chest) ⁵⁷, FLARE22 (abdomen) ⁵⁸, and KiTS21 (lesion) ⁵⁹. We develop CL-Net^{U₅} and CL-Net^{C₅} using the training data of these five internal public datasets under partial label and continual training configurations, respectively. We also train and compare to the leading multi-dataset approach Multi-Talent ¹⁷ on these five internal public datasets. We further compare the performance of the latest SAM-style medical foundation models, SAT-Pro ²², VISTA3D ²⁵ and BiomedParse ²⁴, as they can segment many organ types in these five public datasets. Finally, the performance of CL-Net^{C₅} (as a continual segmentation model) is compared to three of the most popular and leading continual segmentation methods, MiB ⁶⁰, PLOP ⁶¹, and CSCLIP ⁶² under continual training configuration. Detailed experimental settings are described in Supplementary Sec. A2. Note that we did not compare Multi-Talent ¹⁷ or SAM-style medical foundation models in the full evaluation of 36 internal datasets, because SAM-style foundation models ^{22,63} are not capable of segmenting many fine-grained anatomies in our private datasets, and Multi-Talent, on the other hand, lacks the scalability to train on full-scale datasets (it takes over 1,000 GPU hours to converge when training on only five datasets of 1,471 CT scans). Finally, the **external evaluation** is carried out on seven external datasets (a total 1,979 CT scans and 43 anatomy types), including organs and lesions at head & neck, chest, abdomen regions. We compare our CL-Net (CL-Net^{U₃₆}) with the ensemble of nnUNet^{E₃₆}, Multi-Talent ¹⁷, SAT-Pro ²², VISTA3D ²⁵ and BiomedParse ²⁴ by directly performing inference on these seven external datasets. In addition, using five representative internal public datasets, **ablation studies** are performed to evaluate the effectiveness of several key method components of CL-Net, such as the general encoder training scheme, decoder’s Feature Level Supporting (FL-Supporting) function, EMA-based decoder fine-tuning, etc.

2.2 Full Internal Results on 36 Datasets We report the organ-wise segmentation performance of 235 organs for CL-Net under both universal segmentation (CL-Net^{U₃₆}) and continual segmentation settings (CL-Net^{C₃₆}) and compare with the 36-nnUNets ensemble (nnUNet^{E₃₆}). The investigated anatomies (except ‘Body’) are grouped as Head & Neck, Chest, Abdomen, Bone, Lymph node station (LNS), and Lesion, according to different body parts and anatomy types.

1) CL-Net^{U₃₆}, simultaneously trained on 36 datasets under universal segmentation setting, demonstrates superior segmentation performance across 235 anatomies compared to 36 nnUNet ensemble nnUNet^{E₃₆}. The quantitative results are summarized in Table 1 and Fig. S1, and several observations are made. First, our CL-Net^{U₃₆} achieves the organ-wise mean DSC of

¹The TotalSegmentator nnUNet model was trained for 8,000 epochs, while the other models were trained for 1,000 epochs. All nnUNet models utilized the default “3d_fullres” network setting with “more data augmentation” training scheme.

Table 1 | Quantitative segmentation results of nnUNet^{E₃₆}, CL-Net^{U₃₆unpruned}, CL-Net^{C₃₆} and CL-Net^{U₃₆} on 235 whole-body anatomies. Results are grouped into different body regions and anatomy types. Model complexity is also reported. DSC: Dice-Sørensen coefficient (%), ASD: average surface distance (mm), Param#: network parameter size (MB). The best results are highlighted in bold.

Metric	Method	Head & Neck (49)	Chest (52)	Abdomen (28)	Bone (63)	LNS (33)	Lesion (9)	Body (1)	All (235)
DSC (%)↑	nnUNet ^{E₃₆}	75.9	85.5	90.8	94.3	72.1	69.1	97.0	83.9
	CL-Net ^{U₃₆unpruned}	80.6	88.1	91.8	94.6	74.3	69.6	97.2	86.1
	CL-Net ^{C₃₆}	79.6	88.0	91.5	94.5	74.1	69.4	97.1	85.7
	CL-Net ^{U₃₆}	80.6	88.1	91.8	94.6	74.2	69.7	97.1	86.1
ASD (mm)↓	nnUNet ^{E₃₆}	1.18	1.37	1.14	1.06	1.35	3.84	2.20	1.32
	CL-Net ^{U₃₆unpruned}	0.96	1.18	0.98	0.99	1.21	3.90	2.29	1.18
	CL-Net ^{C₃₆}	1.01	1.19	1.02	0.99	1.22	3.92	2.33	1.20
	CL-Net ^{U₃₆}	0.95	1.17	0.97	0.98	1.20	3.72	2.50	1.17
Param# (MB)↓	nnUNet ^{E₃₆}	—	—	—	—	—	—	—	1,126.8
	CL-Net ^{U₃₆unpruned}	438.2	485.2	297.4	172.2	31.3	156.5	15.7	1,612.1
	CL-Net ^{C₃₆}	12.2	6.9	3.5	2.0	3.8	11.6	0.1	55.6
	CL-Net ^{U₃₆}	12.1	6.9	3.5	2.0	3.8	11.6	0.1	55.5

86.1% and the mean ASD of 1.17mm, markedly outperforming nnUNet^{E₃₆} by 2.2% DSC increase and 11.5% (0.15mm) ASD error reduction for 235 anatomies. Second, as illustrated in the detailed organ-wise DSC accuracy (Fig. S1), CL-Net^{U₃₆} outperforms nnUNet^{E₃₆} in 206 out of 235 anatomies with an average improvement in DSC of 2.5%. For the remaining 29 anatomies where CL-Net^{U₃₆} yields lower DSC, the mean difference in DSC is relatively small with an average DSC reduction of 0.4%. In terms of ASD, CL-Net^{U₃₆} exhibits lower ASD errors in 214 out of 235 anatomies, with an average ASD reduction of 0.19mm. Third, CL-Net^{U₃₆} exhibits significant DSC improvement over nnUNet^{E₃₆} on several organs in head & neck and chest regions, such as pituitary (10.1%), optical nerves (11.8%) and chiasm (11.9%), hypothalamus (13.9%), pineal gland (10.5%), vertebral arteries (9.5%), and brachial plexus (13.8%). These organs are more difficult to segment, as they are small and have poor intensity contrast with adjacent anatomies on CT imaging. Due to the organ-specific decoder design and FL-Supporting (The detailed decoder-wise FL-Supporting information is reported in Supplementary Table S5), each decoder can zoom in to focus on segmenting a particular organ, which leads to easier optimization compared to training a single nnUNet to segment all organs simultaneously. Lastly, in terms of model complexity, CL-Net^{U₃₆} has 55.5MB parameters, which are less than two nnUNet model sizes (62.6MB). In comparison, the ensemble of 36 nnUNet specialists contains 1, 126.8MB parameters, 20 times larger than CL-Net^{U₃₆}. These results highlight the superior performance and scalability of CL-Net^{U₃₆} for segmenting 235 fine-grained whole-body anatomies on 3D CT scans (some qualitative segmentation examples are illustrated in Fig. 5 and Fig. 6).

When stratified by different body regions and anatomy types, CL-Net^{U₃₆} delivers high mean DSC scores for the head & neck (80.6%), chest (88.1%), abdomen (91.8%), bone (94.6%) and body (97.1%) subgroups, respectively. CL-Net^{U₃₆} also yields small ASD errors (~1mm) in all subgroups except the lesion group (3.72mm ASD). This is because lesions are usually more difficult to segment due to their ambiguous boundaries, small size, and irregular shapes⁷. Compared to nnUNet^{E₃₆}, CL-Net^{U₃₆} consistently shows higher mean DSC scores in all subgroups, with notable

DSC improvements of 4.7%, 2.6%, 1.0% and 2.1% in head & neck, chest, abdomen and lymph node station (LNS), respectively. Similar error reductions in mean ASD are observed across the subgroups. Note that LNSs are regions that contain different anatomical levels of lymph nodes and their segmentation is highly context-dependent^{36,64}, i.e., LNS boundaries are restricted by anatomical organs. Hence, using the FL-Supporting function in CL-Net^{U₃₆}, we can segment LNS more accurately by injecting decoder features of the adjacent organs of LNS, resulting in 2.1% improved DSC and 10.4% reduction of ASD error compared to nnUNet^{E₃₆}.

2) CL-Net^{C₃₆}, continuously trained on 36 datasets under continual segmentation setting, achieves closely comparable performance from CL-Net^{U₃₆}. As shown in Table 1, CL-Net^{C₃₆} attains a mean DSC of 85.7% and a mean ASD of 1.20mm across all 235 organs. When compared to CL-Net^{U₃₆} that simultaneously trained on 36 datasets, CL-Net^{C₃₆} shows very close performance with a minor performance gap of 0.4% DSC and 0.03mm ASD. Although a slightly increased performance variation between CL-Net^{C₃₆} and CL-Net^{U₃₆} is observed in head & neck (1.0% DSC gap) and the lesion subgroups (0.20mm ASD gap), the results for most subgroups are very close in both metrics, with DSC ranging from 0.02% to 0.3% and ASD from 0.01mm to 0.06mm. These results demonstrate that CL-Net^{C₃₆} exhibits superior universal segmentation performance even in the challenging continual segmentation setting, where datasets are sequentially accessible to the model (only one dataset is available in a learning step). This is primarily due to the design of CL-Net framework that allows to retain the existing anatomical segmentation capability while simultaneously adding and training new decoders for previously unseen anatomy types or updating existing decoders for anatomy types present in earlier datasets using EMA-based fine-tuning scheme. Note that CL-Net^{C₃₆} also markedly outperforms the ensemble of 36 nnUNet specialists nnUNet^{E₃₆} by 1.8% DSC improvement and 9.2%(0.12mm) ASD error reduction.

3) CL-Net^{U₃₆} significantly reduces the model size and parameter growth rate compared to CL-Net^{U₃₆_{unpruned}}, while maintaining similar segmentation accuracy. The performance and model parameters of CL-Net without decoder pruning (CL-Net^{U₃₆_{unpruned}}) are shown in Table 1. It can be seen that CL-Net^{U₃₆_{unpruned}} has a large model size of 1,612.1MB, due to the incrementally expanded decoders that rapidly grow the model size. In comparison, with the optimized and pruned decoders, CL-Net^{U₃₆} has only 55.5M parameters, which is 3.4% of CL-Net^{U₃₆_{unpruned}} model size. As a result, the decoders in CL-Net achieve a substantial mean pruning rate of 97.5%, indicating a very small parameter growth rate of 2.5% averaged across all decoders. The detailed pruning rates of each decoder are illustrated in Fig. 3. The pruning rate for 99 out of 101 decoders in CL-Net is observed to exceed 90%, of which 80 decoders’ pruning rates further exceed 95% (some of the most pruned decoders even reach 99.7% pruning rates). Under significant pruning rates, CL-Net^{U₃₆} still achieves approximately the same performance as the unpruned counterpart CL-Net^{U₃₆_{unpruned}}. For example, CL-Net^{U₃₆_{unpruned}} and CL-Net^{U₃₆} exhibit the same 235 organ-wise mean DSC of 86.1%. Specifically, 47.5% decoders in CL-Net^{U₃₆} have improved DSC by an average of 0.07% after pruning, while 52.5% of its decoders have marginally decreased an average of 0.05% DSC. These results demonstrate the effectiveness and robustness of our decoder pruning in CL-Net, which balances the model scale and

performance accuracy.

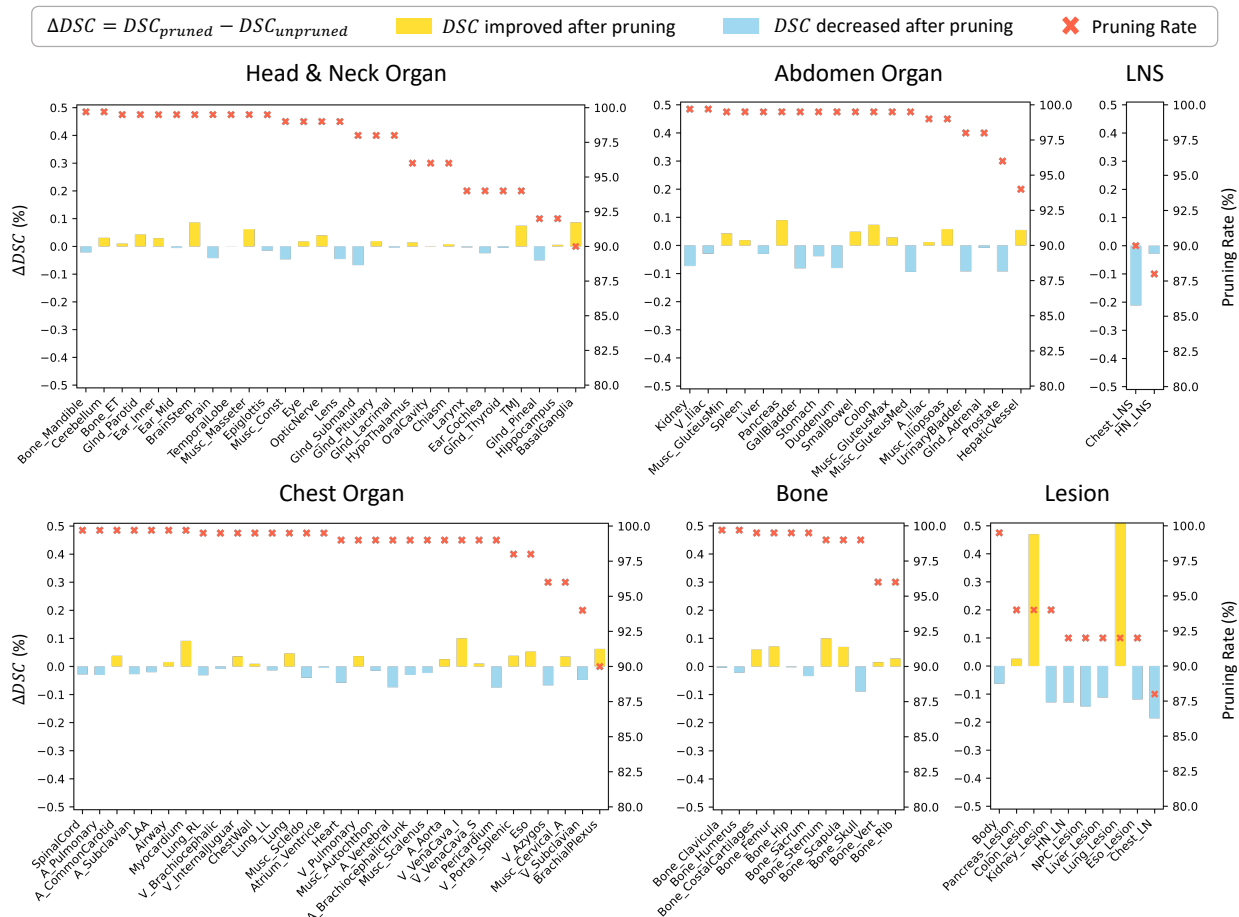


Fig. 3 | The decoder-wise pruning rates and DSC score differences of CL-Net^{U36} after pruning. Evaluation of parameter pruning rates (\mathcal{T} , %) and DSC score differences (ΔDSC , %) for 101 decoders between CL-Net^{U36}_{unpruned} and CL-Net^{U36}. Decoders, except ‘Body’, are grouped into Head & Neck (28 decoders), Chest (31), Abdomen (19), Bone (11), LNS (2), and Lesion (9). Yellow/blue bars (left axis) represent positive/negative ΔDSC for each decoder post-pruning, while red cross markers (right axis) indicate decoder-wise \mathcal{T} . Results show minimal ΔDSC (mostly within $\pm 0.1\%$) and consistently high \mathcal{T} (above 90% for most decoders), highlighting the efficiency of pruning with negligible impact on segmentation performance. Detailed organ-wise metrics and decoder-wise pruning rates are provided in Supplementary Sec. A6 and S12–S17.

2.3 Comparative Internal Results on Five Representative Public Datasets Trained and validated on five internal representative public datasets (total 137 anatomy types), we compare CL-Net to the ensemble of five nnUNet specialists (nnUNet^{E5}) the leading multi-dataset approach, MultiTalent¹⁷. The performance of the latest SAM-style medical foundation models^{22,24,25} is also compared. For comparison with SAM-style models, we only report the quantitative performance of organs that appeared in their training data (unseen organs are not tested in SAM-style models). For example, SAT-Pro²² can segment all 137 anatomies in these five datasets, while VISTA3D²⁵ can segment 115 anatomies. In contrast, BiomedParse²⁴ mainly segments abdomen organs; therefore, we only compare its performance on the FLARE22⁵⁸ dataset. Finally, as a continual segmentation model,

CL-Net^{C5} is further compared to three leading and popular continual segmentation methods, MiB⁶⁰, PLOP⁶¹, and CSCLIP⁶² under continual training configuration.

Table 2 | Performance comparison of universal segmentation models on five representative public datasets. The mean DSC (%) and ASD (mm) of CL-Net^{U5}, nnUNet^{E5}, MultiTalent¹⁷, SAT-pro²², and VISTA3D²⁵ are evaluated on five representative public datasets. The best results are highlighted in bold. Note that, the officially released SAT-pro inference model removes spacing information from the original image headers, making ASD calculation infeasible. Additionally, VISTA3D does not support segmentation of head-neck organs or kidney tumors, precluding its evaluation on StructSeg19 and KiTS21.

Metric	Method	TotalSegmentator V2	StructSeg19	FLARE22	SegThor	KiTS21	Mean
DSC (%)↑	nnUNet ^{E5}	94.1	86.4	89.9	92.6	86.7	92.5
	MultiTalent ¹⁷	92.5	79.0	89.3	90.7	79.6	90.2
	SAT-Pro ²²	86.4	62.9	85.1	90.3	80.0	83.0
	VISTA3D ²⁵	91.6	—	85.9	90.4	—	—
	CL-Net ^{U5}	94.3	87.0	90.7	93.7	87.2	92.9
ASD (mm)↓	nnUNet ^{E5}	0.97	0.29	1.14	0.34	1.18	0.87
	MultiTalent ¹⁷	0.81	1.95	1.83	1.44	9.94	1.13
	SAT-Pro ²²	—	—	—	—	—	—
	VISTA3D ²⁵	3.41	—	1.95	1.52	—	—
	CL-Net ^{U5}	0.85	0.27	1.04	0.32	1.03	0.77

Table 3 | Performance comparison of CL-Net^{U5}, nnUNet^{E5}, and BiomedParse²⁴ on 13 organs of FLARE22. CL-Net^{U5} shows the best DSC and ASD performance. †Note: “DSC* (2D organ-slice)” is the mean DSC computed only on 2D CT slices that contain the foreground target organs (slices are pre-selected using ground truth annotations), which is used in BiomedParse for evaluation. In this table, values for this 2D DSC metric (shown in grey) are directly extracted from BiomedParse paper for reference only and are not intended for comparison.

Metric	Method	Liver	Kidney_R	Kidney_L	Spleen	Pancreas	A_Aorta	V_VenaCava_I
DSC* (2D organ-slice)	BiomedParse† ⁶³	96.6	95.7	96.3	96.1	86.7	94.8	89.6
DSC↑	BiomedParse ⁶³	24.1±19.8	53.9±7.5	64.9±3.6	62.3±6.1	2.4±0.4	27.2±0.5	11.6±1.5
	nnUNet ^{E5}	98.1±14.5	92.4±16.9	92.8±16.9	97.9±15.6	91.6±17.2	96.7±16.5	88.8±10.1
	CL-Net ^{U5}	98.3±5.8	94.3±7.1	92.9±6.7	98.0±6.6	92.4±7.0	97.1±16.5	88.6±9.9
ASD↓	BiomedParse ⁶³	48.34±26.44	57.48±14.48	69.38±10.18	51.41±8.09	60.92±0.61	64.15±3.13	70.89±8.90
	nnUNet ^{E5}	0.83±0.98	1.81±0.74	1.27±0.74	0.30±0.37	0.80±0.69	0.21±0.95	1.08±1.03
	CL-Net ^{U5}	0.81±1.00	1.44±0.76	1.18±0.69	0.19±0.37	0.72±0.38	0.18±0.83	1.12±0.98
Metric	Method	GlnD_Adrenal_R	GlnD_Adrenal_L	Gallbladder	Eso	Stomach	Duodenum	Mean
DSC* (2D organ-slice)	BiomedParse† ⁶³	76.3	79.0	86.8	85.0	92.8	81.1	89.0
DSC↑	BiomedParse ⁶³	0.0±0.0	0.0±0.0	1.0±1.0	59.4±13.7	0.8±0.0	1.0±1.0	23.7
	nnUNet ^{E5}	85.9±12.3	88.0±13.3	80.2±24.7	84.4±3.1	91.7±16.4	79.8±25.9	89.9
	CL-Net ^{U5}	87.9±13.2	87.7±12.5	83.1±8.7	86.0±3.0	92.4±6.5	81.0±16.1	90.7
ASD↓	BiomedParse ⁶³	79.70±2.33	102.87±16.02	134.81±19.78	34.80±28.08	59.16±2.60	58.08±7.51	68.62
	nnUNet ^{E5}	0.39±0.37	0.26±1.16	2.16±0.83	1.70±0.15	1.24±0.67	2.71±1.29	1.14
	CL-Net ^{U5}	0.35±0.39	0.21±0.38	2.12±0.83	1.61±0.14	1.17±0.69	2.39±1.18	1.04

4) CL-Net substantially outperforms the leading multi-dataset segmentation approach MultiTalent¹⁷. As shown in Table 2, averaged across the five datasets, CL-Net^{U5} achieves a DSC of 92.9% and an ASD of 0.77mm, substantially outperforming MultiTalent¹⁷ by 2.7% absolute DSC improvement and 31.9% relative ASD error reduction. Among individual datasets, the multi-talent approach yields much inferior accuracy in segmenting head & neck organs (−8.0% DSC) and kidney lesions (−7.6% DSC). Because MultiTalent simply expands nnUNet’s final convolutional

layer (output) to generate output probabilities for existing anatomies in all datasets with the sigmoid activation function (relying only on the last convolutional layer); hence, encountering difficulty to segment small and hard anatomies (like lesions or many small organs in head & neck region).

5) CL-Net significantly outperforms SAM-style medical segmentation foundation models. The comparison results on five public datasets between CL-Net and the latest 3D SAM-style text prompt foundation model SAT-Pro²² are shown in Table 2. Although SAT-Pro, the strongest SAT model²², is trained using more than 28 CT datasets (including the training set of these five public datasets), it has a large performance gap with Multi-Talent, nnUNet ensemble and our CL-Net (with the largest margin of -9.9% DSC). In individual dataset, SAT-Pro shows the largest performance decrease in StructSeg19 (a significant drop in DSC 24.1% compared to our CL-Net. Although the PDDCA⁶⁵ and SegRap2023⁶⁶ datasets already include the organs in StructSeg19, and have been used in SAT-Pro training data, SAT-Pro still lacks the generalizability to accurately segment head & neck organs (normally harder than chest and abdomen) of a different cohort. Except for StructSeg19, the other four test datasets have all appeared in SAT-Pro’s training set. Even under this condition, SAT-Pro consistently and considerably produces inferior performance in other datasets compared to our CL-Net, e.g., -7.9% DSC in TotalSegmentator V2, -5.6% DSC in FLARE22, -3.4% DSC in SegThor and -7.2% DSC in KiTS21.

Compared to BiomedParse²⁴, the latest 2D SAM-type medical segmentation model, we restrict the comparison to 13 organs in FLARE22 (since its officially released model can only segment a limited number of abdomen organs). BiomedParse reports 2D slice-level DSC scores on a different test set of FLARE22 (copied in Table 3, denoted as BiomedParse \dagger), which is different from the common 3D volume-level DSC. Because in the BiomedParse \dagger evaluation, CT slices to calculate accuracy have been pre-selected using the ground-truth 3D mask of the specific organ (2D evaluation under unrealistic assumption). However, even under this substantially easier evaluation condition, BiomedParse \dagger has a mean DSC of 89.6% , which is 0.9% and 1.7% lower than the nnUNet ensemble nnUNet^{E5} and our CL-Net CL-Net^{L5} (evaluated in a strict 3D volumetric manner without pre-selected slices). To ensure a fair comparison, we also apply the official BiomedParse model to inference on all CT slices of FLARE22 test data using text prompts and calculate its final 3D metrics. Surprisingly, the results reveal that BiomedParse performs poorly in 3D organ segmentation, with only 23.7% DSC (Table 3) reported. Qualitative examples (Fig. 7) illustrate that the substantially low DSC scores and high ASD errors of BiomedParse are due to the large number of false positive predictions outside the target organ region. This is probably due to the intrinsic limitations of its 2D model architecture, which fails to associate the text prompts with the corresponding organs in the 3D space.

6) As a continual segmentation method, CL-Net^{C5} achieves high accuracy (no forgetting) and excellent scalability, significantly surpassing other leading continual segmentation approaches. The forgetting curves of CL-Net^{C5} and other three continual segmentation methods are summarized in Fig. 4. It is observed that CL-Net^{C5}’s mean DSC scores at consecutive continual learning steps remain stable with high accuracy on every dataset across all four continual segmentation orders.

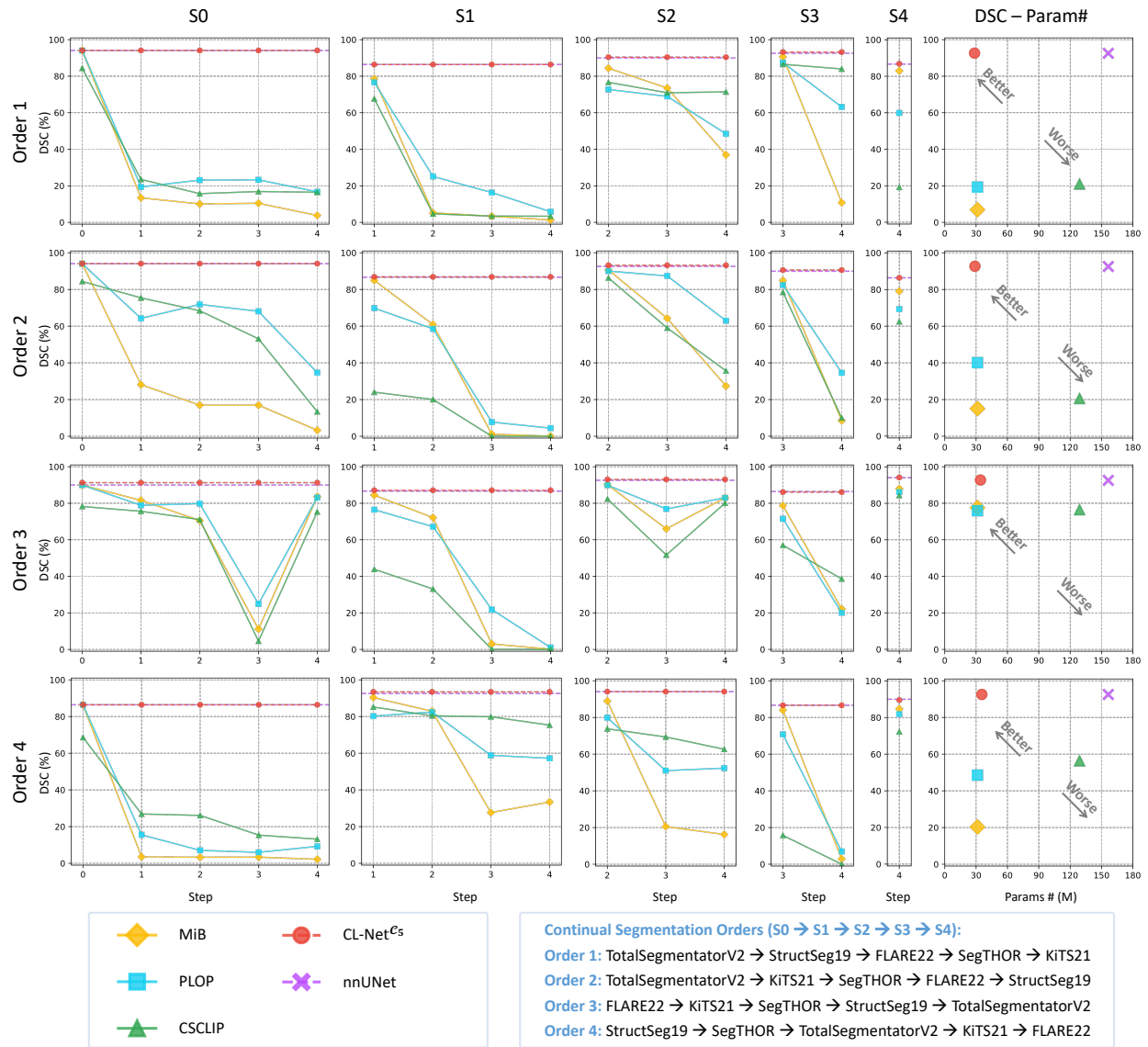


Fig. 4 | Comparison of CL-Net^{C5} with popular continual segmentation methods. Step-wise segmentation performance of CL-Net^{C5}, MiB, PLOP, CSCLIP, and nnUNet (upper bound) is evaluated across four continual segmentation orders (each row for each order) on five public datasets covering various body parts. Columns S0-S4 show the forgetting curves for each method in each dataset and order. The column ‘DSC-Param#’ compares mean DSC scores against the parameter sizes of final models for all methods in each order. Continual segmentation orders of the five datasets are detailed at the bottom. CL-Net^{C5} demonstrates no forgetting of previously learned tasks during continual learning across all orders and achieves the highest mean DSC scores with much smaller model size comparable to the ensemble of nnUNet. The detailed numerical metrics are provided in Table S6, S7, and S40–S48.

Table 4 | External Testing: Performance comparison of SAT-pro, VISTA3D, MultiTalent, nnUNet^{E₃₆}, CL-Net^{C₃₆} and CL-Net^{U₃₆}. The mean DSC (%) and ASD (mm) are evaluated on seven external testing datasets: NPC_SMU (head neck), LungCancer_HHA-FU 24 (chest), BTCV⁶⁷ (abdomen), NPC_CGMH (NPC lesion), EsoCancer_CGMH (eso lesion), LiverCancer_CGMH (liver lesion), and KidneyCancer_SHCH (kidney lesion). We evaluated the average segmentation performance of common chest structures (marked with an asterisk). Note that the SAT-pro inference framework removes image metadata headers during inference, making it impossible to calculate ASD. The best results are highlighted in bold.

Metric	Method	Head & Neck (12)	Chest (14 / 8*)	Abdomen (13)	NPC_Lesion	Eso_Lesion	Liver_Lesion	Kidney_Lesion	Mean
DSC (%)↑	SAT-Pro	46.1	— / 73.9*	—	64.9	—	33.7	—	—
	Vista3D	—	— / 82.9*	85.2	—	—	—	—	—
	MultiTalent	73.1	— / 80.2*	84.2	—	—	—	81.3	—
	nnUNet ^{E₃₆}	75.4	85.5 / 88.5*	84.8	70.4	75.0	69.9	83.6	81.5
	CL-Net ^{C₃₆}	76.7	86.8 / 89.7*	85.0	70.5	74.9	69.9	86.6	82.4
	CL-Net ^{U₃₆}	77.1	87.4 / 90.2*	85.4	70.3	75.1	70.4	86.7	82.8
ASD (mm)↓	SAT-Pro	—	— / —	—	—	—	—	—	—
	Vista3D	—	— / 1.55*	0.85	—	—	—	—	—
	MultiTalent	0.96	— / 37.19*	1.39	—	—	—	7.22	—
	nnUNet ^{E₃₆}	0.94	1.38 / 1.21*	1.33	2.02	8.85	8.41	2.20	1.64
	CL-Net ^{C₃₆}	0.76	1.18 / 1.07*	0.85	2.01	8.87	8.43	1.01	1.48
	CL-Net ^{U₃₆}	0.70	1.08 / 0.99*	0.78	1.98	8.67	7.53	1.00	1.40

In contrast, the forgetting curves of other continual segmentation methods (MiB⁶⁰, PLOP⁶¹, and CSCLIP⁶²) exhibit continuous declines or extensive fluctuations, leading to much lower Dice Similarity Coefficient (DSC) scores in the final step. When evaluating the mean DSC of the final models in all datasets, CL-Net^{C₅} achieves superior segmentation accuracy and model scalability, significantly outperforming other methods in all continual segmentation orders (Fig. 4, column “DSC-Param#”). Specifically, CL-Net^{C₅} has a final mean DSC of 92.6% and a mean ASD of 0.85mm, averaged over all continual segmentation orders (Table S6 and Table S7). In comparison, MiB, PLOP, and CSCLIP all produce catastrophic forgetting, which results in only 30.0%, 46.0%, and 43.6% mean DSC scores, respectively. Meanwhile, the model size of CL-Net^{C₅} is comparable to MiB and PLOP and notable smaller than CSCLIP. Model stability and plasticity, as two essential characteristics in continual learning, are often considered trade-off roles: a stable model resists catastrophic forgetting, while a plastic model adapts effectively to new tasks. However, the above results highlight that our CL-Net achieves both remarkable model stability (nonforgetting) and model plasticity (scalability) in continual learning. CL-Net avoids the knowledge forgetting by freezing the encoder and sequentially adding and training new decoders for new classes or fine-tuning existing decoders for previously existing classes using EMA-based decoder updating scheme. This framework demonstrates strong segmentation performance since CL-Net matches the performance upper bound of nnUNet^{E₅} separately trained on each dataset. Meanwhile, utilizing the LTH-based pruning strategy^{30,31} for the decoders, CL-Net maintains an overall small model size. More detailed results of CL-Net^{C₅} on four continual segmentation orders are provided in the Supplementary Sec. A3.

2.4 External Testing Results on Seven Datasets The external testing results of CL-Net^{U₃₆} and other comparing methods are presented in Table 4. Several conclusions can be drawn. First, SAM-style medical foundation models either segment a limited number of anatomy types (e.g., VISTA3D²⁵ can only segment 21 chest and abdomen organs among the 43 external anatomies), or

exhibit lower segmentation accuracy in external testing (evidently, SAT-Pro²² has 46.1% and 73.9% DSC when segmenting organs in head & neck and chest regions, and 64.9% and 33.7% DSC when segmenting head & neck and liver lesions, showing larger performance gap with CL-Net when compared to that in the internal testing (Table 2). This indicates that existing medical segmentation foundation models struggle to comprehensively and accurately segment common anatomies in CT imaging, which is the most widely used diagnostic modality. Second, Multi-Talent¹⁷ shows a notable performance drop in external tests compared to our CL-Net. Specifically, Multi-Talent¹⁷ has a mean DSC gap of 2.7% as compared to our CL-Net^{U5} in internal testing (Table 2), while the performance gap increases to 4.4% DSC in external testing. Finally, our CL-Net performs consistently on par or higher than the ensemble of 36-nnUNet specialists in external testing with a mean improvement of 1.3% DSC and a reduction of 14.6% ASD error. Notably, our CL-Net^{U36} outperforms nnUNet^{E36} in kidney lesion segmentation by markedly increasing the DSC by 3.1% and reducing the error of half the ASD. Since our external kidney lesion dataset contains a large number of patients (978 testing cases) with various severity of the disease (both very small and large kidney lesions), it is observed that nnUNet^{E36} sometimes has false positive segmentation outside the kidney region or misses small lesions. In contrast, CL-Net utilizes the features of the kidney organ decoder to support the segmentation of kidney lesion (FL-Supporting), reducing the difficulty in segmenting the kidney lesion.

2.5 Ablation Results on Five Representative Public Datasets The ablation results evaluating the effectiveness of CL-Net key components are described in Supplementary Sec A5 and Sec A6, including the general encoder training scheme, general encoder impacts on downstream tasks, the decoder FL-Supporting function, the EMA-based decoder fine-tuning, etc.

3 Discussion

In the medical imaging domain, we refer to a successful universal segmentation model if it meets the following criteria:

- **Comprehensive target coverage:** Trained on a large and diverse dataset, the model should accurately segment a wide range of clinically relevant targets (human anatomical structures and/or even sub-structures if clinically desirable), with a preference for finer-grained structures.
- **Consistently high performance:** The model consistently achieves an accuracy at least comparable to and often higher than the dataset-specific trained state-of-the-art methods/models under rigorous quantitative evaluation.
- **Adaptability:** The model can effectively segment new targets through flexible, adaptive fine-tuning or be efficiently updated to segment new targets using additional datasets, with minimal performance degradation for previously learned targets.

Under these considerations, we build CL-Net, a universal 3D whole-body anatomy segmentation model in CT imaging. Adopting a novel perspective on continuous learning, CL-Net integrates information from 20 public and 16 private partially labeled datasets to segment 235 fine-grained and clinically comprehensive whole-body anatomies, including 193 organs, 33 lymph node stations and 9 lesion types. CL-Net proves its clinical utility by providing high segmentation precision, consistently outperforming or matching the performance of an ensemble of 36 dataset-specific trained nnUNet⁸ specialists (DSC: 86.1% vs. 83.9%) – the current “true” state-of-the-art benchmark⁶⁸ under rigorous training and quantitative comparison. In terms of inference time, CL-Net segments all 235 anatomies in a typical whole-body CT scan in approximately 7 minutes on a single NVIDIA V100 GPU, 2 minutes on 4 GPUs, and just 1 minute on 8 GPUs. In contrast, the ensemble of 36-nnUNet requires approximately 25 minutes to process a single whole-body CT scan. Furthermore, CL-Net can be efficiently updated to segment new anatomies or refine existing anatomies using new datasets without compromising previously acquired knowledge/capacity, overcoming a major limitation of current deep segmentation approaches. Compared to recent universal SAM-style medical models^{19–25} that can only segment a limited subset of fine-grained CT anatomies, CL-Net achieves substantially higher accuracy in both internal and external tests. For example, CL-Net outperforms the recent 3D SAT-Pro²² by 9.9% DSC in internal testing and 24.7% DSC in external testing, despite SAT-Pro being developed with a significantly larger dataset of 22,186 CT scans—nearly double the size of our training data. CL-Net also evidently surpasses the latest 2D BiomedParse²⁴ in abdominal organ segmentation by 67.0% DSC under rigorous 3D quantitative evaluation⁶⁸.

Although SAM¹⁸ has excelled in natural image segmentation, demonstrating impressive performance in interactive (point or text promptable) and zero-shot segmentation, SAM-style models face significant challenges in the medical imaging domain. Our experiments show that the latest foundation models, SAT-Pro²² and BiomedParse²⁴, perform substantially inferior to nnUNet⁸ and our CL-Net in segmenting 3D anatomies in CT scans (Table 3), rendering them impractical in clinical use. As a 2D SAM-based model, BiomedParse²⁴ produces numerous false positives on 3D CT scans (Figure 7), highlighting its inability to effectively link text prompts to correct visual features under the 2D SAM architecture. Although SAT-Pro²² employs a 3D SAM-based network where the text prompt can roughly associate with 3D anatomical locations, its boundary accuracy is notably inferior to nnUNet or our CL-Net (Figure 5). Unlike natural images in which the targets often have distinct visual features, medical imaging targets often exhibit low contrast with adjacent structures or the background. In such cases, Transformer architectures, known for their ability to model long-range spatial dependencies, offer limited advantages. Additionally, SAT-Pro’s use of 3D Transformer dramatically increases the number of parameters, further complicating its network optimization. It is important to note that medical segmentation models are clinically useful only if they achieve high accuracy – that ideally matches the variability between observers^{10,49} or higher, or at least comparable to (or better than) the nnUNet benchmark⁸. Moreover, fully automated segmentation is preferred over interactive approaches, as inputting anatomy names or point prompts consumes physicians’ valuable time (interrupting the regular clinical workflow), making such approaches less practical for routine clinical usage.

The strong universal performance of our CL-Net can be attributed to several key factors. 1) **Comprehensive and high-quality clinically curated datasets:** We compiled a large and diverse set of high-quality, partially annotated CT datasets, including 20 public and 16 private datasets. Public datasets were reviewed to ensure consistency in annotation standards and the absence of obvious errors. Private datasets, comprising primarily pathological patients, were carefully annotated and iterated by our clinical collaborators over the past decade (utilized in many previous peer-reviewed work^{10,32-54}). For instance, to parse the mediastinal lymph node stations³⁶, 35 anatomies were labeled in the chest region, creating the most detailed chest organ dataset. In total, our dataset includes 13,952 CT scans (4,855 public and 9,097 private) covering *a diverse range of vendors, different contrast phases and pathologies*, which is also remarkably larger than the developing dataset of the latest medical segmentation foundation models (e.g., 4,391 CT scans in BiomedParse²⁴ and 4,633 CT scans in VISTA3D²⁵). 2) **A novel CL-Net model network architecture:** the success of CL-Net lies in its model design, where a trained then frozen general encoder paired with independently trainable decoders can extract sufficient features to accurately segment new or update existing organs while preserving existing segmentation capacity. This design naturally handles the issue of partial labeling and ensures that multiple datasets containing a specific organ can be used sequentially or simultaneously; and then integrated to optimize the associated decoder so that more data variations (from all healthy and pathological subjects) are captured by CL-Net. Furthermore, by transforming the simultaneous segmentation of many anatomies from a large number of (often imbalanced) datasets into the sequential segmentation of one or a group of relevant organs, CL-Net significantly reduces optimization complexity and accelerates convergence (e.g., compared to MultiTalent¹⁷ which takes more than 1,000 GPU hours to converge when training on 1,471 CT scans of 137 anatomies). 3) **Scalability through decoder pruning:** CL-Net maintains only a small fraction of effective parameters for each decoder (normally 1~3% model size of the default full-sized decoder) by optimizing each decoder with LTH-based pruning strategy^{30,31}. These important factors collectively enable CL-Net to deliver highly accurate, comprehensive, and scalable segmentation performance, which may serve as a universal model for clinical practice.

In a single dataset scenario, nnUNet⁸ achieves the state-of-the-art segmentation performance compared to the more recent Transformer-based^{25,69,70} and Mamba-based approaches⁷¹ when they are trained and evaluated rigorously without bias^{52,68,72}. Our CL-Net inherits all the advantages of nnUNet (such as intensive data augmentation, auto-optimized patch spacing and size, empirically determined and auto-adaptive hyperparameters, etc.) and more importantly, has the ability to efficiently handle and fully utilize the synergies from a large number of partially labeled datasets no matter whether either sequential or simultaneous data accessibility is available. In contrast, other multi-dataset approaches¹²⁻¹⁷ have limited modeling scalability or capacity when the datasets and organ types increase, e.g., Multi-Talent¹⁷ experiences extremely slow convergence and takes over 1,000 GPU hours when training on only five datasets with 1,471 CT scans (yet not fully optimized with 3%~4% DSC gap to our CL-Net). Additionally, the CL-Net architecture is flexible and can continually and dynamically expand its segmentation capability without affecting previous learned knowledge when new datasets (either new or existing anatomies) are added. By open-sourcing our pretrained models, we empower peers to adaptively fine-tune specific decoders of CL-Net by

incorporating their own data in the continual learning manner and releasing the updated model to foster accelerated development within the research community. This architectural characteristic also ensures that the model size stays fixed when anatomy types in new datasets already exist, or that the model has a very slow and linear parameter growth rate when new anatomy classes are added. The high accuracy, scalability and extendability of CL-Net make it a benchmark model in the multi-dataset segmentation scenario.

As one of the core components of CL-Net, the trained then frozen general encoder is important to train subsequent decoders, which affect the accuracy of the final segmentation. Ideally, for whole-body anatomy segmentation, we expect to construct a sufficiently representative general encoder that extracts deep image features to capture and encode all visual information inside the full human body. Compared to image statistics of broad natural images, medical images appear in a much more confined semantic domain, that is, the human body is anatomically and intrinsically structured composing of distinct body parts. This makes it feasible to learn a strong universal general encoder competently capturing the holistic human body CT imaging statistics using large or not so-limited multi-organ datasets. We demonstrate that TotalSegmentator⁵⁵ (1204 CT scans with 104 organ types) is a suitable dataset for this purpose. Adding more datasets or applying self-supervised pretraining^{73,74} for general encoder training does not bring obvious performance improvements or pruning benefits to the final universal model (as shown in Table S8).

With the advent of automated AI-enabled tools, there is now a rapidly growing appreciation of the potential clinical value added by CT-based segmentation of incidental tissues and organs in CT, often referred to as opportunistic screening^{5,6}. Systematic quantitative cardiometabolic assessment of CT scans can opportunistically yet conveniently produce robust risk stratification related to all-cause mortality, cardiovascular events, osteoporotic fractures, diabetes, metabolic syndrome, sarcopenia, and more⁷⁵⁻⁷⁹. For patients diagnosed with cancer, undergoing major surgery, or in need of organ transplant, CT biomarkers can also provide pre- and post-treatment frailty assessment, in addition to any specific radiomic tasks. Such opportunistic screening processes and assessments can be broadly applied to nearly any body CT scan, and an automated universal segmentation approach provides almost limitless clinical potential. Furthermore, no additional patient time, effort, or radiation exposure is required for this repurposed usage of data, which may not only be highly cost-effective, but may even save cost⁸⁰ in practice.

This work has several limitations. First, we do not include detailed brain anatomies or more lesion types in current CL-Net. However, given the demonstrated effectiveness of CL-Net in segmenting numerous fine-grained anatomies and nine lesion types, we are confident that incorporating more anatomies would not change observations and conclusions derived from the current edition. Second, although we demonstrate the effectiveness of current CNN-based encoder in 3D whole-body universal segmentation, other encoder architectures, e.g., Transformer-, Mamba- or hybrid-based general encoders, may be examined to explore the possibility of further improving the universal segmentation performance. Third, while LTH-based pruning has effectively reduced the number of parameters in CL-Net, it does not alter the channel count or network topology, leaving

the number of FLOPs unchanged. Exploring alternative pruning methods to address this limitation is part of our future work. Lastly, current CL-Net includes lymph node stations (critical for cancer diagnosis and treatment planning) at only head & neck and chest regions. To serve as a universal CT segmentation model in radiology and oncology, we plan to systemically curate the annotation of lymph node stations in the abdominal and pelvic regions (ongoing work). These will be efficiently integrated into CL-Net in the near future without affecting previously learned knowledge, thanks to the expandably designed network architecture of CL-Net.

4 Method

Problem Formulation. We aim to simultaneously or continuously learn a whole-body organ segmentation model from T partially labeled datasets $D = \{D_1, \dots, D_T\}$. In universal segmentation setting, all datasets in D are simultaneously accessible. While in the continual segmentation setting, $\{D_1, \dots, D_T\}$ are sequentially available at each step, which means that all previous training data $\{D_k, k < t\}$ are not accessible when learning on the t^{th} dataset D_t . Let Ψ_t denotes the target organ set of D_t , the total output organ set is:

$$\Psi = \bigcup_{t=1}^T \Psi_t \quad (1)$$

When using ψ to denote an anatomy type, Ψ can also be represented as $\Psi = \{\psi_1, \dots, \psi_M\}$, where M is the total number of anatomy types. Let X be the input image. The prediction map \hat{Y}_ψ for a particular anatomy $\psi \in \Psi$ is given by:

$$\hat{Y}_\psi = f_\psi(f_e(X; W_e); W_\psi) \quad (2)$$

$$\hat{Y} = \bigcup_{\psi \in \Psi} \hat{Y}_\psi \quad (3)$$

where f_e , f_ψ , W_e , and W_ψ denote the CNN functions and the corresponding parameters of the encoding and decoding paths, respectively. For simplicity, we drop explicit notation of voxel spatial locations. The final prediction, \hat{Y} , is formed by taking the union of the predictions from all decoders, allowing each voxel to potentially have multiple labels.

Overall Framework. The proposed CL-Net is designed to address both partial label segmentation and continual semantic segmentation tasks. In the partial label setting, the model utilizes all datasets' samples and labels simultaneously, whereas, in the continual setting, it is trained using one dataset at a time. The CL-Net architecture comprises a shared encoder to extract general characteristics, as illustrated in Figure 2B, multiple stratified and pruned decoders (each corresponding to a pre-defined anatomy or a group of relevant anatomies, Supplementary Table S5), a Body Part Regression (BPR) module, and a prediction-merging module. The process begins by training an encoding segmentation base network with a general encoder. We show that the well-trained encoder, referred to as General Encoder (GE), can effectively extract universal features across various organs and datasets, thus enhancing the performance of subsequent downstream learning tasks. Once GE is trained, it remains

fixed, while additional trainable decoders are updated. This approach forms a unified, scalable, and nonforgetting architecture. At each decoder training stage, optimization and pruning are performed to control model complexity and prevent model escalation. Finally, predictions are merged based on body part regions (e.g., head and neck, chest, and abdomen) and potential lesion locations, resulting in a single unified model capable of segmenting all target organs. The CL-Net supports both single and multi-GPU inference setups, optimizing deployment costs, improving prediction efficiency, and streamlining clinical workflows. The following subsections provide a detailed explanation of each component and the methods employed in CL-Net’s implementation.

4.1 Body Part Regression (BPR) The BPR scores can be obtained based on axial CT slice scores predicted by an automated body part regression algorithm⁸¹. As the slice score monotonically correlates with the patient’s anatomical height, each targeted anatomy can be located based on its relative position. By incorporating this additional task, the CL-Net is trained to explicitly recognize the anatomical region (body part) associated with each target. This enhanced understanding of anatomy distribution is beneficial for learning better voxel representations of target organs and tissues, leading to more precise segmentation and reducing the likelihood of false positives from regions outside of the target anatomy.

4.2 General Encoder (GE) Training In the segmentation of whole-body organs, our goal is to develop a GE that is both representative and universally effective. This encoder should be capable of extracting deep image features that comprehensively capture and encode all visual information pertaining to the entire human body. Unlike the broad image statistics commonly seen in general natural image datasets, medical images, especially radiology scans such as CT and MRI, are confined to a more specific semantic domain: the human body, which is anatomically structured and often includes targets with ambiguous boundary and potential diseases. Based on this, our objective is to develop a robust universal GE that effectively and adeptly captures the comprehensive statistical characteristics of the human body for segmenting whole-body anatomies in CT scans. To train GE for whole-body organ segmentation, we propose starting with the publicly available TotalSegmentator V2 dataset⁵⁵ using the proposed CL-Net framework. In this setup, different types of anatomical structure (e.g., bones, muscles, organs) are assigned to separate decoders, while the GE is updated alongside all decoding paths. In addition to utilizing comprehensive CT datasets for training, we also supplement the details of GE training under the condition that only limited training data or a restricted variety of training classes is available, as described in the Supplementary.

4.3 Multi-path Decoding Following completion and fixation of GE training, trainable decoding heads targeting subsequent downstream tasks are learned. By independently training each decoding path, knowledge forgetting can be mitigated. However, several questions regarding the clinical applicability and generalizability of this approach remain unresolved: 1) As the segmentation target extends, the proposed model complexity may escalate. How can we effectively prune the network without compromising segmentation performance? 2) Automated segmentation of anatomical structures continues to present challenges, particularly for small and difficult-to-identify organs. How can we improve segmentation accuracy for these targets? 3) In a clinical setting, the continuous

collection of new data is a routine practice. How can we efficiently and effectively update the decoders with minimal cost? To address these challenges, we propose the following strategies: 1) *Lottery Ticket Hypothesis (LTH)-based Pruning*, 2) *Feature Level Supporting (FL-Supporting)*, and 3) *Exponential Moving Average (EMA)-based Decoder Updating*.

LTH-based Pruning. The LTH, introduced by Frankle and Carbin³⁰, defines a “winning ticket” as a sub-network that, when trained in isolation from its original initialization, achieves comparable or even better performance to the full network. This hypothesis implies that not all weights in a large network are essential for learning; instead, a critical subset of weights, if properly initialized⁸², can effectively drive the learning process. In our implementation, we focus on pruning the decoding heads while leaving the GE intact. To stabilize the pruning process, each decoding head is initialized using the default nnUNet decoder and trained to convergence without pruning³¹. Then, the proposed LTH-based pruning process is repeated iteratively, with each round involving training, pruning, and rewinding, to progressively identify a smaller winning ticket. During each pruning iteration, we evaluate the performance using the DSC on the validation set. If the performance drop exceeds a pre-defined threshold ($\delta > 1\%$ for 5% – 95% percentile DSC) compared to the validation performance before pruning, the pruning process is stopped and the network is rewound to the previous pruning stage. After pruning is complete, additional training epochs 20 are applied to recover any potential performance drop.

FL-Supporting. To further enhance segmentation accuracy and robustness, we introduce a FL-Supporting mechanism. The FL-Supporting is intuitively simple yet effective. This involves incorporating features from previously learned decoders into the current decoder during training. Using these previously learned features, the current decoder can build on a richer and more informative set of features, leading to improved performance. This approach helps to capture finer details and ensures more consistent and accurate segmentation, particularly for challenging targets. For each decoding block, learnable projection convolutions $[1 \times 1 \times 1]$ are used to adapt relevant features from the output of the previously learned decoder while maintaining the same feature dimensions. The projected features are channel-wise concatenated to the current decoder’s features, providing enriched information for improved segmentation accuracy. Note that the previously learned decoder head is fixed and is not pruned during the learning of the current decoder head. This ensures that the valuable features learned in the previous stages are preserved. The supporting projection convolutions and the current decoding head are targeted for pruning.

EMA-based Decoder Fine-tuning. We adopt EMA to ensure stability and preserve knowledge in continual segmentation setting when new data is included for the update of the decoder. The decay rate is set to $\alpha = 0.999$. The EMA-based decoder fine-tuning is:

$$f_{\psi}^{EMA} = \alpha f_{\psi}^{EMA} + (1 - \alpha) f_{\psi}. \quad (4)$$

Leveraging on EMA, the decoder can be efficiently trained with a mitigated risk of overfitting. During model inference, by default, CL-Net loads the weights of the EMA module to ensure stability and preserve the learned knowledge. Note that EMA updating is optional based on the user’s design;

however, we strongly recommend adopting EMA updating as the default. In the proposed CL-Net, the EMA module is updated only when the decoder pruning is complete. Please note that the pruned mask of the decoder, which identifies the weights to be zeroed out based on their insignificance, is recommended to be *not* updated during training with new data, ensuring consistent performance and stability. On the other hand, only for the decoding head that includes an EMA module, the corresponding pruned mask can be updated. Starting from the existing pruning rate, instead of applying the pruning to the non-smoothed counterpart, the pruning process is conducted to the EMA module, and only the pruned mask of the EMA module is saved.

4.4 Prediction Merging The prediction merging in the proposed CL-Net is *NOT* designed to combine all predictions into a single prediction map. This is because organ-wise predictions include both primary organs and their substructures, as well as potentially overlapping structures between predictions, such as the lungs vs. lung lobes and organs vs. lymph node stations. Forcefully merging all predictions together could lead to overlapping segmentation masks and inaccuracies. Instead, the merging process is carefully structured to consolidate these predictions while considering BPR-based anatomical regions and any identified potential lesions, ensuring an anatomical structured and contextually accurate anatomical representation. Since the lesions could be distributed throughout the human body, BPR is not applied to the lesion decoding heads. Consequently, simply overlaying lesion predictions onto the predicted anatomy may cause false alarms. For example, this approach could mistakenly predict kidney cancer in healthy parotid regions, highlighting the need for more precise integration strategies. The proposed prediction merging includes: 1) *BPR-based Bounding*, and 2) *Lesion-aware Merging*.

BPR-based Bounding. For each decoding path, we pre-compute the BPR scores BPR_ψ of target organs of the decoder. Let z denote the input CT image dimension in the axial direction and σ_ψ denote the standard deviation of the depth of the anatomies of the ψ for the decoder in the axial direction. The body part range of the decoder is determined using:

$$\text{BPR}_\psi^U = \min(z, P_{95}(\text{BPR}_\psi) + 2\sigma_\psi), \quad (5)$$

$$\text{BPR}_\psi^L = \max(0, P_5(\text{BPR}_\psi) - 2\sigma_\psi), \quad (6)$$

$$\mathcal{B}_\psi = J_{[\text{BPR}_\psi^L, \text{BPR}_\psi^U]}, \quad (7)$$

where $P_*(\cdot)$ denotes the $*$ percentile calculation, BPR_ψ^U and BPR_ψ^L denote the upper and lower body part bounds of the decoder, J denote the matrix of ones, and \mathcal{B}_ψ denote the foreground target bounding range of the decoder in the head-to-foot/axial direction, respectively. During model inference, for each decoding head, the prediction \hat{Y}_ψ is updated as $\hat{Y}_\psi = \hat{Y}_\psi \odot \mathcal{B}_\psi$ before merging the decoder output, ensuring that predictions outside the bounding range are removed, where \odot denote element-wise multiplication. This guarantees that the out-of-bound false positives of each decoder prediction are fully cleaned so that potential label conflicts during output merging are mitigated.

Lesion-aware Merging. The proposed Lesion-aware Merging aims to merge the predicted lesion to the target structure considering the target’s BPR range. Let \hat{Y}_ψ^ϵ denote the lesion prediction

of the target structure ψ , and let BPR_ψ denote the body-part bounding range of the target structure. The weighting map M_ψ for the decoder f_ψ is calculated such that only when $\hat{Y}_\psi^\epsilon \rightarrow 0$ and $\mathcal{B}_\psi \rightarrow 1$, s.t., the $M_\psi \rightarrow 1$; whereas $M_\psi \rightarrow 0.5$ for the rest states.

$$M_\psi = J - \frac{1}{2} \left(J - \mathcal{B}_\psi + \hat{Y}_\psi^\epsilon \odot \mathcal{B}_\psi \right), \quad (8)$$

$$H_\psi = - \left(M_\psi \odot \hat{Y}_\psi \right) \log \left(M_\psi \odot \hat{Y}_\psi \right), \quad (9)$$

$$\mathbf{H}(j) = \bigcup_{\forall \hat{Y}(j)_\psi \neq 0} H_\psi(j), \quad (10)$$

$$\hat{\mathbf{Y}}(j) = \hat{Y}^{\text{argmin}(\mathbf{H}(j))}(j). \quad (11)$$

For each voxel j , we collect a set $\mathbf{H}(j)$, for all $\hat{Y}(j)_\psi \neq 0$. Depicted in Eq. (11), the final output class $\hat{\mathbf{Y}}(j)$ is determined using the prediction $\hat{Y}_\psi(j)$, of which the smallest is $H_\psi(j)$. Note that if lesion is not specific to any particular anatomy, such as metastasis cancers or lymph nodes, the bounding range \mathcal{B} is set to encompass the entire image.

4.5 Implementation Overview We provide an overview of the CL-Net implementation. More detailed implementation is reported in the Supplementary Sec. A4.

Image Preprocessing. CL-Net adopts its general training framework from nnUNet². A CT windowing range of $[-1, 024, 1, 024]$ HU is applied to each CT image, which is subsequently pre-processed to the RAI (Right-Anterior-Inferior) orientation. Following this, the standard nnUNet pre-processing pipeline is applied. By default, all CT scans are resampled to a uniform resolution of $1.0 \times 1.0 \times 1.5$ mm and configured with a fixed input patch size of $128 \times 96 \times 112$ for all tasks. Additionally, similar to nnUNet, CL-Net also supports automatic resample resolution and patch size selection based on the training dataset, provided that this option is enabled by the user.

Network Architecture. The architecture backbone is adapted on the basis of nnUNet’s “3D full-resolution” setting. CL-Net includes a 6-block encoding path and a 5-block decoding path, designed to provide robust performance and detailed feature extraction. Similarly to nnUNet, the base number of features for GE is 32 and the maximum number of features (toward the bottleneck block) is capped at 320. Each *encoding* convolutional block consists of two convolutional layers, with instance normalization and leaky ReLU activation applied. Downsampling is performed using strided convolution. The *decoding* block consists of two convolutional layers, also featuring instance normalization and leaky ReLU activation, and is paired with an EMA module. The decoder’s base feature number is configured according to a rule-based adaptation. Upsampling is achieved with transposed convolution, which upscales the output features of each decoding block. The data augmentation pipeline is implemented with the public available “BatchGenerator” framework³.

²<https://github.com/MIC-DKFZ/nnUNet>

³<https://github.com/MIC-DKFZ/batchgeneratorsv2>

Training Efficiency. We have tested that all training tasks can be performed using a single GPU with a standard 12 GiB RAM and 64 GiB of CPU memory. The average training time for a two-class head (e.g., left and right counterparts) in CL-Net is approximately 86 seconds per epoch on a single Nvidia V100 GPU, which can be accelerated to 32 seconds per epoch using a Distributed Data Parallel (DDP) setup with four Nvidia V100 GPUs. The average GPU memory consumption is under 10 GiB during the training of each decoding head. Each trained decoding head has a model size of approximately 80 MiB, which can be reduced to just 18 MiB when saved as a sparse model using PyTorch’s sparse format ⁴. Please note that sparse computation was not applied during model training. Hence, GPU RAM consumption remains unchanged during the training process. The network optimizer used is SGD with the Poly learning rate scheduler.

Inference Efficiency. The CL-Net inference supports both single and multi-GPU setups, aiming to minimize deployment costs, improve prediction efficiency, and streamline clinical workflows. In a single GPU setup, segmentation is performed sequentially by processing each decoding head one at a time. In a multi-GPU setup, decoding heads are evenly distributed across GPUs to accelerate the process. The inference time on a single Nvidia V100 GPU is averagely less than 5 seconds per stratified head. The total inference time for our 235-organ segmentation on a single Nvidia V100 GPU averages 430 seconds per patient, comprising approximately 10s for image pre-processing, 5s for model loading (only once), 400s for inference, 5s for merging and saving, as well as additional system overhead. We strongly suggest using Solid-State Drive (SSD) to store the training data, as SSD improves input/output (BIOS) speed and facilitates faster inter-communication with CPU and GPU memories. When parallel predictions are performed using 4 or 8 GPUs, the total inference time can be reduced to approximately 118s or 58s per patient, respectively. The average consumption of GPU memory is approximately 6 GiB of RAM throughout the entire prediction process.

⁴<https://pytorch.org/docs/stable/sparse.html>

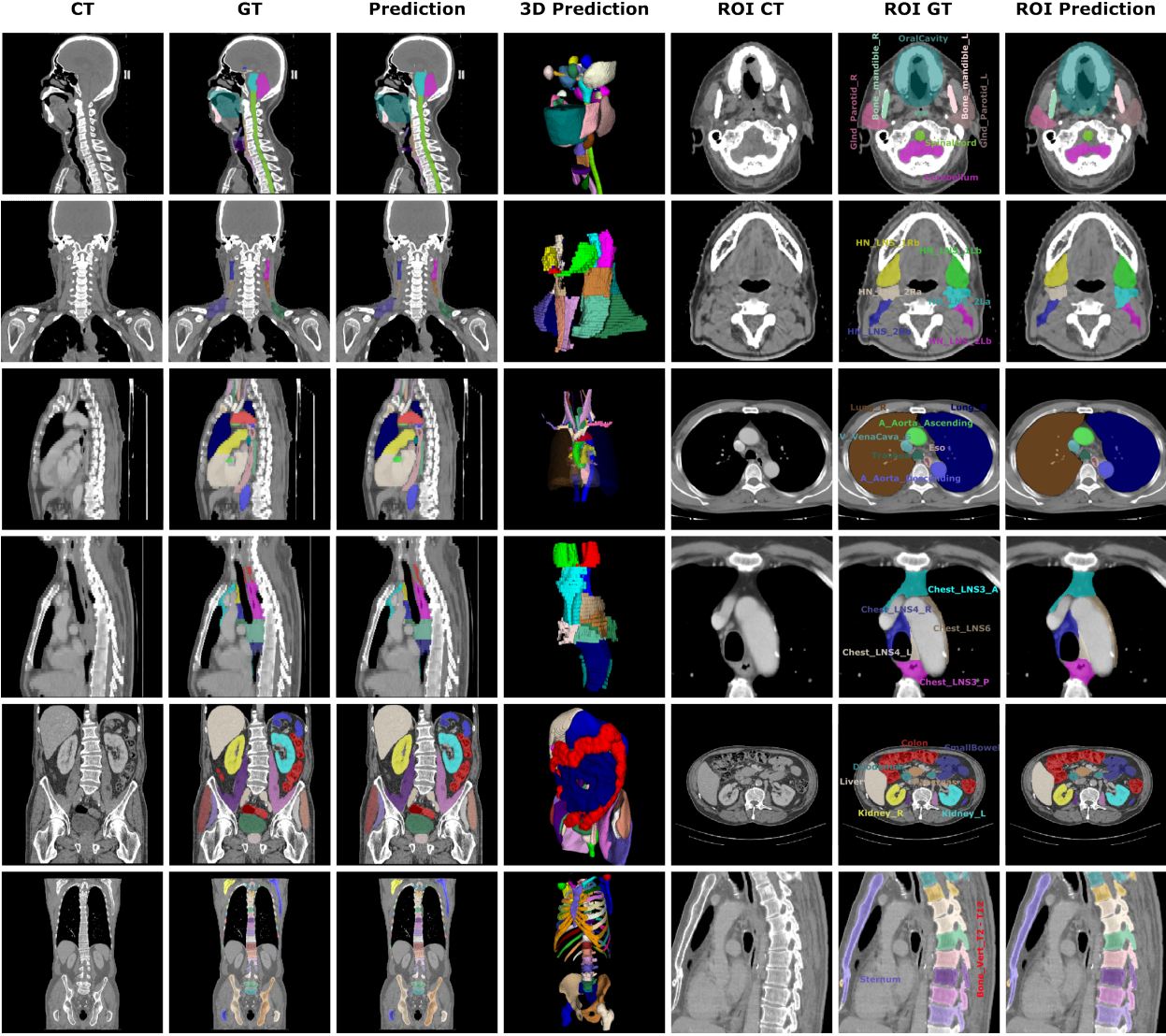


Fig. 5 | Qualitative visualization of CL-Net whole-body anatomy structure segmentation. The first two rows depict the segmentation results of head & neck organs and corresponding lymph node stations, respectively. The third and fourth rows show the segmentation of chest organs and corresponding lymph node stations. The fifth row illustrates the segmentation of abdominal organs, while the final row shows bone segmentation. For better illustration, some organs (such as ChestWall) has been excluded, and certain sub-group organs, such as lung lobes and heart atria and ventricles, have been merged and rendered semi-transparent.

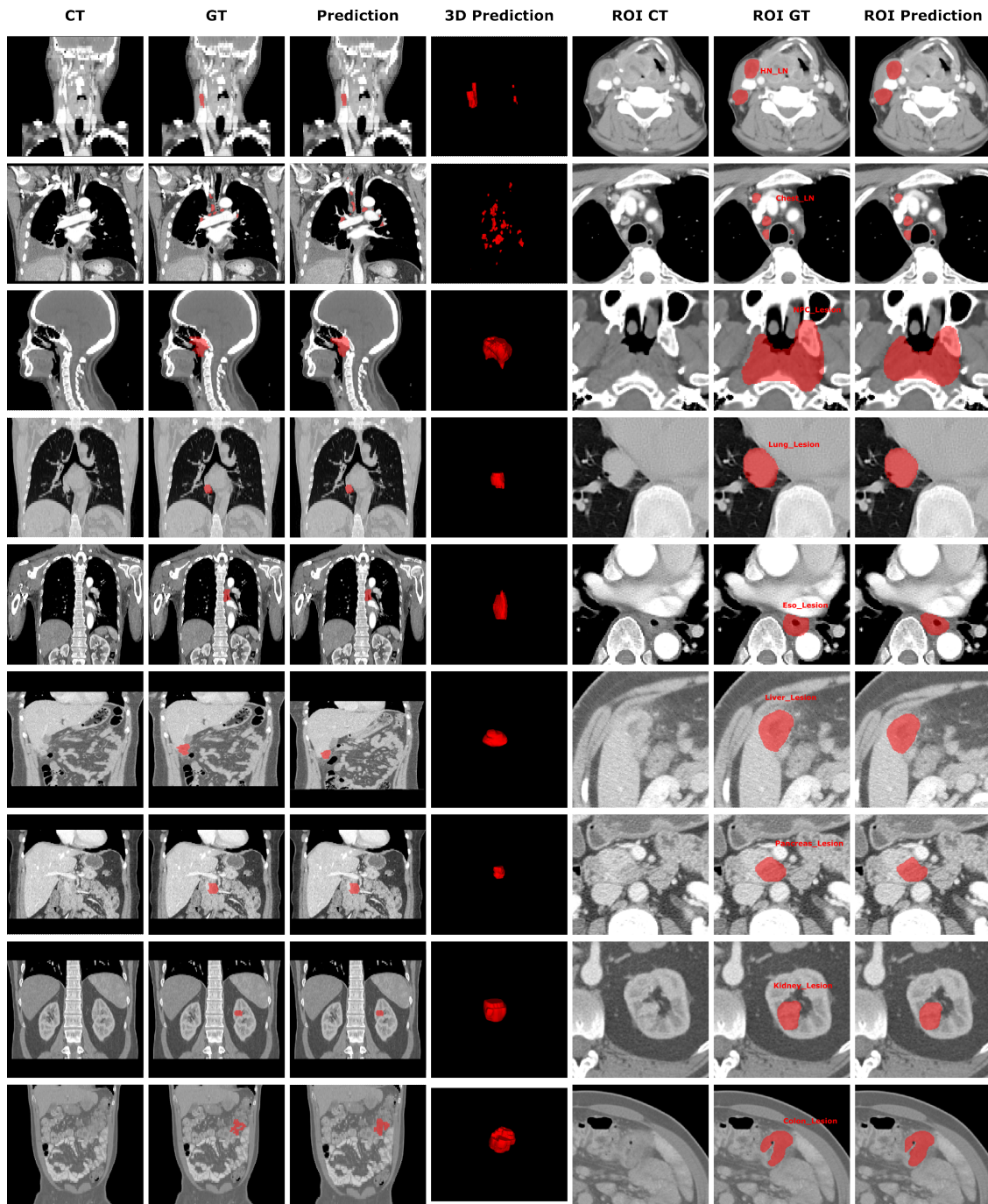


Fig. 6 | Qualitative visualization of CL-Net lymph node and lesion segmentation. The first two rows depict the segmentation results of head & neck and chest regions lymph nodes segmentation, respectively. For better illustration, lymph node stations are superimposed onto the CT images. The third to ninth rows show the lesion segmentation at nasopharynx, lung, esophagus, liver, pancreas, kidney, and colon, respectively.

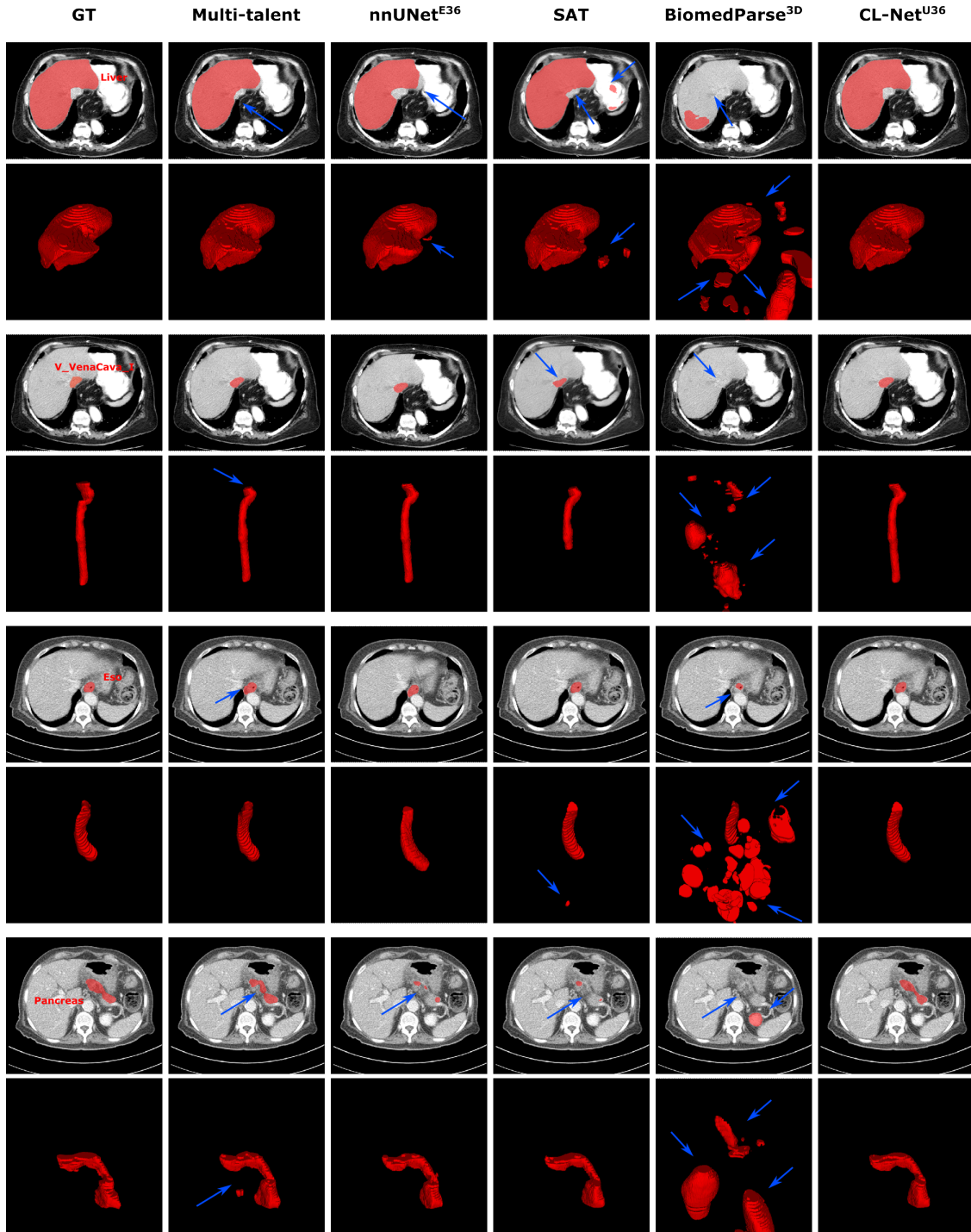


Fig. 7 | Examples of qualitative comparisons. We compared the proposed CL-Net to nnUNet ensemble⁸, MultiTal-ent¹⁷, SAT-Pro²² and BiomedParse²⁴ on predicting liver, inferior vena cava (IVC), esophagus, and pancreas. SAT-Pro and BiomedParse are tested using their official published models. Blue arrow indicates the segmentation errors.

References

1. Ardila, D. *et al.* End-to-end lung cancer screening with three-dimensional deep learning on low-dose chest computed tomography. *Nature medicine* **25**, 954–961 (2019).
2. Lotter, W. *et al.* Robust breast cancer detection in mammography and digital breast tomosynthesis using an annotation-efficient deep learning approach. *Nature medicine* **27**, 244–249 (2021).
3. Wang, C. *et al.* Data-driven risk stratification and precision management of pulmonary nodules detected on chest computed tomography. *Nature Medicine* 1–12 (2024).
4. McIntosh, C. *et al.* Clinical integration of machine learning for curative-intent radiation treatment of patients with prostate cancer. *Nature medicine* **27**, 999–1005 (2021).
5. Pickhardt, P. J. Value-added opportunistic ct screening: state of the art. *Radiology* **303**, 241–254 (2022).
6. Pickhardt, P. J. Harnessing the value of incidental tissue and organ data at body ct (2024).
7. Antonelli, M. *et al.* The medical segmentation decathlon. *Nature communications* **13**, 4128 (2022).
8. Isensee, F., Jaeger, P. F., Kohl, S. A., Petersen, J. & Maier-Hein, K. H. nnu-net: a self-configuring method for deep learning-based biomedical image segmentation. *Nature methods* **18**, 203–211 (2021).
9. Tang, H. *et al.* Clinically applicable deep learning framework for organs at risk delineation in ct images. *Nature Machine Intelligence* **1**, 480–491 (2019).
10. Ye, X. *et al.* Comprehensive and clinically accurate head and neck cancer organs-at-risk delineation on a multi-institutional study. *Nature communications* **13**, 1–15 (2022).
11. Shi, F. *et al.* Deep learning empowered volume delineation of whole-body organs-at-risk for accelerated radiotherapy. *Nature Communications* **13**, 1–13 (2022).
12. Zhang, J., Xie, Y., Xia, Y. & Shen, C. Dodnet: Learning to segment multi-organ and tumors from multiple partially labeled datasets. In *Proceedings of the IEEE/CVF Conference on Computer Vision and Pattern Recognition*, 1195–1204 (2021).
13. Xie, Y., Zhang, J., Xia, Y. & Shen, C. Learning from partially labeled data for multi-organ and tumor segmentation. *IEEE Transactions on Pattern Analysis and Machine Intelligence* (2023).
14. Liu, J. *et al.* Clip-driven universal model for organ segmentation and tumor detection. In *Proceedings of the IEEE/CVF International Conference on Computer Vision*, 21152–21164 (2023).

15. Fang, X. & Yan, P. Multi-organ segmentation over partially labeled datasets with multi-scale feature abstraction. *IEEE Transactions on Medical Imaging* **39**, 3619–3629 (2020).
16. Shi, G., Xiao, L., Chen, Y. & Zhou, S. K. Marginal loss and exclusion loss for partially supervised multi-organ segmentation. *Medical Image Analysis* **70**, 101979 (2021).
17. Ulrich, C. *et al.* Multitalent: A multi-dataset approach to medical image segmentation. In *International Conference on Medical Image Computing and Computer-Assisted Intervention*, 648–658 (Springer, 2023).
18. Kirillov, A. *et al.* Segment anything. In *Proceedings of the IEEE/CVF International Conference on Computer Vision*, 4015–4026 (2023).
19. Ma, J. *et al.* Segment anything in medical images. *Nature Communications* **15**, 654 (2024).
20. Wu, J. *et al.* Medical sam adapter: Adapting segment anything model for medical image segmentation. *arXiv preprint arXiv:2304.12620* (2023).
21. Chen, C. *et al.* Ma-sam: Modality-agnostic sam adaptation for 3d medical image segmentation. *Medical Image Analysis* **98**, 103310 (2024).
22. Zhao, Z. *et al.* One model to rule them all: Towards universal segmentation for medical images with text prompts. *arXiv:2312.17183* (2023).
23. Ouyang, X. *et al.* Towards a general computed tomography image segmentation model for anatomical structures and lesions. *Communications Engineering* (2024).
24. Zhao, T. *et al.* A foundation model for joint segmentation, detection and recognition of biomedical objects across nine modalities. *Nature Methods* 1–11 (2024).
25. He, Y. *et al.* Vista3d: Versatile imaging segmentation and annotation model for 3d computed tomography. *arXiv preprint arXiv:2406.05285* (2024).
26. Goodfellow, I. J., Mirza, M., Xiao, D., Courville, A. & Bengio, Y. An empirical investigation of catastrophic forgetting in gradient-based neural networks. *Proceedings of the International Conference on Learning Representations (ICLR)* (2014).
27. Li, Z. & Hoiem, D. Learning without forgetting. *IEEE transactions on pattern analysis and machine intelligence* **40**, 2935–2947 (2017).
28. Delange, M. *et al.* A continual learning survey: Defying forgetting in classification tasks. *IEEE Transactions on Pattern Analysis and Machine Intelligence* 1–1 (2021).
29. Van de Ven, G. M., Tuytelaars, T. & Tolias, A. S. Three types of incremental learning. *Nature Machine Intelligence* **4**, 1185–1197 (2022).
30. Frankle, J. & Carbin, M. The lottery ticket hypothesis: Finding sparse, trainable neural networks. In *International Conference on Learning Representations* (2019).

31. Frankle, J., Dziugaite, G. K., Roy, D. M. & Carbin, M. Stabilizing the lottery ticket hypothesis. *arXiv preprint arXiv:1903.01611* (2019).
32. Ji, Z. *et al.* Continual segment: Towards a single, unified and non-forgetting continual segmentation model of 143 whole-body organs in ct scans. In *Proceedings of the IEEE/CVF International Conference on Computer Vision (ICCV)*, 21140–21151 (2023).
33. Jin, D. *et al.* Accurate esophageal gross tumor volume segmentation in pet/ct using two-stream chained 3d deep network fusion. In *Medical Image Computing and Computer Assisted Intervention–MICCAI 2019: 22nd International Conference, Shenzhen, China, October 13–17, 2019, Proceedings, Part II 22*, 182–191 (Springer, 2019).
34. Jin, D. *et al.* Deep esophageal clinical target volume delineation using encoded 3d spatial context of tumors, lymph nodes, and organs at risk. In *Medical Image Computing and Computer Assisted Intervention–MICCAI 2019: 22nd International Conference, Shenzhen, China, October 13–17, 2019, Proceedings, Part VI 22*, 603–612 (Springer, 2019).
35. Guo, D. *et al.* Organ at risk segmentation for head and neck cancer using stratified learning and neural architecture search. In *Proceedings of the IEEE/CVF Conference on Computer Vision and Pattern Recognition*, 4223–4232 (2020).
36. Guo, D. *et al.* Deepstationing: thoracic lymph node station parsing in ct scans using anatomical context encoding and key organ auto-search. In *Medical Image Computing and Computer Assisted Intervention–MICCAI 2021: 24th International Conference, Strasbourg, France, September 27–October 1, 2021, Proceedings, Part V 24*, 3–12 (Springer, 2021).
37. Liu, F. *et al.* Same: Deformable image registration based on self-supervised anatomical embeddings. In *Medical Image Computing and Computer Assisted Intervention–MICCAI 2021: 24th International Conference, Strasbourg, France, September 27–October 1, 2021, Proceedings, Part IV 24*, 87–97 (Springer, 2021).
38. Guo, D. *et al.* Thoracic lymph node segmentation in ct imaging via lymph node station stratification and size encoding. In *International Conference on Medical Image Computing and Computer-Assisted Intervention*, 55–65 (Springer, 2022).
39. Guo, H. *et al.* Towards a comprehensive, efficient and promptable anatomic structure segmentation model using 3d whole-body ct scans. In *Thirty-Ninth AAAI Conference on Artificial Intelligence* (2025).
40. Jin, D. *et al.* Deeptarget: Gross tumor and clinical target volume segmentation in esophageal cancer radiotherapy. *Medical Image Analysis* **68**, 101909 (2021).
41. Jin, D., Guo, D., Ge, J., Ye, X. & Lu, L. Towards automated organs at risk and target volumes contouring: Defining precision radiation therapy in the modern era. *Journal of the National Cancer Center* **2**, 306–313 (2022).

42. Wang, P. *et al.* Anatomy-guided deep learning model for accurate and robust gross tumor volume segmentation in lung cancer radiation therapy. *International Journal of Radiation Oncology, Biology, Physics* **117**, e71 (2023).
43. Zhang, Y. *et al.* Deep learning-based multi-modality segmentation of primary gross tumor volume in ct and mri for nasopharyngeal carcinoma. *International Journal of Radiation Oncology, Biology, Physics* **117**, e498 (2023).
44. Yan, K. *et al.* Sam: Self-supervised learning of pixel-wise anatomical embeddings in radiological images. *IEEE Transactions on Medical Imaging* **41**, 2658–2669 (2022).
45. Yan, K. *et al.* Liver tumor screening and diagnosis in ct with pixel-lesion-patient network. In *International Conference on Medical Image Computing and Computer-Assisted Intervention*, 72–82 (Springer, 2023).
46. Yan, K. *et al.* Anatomy-aware lymph node detection in chest ct using implicit station stratification. In *International Conference on Medical Image Computing and Computer-Assisted Intervention*, 299–310 (Springer, 2023).
47. Yu, Q. *et al.* Effective lymph nodes detection in ct scans using location debiased query selection and contrastive query representation in transformer. In *European Conference on Computer Vision*, 180–198 (Springer, 2025).
48. Yu, Q. *et al.* Slice-consistent lymph nodes detection transformer in ct scans via cross-slice query contrastive learning. In *International Conference on Medical Image Computing and Computer-Assisted Intervention*, 616–626 (Springer, 2024).
49. Ye, X. *et al.* Multi-institutional validation of two-streamed deep learning method for automated delineation of esophageal gross tumor volume using planning ct and fdg-pet/ct. *Frontiers in Oncology* **11**, 785788 (2022).
50. Li, Z. *et al.* Lvit: language meets vision transformer in medical image segmentation. *IEEE transactions on medical imaging* (2023).
51. Tian, L. *et al.* Same++: A self-supervised anatomical embeddings enhanced medical image registration framework using stable sampling and regularized transformation. *arXiv preprint arXiv:2311.14986* (2023).
52. Zhu, V. *et al.* Low-rank continual pyramid vision transformer: Incrementally segment whole-body organs in ct with light-weighted adaptation. In *International Conference on Medical Image Computing and Computer-Assisted Intervention*, 371–381 (Springer, 2024).
53. Li, Z. *et al.* Leveraging semantic asymmetry for precise gross tumor volume segmentation of nasopharyngeal carcinoma in planning ct. *arXiv preprint arXiv:2411.18290* (2024).
54. Ye, X. *et al.* Development and validation of thoracic rtog organs at risk delineation with deep learning under multiple datasets’ fusion. *Intelligent Oncology* (2024).

55. Wasserthal, J. *et al.* Totalsegmentator: robust segmentation of 104 anatomical structures in ct images. *arXiv preprint arXiv:2208.05868* (2022).
56. Organizers, S. . C. Structseg 2019: Automatic structure segmentation for radiotherapy planning challenge 2019. <https://structseg2019.grand-challenge.org/> (2019).
57. Lambert, Z., Petitjean, C., Dubray, B. & Kuan, S. Segthor: Segmentation of thoracic organs at risk in ct images. In *2020 Tenth International Conference on Image Processing Theory, Tools and Applications (IPTA)*, 1–6 (IEEE, 2020).
58. Ma, J. *et al.* Unleashing the strengths of unlabeled data in pan-cancer abdominal organ quantification: the flare22 challenge. *arXiv preprint arXiv:2308.05862* (2023).
59. Heller, N. *et al.* The state of the art in kidney and kidney tumor segmentation in contrast-enhanced ct imaging: Results of the kits19 challenge. *Medical Image Analysis* 101821 (2020).
60. Cermelli, F., Mancini, M., Bulò, S. R., Ricci, E. & Caputo, B. Modeling the background for incremental learning in semantic segmentation. In *IEEE/CVF Conference on Computer Vision and Pattern Recognition*, 9233–9242 (2020).
61. Douillard, A., Chen, Y., Dapogny, A. & Cord, M. Plop: Learning without forgetting for continual semantic segmentation. In *Proceedings of the IEEE/CVF Conference on Computer Vision and Pattern Recognition*, 4040–4050 (2021).
62. Zhang, Y. *et al.* Continual learning for abdominal multi-organ and tumor segmentation. In *International conference on medical image computing and computer-assisted intervention*, 35–45 (Springer, 2023).
63. Zhao, T. *et al.* Biomedparse: a biomedical foundation model for image parsing of everything everywhere all at once. *Nature Methods* (2024).
64. Liu, J. *et al.* Mediastinal lymph node detection and station mapping on chest ct using spatial priors and random forest. *Medical physics* **43**, 4362–4374 (2016).
65. Raudaschl, P. F. *et al.* Evaluation of segmentation methods on head and neck ct: auto-segmentation challenge 2015. *Medical physics* **44**, 2020–2036 (2017).
66. Luo, X. *et al.* Segrap2023: A benchmark of organs-at-risk and gross tumor volume segmentation for radiotherapy planning of nasopharyngeal carcinoma. *arXiv preprint arXiv:2312.09576* (2023).
67. Landman, B. *et al.* Miccai multi-atlas labeling beyond the cranial vault—workshop and challenge. In *Proc. MICCAI Multi-Atlas Labeling Beyond Cranial Vault—Workshop Challenge*, vol. 5, 12 (2015).

68. Isensee, F. *et al.* nnu-net revisited: A call for rigorous validation in 3d medical image segmentation. In *International Conference on Medical Image Computing and Computer-Assisted Intervention*, 488–498 (Springer, 2024).
69. Hatamizadeh, A. *et al.* Unetr: Transformers for 3d medical image segmentation. In *Proceedings of the IEEE/CVF Winter Conference on Applications of Computer Vision*, 574–584 (2022).
70. Cao, H. *et al.* Swin-unet: Unet-like pure transformer for medical image segmentation. In *European conference on computer vision*, 205–218 (Springer, 2022).
71. Ma, J., Li, F. & Wang, B. U-mamba: Enhancing long-range dependency for biomedical image segmentation. *arXiv preprint arXiv:2401.04722* (2024).
72. Huang, Z. *et al.* Stu-net: Scalable and transferable medical image segmentation models empowered by large-scale supervised pre-training. *arXiv preprint arXiv:2304.06716* (2023).
73. Chen, T., Kornblith, S., Norouzi, M. & Hinton, G. A simple framework for contrastive learning of visual representations. In *International conference on machine learning*, 1597–1607 (PMLR, 2020).
74. Chen, X. & He, K. Exploring simple siamese representation learning. In *Proceedings of the IEEE/CVF conference on computer vision and pattern recognition*, 15750–15758 (2021).
75. Pickhardt, P. J. *et al.* Automated abdominal ct imaging biomarkers for opportunistic prediction of future major osteoporotic fractures in asymptomatic adults. *Radiology* **297**, 64–72 (2020).
76. Pickhardt, P. J. *et al.* Utilizing fully automated abdominal ct-based biomarkers for opportunistic screening for metabolic syndrome in adults without symptoms. *American Journal of Roentgenology* **216**, 85–92 (2021).
77. Pickhardt, P. J. *et al.* Automated ct biomarkers for opportunistic prediction of future cardiovascular events and mortality in an asymptomatic screening population: a retrospective cohort study. *The Lancet Digital Health* **2**, e192–e200 (2020).
78. Tallam, H. *et al.* Fully automated abdominal ct biomarkers for type 2 diabetes using deep learning. *Radiology* **304**, 85–95 (2022).
79. Nachit, M., Horsmans, Y., Summers, R. M., Leclercq, I. A. & Pickhardt, P. J. Ai-based ct body composition identifies myosteatosi s as key mortality predictor in asymptomatic adults. *Radiology* **307**, e222008 (2023).
80. Pickhardt, P. J., Correale, L. & Hassan, C. Ai-based opportunistic ct screening of incidental cardiovascular disease, osteoporosis, and sarcopenia: cost-effectiveness analysis. *Abdominal Radiology* **48**, 1181–1198 (2023).

81. Yan, K., Lu, L. & Summers, R. M. Unsupervised body part regression via spatially self-ordering convolutional neural networks. In *IEEE ISBI*, 1022–2025 (2018).
82. Malach, E., Yehudai, G., Shalev-Schwartz, S. & Shamir, O. Proving the lottery ticket hypothesis: Pruning is all you need. In *International Conference on Machine Learning*, 6682–6691 (PMLR, 2020).
83. Zhang, C., Zheng, H. & Gu, Y. Dive into the details of self-supervised learning for medical image analysis. *Medical Image Analysis* **89**, 102879 (2023).
84. He, K., Fan, H., Wu, Y., Xie, S. & Girshick, R. Momentum contrast for unsupervised visual representation learning. In *Proceedings of the IEEE/CVF conference on computer vision and pattern recognition*, 9729–9738 (2020).
85. Gotmare, A., Keskar, N. S., Xiong, C. & Socher, R. A closer look at deep learning heuristics: Learning rate restarts, warmup and distillation. *arXiv preprint arXiv:1810.13243* (2018).
86. Tian, Z., He, T., Shen, C. & Yan, Y. Decoders matter for semantic segmentation: Data-dependent decoding enables flexible feature aggregation. In *Proceedings of the IEEE/CVF conference on computer vision and pattern recognition*, 3126–3135 (2019).
87. Radford, A. *et al.* Learning transferable visual models from natural language supervision. In *International conference on machine learning*, 8748–8763 (PMLR, 2021).
88. Guo, D. *et al.* Comprehensive and clinically accurate head and neck organs at risk delineation via stratified deep learning: a large-scale multi-institutional study. *arXiv preprint arXiv:2111.01544* (2021).
89. Li, H. *et al.* Semi-supervised lymph node metastasis classification with pathology-guided label sharpening and two-streamed multi-scale fusion. In *International Conference on Medical Image Computing and Computer-Assisted Intervention*, 623–633 (Springer, 2024).
90. Zhang, M. *et al.* Multi-site, multi-domain airway tree modeling. *Medical image analysis* **90**, 102957 (2023).
91. Wang, P. *et al.* Accurate airway tree segmentation in ct scans via anatomy-aware multi-class segmentation and topology-guided iterative learning. *IEEE transactions on medical imaging* (2024).
92. Podobnik, G., Strojjan, P., Peterlin, P., Ibragimov, B. & Vrtovec, T. Han-seg: The head and neck organ-at-risk ct and mr segmentation dataset. *Medical physics* **50**, 1917–1927 (2023).
93. Ji, Y. *et al.* Amos: A large-scale abdominal multi-organ benchmark for versatile medical image segmentation. *Advances in neural information processing systems* **35**, 36722–36732 (2022).

94. Ma, J. *et al.* Abdomenct-1k: Is abdominal organ segmentation a solved problem? *IEEE Transactions on Pattern Analysis and Machine Intelligence* **44**, 6695–6714 (2021).
95. Luo, X. *et al.* Word: A large scale dataset, benchmark and clinical applicable study for abdominal organ segmentation from ct image. *Medical Image Analysis* **82**, 102642 (2022).
96. Bilic, P. *et al.* The liver tumor segmentation benchmark (lits). *Medical Image Analysis* **84**, 102680 (2023).
97. Heller, N. *et al.* The kits19 challenge data: 300 kidney tumor cases with clinical context, ct semantic segmentations, and surgical outcomes. *arXiv preprint arXiv:1904.00445* (2019).
98. Roth, H. *et al.* A new 2.5 d representation for lymph node detection in ct. <https://doi.org/10.7937/K9/TCIA.2015.AQIIDCNM> (2015).
99. Roth, H. R. *et al.* A new 2.5 d representation for lymph node detection using random sets of deep convolutional neural network observations. In *Medical Image Computing and Computer-Assisted Intervention–MICCAI 2014: 17th International Conference, Boston, MA, USA, September 14–18, 2014, Proceedings, Part I* 17, 520–527 (Springer, 2014).
100. Santanam, L. *et al.* Standardizing naming conventions in radiation oncology. *International Journal of Radiation Oncology* Biology* Physics* **83**, 1344–1349 (2012).

Acknowledgments

We'd like to cordially thank Prof. Gregory D. Hager from Department of Computer Science, the Johns Hopkins University who read our manuscript and provided invaluable suggestions, feedback and encouragement on its technical feasibility and possible clinical utility.

A1 Details of Datasets

An overview of the public and private datasets used in our experiments is provided in Fig. 1 and Tab. S1. The complete 36 training dataset collection consists of 16 private datasets and 20 public datasets, spanning whole-body regions and various anatomical structures, including the head and neck, chest, abdomen, bone, lymph node station (LNS) and lesion. This comprehensive dataset collection contains a total of 7,278 private and 3,904 public CT scans, along with 37,827 private and 172,607 public annotations. Together, these annotations cover 235 anatomical structures, 125 from private sources and 162 from public sources with 52 overlapping classes. Tab. S1 provides a comprehensive summary of the fingerprints of all datasets. In addition to standard statistics, such as the name of the dataset, the number of training and testing samples, the number of target organs, the median image size, and the median voxel spacing, we also report two specialized statistics to better characterize the body part distribution of each dataset. These include the axial bounding ranges of body part regression (BPR) ⁸¹ for both the images and the foreground organs. Further details on the target organs for each private and public dataset are presented in Tab. S2 and Tab. S3, respectively.

As shown in Fig. 1, the 36 datasets are grouped by the corresponding main body part of the dataset’s targets, i.e. head and neck, chest, and abdomen, except for TotalSegmentator and Body_LinkMed_OAR which widely cover the entire body. The dataset distribution of each group is as follows: Head and neck group has 5 private datasets and 4 public datasets, including brain regions, visual organs, auditory organs, oral and larynx, glands, LNS, and NPC lesion, where the image BPR scores mainly range from mid chest (0.6) to upper head (1.0); Chest group has 8 private datasets and 3 public datasets, covering respiratory organs, cardiovascular organs, LNS, as well as lung and esophagus lesion, where the image BPR scores mainly range from mid-lower abdomen (0.3) to upper throat (0.8); Abdomen group has two private datasets and 12 public datasets, targeting digestive organs, urinary organs, vessels and glands, and common abdomen lesions, where the image BPR scores mainly range from lower pelvis (0.0) to upper chest (0.7); Whole-body group has one public dataset – TotalSegmentator, which contributes bones and muscles such as ribs, vertebrae, and limbs, and one private dataset – Body_LinkMed_OAR, which provides whole-body mask to segment the foreground body area. The image BPR scores cover the entire body from 0 to 1.

To further demonstrate the generalizability and robustness of our method, we collect 7 external datasets for validation, comprising 1 public dataset (BTCV) and 6 newly acquired private datasets. These external datasets span whole-body anatomical regions, covering 1,979 testing samples and 43 target anatomical structures in the head and neck, chest, abdomen and lesions. Four types of lesions are included: NPC, esophageal, liver, and kidney lesions. Comprehensive fingerprints of the external datasets, including dataset name, body part coverage, number of target classes, number of testing samples, median image size, median voxel spacing, and a detailed target organ list, are provided in Tab. S4.

A2 Details on Experimental Settings

Internal Full Evaluation Experimental Setting The goal is to train a unified model that not only accurately and robustly segments a wide range of whole-body organs in CT but also has sufficient generalizability and scalability to be easily and efficiently extended to new datasets and segmentation tasks. Therefore, our internal full experiment results are evaluated on the full-scale CL-Net trained across the entire 36 dataset collection, covering a large amount of 11,182 training samples and 235 whole-body anatomical structures, involving the following settings: 1) universal segmentation setting, in which CL-Net is fully trained across all datasets simultaneously and compared with the segmentation upper-bound nnUNet ensemble; 2) continual semantic segmentation setting, where we continuously train CL-Net on 36-dataset sequence; 3) ablation study for decoder pruning module.

Dataset Setting: As outlined in Sec. Overview of Datasets, all 36 datasets are used to train the full-scale CL-Net segmentation model, covering whole-body region. The dataset collection contains a total of 13,952 CT scans – 11,182 for training and 2,770 for testing – annotating 235 target anatomical structures. To conveniently report organ-wise statistical results of our model, we divide the 235 whole-body organs (excluding “Body Mask”) into 6 groups according to their body parts and anatomical types: head and neck (head-neck, 49 organs), chest (52 organs), abdomen (28 organs), bone (63 organs), lymph node station (LNS, 33 organs), and lesion (9 organs). Note that each dataset only labels a subset of our universal anatomy set and is therefore treated as a partially labeled dataset. The dataset details are introduced in Supplementary Sec. A1.

Universal Segmentation Setting: Considering the ever-increasing amount of public medical imaging datasets, it is possible to directly get a large collection of partially labeled datasets for medical segmentation. Thus, in universal segmentation setting, we directly train CL-Net on 36 datasets with simultaneous access to all training samples, resulting in a full-scale, unified model (CL-Net^{U36}) with comprehensive and integrated organ segmentation capabilities. CL-Net^{U36} follows the multi-decoder network architecture, and all decoders are pruned at the end of training. Note that only 101 decoders are included in our final model, fewer than the total number of anatomies, as symmetric anatomical instances and substructures are typically bundled and segmented by the same decoder head. To showcase the superior performance of our model, organ-wise segmentation results are evaluated for CL-Net^{U36} and compared with the 36-nnUNet ensemble (nnUNet^{E36}) as the upper bound for multi-dataset multi-organ segmentation, with each nnUNet specialist trained on separate dataset.

Continual Semantic Segmentation (CSS) Setting: Compared to universal segmentation setting where all training data and labels are accessible, CSS setting is more general and practical in real world situation. In CSS setting, we continuously train and evaluate a CSS version CL-Net (CL-Net^{C36}) on 36 dataset sequence. The continual learning dataset sequence follows the default order of public datasets (D1-D20) and private datasets (P1-P16) listed in Fig. 1. We firstly pretrain and freeze the general encoder on TotalSegmentator V2 (D1) at initial step, and then continually

train CL-Net on the subsequent datasets , incrementally adding or updating decoder heads for new anatomies and labels. At the end of each learning step, the newly added decoder heads are pruned. In accordance with the CSS protocol, only the current dataset is available at each continual learning step, while all previous training datasets remain inaccessible. The segmentation performance of CL-Net^{C36} is also evaluated and compared with CL-Net^{U36} to confirm the effectiveness of our method’s CSS capability.

Ablation Study: To evaluate the impact of decoder pruning on segmentation accuracy and decoder parameter size, we compare the DSC difference and the pruning rate of each CL-Net^{U36} decoder against the unpruned model CL-Net^{U36_{unpruned}}, as shown in Fig. 3. The DSC score for each decoder is computed as the mean DSC across its corresponding target anatomies. Consistent with the organ-wise results, the performance of all 101 decoders is also reported within 6 organ groups.

Internal Comparative Evaluation Experimental Setting We aim to comprehensively validate the effectiveness and robustness of CL-Net in whole-body organ segmentation under both CSS and universal segmentation settings, compare it with other common continual segmentation methods and leading multi-dataset organ segmentation models, and explore the impact of each key module. Directly conducting all validation experiments on full-scale datasets would require excessive computational resources and training time, making it impractical and environmentally unfriendly. Moreover, some comparison methods are not scalable to a large number of datasets or organ classes, leading to unfair comparisons and rendering such experiments infeasible. Therefore, we conduct a small-scale internal evaluation experiment using five representative public datasets selected from the original 36 datasets. These datasets include 1,471 training samples and 137 organs in various body parts and organ types, covering the head and neck, chest, abdomen, bone, and lesion. This experimental design allows us to efficiently and comprehensively validate and evaluate our method. The evaluation experiments involve: 1) CSS setting, in which we continuously train CL-Net on the five datasets, evaluate the performance of different dataset orders, and compare our method with other continual segmentation methods; 2) universal segmentation setting, where CL-Net is simultaneously trained on the five datasets and compared its performance with other leading multi-dataset multi-organ segmentation models; 3) Ablation study for the key modules of CL-Net.

Dataset Selection: From the 36 datasets collected in Sec. A1, we carefully select five representative public datasets spanning different body regions and organ groups to ensure experimental reproducibility and a comprehensive evaluation of the segmentation capacity of our method across various body parts and anatomical structures. Brief descriptions of the five datasets are listed below:

- **TotalSegmentator V2:** This large and diverse dataset contains totally 1,228 CT scans covering all regions of the body and are officially divided into 1,139 training data and 89 testing data. Totally 115 whole-body organs are annotated (left & right kidney cysts are removed);
- **StructSeg19:** The dataset focuses mainly on head and neck regions and includes 50 CT scans,

divided into training and testing sets with 40 and 10 images, separately. The annotations cover 22 head and neck organs, in which 21 organs are not included in TotalSegmentator V2 and only spinal cord is overlapped;

- **SegThor**: This dataset has 40 chest CT scans with only four chest organs, which overlap with TotalSegmentator V2. We split the dataset into training and testing sets with a ratio of 4:1;
- **FLARE22**: The dataset provides the annotations of 13 abdominal organs, which are also included in TotalSegmentator V2. 50 training data and 20 testing data are officially released to public;
- **KiTS21**: This is a large dataset specifically collected for kidney lesion segmentation, where kidney and its lesions are carefully annotated. In this experiment, since KiTS21 is simply used to demonstrate the performance of CL-Net on lesion segmentation, only kidney lesion annotations are used for training while kidney labels are removed. The 300 CT scans are officially divided into 210 training data and 90 testing data.

Universal segmentation Setting: We denote the universal segmentation version of CL-Net trained on five representative public datasets as CL-Net^{U₅}. Under the universal segmentation setting, CL-Net^{U₅} is trained with all decoder heads across the 5 datasets simultaneously to segment all 137 organs. For training samples from any specific partially labeled dataset, only the decoder heads corresponding to the target organ classes of the dataset are updated. At the final training stage, all decoder heads are pruned to reduce the model’s scale. The performance of CL-Net^{U₅} is evaluated on the test set of each dataset for its respective target organs, with an overall assessment conducted across all 137 organs. In particular, the performance of the model under the universal segmentation setting is independent of the order of the dataset, since all datasets are available concurrently. Further implementation details of CL-Net^{U₅} are provided in Supplementary Sec. A4. For comparison, we used nnUNet, the most widely adopted and leading method for medical segmentation, as a benchmark. we independently train nnUNet specialists on each of the five datasets and create a 5-nnUNets ensemble (nnUNet^{E₅}) to represent the upper-bound performance. Additionally, we re-implement and evaluate Multi-talent¹⁷, a state-of-the-art universal segmentation approach for multi-organ segmentation, using the same experimental setup. Furthermore, considering recent advances in large foundation models, we assess the segmentation performance of CLIP-/SAM-based multi-organ segmentation models, including SAT-pro²², VISTA3D²⁵, and BiomedParse²⁴, by testing their officially released models on the five datasets.

CSS Setting: To comprehensively evaluate the performance of continual segmentation, the rate of forgetting, and the sensitivity of the order of CL-Net, we design four distinct dataset orders for training in the CSS setting. Each order consists of five sequential learning steps, S0 to S4, corresponding to incremental learning of the five datasets. The CSS version of CL-Net trained on the five datasets is denoted as CL-Net^{C₅}. During the initial training phase (S0), the general encoder of CL-Net^{C₅} is pretrained on the initial dataset of the current order to acquire general visual feature extraction capabilities. Concurrently, the decoder heads corresponding to the target organs in the S0

dataset are trained and subsequently pruned. In each subsequent continual learning phases (S1-S4), the general encoder and decoder heads for organs not present in the current dataset are frozen to mitigate catastrophic forgetting of previously acquired knowledge. CL-Net^{C5} is sequentially trained and extended on each dataset for new segmentation tasks. For previously unseen organs, new decoder heads are introduced, while existing decoders are updated for overlapping organs, if present. At the end of each step, the added and updated decoders are pruned to reduce the model’s parameter size. Importantly, in accordance with the CSS setting, only the current dataset is accessible during training and pruning at each continual learning step, while previously learned datasets remain unavailable.

The four CSS learning orders (O1-O4) of the five datasets are outlined at the bottom of Fig. 4 and are carefully designed to reflect various sequences of body parts or anatomical types. Both O1 and O2 begin with the same initial dataset (S0) as TotalSegmentator V2, which covers a diverse range of whole-body organs. In O1, the sequence progresses through body parts in the order of head-neck, abdomen, chest, and lesion, while O2 reverses this order to lesion, chest, abdomen, and head-neck. In contrast, O3 starts with the abdomen dataset, followed by lesion, chest, head-neck, and whole-body organs, whereas O4 rearranges the sequence to head-neck, chest, whole-body, lesion, and abdomen. By training CL-Net under CSS settings with different dataset sequences, we explore the impact of body part and organ type order on segmentation performance. Specifically, the comparative design of O1 and O2 allows us to evaluate the order sensitivity of CL-Net^{C5} when using an identical initial step and shared GE. For the technical implementation and hyperparameter settings of CL-Net^{C5}, please refer to Supplementary Sec. A4.

To highlight the advantages of CL-Net, we reimplement three CSS methods – MiB⁶⁰, PLOP⁶¹, and CSCLIP⁶² – and compare their performance with our model under the same experimental conditions. MiB and PLOP are widely used regularization-based CSS benchmarks in both natural and medical imagery domains, employing knowledge distillation to alleviate catastrophic forgetting. CSCLIP, the latest CSS method for continual multi-organ segmentation in the abdomen, mitigating knowledge forgetting through pseudo-labeling of previously learned organs and task prompts from CLIP-based text embeddings of organ names. For details on the re-implementation of these comparison methods, please refer to Supplementary Sec. A7.

Ablation Study: Beyond the evaluation of the performance of the model, the key components of CL-Net are further validated through comprehensive ablation studies. Given that model size and parameter growth rate are the major challenges for architecture-based CSS methods, we evaluate the final performance and the model size of CL-Net^{C5} model without applying the decoder pruning process, referred to as CL-Net^{C5}_{unpruned}. Comparing CL-Net^{C5} with CL-Net^{C5}_{unpruned} demonstrates the effectiveness of decoder pruning in reducing the model size and its potential impact on segmentation accuracy. To investigate other essential components of CL-Net, we pre-train GE using different initial datasets and self-supervised learning methods to explore how pre-training configurations influence the GE’s ability to extract general visual semantic features. In addition, the contributions of FL-Supporting and EMA to improving hard organ segmentation and updating existing decoder

heads are examined in detail. For further information on the experimental settings for these ablation studies, please refer to Supplementary Sec. A5 and A6.

External Evaluation Experimental Setting To further demonstrate the advanced segmentation accuracy, generalizability, and robustness of CL-Net, an external evaluation is performed on one public dataset (BTCV) and six newly collected private datasets, covering whole-body regions, four lesions, 43 anatomical classes, and a total of 1,979 testing samples (Tab. S4). Models from the main experiments, including CL-Net^{U36}, CL-Net^{C36}, and nnUNet^{E36}, are evaluated. Additionally, comparative methods from the universal segmentation experimental setting in the internal validation, including Multi-talent¹⁷, SAT-pro²², and VISTA3D²⁵, are also evaluated on these external datasets. Consistent with internal comparative experiments, SAT-pro and VISTA3D are tested using their official released models, which are limited to segmenting only the organs covered within their predefined target classes. Therefore, we report their performance exclusively for these overlapping organ classes.

Evaluation Metrics To assess the segmentation performance of our method, we employ the Dice Similarity Coefficient (DSC) and Average Surface Distance (ASD), two widely used metrics in organ and lesion segmentation studies. DSC measures the overlap between the predicted segmentation mask and ground-truth annotation, serving as a key indicator of volumetric accuracy. In contrast, ASD evaluates the accuracy of the boundary and the shape by quantifying the average distance between the predicted and ground truth surfaces, providing additional insights into structural fidelity. For comprehensive evaluations across entire datasets or organ groups, we report mean DSC (mDSC) and mean ASD (mASD), offering averaged measures of segmentation accuracy and surface agreement across whole-body anatomical structures. These metrics collectively provide a robust measurement for evaluating the precision of segmentation performance.

A3 Continual Segmentation Results of CL-Net on Five Representative Public Datasets

CL-Net outperforms other leading CSS methods across all datasets under various orders.

Fig. 4 illustrates the forgetting curves of CL-Net and other leading CSS methods on each dataset under four orders. Notably, the dice scores of our method are consistently above MiB, PLOP and CSCLIP at every step of each dataset in all orders, with a particularly notable superiority in the final step of most datasets, e.g., CL-Net keeps 94.1% DSC at step 4 on Order1-S0 while the DSCs of MiB, PLOP and CSCLIP drop to 3.8%, 16.7% and 16.5%, respectively; On Order3-S1 (KiTS21), CL-Net’s DSC remains 87.1% at the last step, in contrast, the other three methods entirely forget the lesion segmentation task, with DSCs less than 1.0%. The superior performance of CL-Net can also be supported by the final mean dice scores after the entire CSS training process illustrated “DSC-Param#” plots, in which our CL-Net^{C5} achieves the top mean DSC and remarkably outperforms other comparison CSS methods in all orders. Compared to MiB, PLOP and CSCLIP, CL-Net demonstrates significant improvements in mean DSC by 85.7%, 73.3% and 71.6% on order 1, 77.6%, 52.5% and 72.1% on order 2, 15.1%, 16.8% and 16.3% on order 3, and 72.2%, 43.9% and

36.1% on order 4, respectively. Please refer to supplementary Table S40-S48 for detailed organ-wise performance of CL-Net^{C5} on all datasets of each order.

CL-Net shows quantitative segmentation performance on par with or even surpassing the nnUNet upper bound performance. As nnUNet performance can be treated as the single model upper bound performance trained on each dataset, the dice score curves of our method (red dashed lines) mostly overlaps with, and sometimes even be above, the nnUNet dice scores (purple dashed lines), which indicates that CL-Net can reach or even exceed the single model upper bound even under CSS setting. CL-Net has very similar (but slightly higher) DSCs as nnUNet in Order1-S0 (TotalSegmentator V2) (94.09% vs. 94.05%) and Order1-S1 (StructSeg19) (86.40% vs. 86.39%); in Order3-S0 (FLARE22), CL-Net reaches a significantly higher score than nnUNet (91.3% vs. 89.7%). The comparable final dice score of CL-Net^{C5} and the 5-nnUNets ensemble (nnUNet^{E5}) of each order in “DSC-Param#” column further highlights the stable and superior performance of our method. The final CL-Net^{C5} achieves similar or slightly higher mean DSCs as 92.6%, 92.6%, 92.7% and 92.5% over order 1-4 separately, in comparison to the 92.5% upper bound dice score of nnUNet^{E5}. The above results also reveal that our general encoder is able to guarantee top-level segmentation performance even without fine-tuning. Please refer to supplementary Table S40-S48 for detailed organ-wise performance of nnUNet on each dataset.

CL-Net demonstrates performance advantages in both model stability and plasticity. These two characteristics play significant roles and trade-off in continual learning and segmentation, i.e. a stable model resists catastrophic forgetting, while a plastic model learns better on new tasks. The advanced model stability of CL-Net is mainly supported by its non-forgetting ability. As illustrated in Fig.4, a flat trend is found in the forgetting curves of CL-Net (blue and red) in every dataset under all orders (except the final dataset which is only validated once), which demonstrates that CL-Net has no forgetting on all the previous learned datasets during continual learning. In comparison, the forgetting curves of other CSS leading methods mainly have a descending trend, which reveals a severe catastrophic forgetting drawback of these methods. The performance of MiB, PLOP and CSCLIP shows a general decrease of 86.1%, 73.1% and 67.9% in Order1-S0 and 76.1%, 69.0% and 55.5% in Order4-S0, respectively; severe dice drops are observed at step 3 on S1 in order 2 & 3 (1-step DSC drop: MiB – 59.7% & 69.1%; PLOP – 50.8% & 45.4%; CSCLIP – 20.1% & 33.1%) and the last step in S3 in all orders (order 1-4, last-step DSC drop: MiB – 79.8%, 76.4%, 56.6% & 81.2%; PLOP – 24.3%, 47.9%, 51.5% & 63.8%). Two cases are found in which the dice scores of the comparison methods increase at some specific CSS steps. MiB, PLOP and CSCLIP resume DSC by 72.4%, 58.2% & 70.8% at step 4 of S0 (FLARE22) and 16.9%, 6.1% & 28.4% at step 4 of S2 (SegThor) in order 3, separately. This performance recovery phenomenon is mainly caused by the model learning in TotalSegmentator V2 at the last step, which contains the same overlapping organs as FLARE22 at step 0 and SegThor at step 2, thus helping the model rehearsal and regains dice on these old tasks.

On the other hand, CL-Net also has a superior plasticity, which is gained from the generalizability of GE and continually incremented decoder heads. Although CL-Net freezes its encoder

when it continually learns new datasets, the general and robust visual features extracted from GE is able to cover most of the body contents in CT scans. Furthermore, the newly added decoder head provides additional parameters for knowledge updating. Since the performance of the first training step on each sequential dataset (step 1 on S1, step 2 on S2, step 3 on S3, and the last single step on S4) is not affected by the forgetting issue, we inspect the model plasticity of CL-Net at the first step of the forgetting curves on S1-S4 within Fig. 4. As CL-Net reaches the upper bound of nnUNet performance when it is adapted to sequential datasets of each order for the first time, our model demonstrates extraordinary plasticity on various datasets. In comparison, all the other CSS methods remain some gaps to the upper bound at the first training step on S1-S4, specifically, PLOP and CSCLIP show poor plasticity, where large DSC gaps are observed at the first steps in several datasets. PLOP and CSCLIP only get DSCs 59.9% and 19.2% on Order1-S4 (KiTS21), result in large gaps as 27.3% and 68.0% compared to the nnUNet upper bound 87.2%; Similarly, large gaps to the upper bound are also observed on KiTS21 in other orders (Order2-S1, Oder3-S1 & Order4-S3) and other datasets (Order3-S3 StructSeg19 & Order4-S2 TotalSegmentator V2). The deficient plasticity of the comparison methods is mainly caused by their knowledge distillation strategy, which enhances stability, alleviates forgetting but severely reduces the plasticity and makes the model hard for new task adaptation.

CL-Net achieves the best overall organ segmentation performance while maintaining significantly tiny model scale and low parameter increasing rate. Considering model deployment and upgrading issues in the real world scenario, both the prediction accuracy and parameter size should be of great importance for a comprehensive CSS method evaluation. After continually learning the entire sequence of the dataset, the model with a smaller parameter size and higher dice score demonstrates superior performance. Thus, we report the mean dice score for all organs and the number of parameters of the final model of each CSS method in the “DSC-Param#” plots of Fig. 4, where a better method with a smaller size and higher precision appears in the upper left corner, while the larger model size with a lower dice score in the lower right corner indicates the worse method. As illustrated in the “DSC-Param#” plots, CL-Net^{C₅} (red) consistently locates on the most top-left corner over all orders, outperforms other regularization-based CSS methods (MiB, PLOP, CSCLIP) while keeps merely about a single nnUNet size (31.3M), which is much lower than 5-nnUNets ensemble (nnUNet^{E₅}) or Transformer-based CSCLIP. Compared with the 92.5% upper bound dice score and 156.5M model size (five times the size of nnUNet) of nnUNet^{E₅}, the final CL-Net^{C₅} achieves slightly higher mean DSCs as 92.6%, 92.6%, 92.7% and 92.5% while limits its parameter number to 28.5M, 28.9M, 34.2M and 35.5M in order 1-4, respectively. The segmentation performance stability of our final model on all CSS orders also demonstrates the robustness of CL-Net to CSS order variations.

The decoder pruning process effectively maintains CL-Net performance while efficiently reducing the model size. In practical model training, the trade-off between model scale and model accuracy, i.e., the scaling-law, must be deliberately designed so that the model avoids holding an extensive cost of physical storage and GPU memory. This is even more significant in the architecture-based CSS method like CL-Net, as our model incrementally expands the decoder

head over each new task. Such a considerable parameter increasing rate would rapidly grow the model size during CSS and eventually cause model parameter explosion. Therefore, we develop the decoder pruning process in CL-Net to effectively constrain the parameter increasing rate and the final model scale. Fig. 4 illustrates the dice scores of both pruned (CL-Net^{C5}, red) and unpruned (CL-Net^{C5}_{unpruned}, blue) settings to demonstrate the effectiveness of our decoder pruning. As shown in the forgetting curves of all datasets and orders, CL-Net^{C5} remains the similar DSC scores and overlaps the curve with CL-Net^{C5}_{unpruned}. This can be further supported by the overall segmentation performance of the final CL-Net^{C5} and CL-Net^{C5}_{unpruned} models, where CL-Net^{C5} consistently keep the same level of mean DSC and ASD values as CL-Net^{C5}_{unpruned}, with a marginal average increase in DSC of 0.045% and an ASD reduction of 0.002mm in all orders. Moreover, the final parameter size in “DSC-Param#” plot underscores the robust and effective model compression capability of our decoder pruning, where more than 60% parameter reductions are observed across all orders. Compared to 93.9M parameters of the unpruned CL-Net, the modal size of each order after pruning is trimmed to 33.84±3.83% of original size on average. To further validate the effectiveness of other main modules/processes of CL-Net and explore their impacts on final performance, we conduct comprehensive ablation studies on GE, EMA and FL-Supporting. The detailed experimental results and analyses are reported in the supplementary Sec. A5 & A6.

A4 Details on CL-Net Implementation

Image Preprocessing CL-Net adapts its general training framework from the powerful nnUNet⁵, leveraging its robust preprocessing and training strategies. For input preparation, a CT windowing range of $[-1, 024, 1, 024]$ HU is applied uniformly to all CT images, followed by resampling to a consistent resolution of $1.0 \times 1.0 \times 1.5$ mm to ensure spatial uniformity. The images are pre-processed to the RAI (Right-Anterior-Inferior) orientation before undergoing the pre-processing pipeline, which includes intensity normalization, ROI cropping, and outlier removal. While nnUNet dynamically adjusts the input patch size for each task, CL-Net enhances this approach by introducing a standardized default patch size of $128 \times 96 \times 112$ voxels (or a user-defined size), providing a balanced solution that combines consistency with task-specific flexibility.

Network Architecture The architecture backbone of CL-Net is built on the *3D full resolution* configuration of nnUNet, tailoring its design to provide robust performance and fine-grained feature extraction. It features a 6-block encoding path and a 5-block decoding path, ensuring a deep and hierarchical representation of the input data. The base number of features for the general encoder (GE) starts at 32, following a systematic expansion of the features as the network deepens. Each *encoding* block comprises two convolutional layers, both incorporating instance normalization and leaky ReLU activation for efficient feature transformation and gradient flow. Downsampling between encoding blocks is performed via stride convolution, which reduces spatial dimensions while preserving critical feature information. The *decoding* blocks also contain two convolutional

⁵<https://github.com/MIC-DKFZ/nnUNet>

layers with instance normalization and leaky ReLU activation. In addition, each decoding block integrates an EMA (Exponential Moving Average) module to enhance feature refinement and temporal stability in training. Upsampling within the decoding path is handled by transposed convolution, which restores spatial resolution while enabling learnable upscaling of feature maps. The default GE configuration of the $[[1, 3, 3], [3, 3, 3], [3, 3, 3], [3, 3, 3], [3, 3, 3], [3, 3, 3]]$ convolution kernels. For each decoding path, we recommend a mirroring of the GE convolutional kernels. Additionally, CL-Net, like nnUNet, supports optional automatic kernel selection for enhanced flexibility.

Evaluation Metrics The DSC, ASD, and pruning rate \mathcal{T} are used for evaluation. To better understand the implications of the pruning rate \mathcal{T} , we review U-shaped CNN networks, focusing on the learned features of downstream decoding heads. Typically, better segmentation performance with fewer predicted targets correlates with a higher pruning rate, indicating a denser distribution of features in the latent space. In contrast, performing segmentation on difficult-to-predict organs or inferring a large number of output labels may result in a lower pruning rate.

Hardware Requirement All experiments were performed on a server with 8 Nvidia V100 GPUs, each with 16 GiB of RAM, 330 GiB of CPU memory, and an Intel(R) Xeon(R) Platinum 8163 CPU, featuring 82 threads. We have tested that all training tasks can be performed using a single GPU with a standard 12 GiB RAM and 64 GiB CPU memory. The default number of threads for training and testing is set to 12. It is preferred to use DDP to leverage all available GPUs for efficient computation.

Training Efficiency The average training time for a two-target head (e.g., left and right counterparts) in CL-Net is approximately 86 seconds per epoch on a single Nvidia V100 GPU, which can be accelerated to 32 seconds per epoch using a DDP setup with four Nvidia V100 GPUs. The average GPU memory consumption is less than 10 GiB during the training of each decoding head. Each trained decoding head has a model size of approximately 80 MiB, which can be reduced to just 18 MiB when saved as a sparse model using PyTorch’s sparse format ⁶. Please note that sparse computation was not applied during model training. Hence, GPU RAM consumption remains unchanged during the training process. The data augmentation pipeline is implemented with the public available ‘BatchGenerator’ framework ⁷.

Inference Efficiency The CL-Net inference supports single- and multi-GPU setups, with the aim of minimizing deployment costs, improving prediction efficiency, and streamlining clinical workflows. In a single GPU setup, segmentation is performed sequentially, with each decoding head processed one at a time. In a multi-GPU setup, decoding heads are evenly distributed across GPUs to accelerate the process. The inference time on a single Nvidia V100 GPU is averagely less than 5 seconds per stratified head. The total inference time for our 235-organ segmentation

⁶<https://pytorch.org/docs/stable/sparse.html>

⁷<https://github.com/MIC-DKFZ/batchgeneratorsv2>

on a single V100 GPU averages 430 seconds per patient, comprising approximately 10s for image pre-processing, 5s for model loading (only once), 400s for inference, 5s for merging and saving, as well as additional system overhead. We strongly suggest using Solid-State Drive (SSD) to store the training data, as SSD improves basic input/output system (BIOS) speed and facilitates faster inter-communication with CPU and GPU memories. When performing parallel predictions using 4 or 8 GPUs, the total inference time can be reduced to approximately 118 or 58 seconds per patient, respectively. The average GPU memory consumption is approximately 6 GiB of RAM throughout the entire prediction process.

GE Training Using Comprehensive Dataset The network architecture is based on the encoder of the nnUNet’s default “3D full resolution” architecture. The base number of features of GE is 32, and each encoding convolutional block consists of 2 convolutional layers. Similarly to nnUNet, the maximum number of features (toward the bottleneck block) is capped at 320. Instance normalization and leaky ReLU are also applied. All decoding paths share the same architecture, consisting of two convolutional layers, with transposed convolution used to upscale the output features of each decoding block. To enhance training effectiveness, side supervisions are applied throughout the model training process. We follow nnUNet’s training strategy and use the SGD optimizer for network training, starting with an initial learning rate of 0.01. The learning rate is adjusted using a polynomial schedule. The batch size is set to 2. This design ensures the adaptability and scalability of the network while maintaining an efficient memory footprint, requiring less than 16 GiB of RAM for GE and three decoding paths.

GE Training Using Constrained Datasets In addition to leveraging comprehensive CT datasets for training, we enhance the generalized encoder GE’s training capability in scenarios where only limited training data (e.g., MRI or PET imaging) or a restricted variety of training classes (e.g., disease-specific imaging) are available. To achieve effective and efficient GE pre-training, we employ SSL, which enables GE to extract meaningful knowledge from constrained datasets. Furthermore, the domain gaps⁸³ between SSL and semantic segmentation can be mitigated by fine-tuning the pre-trained SSL network using semantic labels. Specifically, we begin by pre-training only the encoder component of the network using the SimSiam framework⁷⁴. This approach employs two GEs: predictor encoder f_e^p and target encoder f_e . These encoders iteratively refine data representations without explicit labels. The predictor generates augmented representations of the input data, while the target encoder learns robust features by ensuring consistency between different augmentations of the same input. For the pre-training process, we adapted the nnUNet data augmentation scheme for view augmentation. Let \mathcal{A} denote the view augmentation function. We follow SimSiam and use negative cosine similarity loss \mathcal{L}_{ncos} for training. The pseudo-code for proposed GE pre-training is detailed in Algorithm 1. Once pre-training with SimSiam is completed, the target encoder f_e is then paired with a randomly initialized decoding path to minimize the domain gaps between SSL and segmentation tasks via fine-tuning. To better preserve previously learned features for various body parts, motivated by MoCo⁸⁴, we employ a momentum queue to store a large number of feature representations of GE. To improve efficiency, the momentum queue is detached from the GPU and set to a total size of 1,024, significantly reducing CPU, GPU, and

memory usage while maintaining training speed. This strategy ensures efficient and scalable GE training, even in resource-constrained environments.

Input: Dataset $D = \{X_i, Y_i\}_{i=1}^n$, Target GE f_e , Predictor GE f_e^p
Output: Trained target GE f_e
for $i \leftarrow 1$ **to** n **do**
 $X_i^1, X_i^2 \leftarrow \mathcal{A}(X_i), \mathcal{A}(X_i)$;
 $Z_i^1, Z_i^2 \leftarrow f_e(X_i^1), f_e(X_i^2)$;
 $P_i^1, P_i^2 \leftarrow f_e^p(Z_i^1), f_e^p(Z_i^2)$;
 $\mathcal{L} \leftarrow \frac{1}{2}\mathcal{L}_{ncos}(P_i^1, Z_i^2) + \frac{1}{2}\mathcal{L}_{ncos}(P_i^2, Z_i^1)$;
end

Algorithm 1: SimSiam-based General Encoder Pre-training

SSL Pre-training Setup We adopt SimSiam for GE pre-training. The implementation of SimSiam is based on the publicly released code ⁸. Unlike SimSiam for natural images, our pre-training augmented views do not include large resizing and cropping or head-to-foot flipping. These augmentations could eliminate small targets or confuse the model with respect to CT anatomical structures. We adapt the nnUNet data augmentation scheme for view augmentation:

- **Rotation and scaling:** Scaling and rotation transformations are applied with a triggering probability of 50% for scaling, 50% for rotation, and 50% for both scaling and rotation. The rotation angles are constrained within the range of $[-45, 45]$ degrees and applied sequentially to the directions from left to right, front to back, and head to foot. The PyTorch’s ⁹ tri-linear and nearest neighbor interpolations are applied to the image and label, respectively. The scaling factor is sampled in a random ratio between $[0.7, 1.4]$ for all patch types.
- **Gaussian noise & blur.** For each voxel, the Gaussian noise with a mean $\mu = 0$ and a random standard deviation $\sigma \in [0, 0.1]$ is added. The Gaussian blur with kernel $\sigma \in [0.5, 1.5]$ is applied to the input image. Blurring is triggered with a probability of 50% per sample.
- **Intensity re-scaling.** The intensity of each voxel is multiplied by a factor between $[0.65, 1.5]$. The CT intensity values are clipped to a range of $[-1, 0.24, 1, 0.24]$.
- **Simulation of low resolution.** The sampled 3D image patches are first down-sampled by a factor between $[1, 2]$ on the axial or xy plane and a random factor between $[2, 4]$ along the head-to-foot direction using nearest neighbor interpolation. Then, those patches are sampled back to their original size using tri-linear interpolation. This augmentation is triggered with a probability of 50%.
- **Gamma augmentation.** The Gamma augmentation is the same as the default nnUNet’s Gamma augmentation.

⁸<https://github.com/facebookresearch/simsiam?tab=readme-ov-file>

⁹<https://pytorch.org/>

- **Mirroring.** All patches are only mirrored with a probability of 50% along the axial and coronal axes.

The initial learning rate is set to 1×10^{-3} . The cosine annealing strategy is adopted to schedule the learning rate. The total training epoch is 5,000 with 256 mini-batches.

Momentum Multi-dataset Fine-tuning Setup The GE momentum queue is stored independently of the GPU and is configured to a size of 1,024. The default GE momentum queue $\mathcal{Q}_{1,024}$ requires approximately 90 GiB of CPU memory. During fine-tuning on multiple datasets, the paired decoder – *used exclusively for GE fine-tuning and usually exhibiting inferior/less optimized performance* – is re-initialized for each dataset, and the output convolutional layer’s channel dimension is adjusted to match the number of output classes for each specific dataset. Each dataset is trained for 1,000 with mini-batch sizes of 256. The fine-tuning learning rate for GE is set to 1×10^{-4} , while the learning rate for the paired decoder is set to 1×10^{-3} . Data augmentation follows the nnUNet “more data augmentation” scheme.

Stratified Decoder Training Details The decoding path, with or without FL-Supporting, is determined on the basis of the user’s design. We recommend parsing target anatomies into stratified structure-based decoders, such as the Eyes decoder, Liver decoder, and Ribs decoder. Since training from scratch and fixing GE can occasionally lead to large updates of the decoder in the early stages of training⁸⁵, we initially warm up the decoder and then train the decoder until convergence, followed by LTH-based weight pruning. Once the decoding path is pruned, the EMA component of the decoding path is updated. Inherited from nnUNet, the data augmentation is nnUNet “more data augmentation” scheme. We recommend training the decoding paths using DDP implementations, as it significantly accelerates the training process.

Decoding Path Initial Training & Pruning Setup By default, we warm up the decoder for five epochs with an initial learning rate of 1×10^{-3} . Following this, the momentum is reset and the decoder’s learning rate is adjusted to 1×10^{-2} for training over 300 epochs. Then, the proposed LTH-based pruning process is applied iteratively, where each cycle of training, pruning, and rewinding progressively identifies a smaller winning ticket. Heuristically, most stratified decoders target only two organs, such as left and right counterparts, leading us to assume that the weights within these decoding heads are sparsely distributed. We suggest starting with the progressive overall pruning rates ranging from 80% to 92%, with an interval of 4%. If the performance drop criteria ($\delta \leq 1\%$) are still met, the pruning continues from 93% to 99%, with an interval of 2%. If the criteria continue to hold, the pruning proceeds from 99.1% to 99.7%, with intervals of 0.2%. The PyTorch built-in “global-unstructured” pruning with the “L1Unstructured” method is adopted throughout all pruning processes. The pruning process is applied to all convolution layers, targeting both weights and biases for pruning. To smooth the pruning process, we linearly increase the mini-batches per epoch, up to 512, in proportion to the pruning rate. After pruning is complete, the number of minibatches per epoch is reset to 256. To mitigate any potential performance drop, additional training epochs 20

are applied.

EMA Module Updating Configuration Most of EMA updating begins at the start of training. However, during the pruning process, the EMA updating might experience significant performance fluctuations. The assumed reason is that, with a decay rate of $\alpha = 0.999$ and a mini-batch size for pruning of 256, the EMA update process is effectively 1,000 times slower than its non-smoothed counterpart. This indicates that EMA could have only updated 25.6% of its parameters compared to the unpruned state, making it difficult for the weights in the EMA module to timely adapt to the newly pruned state. Although enlarging the size of training mini-batches or using finer pruning steps could address this issue, it would lead to extended training times and increased resource consumption. To address this issue in CL-Net, after pruning is complete, we copy the pruned counterpart to EMA and subsequently update only the unpruned weights in the EMA module.

Continuous Decoder Updating Benefiting from the EMA updating, the decoder of the target organs can be continuously and smoothly updated. We recommend using a smaller learning rate (e.g., 1×10^{-4}) to update both the non-smooth decoder and the EMA counterpart. To maintain consistency, it is recommended that the pruned mask remain unchanged. However, the pruned mask can optionally be updated when using new data. Instead of applying the pruning process to the non-smoothed counterpart, we perform the pruning process directly on the EMA parameters using a refined pruning interval of 0.1%. During model inference, the weights are loaded from the EMA module to leverage the benefits of EMA smoothing.

A5 Details on Ablation Studies of General Encoder (GE)

The primary objective of GE is to extract representative features that are applicable in a wide range of potential downstream tasks. To achieve this, it is essential for GE to maintain a high degree of comprehensiveness, ensuring versatility and robustness in feature representation. Based on our experiments, we have identified two pivotal factors that profoundly influence the performance of downstream tasks: 1) the comprehensiveness of the training datasets and 2) the necessity of the popular self-supervised pre-training. To evaluate these factors, for GE training, we conducted comprehensive validation experiments using the following dataset configurations: 1) A single comprehensive dataset – TotalSegmentator V2. 2) A single head & neck region dataset – StructSeg19. 3) The union of separate body part-wise datasets \mathcal{U}_4 – StructSeg19 (head & neck), SegThor (thoracic), FLARE22 (abdomen), and KiTS21 (kidney lesion). 4) The union of all five \mathcal{U}_5 datasets. Once GE is fully trained using the aforementioned four GE training setups, the trained GEs are fixed and subsequently utilized for downstream validation experiments. Two downstream tasks were selected for evaluation: 1) TotalSegmentator V2 and 2) FLARE22 downstream tasks, which provided whole-body segmentation and local (abdomen) region segmentation, respectively. Consistent with the previously determined decoding path configuration, the TotalSegmentator V2 downstream task includes 48 stratified decoders, and the FLARE22 downstream task includes 11 stratified decoders. We also calculated the cumulative sum of the complements, $\mathcal{T}' = 1 - \mathcal{T}$, of the pruning rates in the

target evaluation dataset $\sum \mathcal{T}'$. This sum represents the percentage of the total size of the decoder models after pruning compared to the default unpruned counterpart, $\sum \mathcal{T}' = 100\%$, with smaller values indicating more efficient pruning.

Impact of Training Datasets The experiments designed to evaluate the impact of training datasets in two major respects:

- *Image-wise Body Part Coverage.* It determines the overall range of anatomical structures present in the images, impacting the GE’s ability to recognize and generalize across different body regions. A dataset with a broad coverage of body parts ensures that GE can identify a wide array of anatomical characteristics, facilitating robust learning in downstream tasks.
- *Label Completeness.* It refers to the variety of anatomical structures annotated within the dataset. This diversity is crucial for training the GE to distinguish and extract relevant features from different anatomical regions. A diverse set of labeled structures enhances GE’s capacity to learn distinctions between various tissues and organs, thus improving its segmentation capabilities across a range of downstream tasks.

For completeness, we follow the same GE training setup discussed in Section A4 and conducted experiments with both the GE pre-trained by SimSiam and the GE trained from scratch.

Image-wise Body Part Coverage The experiments are designed for two primary comparisons: 1) to assess how well a GE trained in whole-body images generalizes to different body parts, and 2) to determine the effectiveness of a GE trained in localized body parts when applied to other anatomical regions. When training GE from scratch, as shown in Tab S8, GE trained using a whole-body dataset achieved DSC of 94.1%, ASD of 0.89mm, and $\sum \mathcal{T}'$ of 38.6%. When evaluated on the abdominal downstream task, as shown in Tab S9, where the whole-body dataset-trained GE yielded the DSC of 90.4%, ASD of 1.05 mm, and $\sum \mathcal{T}'$ of 15.2%. In contrast, training GE with the head and neck region dataset led to a decrease in performance on the TotalSegmentator downstream task, with a DSC of 91.1%. Furthermore, this model showed a higher ASD of 1.20 mm, indicating less precise segmentation boundaries, and a significantly larger $\sum \mathcal{T}'$ of 72.4%, suggesting the need for compensation in the extraction of features for the GE compared to the model trained with the whole-body dataset. Similar performance trends were observed when evaluating experiments using GE pre-trained using SimSiam. Using a whole-body dataset for training, it yielded a DSC of 94.2%, ASD of 0.90mm and $\sum \mathcal{T}'$ of 38.2%. However, when only head & neck region dataset is available, the performance is decreased to a DSC of 92.8%, ASD of 1.14mm, and the $\sum \mathcal{T}'$ of 62.4%.

To assess how well a GE trained in specific body parts can generalize to mostly unseen regions, as demonstrated in Tab S9, we evaluated the head and neck dataset trained GE on the abdominal downstream task. In particular, there is minimal overlap between the head and neck dataset and the abdomen FLARE22 dataset. In this setup, CL-Net exhibited degraded performance, with a DSC

of 89.5%, an ASD of 1.28 mm, and $\sum \mathcal{T}'$ of 26.0%. Using SimSiam to pre-train GE could help downstream decoders improve segmentation performance, achieving a DSC of 90.1%, an ASD of 1.20 mm, and $\sum \mathcal{T}'$ of 20.3%. The inferior performance could suggest that the model struggled to accurately segment abdominal structures, likely because its previous exposure was limited to head and neck anatomies. The lack of overlap in anatomical structures between the training and evaluation datasets can lead to ineffective adaptation of learned characteristics to new and distinct abdominal anatomies.

Label Completeness We assessed the impact of the diversity of the labels by training GE from scratch using the whole-body dataset (restricted to only the bone label set). This approach limited the model’s exposure to a variety of anatomical structures, focusing exclusively on bone-related organs. When evaluated in the downstream TotalSegmentator task, CL-Net showed a noticeable decline in performance. It led to a DSC of 92.9%, ASD of 1.13mm, and $\sum \mathcal{T}'$ of 58.8%. Most organ segmentation tasks showed less effective performance, whereas bone stratified decoders achieved minor yet significant improved segmentation performance (+0.2% DSC and -0.06 mm ASD, $p < 0.1$), suggesting that GE trained using the bone label set was optimized biased towards bone anatomy feature extraction. Using multiple datasets from separate body parts, called \mathcal{U}_4 data sets, for GE training can effectively enhance the coverage of body parts and increase the variety of anatomical labels. To fully exploit all available labels, the most straightforward approach is to complement incomplete label sets with pseudo-labels. This approach resulted in a DSC of 94.0%, ASD of 1.09 mm, and $\sum \mathcal{T}'$ of 56.8%. Although this performance shows improvement over using the head and neck label trained GE, it remains inferior to the GE trained with the whole-body dataset. This observed sub-optimal performance may be attributed to the error propagation in pseudo-labels.

Impact of View Augmentations To exclude the effects introduced by domain adaptation from the analysis of view augmentation schemes, we compared two sets of experimental setups on the TotalSegmentator downstream task:

- Evaluating the impact of view augmentation schemes by directly applying the SimSiam pre-trained GE to the training of downstream task decoding heads without any fine-tuning.
- Evaluating the impact of view augmentation schemes by applying the SimSiam pre-trained GE with full label set fine-tuning to the training of downstream task decoding heads.

The experimental results are shown in Tab S8. In the *first* setup. Using the default view augmentation, it produced the least effective segmentation results. The CL-Net achieved a DSC of 88.6%, a ASD of 1.73mm, and $\sum \mathcal{T}' = 328.6\%$. In contrast, with the proposed view enhancement, the SimSiam pre-trained GE produced improved results on the same task, achieving a DSC of 89.6%, an ASD of 1.28 mm, and $\sum \mathcal{T}' = 315.8\%$. In the *second* setup. A similar performance trend was observed. Using the default view augmentation, CL-Net achieved an inferior DSC of 93.0%, an ASD of 1.17 mm, and $\sum \mathcal{T}' = 52.4\%$. In contrast, with the proposed view augmentation, CL-Net achieved

an improved DSC of 94.2%, an ASD of 0.90mm, and $\sum \mathcal{T}^l = 38.2\%$. After carefully examining the results, we observed that the degradation in performance was accompanied by an increase in false-positive predictions. This issue highlighted the model’s tendency to misidentify large organs as smaller structures or to make incorrect predictions, such as classifying parotid glands as kidneys or making errors in head-to-foot direction identification.

Impact of Supervised Domain Adaptations The domain gap between SSL pre-training and supervised semantic segmentation remains a challenge in medical imaging segmentation tasks⁸³. We begin by first analyzing the conventional “pre-train then fine-tune” workflow domain adaptation approach for domain gap minimization. As demonstrated in Tab S8, when directly applying SimSiam pre-trained GE, it predicted a DSC of 89.6%, an ASD of 1.28 mm, and $\sum \mathcal{T}^l$ of 315.8%. Notably, simply fine-tuning GE boosted performance significantly to a DSC of 94.2%, an ASD of 0.90 mm. Notably, $\sum \mathcal{T}^l$ dropped dramatically, reaching as low as 38.2%, which is 8.5 times smaller than the $\sum \mathcal{T}^l$ observed when the GE was not fine-tuned. This substantial improvement indicates that fine-tuning helps the model better adapt to specific tasks by refining its understanding of the target anatomical features.

Fine-tuning GE is a straightforward and effective approach to minimize the domain gap between SSL and supervised semantic segmentation. However, in clinical practice, it is common to collect multiple separate datasets that aim for various types of diagnosis. While SimSiam-based pre-training does not depend on semantic labels and using multiple datasets can help cover more body parts, issues may arise when sequentially fine-tuning GE on multiple individual or partially labeled datasets. This approach might lead to knowledge forgetting or over-fitting, where the GE fails to retain knowledge across diverse datasets or becomes overly specialized in the most recent dataset on which it was trained. Using EMA can stabilize fine-tuning and enhance feature robustness by mitigating abrupt gradient changes. However, it may also smooth out task-specific features, such as those that distinguish head organs from the abdomen, potentially leading to a loss of distinct features. To address the issues of knowledge forgetting and dataset over-fitting, the momentum queue⁸⁴ is adopted. This technique involves maintaining a dynamic memory bank of feature representations, which allows the model to retain information from earlier datasets while learning from new ones. By continuously updating the queue with representations from the most recent data, the model can effectively balance the retention of diverse knowledge, ensuring that it remains robust and generalizable across various medical imaging tasks.

To evaluate the effectiveness of the momentum updating strategy, we evaluate the segmentation performance using \mathcal{U}_4 with an order of StructSeg19 \rightarrow SegTHOR \rightarrow FLARE22 \rightarrow KiTS21. We conducted experiments using EMA with $\alpha = 0.999$ for GE fine-tuning. Furthermore, to understand the impact of the momentum queue size, we conducted three separate experiments with queue sizes of 128, 1,024, and 4,096. For comparison, when sequentially fine-tuning GE using \mathcal{U}_4 datasets, the segmentation results showed a DSC of 93.0%, ASD of 1.14 mm, and $\sum \mathcal{T}^l$ of 62.6%. When using EMA for updating and following the same fine-tuning dataset sequence, we observed only very minor gains or comparable performance compared to sequential fine-tuning of the full label

set. Notably, when tested on the FLARE22 downstream task, the EMA approach yielded inferior segmentation performance compared to the sequential full label set fine-tuning. The assumed reason for this is that the KiTS dataset, being the largest and last dataset used for fine-tuning, could have overly influenced GE, leading to a model that is more specialized for kidney-related tasks and less effective in generalizing to the wider range of anatomical features required for the FLARE22 task.

When adopting the proposed momentum updating, we find that the smaller queue size, \mathcal{Q}_{128} , is still prone to knowledge forgetting, as small sized queue may not store enough representations from previous datasets, leading to 93.1% in DSC, 1.12 mm in ASD, and 58.6% in $\sum \mathcal{T}'$. Momentum updating GE with larger queue sizes leads to better performance. Using momentum queue size of 1,024, CL-Net with $\mathcal{Q}_{1,024}$ achieved 94.2% in DSC, 0.86 mm in ASD, and 37.2% in $\sum \mathcal{T}'$. However, larger queue sizes entail longer training times and increased memory consumption. Specifically, for momentum queue sizes of $\mathcal{Q}_{1,024}$ and $\mathcal{Q}_{4,096}$, the memory consumption is approximately 90 GB and 380 GB of CPU memory, respectively. The training time when using a momentum queue size of $\mathcal{Q}_{4,096}$ is approximately $6\times$. Nevertheless, the additional performance gains achieved with the momentum queue of $\mathcal{Q}_{4,096}$ are marginal, yielding an improvement of only +0.03% in DSC, -0.01 mm in ASD, and -0.3% in $\sum \mathcal{T}'$. A similar segmentation trend was also observed when evaluating the FLARE22 downstream task, with results resulting in a DSC of 90.4%, ASD of 1.04mm, and $\sum \mathcal{T}'$ of 15.2%. To evaluate the added value of incorporating multiple separate datasets into a comprehensive dataset when training GE, we conduct experiments using the five datasets \mathcal{U}_5 . The momentum update with a queue size of 1,024 is adopted. Unfortunately, the results showed only marginal improvements, despite achieving the best performance in both the TotalSegmentator and FLARE22 segmentation downstream tasks. The results included a DSC of 94.3% (+0.1%), ASD of 0.85 mm (-0.05 mm), and $\sum \mathcal{T}'$ of 35.8% (-2.4%) on the TotalSegmentator downstream task, as well as a DSC of 90.5% (+0.03%), ASD of 1.04 mm (-0.01 mm), and $\sum \mathcal{T}'$ of 14.9% (-0.03%) on the FLARE22 downstream task.

Discussion on GE In conclusion, when a comprehensive dataset is available, we recommend training the GE directly using such datasets, e.g., TotalSegmentator. This approach is preferable because the additional resource consumption required for SSL pre-training and momentum fine-tuning may outweigh the modest performance gains achieved. Using a comprehensive dataset directly, the training process becomes more efficient without severely compromising the quality of the segmentation results. However, when only limited training data or a restricted variety of training classes are available, we recommend adopting SSL pre-training and momentum fine-tuning for GE training. Given the balance between segmentation performance and resource consumption, we heuristically recommend a queue size of 1,024. These strategies enhance the GE’s ability to generalize and improve performance, making it more robust and effective in scenarios with constrained data availability. If training GE from scratch is necessary, we strongly suggest using multiple GPUs with substantial CPU memory, e.g., a server system setup that includes 8 Nvidia V100 GPUs of 16GB RAM each and 64GB of CPU memory. The learned decoding features can serve both feature extraction and feature decoding purposes⁸⁶. However, these two types of characteristics often exhibit distinguished distributions in the latent space⁸³. For simplicity,

assuming a constant level of decoder optimization difficulty, we hypothesize that a better optimized GE may lead decoders to place greater emphasis on feature decoding, thereby allowing the learned features to cluster more effectively with improved sparsity in the latent space. Therefore, when training the same stratified decoder using different GEs, a less pruned decoding head might indicate that the decoding head compensates for sub-optimal feature extraction from a less optimized GE.

A6 Details on Ablation Studies of Multi-path Decoding Heads

In the CL-Net framework, trainable decoding heads are introduced for subsequent downstream tasks after completing and fixing the GE training. By independently training each decoding path, this approach mitigates knowledge forgetting and ensures that each task-specific model retains its learned features. We conducted experiments to assess the impacts of EMA, FL-Supporting, and the fine-tuning of the GE on the downstream tasks. These tasks include TotalSegmentation, StructSeg19, SegTHOR, FLARE22, and KiTS datasets. The training order for the tasks follows ‘Order 1’: TotalSegmentator \rightarrow StructSeg19 \rightarrow FLARE22 \rightarrow SegTHOR \rightarrow KiTS21. Please note that the StructSeg19 downstream task does not share any decoders with the other tasks. The GE is pre-trained using SimSiam and later momentum-updated using \mathcal{U}_5 datasets. The baseline stratified decoders of the CL-Net is trained without EMA update or FL-Supporting.

Impact of Fine-tuning GE As with most universal models, it is common practice to fine-tune the entire network to adapt to the downstream tasks. An important question arises: Despite the risk of catastrophic forgetting previously learned knowledge, does fine-tuning the entire CL-Net guarantee upper bound segmentation performance? This fine-tuning process involves adjusting the model’s parameters based on the characteristics and requirements of the new task, allowing it to specialize and optimize performance. We conducted ablation experiments by making apple-to-apple comparisons between the segmentation performance of models with fixed GE parameters and those with fine-tuned GE parameters. Specifically, both GE and stratified decoders were individually fine-tuned on each downstream task. The learning rate for the fine-tuning of the entire network is 1×10^{-4} , the total fine-tuning epoch is set to 300.

As shown in Tab S10, fine-tuning GE led to improved overall pruning rates for downstream tasks. However, when evaluating segmentation performance, the quantitative results were comparable to those achieved without fine-tuning the whole CL-Net. This suggests that while fine-tuning enhances model efficiency by increasing pruning rates, it does not necessarily translate into significantly better segmentation accuracy. However, for some tasks, fine-tuning the whole framework even degrades performance. For example, in the downstream task of StructSeg19, the fine-tuning GE resulted in a decrease of 0.6% in DSC and an increase of 0.03 mm in ASD. Upon closer examination of the predictions, we found that the segmentation of optical chiasm and optical nerves showed the most significant degradation, with an increase in false negatives. This degradation might be attributed to the fine-tuning process causing overfitting to a relatively small dataset, where the GE could have become too specialized to the training set.

Impact of EMA In clinical practice, when new images are collected, it is desirable to promptly and efficiently update the decoding head to incorporate the latest data. The EMA updating is an easy and powerful tool to stabilize training and mitigate overfitting to newly collected data. To assess the impact of EMA, we evaluated each downstream task with and without the EMA updating component. When using EMA for updating, we followed the same training setup discussed in Section A4 for updating EMA component and pruning mask. In contrast, when the EMA component is not used, the decoder is trained sequentially for each task. As demonstrated in Tab S10, exploiting EMA module for stratified decoder training consistently yielded better performance compared to training without it. We compared the performance gaps of the five downstream tasks:

- TotalSegmentator: +0.1% in DSC, -0.1 mm in ASD, and -1.9% in $\sum \mathcal{T}'$,
- StructSeg: +0.2% in DSC and -2.5% in $\sum \mathcal{T}'$,
- SegTHOR: +0.4% in DSC and -0.3 mm in ASD,
- FLARE22: +0.5% in DSC, -0.11 mm in ASD, and -2.8% in $\sum \mathcal{T}'$,
- KiTS21: +1.6% in DSC, -0.07 mm in ASD, and -2.0% in $\sum \mathcal{T}'$.

It was observed that a substantial portion of the CT images in the FLARE22 dataset contain kidney lesion. The EMA module helps stabilize the training process by averaging the model parameters over time, reducing the impact of sudden changes and fluctuations in the decoder weights. This stabilization was particularly noticeable in the performance gains achieved with EMA in the segmentation of the kidney lesion using the KiTS21 dataset. This approach mitigates over-fitting and helps the decoders retain knowledge across multiple tasks, leading to improved generalization and accuracy.

Impact of FL-Supporting For demonstration purposes, only the kidney lesion decoder is provided with FL-Supporting using the learned features of the kidney decoder, as shown in Tab S10. Leveraging supporting organs for difficult organ segmentation can reduce optimization difficulty and potentially provide spatial context, which helps to reduce false positives. This approach allows the model to utilize anatomical relationships and spatial information from nearby structures, improving the accuracy and consistency of segmentation, especially for challenging cases. The conventional approach to leveraging easy organ predictions for segmenting harder anatomies involves concatenating the predictions of the easier organs as additional input channels. However, this method requires adjusting the number of input channels, which inevitably necessitates fine-tuning both the GE and the decoding paths. This process can be resource-intensive and may introduce complexities in maintaining the model’s generalization capabilities across various tasks. Nevertheless, we conducted experiments using predicted kidney masks as an additional channel input for kidney lesion segmentation. In contrast, the decoder with FL-Supporting was trained using the fixed GE.

When training directly the kidney lesion decoder using the KiTS21 dataset, it showed a DSC of 84.2%, ASD of 1.18 mm, and $\sum \mathcal{T}'$ of 6.0%. We observed a significant ($P < 0.01$) improvement by channel-wisely concatenating predicted kidney masks for the kidney lesion segmentation, demonstrating +1.7% in DSC. In comparison, when using FL-Supporting for training, it demonstrated +2.1% in DSC. A similar performance trend was observed, but a further improved prediction was observed when using EMA for updating the decoding path, leading to the DSC of 86.4% vs. 86.9%, ASD of 1.14 mm vs. 1.12 mm. The predictions of the diseased kidney were found to contain errors, particularly in cases with very enlarged lesions located on top (head-direction) of the kidneys. The assumed reasons for the inferior performance compared to the model using FL-Supporting could be: 1) including GE for fine-tuning, which may lead the model to capture noisy distributions and potentially overfitting to these noise patterns, and 2) unlike binarized predictions, providing support at the feature level can offer a smoother representation of the data. Feature-level support allows the model to leverage more information, which may help to better capture subtle variations and complexities in the data, thus improving the segmentation performance.

To further evaluate the impact of FL-Supporting, we conducted an ablation study using LNS datasets, which include 18 head & neck LNSs and 15 chest LNSs. The performance of CL-Net^{C36} and CL-Net^{U36} were compared to their counterparts without FL-Supporting, denoted as CL-Net^{C36}_{noFL-Supporting} and CL-Net^{U36}_{noFL-Supporting}, respectively (Tab. S11). For head and neck LNS segmentation, the supporting structures included Musc_Cervial_A, Musc_Scalenus, Musc_Scalenus_A, and Musc_Scleido, while for chest LNS segmentation, the supporting structures were A_Aorta, Bronchus_L, Bronchus_R, Eso, and Heart³⁶. The results revealed performance declines in both CL-Net^{C36} and CL-Net^{U36} when FL-Supporting was excluded, with a 1.9% decrease in DSC and a 0.08 mm increase in ASD in 33 LNS classes. These findings demonstrate that FL-Supporting enhances the segmentation of small and challenging structures such as LNSs, potentially by leveraging additional localization information derived from supporting organ features.

Discussion on Stratified Decoder When a comprehensively pre-trained GE is available, we recommend directly utilizing it for the training of downstream tasks without fine-tuning GE. For optimal results, it is recommended to train the decoding paths with EMA and FL-Supporting to enhance stability and performance. Under an 8 Nvidia V100 GPUs DDP setup, the average training time for a two-class head (left and right counterparts) in DDP nnUNet is approximately 192 seconds per epoch with mini-batch sizes of 256. Using the froth of GE during decoding path training and dynamically adapting the decoder’s base number of features, the average training time is significantly reduced to approximately 32 seconds per epoch using the same system setup. Furthermore, for a 22 output class (e.g., StructSeg19) decoding head, the average training time of DDP nnUNet is approximately 242 seconds, and the average training time of CL-Net is approximately 43 seconds.

A7 Related Work and Reimplementation of Comparison Methods

For all comparison methods, we start with the same pre-trained nnUNet model on the TotalSegmentator dataset, which has been trained using the 3D nnUNet setting for 8000 epochs, with 250 iterations per epoch and initial learning rate 0.01. After that, the model is fine-tuned sequentially on continual segmentation tasks (ChestOrgan, HNOrgan and EsoOrgan), where each dataset is fine-tuned for 500 epochs, with 250 iterations per epoch and initial learning rate 0.005. All other nnUNet settings, such as data augmentation, remain the same as our implementation. Moreover, since our segmentation datasets/tasks are 3D CT scans (different from the previous continual segmentation works in natural images), adjustments to these comparison methods are required (extending 2D methods to 3D), as well as transferring their implementations to the nnUNet framework. We describe the detailed re-implementation of previous methods, especially our modifications, in the following subsections.

MiB MiB⁶⁰ proposes two marginal losses, or unbiased losses to solve the background shift issue in continual segmentation in their original paper: unbiased cross-entropy (UNCE) loss, which merges the probabilities of old classes to the background label, and unbiased knowledge distillation (UNKD) loss, which merges the probabilities of all new classes (belonging unseen classes of the old model) to the background label. Notice that the original unbiased loss assumes that new classes from the current dataset are completely disjoint with all the old classes, however, this assumption is not holding in our datasets. For example, TotalSegmentator and ChestOrgan contain four overlapping organs: inferior vena cava, trachea, esophagus, and pulmonary artery. Therefore, in order to reimplement MiB losses in the nnUNet framework and make them compatible with our datasets, we slightly modifies and generalizes both unbiased losses to handle overlapping labels in the continual learning setting. The modified UNCE loss is as follows:

$$\ell_{ce}^{\theta^t}(x, y) = -\frac{1}{|\mathcal{I}|} \sum_{i \in \mathcal{I}} \log \tilde{q}_x^t(i, y_i) \quad (12)$$

where:

$$\tilde{q}_x^t(i, c) = \begin{cases} q_x^t(i, c) & \text{if } c \neq b \\ \sum_{k \in Y^{t-1} \setminus C_p^t} q_x^t(i, k) & \text{if } c = b \end{cases} \quad (13)$$

Here, the same notation as that in the original article is used, except $C_p^t = Y^{t-1} \cup C^t - b$, which indicates the overlapping classes (excluding the background label) between the current data set C^t and all previous classes Y^{t-1} at the learning step t . When calculating the UNCE loss, we merge all the old labels in the background except the overlapping classes.

Similarly, we adapt UNKD loss as follows:

$$\ell_{kd}^{\theta^t}(x, y) = -\frac{1}{|\mathcal{I}|} \sum_{i \in \mathcal{I}} \sum_{c \in Y^{t-1} \setminus C_p^t} q_x^{t-1}(i, c) \log \hat{q}_x^t(i, y_i) \quad (14)$$

where:

$$\hat{q}_x^t(i, c) = \begin{cases} q_x^t(i, c) & \text{if } c \neq b \\ \sum_{k \in C^t} q_x^t(i, k) & \text{if } c = b \end{cases} \quad (15)$$

In the above formula, overlapping organs from the old class set are excluded so that the knowledge distillation works on the real old classes that cannot be learned from the current dataset.

Using two modified losses, we always train the model with the latest labels and ignore the previously learned overlapping labels when overlapping organs occur. Thus, overlapping labels are trained directly using the cross-entropy loss and merged to the background in the knowledge distillation loss. In addition, we use the same hyperparameters as the MiB setting: the weights of UNKD loss are set as 10 with balanced classifier initialization strategy.

PLOP PLOP⁶¹ was originally implemented for 2D images, especially its local distillation loss on multiple scales based on local POD. Local POD is a multi-scale feature pooling strategy consisting of computing width- and height-pooled slices on multi-scale regions, which aims to better retain both global and local spatial knowledge from the old model. However, since our data are all 3D CT scans with an additional depth dimension, we specifically extend the local POD to higher dimensions when reimplementing the method. Two pooling strategies can be adopted for 3D cases: 1) Pooling 3D feature map along each single dimension and extracting three 2D projections along each axis:

$$\Phi(\mathbf{x}) = \left(\frac{1}{H} \sum_{h=1}^H \mathbf{x}[h, :, :, :] \left\| \frac{1}{W} \sum_{w=1}^W \mathbf{x}[:, w, :, :] \right\| \frac{1}{D} \sum_{d=1}^D \mathbf{x}[:, :, d, :] \right) \in R^{(WD+HD+HW) \times C} \quad (16)$$

where notations follow the original PLOP paper. This pooling method can preserve enough spatial

information while providing some level of plasticity to the model. 2) Pooling 3D feature map on two dimensions and only extract 1D projection along the remaining axis:

$$\Phi(\mathbf{x}) = \left(\frac{1}{HW} \sum_{h=1}^H \sum_{w=1}^W \mathbf{x}[h, w, :, :] \left\| \frac{1}{WD} \sum_{w=1}^W \sum_{d=1}^D \mathbf{x}[:, w, d, :] \right. \right. \\ \left. \left. \left\| \frac{1}{HD} \sum_{h=1}^H \sum_{d=1}^D \mathbf{x}[h, :, d, :] \right) \in R^{(H+W+D) \times C} \right. \quad (17)$$

This pooling strategy has similar feature shape; however, when pooling on two axes together, most of the spatial information is lost and POD loss cannot retain the former knowledge. After comparing the performance using two strategies, we select the former, which better handles the trade-off between model rigidity and plasticity. For **hyperparameters**, the original paper uses the pod weighting factor of 0.01, which is too large for the 3D pooling case. The L2 norm of 3D pooled features is more than 10 times larger than that of 2D pooled features. In our experiments, we set this pod factor to 0.001. Other hyperparameters are consistent with those used in the original paper.

CSCLIP The original CSCLIP⁶² empowers a continual multi-organ segmentation framework with pseudo-labels, lightweight three-layer class-specific heads and Contrastive Language–Image Pretraining (CLIP)⁸⁷ text embeddings to mitigate catastrophic forgetting. Since the authors have made their source code public available, we can directly implement and adapt their method to our datasets and tasks. We would like to mention several adjustments of the code: (1) The original paper contains only 38 target organs and their corresponding organ name text embeddings. In order to match our 5-dataset CSS experiments including 137 target organs under different orders, we replace the original CSCLIP text embeddings with our order-specific 137 text embeddings generated by the CLIP text encoder. (2) Similarly, we increase the number of lightweight class-specific heads to 137 to fully cover our organ classes. (3) Inference of the original code is fully processed in GPU memory, which is limited to 80GB on NVIDIA A100. This may result in an “out of memory” error when the input 3D full-body CT image has a large size exceeding a certain threshold. To prevent such a memory overflow issue, we equally partition the input scan into three segments with a 20% overlap along the axial direction, predict each separately and subsequently concatenate them to restore the original size.

Supplementary Figures and Tables

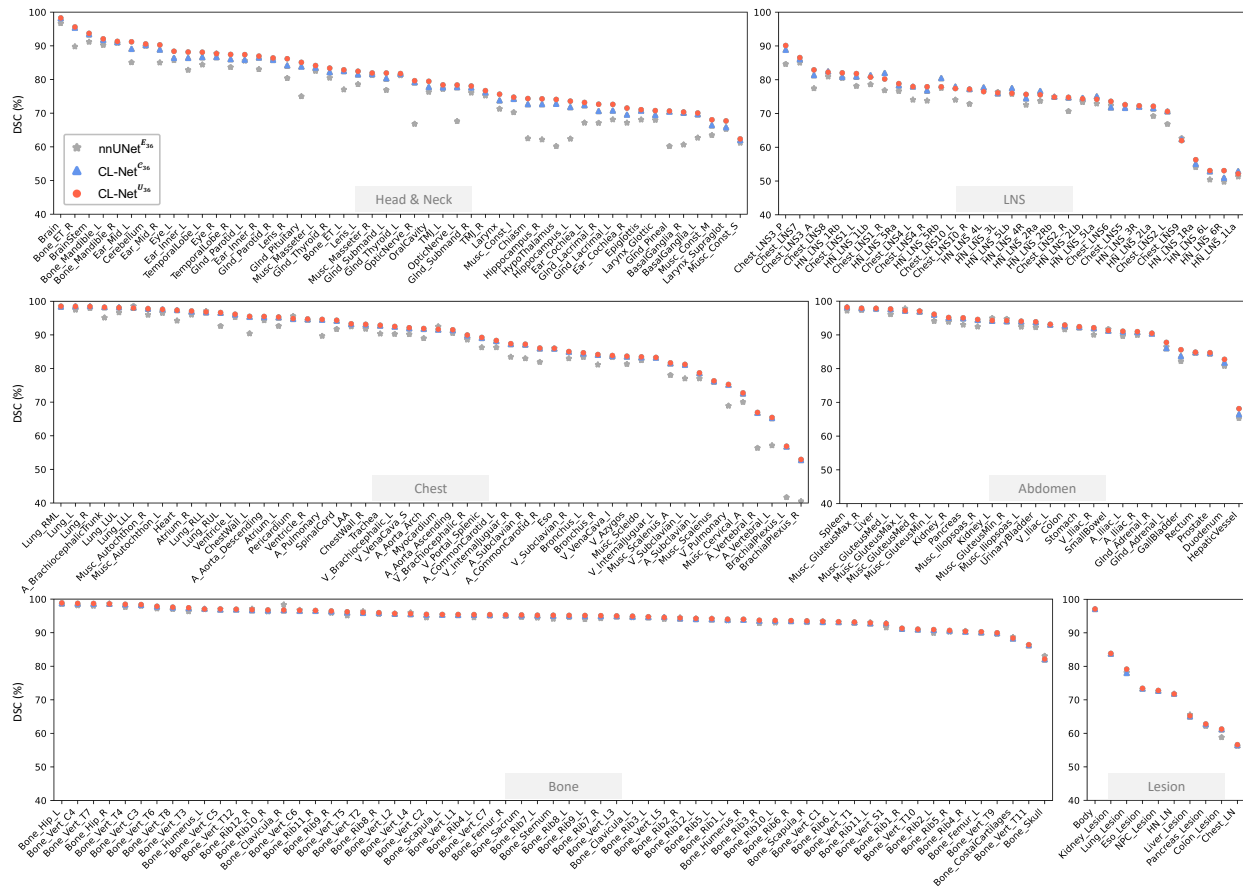


Fig. S1 | Organ-wise segmentation comparison of CL-Net^{U36}, CL-Net^{C36}, nnUNet^{E36}. DSC (%) of 235 individual anatomies are illustrated. Anatomies are grouped as Head & Neck (49 organs), Chest (52), Abdomen (28), Bone (63), LSN (33), Lesion (9), and Body (shown in Lesion panel).

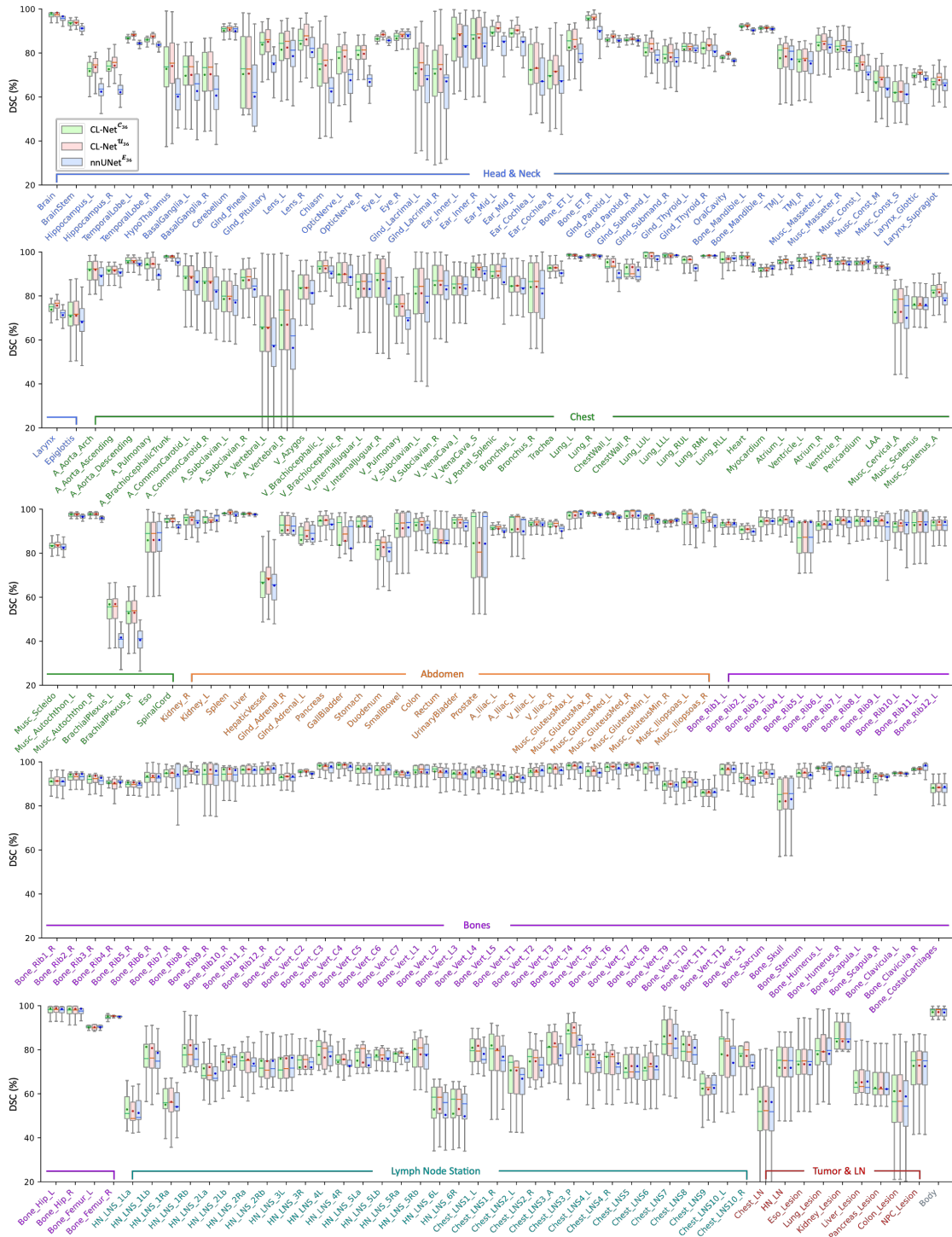


Fig. S2 | The segmentation dice score (%) of our method CL-Net^{U36} and CL-Net^{E36}, and the leading segmentation model nnUNet^{E36} over all 235 organs. Organs are grouped and colored by body parts or organ types.

Dataset Name	Organ#	Train#	Test#	Median Size (XYZ)	Median Spacing (XYZ)	Image BPR Range (Bottom-Top)	Label BPR Range (Bottom-Top)
Private Datasets							
NPC_FAH-ZU_OAR ^{52,88}	15	58	14	512x512x128	0.98x0.98x3.00	0.59-1.00	0.62-1.00
HN_CGMH_OAR ^{35,88}	42	114	28	478x312x284	1.00x1.00x1.25	0.61-1.00	0.60-1.00
LungCancer_FAH-ZU_OAR ^{36,37}	12	78	20	512x512x67	0.68x0.68x5.00	0.06-0.79	0.38-0.82
EsoCancer_FAH-ZU_OAR ^{36,44}	35	154	38	512x512x80	0.68x0.68x5.00	0.39-0.92	0.37-0.92
LungCancer_HHA-FU_OAR ^{36,52}	13	304	76	512x512x80	0.68x0.68x5.00	0.02-1.00	0.38-0.87
Cervix_LinkingMed_OAR	5	45	11	768x768x104	0.65x0.65x3.00	0.00-0.32	0.00-0.35
Body_LinkingMed_OAR	1	800	201	512x512x122	0.98x0.98x3.00	0.00-1.00	0.00-1.00
HN_FAH-ZU_LNS ⁸⁹	18	93	23	512x512x129	0.98x0.98x3.00	0.61-1.00	0.72-0.93
Chest_FAH-ZU_LNS ^{36,38}	15	149	37	512x512x78	0.68x0.68x5.00	0.38-0.92	0.51-0.78
NPCCancer_FAH-ZU_Lesion ⁹⁰	1	207	52	512x512x137	0.98x0.98x3.00	0.59-1.00	0.88-0.96
LungCancer_SCH_Lesion ^{42,91}	1	952	239	512x512x63	0.78x0.78x5.00	0.31-0.84	0.60-0.65
EsoCancer_SCH_Lesion ⁵⁰	2	1132	283	512x512x94	0.98x0.98x5.00	0.16-0.97	0.50-0.76
LiverCancer_SHCH_Lesion ⁴⁵	2	2815	704	512x512x51	0.74x0.74x5.00	0.00-0.81	0.35-0.53
HN_ZH-FU_LN ^{47,48}	1	195	47	512x512x57	0.49x0.49x5.00	0.64-1.00	0.79-0.87
LungCancer_FAH-ZU_LN ^{46,47}	1	66	16	512x512x68	0.69x0.69x5.00	0.03-0.79	0.60-0.73
EsoCancer_FAH-ZU_LN ^{36,38,47}	1	116	30	512x512x80	0.68x0.68x5.00	0.38-0.92	0.53-0.74
Public Datasets							
TotalSegmentator ⁵⁵	120	1139	89	240x229x228	1.50x1.50x1.50	0.00-1.00	0.00-0.99
StructSeg 2019 ⁵⁶	22	40	10	512x512x124	1.14x1.14x3.00	0.62-1.00	0.61-1.00
HaN-Seg ⁹²	30	34	8	1024x1024x185	0.67x0.67x2.00	0.42-1.00	0.70-1.00
SegRap ⁶⁶	38	192	48	1024x1024x127	0.54x0.54x3.00	0.51-1.00	0.65-1.00
SegTHOR ⁵⁷	4	32	8	512x512x171	0.98x0.98x2.50	0.27-0.94	0.44-0.76
FLARE22 ⁵⁸	13	50	20	512x512x97	0.80x0.80x2.50	0.06-0.58	0.28-0.55
AMOS ⁹³	15	300	200	512x512x104	0.68x0.68x5.00	0.00-0.76	0.07-0.60
AbdomenCTIK 4 ⁹⁴	4	800	200	512x512x102	0.79x0.79x2.50	0.00-0.76	0.26-0.55
AbdomenCTIK 12 ⁹⁴	12	42	8	512x512x97	0.80x0.80x2.50	0.06-0.58	0.27-0.59
WORD ⁹⁵	16	96	24	512x512x201	0.98x0.98x3.00	0.00-0.67	0.00-0.74
StructSeg NPC ⁵⁶	1	40	10	512x512x125	1.14x1.14x3.00	0.62-1.00	0.90-0.95
MSD Spleen ⁷	1	32	9	512x512x90	0.79x0.79x5.00	0.01-0.72	0.40-0.50
MSD Lung ⁷	1	50	13	512x512x256	0.78x0.78x1.25	0.10-0.78	0.61-0.64
MSD Liver ⁷	2	104	27	512x512x430	0.77x0.77x1.00	0.00-0.77	0.33-0.53
MSD Hepatic Vessel ⁷	2	242	61	512x512x49	0.80x0.80x5.00	0.10-0.59	0.37-0.51
MSD Colon ⁷	1	100	26	512x512x95	0.78x0.78x5.00	0.00-0.74	0.24-0.30
MSD Pancreas ⁷	2	224	57	512x512x92	0.80x0.80x2.50	0.03-0.57	0.35-0.44
LiTS17 ⁹⁶	2	105	26	512x512x432	0.77x0.77x1.00	0.00-0.77	0.26-0.55
KiTS21 ^{59,97}	2	210	90	512x512x110	0.78x0.78x3.00	0.00-0.75	0.25-0.47
NIH LN ^{98,99}	1	72	17	512x512x154	0.79x0.79x2.00	0.32-0.80	0.53-0.75

Table S1 | Dataset fingerprints for CL-Net training. Overview of 36 datasets used to train CL-Net, including 16 private and 20 public datasets, spanning a wide range of segmentation tasks across various anatomical regions of the human body, including the Head & Neck, Chest, Abdomen, Bones, lymph node stations (LNS), and Lesions. This comprehensive dataset collection comprises a total of 7,278 private and 3,904 public CT scans, along with 37,827 private and 172,607 public annotations, covering 235 anatomical structures - 125 private and 162 public anatomical types with 52 organs overlapping between the two groups. In addition to standard statistics such as dataset name, training/testing sizes, number of target organ classes, median image size, and voxel spacing, we also report two specific metrics to better characterize the body part distribution within each dataset: the Body Part Regression (BPR, head – 1, pelvic – 0) axial bounding ranges for both the images and the foreground organs.

Dataset Name	Target Organs
NPC_FAH-ZU_OAR ^{52,88}	BrainStem, Eye_L, Eye_R, Lens_L, Lens_R, Chiasm, OpticNerve_L, OpticNerve_R, Gnd_Parotid_L, Gnd_Parotid_R, TMJ_L, TMJ_R, SpinalCord, Musc_Masseter_L, Musc_Masseter_R
HN_CGMH_OAR ^{35,88}	Bronchus_L, Bronchus_R, BasalGanglia_L, BasalGanglia_R, BrainStem, Cerebellum, Ear_Cochlea_L, Ear_Cochlea_R, Musc_Const_I, Musc_Const_M, Musc_Const_S, Ear_Inner_L, Ear_Inner_R, Eye_L, Eye_R, Epiglottis, Eso, Hippocampus_L, Hippocampus_R, HypoThalamus, Gnd_Lacrimal_L, Gnd_Lacrimal_R, Larynx, Bone_Mandible_L, Bone_Mandible_R, Chiasm, OpticNerve_L, OpticNerve_R, OralCavity, Gnd_Parotid_L, Gnd_Parotid_R, Gnd_Pineal, Gnd_Pituitary, SpinalCord, Gnd_Submand_L, Gnd_Submand_R, TemporalLobe_L, TemporalLobe_R, Gnd_Thyroid_L, Gnd_Thyroid_R, TMJ_L, TMJ_R
LungCancer_FAH-ZU_OAR ^{36,37}	Eso, Lung_L, Lung_R, Pericardium, SpinalCord, BrachialPlexus, ProximalBronchi, A_Aorta, V_VenaCava_S, A_Pulmonary, V_Pulmonary, V_VenaCava_I, ChestWall_L, ChestWall_R
EsoCancer_FAH-ZU_OAR ^{36,44}	A_Aorta_Arch, A_Aorta_Ascending, A_Aorta_Descending, A_Pulmonary, Bronchus_L, Bronchus_R, Heart, Lung_L, Lung_R, SpinalCord, Bone_Sternum, Gnd_Thyroid_L, Gnd_Thyroid_R, Trachea, V_VenaCava_I, V_VenaCava_S, Musc_Cervical_A, Musc_Scalenus, Musc_Scalenus_A, Musc_Scleido, A_CommonCarotid_L, A_CommonCarotid_R, A_Subclavian_L, A_Subclavian_R, A_Vertebral_L, A_Vertebral_R, Eso, V_Azygos, V_Brachiocephalic_L, V_Brachiocephalic_R, V_InternalJuguar_L, V_InternalJuguar_R, V_Pulmonary, V_Subclavian_L, V_Subclavian_R, BrachialPlexus
LungCancer_HHA-FU_OAR ^{36,52}	Eso, Lung_L, Lung_R, ChestWall_L, ChestWall_R, Pericardium, SpinalCord, BrachialPlexus, ProximalBronchi, A_Aorta, A_Pulmonary, V_VenaCava_S, V_VenaCava_I, V_Pulmonary
Cervix_LinkingMed_OAR	UrinaryBladder, Rectum, Colon, SmallBowel
Body_LinkingMed_OAR	Body
HN_FAH-ZU_LNS ⁸⁹	HN_LNS_1La, HN_LNS_1Lb, HN_LNS_1Ra, HN_LNS_1Rb, HN_LNS_2La, HN_LNS_2Lb, HN_LNS_2Ra, HN_LNS_2Rb, HN_LNS_3L, HN_LNS_3R, HN_LNS_4L, HN_LNS_4R, HN_LNS_5La, HN_LNS_5Lb, HN_LNS_5Ra, HN_LNS_5Rb, HN_LNS_6L, HN_LNS_6R
Chest_FAH-ZU_LNS ^{36,38}	Chest_LNS1_L, Chest_LNS1_R, Chest_LNS2_L, Chest_LNS2_R, Chest_LNS3_A, Chest_LNS3_P, Chest_LNS4_L, Chest_LNS4_R, Chest_LNS5, Chest_LNS6, Chest_LNS7, Chest_LNS8, Chest_LNS9, Chest_LNS10_L, Chest_LNS10_R
NPCCancer_FAH-ZU_Lesion ^{53,90}	NPC_Lesion
LungCancer_SCH_Lesion ^{42,91}	Lung_Lesion
EsoCancer_SCH_Lesion ⁵⁰	Eso, Eso_Lesion
LiverCancer_SHCH_Lesion ⁴⁵	Liver, Liver_Lesion
HN_ZH-FU_LN ^{47,48}	HN_LN
LungCancer_FAH-ZU_LN ^{46,47}	Chest_LN
EsoCancer_FAH-ZU_LN ^{36,38,47}	Chest_LN

Table S2 | Detailed organ classes of 16 private datasets used for training CL-Net. The datasets cover 125 clinically relevant anatomical structures across whole-body regions, including 73 novel structures not available in public datasets. In addition to the common organ groups (Head & Neck, Chest, Abdomen, Bones, and Lesions), lymph node stations (LNS) in the head-neck and chest regions are specifically included. All organ labels follow standardized naming conventions in radiation oncology¹⁰⁰.

Dataset Name	Target Organs
TotalSegmentator ⁵⁵	Spleen, Kidney_R, Kidney_L, GallBladder, Liver, Stomach, Pancreas, GlnD.Adrenal_R, GlnD.Adrenal_L, Lung_LUL, Lung_LLL, Lung_RUL, Lung_RML, Lung_RLL, Eso, Trachea, GlnD.Thyroid, SmallBowel, Duodenum, Colon, UrinaryBladder, Prostate, Kidney_Cyst_L, Kidney_Cyst_R, Bone.Sacrum, Bone.Vert.S1, Bone.Vert.L5, Bone.Vert.L4, Bone.Vert.L3, Bone.Vert.L2, Bone.Vert.L1, Bone.Vert.T12, Bone.Vert.T11, Bone.Vert.T10, Bone.Vert.T9, Bone.Vert.T8, Bone.Vert.T7, Bone.Vert.T6, Bone.Vert.T5, Bone.Vert.T4, Bone.Vert.T3, Bone.Vert.T2, Bone.Vert.T1, Bone.Vert.C7, Bone.Vert.C6, Bone.Vert.C5, Bone.Vert.C4, Bone.Vert.C3, Bone.Vert.C2, Bone.Vert.C1, Heart, A.Aorta, V.Pulmonary, A.BrachiocephalicTrunk, A.Subclavian_R, A.Subclavian_L, A.CommonCarotid_R, A.CommonCarotid_L, V.Brachiocephalic_L, V.Brachiocephalic_R, LAA, V.VenaCava_S, V.VenaCava_I, V.Portal.Splenic, A.Iliac_L, A.Iliac_R, V.Iliac_L, V.Iliac_R, Bone.Humerus_L, Bone.Humerus_R, Bone.Scapula_L, Bone.Scapula_R, Bone.Clavicula_L, Bone.Clavicula_R, Bone.Femur_L, Bone.Femur_R, Bone.Hip_L, Bone.Hip_R, SpinalCord, Musc.GluteusMax_L, Musc.GluteusMax_R, Musc.GluteusMed_L, Musc.GluteusMed_R, Musc.GluteusMin_L, Musc.GluteusMin_R, Musc.Autochthon_L, Musc.Autochthon_R, Musc.Iliopsoas_L, Musc.Iliopsoas_R, Brain, Bone.Skull, Bone.Rib4_R, Bone.Rib3_R, Bone.Rib1_L, Bone.Rib2_L, Bone.Rib3_L, Bone.Rib4_L, Bone.Rib5_L, Bone.Rib6_L, Bone.Rib7_L, Bone.Rib8_L, Bone.Rib9_L, Bone.Rib10_L, Bone.Rib11_L, Bone.Rib12_L, Bone.Rib1_R, Bone.Rib2_R, Bone.Rib5_R, Bone.Rib6_R, Bone.Rib7_R, Bone.Rib8_R, Bone.Rib9_R, Bone.Rib10_R, Bone.Rib11_R, Bone.Rib12_R, Bone.Sternum, Bone.CostalCartilages, Myocardium, Atrium_L, Atrium_R, Ventricle_L, Ventricle_R
StructSeg 2019 ⁵⁶	BrainStem, Eye_L, Eye_R, Lens_L, Lens_R, OpticNerve_L, OpticNerve_R, Chiasm, TemporalLobe_L, TemporalLobe_R, GlnD.Pituitary, GlnD.Parotid_L, GlnD.Parotid_R, Ear.Inner_L, Ear.Inner_R, Ear.Mid_L, Ear.Mid_R, TMJ_L, TMJ_R, SpinalCord, Bone.Mandible_L, Bone.Mandible_R
HaN-Seg ⁹²	A.CommonCarotid_L, A.CommonCarotid_R, Arytenoid, Bone.Mandible, BrainStem, BuccalMucosa, OralCavity, Ear.Cochlea_L, Ear.Cochlea_R, Cricopharyngeus, Eso, Eye.AL, Eye.AR, Eye.PL, Eye.PR, GlnD.Lacrimal_L, GlnD.Lacrimal_R, GlnD.Submand_L, GlnD.Submand_R, GlnD.Thyroid, Larynx.Glottic, Larynx.Supraglot, Lips, Chiasm, OpticNerve_L, OpticNerve_R, GlnD.Parotid_L, GlnD.Parotid_R, GlnD.Pituitary, SpinalCord
SegRap ⁶⁶	Brain, TemporalLobe_L, TemporalLobe_R, Hippocampus_L, Hippocampus_R, GlnD.Pituitary, Chiasm, OpticNerve_L, OpticNerve_R, Eye_L, Eye_R, Lens_L, Lens_R, Ear.Cochlea_L, Ear.Cochlea_R, Mastoid_L, Mastoid_R, Ear.Mid_L, Ear.Mid_R, Bone.ET_L, Bone.ET_R, Bone.Mandible_L, Bone.Mandible_R, GlnD.Submand_L, GlnD.Submand_R, OralCavity, GlnD.Parotid_L, GlnD.Parotid_R, TMJ_L, TMJ_R, Larynx, Larynx.Glottic, Larynx.Supraglot, BrainStem, SpinalCord, Eso, GlnD.Thyroid, Trachea
SegTHOR ⁵⁷	Eso, ProximalBronchi, Heart, A.Aorta
FLARE22 ⁵⁸	Liver, Eso, Stomach, Duodenum, Kidney_L, Kidney_R, Spleen, Pancreas, A.Aorta, V.VenaCava_I, GlnD.Adrenal_R, GlnD.Adrenal_L, GallBladder
AMOS ⁹³	Spleen, Kidney_R, Kidney_L, GallBladder, Eso, Liver, Stomach, Aorta, V.VenaCava_I, Pancreas, GlnD.Adrenal_R, GlnD.Adrenal_L, Duodenum, UrinaryBladder, Prostate/Uterus
AbdomenCTIK 4 ⁹⁴	Liver, Kidney, Spleen, Pancreas
AbdomenCTIK 12 ⁹⁴	Liver, Kidney, Spleen, Pancreas, A.Aorta, V.VenaCava_I, Stomach, GallBladder, Eso, GlnD.Adrenal_R, GlnD.Adrenal_L, A.CeliacTrunk
WORD ⁹⁵	Liver, Spleen, Kidney_L, Kidney_R, Stomach, GallBladder, Eso, Pancreas, Duodenum, Colon, SmallBowel, GlnD.Adrenal, Rectum, UrinaryBladder, Bone.FemurHead_L, Bone.FemurHead_R
StructSeg NPC ⁵⁶	NPC.Lesion
MSD Spleen ⁷	Spleen
MSD Lung ⁷	Lung.Lesion
MSD Liver ⁷	Liver, Liver.Lesion
MSD Hepatic Vessel ⁷	HepaticVessel, Liver.Lesion
MSD Colon ⁷	Colon.Lesion
MSD Pancreas ⁷	Pancreas, Pancreas.Lesion
LiTS17 ⁹⁶	Liver, Liver.Lesion
KiTS21 ^{59,97}	Kidney, Kidney.Lesion
NIH LN ^{98,99}	Chest.LN

Table S3 | Detailed organ classes of all 20 public datasets used for training CL-Net. The datasets cover 162 common anatomical structures across whole-body regions, including Head & Neck, Chest, Abdomen, Bones, and Lesions. All organ labels follow standardized naming conventions in radiation oncology¹⁰⁰.

Dataset Name	Body Part	Organ#	Test#	Med Shape (XYZ)	Med Spacing (XYZ)	Target Organs
NPC_SMU_OAR	Head & Neck	12	268	406x227x95	0.99x0.99x3.00	BrainStem, Eye_L, Eye_R, Lens_L, Lens_R, Chiasm, OpticNerve_L, OpticNerve_R, GlnD_Parotid_L, GlnD_Parotid_R, TMJ_L, TMJ_R
LungCancer_NLH_OAR	Chest	14	60	512x512x93	1.17x1.17x5.00	Eso, Lung_L, Lung_R, Pericardium, SpinalCord, BrachialPlex, ProximalBronchi, A_Aorta, V_SVC, A_Pulmonary, V_Pulmonary, V_IVC, ChestWall_L, ChestWall_R
BTCV ⁶⁷	Abdomen	13	30	512x512x127	0.76x0.76x3.00	Spleen, Kidney_R, Kidney_L, GallBladder, Eso, Liver, Stomach, A_Aorta, V_VenaCava_I, V_Portal_Splenic, Pancreas, GlnD_Adrenal_R, GlnD_Adrenal_L
NPC_CGMH_Lesion	Head & Neck	1	319	512x512x137	0.98x0.98x3.00	NPC_lesion
EsoCancer_CGMH_Lesion	Chest	1	148	366x273x212	1.00x1.00x2.50	Eso_lesion
KidneyCancer_SHCH_Lesion	Abdomen	1	978	512x512x343	0.74x0.74x1.00	Kidney_lesion
LiverCancer_CGMH_Lesion	Abdomen	1	176	512x512x224	0.98x0.98x1.25	Liver_lesion

Table S4 | Dataset fingerprints for CL-Net external validation. Overview of seven external datasets used for external validation, including one public dataset BTCV and six private datasets. The external datasets span whole-body anatomical regions and cover 1,979 testing samples and 43 targeting anatomical structures from head & neck, chest, abdomen, and four lesions. Basic dataset fingerprints are provided, including dataset name, body part coverage, number of target organ classes, testing number, median image size and voxel spacing, and detailed target organ list.

Decoder Name	Structure List	FL-Supporting	Decoder Name	Structure List	FL-Supporting
Brain	Brain		Pericardium	Pericardium	Heart
BrainStem	BrainStem		Airway	Bronchus.L, Bronchus.R, Trachea	
TemporalLobe	TemporalLobe.L, TemporalLobe.R		LAA	LAA	
BasalGanglia	BasalGanglia.L, BasalGanglia.R	TemporalLobe	Eso	Eso	
Hippocampus	Hippocampus.L, Hippocampus.R	TemporalLobe	Musc.Cervical.A	Musc.Cervical.A	
HypoThalamus	HypoThalamus	BrainStem	Musc.Scalenus	Musc.Scalenus, Musc.Scalenus.A	
GlnD.Pineal	GlnD.Pineal	BrainStem	Musc.Scleido	Musc.Scleido	
Cerebellum	Cerebellum		Musc.Autochthon	Musc.Autochthon.L, Musc.Autochthon.R	
Chiasm	Chiasm	OpticNerve, GlnD.Pituitary	BrachialPlexus	BrachialPlexus.L, BrachialPlexus.R	A.Subclavian, Musc.Scalenus
Eye	Eye.L, Eye.R		SpinalCord	SpinalCord	
Lens	Lens.L, Lens.R	Eye	Liver	Liver	
OpticNerve	OpticNerve.L, OpticNerve.R	Eye	Kidney	Kidney.L, Kidney.R	
GlnD.Lacrimal	GlnD.Lacrimal.L, GlnD.Lacrimal.R	Eye	Pancreas	Pancreas	
GlnD.Pituitary	GlnD.Pituitary		Spleen	Spleen	
Ear.Mid	Ear.Mid.L, Ear.Mid.R		Prostate	Prostate	
Ear.Inner	Ear.Inner.L, Ear.Inner.R		Stomach	Stomach	
Ear.Cochlea	Ear.Cochlea.L, Ear.Cochlea.R	Ear.Inner	SmallBowel	SmallBowel	
Bone.ET	Bone.ET.L, Bone.ET.R		Colon	Colon, Rectum	
Bone.Mandible	Bone.Mandible.L, Bone.Mandible.R		Duodenum	Duodenum	Stomach
TMJ	TMJ.L, TMJ.R		GallBladder	GallBladder	
GlnD.Parotid	GlnD.Parotid.L, GlnD.Parotid.R		GlnD.Adrenal	GlnD.Adrenal.L, GlnD.Adrenal.R	Kidney
GlnD.Submand	GlnD.Submand.L, GlnD.Submand.R		HepaticVessel	HepaticVessel	Liver
GlnD.Thyroid	GlnD.Thyroid.L, GlnD.Thyroid.R		Musc.GluteusMax	Musc.GluteusMax.L, Musc.GluteusMax.R	
OralCavity	OralCavity		Musc.GluteusMed	Musc.GluteusMed.L, Musc.GluteusMed.R	
Larynx	Larynx, Larynx.Glottic, Larynx.Supraglot		Musc.GluteusMin	Musc.GluteusMin.L, Musc.GluteusMin.R	
Epiglottis	Epiglottis		Musc.Iliopsoas	Musc.Iliopsoas.L, Musc.Iliopsoas.R	
Musc.Const	Musc.Const.I, Musc.Const.M, Musc.Const.S		UrinaryBladder	UrinaryBladder	
Musc.Masseter	Musc.Masseter.L, Musc.Masseter.R		A.Iliac	A.Iliac.L, A.Iliac.R	
Lung	Lung.L, Lung.R		V.Iliac	V.Iliac.L, V.Iliac.R	
Lung.LL	Lung.LLL, Lung.LUL		Bone.Skull	Bone.Skull	
Lung.RL	Lung.RLL, Lung.RML, Lung.RUL		Bone.Clavicula	Bone.Clavicula.L, Bone.Clavicula.R	
ChestWall	ChestWall.L, ChestWall.R	Lung	Bone.Humerus	Bone.Humerus.L, Bone.Humerus.R	
A.Aorta	A.Aorta.Arch, A.Aorta.Ascending, A.Aorta.Descending		Bone.Scapula	Bone.Scapula.L, Bone.Scapula.R	
A.BrachiocephalicTrunk	A.BrachiocephalicTrunk		Bone.Sternum	Bone.Sternum	
A.CommonCarotid	A.CommonCarotid.L, A.CommonCarotid.R		Bone.CostalCartilages	Bone.CostalCartilages	
A.Pulmonary	A.Pulmonary		Bone.Femur	Bone.Femur.L, Bone.Femur.R	
A.Subclavian	A.Subclavian.L, A.Subclavian.R		Bone.Hip	Bone.Hip.L, Bone.Hip.R	
A.Vertebra	A.Vertebra.L, A.Vertebra.R	A.CommonCarotid	Bone.Sacrum	Bone.Sacrum	
V.Azygos	V.Azygos		HN.LN	HN.LN	HN.LNS
V.Brachiocephalic	V.Brachiocephalic.L, V.Brachiocephalic.R		Chest.LN	Chest.LN	Chest.LNS
V.InternalJuguar	V.InternalJuguar.L, V.InternalJuguar.R		NPC.Lesion	NPC.Lesion	
V.Portal.Splenic	V.Portal.Splenic		Lung.Lesion	Lung.Lesion	Lung
V.Pulmonary	V.Pulmonary	Heart	Eso.Lesion	Eso.Lesion	Eso
V.Subclavian	V.Subclavian.L, V.Subclavian.R		Liver.Lesion	Liver.Lesion	Liver
V.VenaCava.I	V.VenaCava.I		Kidney.Lesion	Kidney.Lesion	Kidney
V.VenaCava.S	V.VenaCava.S		Pancreas.Lesion	Pancreas.Lesion	Pancreas
Heart	Heart		Colon.Lesion	Colon.Lesion	Colon
Atrium.Ventricle	Atrium.L, Atrium.R, Ventricle.L, Ventricle.R		Body	Body	
Myocardium	Myocardium	Heart			
HN.LNS	HN.LNS.1La, HN.LNS.1Lb, HN.LNS.1Ra, HN.LNS.1Rb, HN.LNS.2La, HN.LNS.2Lb, HN.LNS.2Ra, HN.LNS.2Rb, HN.LNS.3L, HN.LNS.3R, HN.LNS.4L, HN.LNS.4R, HN.LNS.5La, HN.LNS.5Lb, HN.LNS.5Ra, HN.LNS.5Rb, HN.LNS.6L, HN.LNS.6R	Musc.Cervical.A, Musc.Scalenus, Musc.Scleido	Chest.LNS	Chest.LNS1.L, Chest.LNS1.R, Chest.LNS2.L, Chest.LNS2.R, Chest.LNS3.A, Chest.LNS3.P, Chest.LNS4.L, Chest.LNS4.R, Chest.LNS5, Chest.LNS6, Chest.LNS7, Chest.LNS8, Chest.LNS9, Chest.LNS10.L, Chest.LNS10.R	A.Aorta, Airway, Eso, Heart
Bone.Rib	Bone.Rib1.L, Bone.Rib2.L, Bone.Rib3.L, Bone.Rib4.L, Bone.Rib5.L, Bone.Rib6.L, Bone.Rib7.L, Bone.Rib8.L, Bone.Rib9.L, Bone.Rib10.L, Bone.Rib11.L, Bone.Rib12.L, Bone.Rib1.R, Bone.Rib2.R, Bone.Rib3.R, Bone.Rib4.R, Bone.Rib5.R, Bone.Rib6.R, Bone.Rib7.R, Bone.Rib8.R, Bone.Rib9.R, Bone.Rib10.R, Bone.Rib11.R, Bone.Rib12.R		Bone.Vert	Bone.Vert.C1, Bone.Vert.C2, Bone.Vert.C3, Bone.Vert.C4, Bone.Vert.C5, Bone.Vert.C6, Bone.Vert.C7, Bone.Vert.T1, Bone.Vert.T2, Bone.Vert.T3, Bone.Vert.T4, Bone.Vert.T5, Bone.Vert.T6, Bone.Vert.T7, Bone.Vert.T8, Bone.Vert.T9, Bone.Vert.T10, Bone.Vert.T11, Bone.Vert.T12, Bone.Vert.L1, Bone.Vert.L2, Bone.Vert.L3, Bone.Vert.L4, Bone.Vert.L5, Bone.Vert.S1	

Table S5 | Anatomy structure mapping of all 101 decoders. Anatomical structures of the same type are grouped and trained within a single decoder to streamline segmentation and improve efficiency. For more complex and challenging structures, the FL-Supporting is adopted, enhancing prediction accuracy and addressing spatial precision associated with these structures.

	TotalSegmentator V2		StructSeg19		FLARE22		SegThor		KiTS21		All		Param# (MB)↓
	DSC↑	ASD↓	DSC↑	ASD↓	DSC↑	ASD↓	DSC↑	ASD↓	DSC↑	ASD↓	DSC↑	ASD↓	
CL-Net^{C5}													
Order 1	94.1	0.89	86.4	0.28	90.4	1.05	93.2	0.33	86.9	1.32	92.6	0.81	28.5
Order 2	94.1	0.89	86.4	0.28	90.6	1.06	93.2	0.33	86.9	1.32	92.6	0.81	28.9
Order 3	94.2	0.97	86.1	0.29	91.3	1.10	93.1	0.48	87.1	0.92	92.7	0.87	34.2
Order 4	94.1	0.99	86.4	0.29	89.5	1.28	93.5	0.32	86.6	1.13	92.5	0.90	35.5
Mean	94.1	0.94	86.3	0.28	90.5	1.12	93.2	0.36	86.9	1.17	92.6	0.85	31.8
CL-Net^{C5}_{unpruned}													
Order 1	94.1	0.90	86.4	0.28	90.6	1.09	93.1	0.34	86.8	1.21	92.6	0.82	93.9
Order 2	94.1	0.90	86.4	0.28	90.5	1.08	93.0	0.32	86.8	1.21	92.6	0.81	93.9
Order 3	94.2	0.97	86.0	0.28	91.2	1.12	92.9	0.51	87.0	0.97	92.7	0.87	93.9
Order 4	94.1	0.98	86.4	0.29	88.8	1.28	93.3	0.34	86.4	1.21	92.5	0.89	93.9
Mean	94.1	0.94	86.3	0.28	90.3	1.14	93.1	0.37	86.8	1.15	92.6	0.85	93.9
nnUNet^{E5}													
Mean	94.1	0.97	86.4	0.29	90.0	1.14	92.6	0.34	86.7	1.18	92.5	0.87	156.5

Table S6 | CSS order-wise and dataset-wise segmentation performance of CL-Net^{C5} and CL-Net^{C5}_{unpruned} on five representative public datasets. The mean DSC (%) and ASD (mm) are evaluated on four CSS orders and five datasets separately for CL-Net^{C5} and CL-Net^{C5}_{unpruned}. The final parameter number of each order is also provided. nnUNet^{E5} is used as segmentation upper bound of each dataset.

	Order 1		Order 2		Order 3		Order 4		Mean		Param# (MB)↓
	DSC↑	ASD↓	DSC↑	ASD↓	DSC↑	ASD↓	DSC↑	ASD↓	DSC↑	ASD↓	
MiB ⁶⁰	6.9	67.78	15.1	66.66	77.6	2.34	20.3	49.45	30.0	46.56	31.3
PLOP ⁶¹	19.3	68.66	40.1	8.33	75.9	2.24	48.6	14.52	46.0	23.44	31.3
CSCLIP ⁶²	21.0	32.07	20.5	25.92	76.5	3.18	56.4	4.31	43.6	16.37	129
CL-Net ^{C5}	92.6	0.81	92.6	0.81	92.7	0.87	92.5	0.90	92.6	0.85	31.8

Table S7 | CSS performance comparison of CL-Net^{C5}, MiB ⁶⁰, PLOP ⁶¹, and CSCLIP ⁶² across four orders of five representative public datasets. The order-wise mean DSC (%) and ASD (mm) are evaluated on four CSS orders of five representative public datasets. The final parameter number averaged over 4 orders are also provided. CL-Net^{C5} significantly outperforms other comparison methods, with similar small parameter size as MiB and PLOP.

Pretrain Dataset	Pretrain Method	Supervision	View Augmentation	DSC \uparrow	ASD \downarrow	$\sum \mathcal{T}' \downarrow$
TotalSegmentator	Train from scratch	Bone label set train	—	92.9	1.13	58.8
	Train from scratch	Full label set train	—	94.1	0.89	38.6
	SimSiam	—	Default	88.6	1.73	328.6
	SimSiam	—	Proposed	89.6	1.28	315.8
	SimSiam	Full label set fine-tune	Default	93.0	1.17	52.4
	SimSiam	Bone label set fine-tune	Proposed	93.2	1.02	51.6
	SimSiam	Full label set fine-tune	Proposed	94.2	0.90	38.2
StructSeg19	Train from scratch	Head label set train	—	91.1	1.20	72.4
	SimSiam	Head label set fine-tune	Proposed	92.8	1.14	62.4
\mathcal{U}_4 Datasets	Train from scratch	Pseudo label train	—	94.0	1.09	56.8
	SimSiam	Sequential full label set fine-tune	Proposed	93.0	1.14	62.6
	SimSiam	EMA update	Proposed	93.0	1.13	60.6
	SimSiam	Full label set momentum update \mathcal{Q}_{128}	Proposed	93.1	1.12	58.6
	SimSiam	Full label set momentum update $\mathcal{Q}_{1,024}$	Proposed	94.2	0.86	37.2
	SimSiam	Full label set momentum update $\mathcal{Q}_{4,096}$	Proposed	94.2	0.85	36.9
\mathcal{U}_5 Datasets	SimSiam	Full label set momentum update $\mathcal{Q}_{1,024}$	Proposed	94.3	0.85	35.8

Table S8 | Impact of GE pre-training on TotalSegmentator downstream task evaluation: The ' \mathcal{U}_4 datasets' represent the union of body part-wise StructSeg19, SegTHOR, FLARE22, and KiTS21 datasets. The ' \mathcal{U}_5 datasets' represent the combined of TotalSegmentator and \mathcal{U}_4 datasets.

Pretrain Dataset	Pretrain Method	Supervision	View Augmentation	DSC \uparrow	ASD \downarrow	$\sum \mathcal{T}' \downarrow$
TotalSegmentator	Train from scratch	Full label set train	—	90.4	1.05	15.2
	SimSiam	Full label set fine-tune	Proposed	90.5	1.05	14.9
StructSeg19	Train from scratch	Head label set train	—	89.5	1.28	26.0
	SimSiam	Head label set fine-tune	Proposed	90.1	1.20	20.3
\mathcal{U}_4 Datasets	SimSiam	EMA update	Proposed	89.9	1.14	18.2
	SimSiam	Full label set momentum update $\mathcal{Q}_{1,024}$	Proposed	90.4	1.04	15.2
\mathcal{U}_5 Datasets	SimSiam	Full label set momentum update $\mathcal{Q}_{1,024}$	Proposed	90.5	1.04	14.9

Table S9 | Impact of GE pre-training on FLARE22 downstream task evaluation: The ' \mathcal{U}_4 datasets' represent the union of body part-wise StructSeg19, SegTHOR, FLARE22, and KiTS21 datasets. The ' \mathcal{U}_5 datasets' represent the combined of TotalSegmentator and \mathcal{U}_4 datasets.

Testing Dataset	GE Params	Updating Scheme	Supporting	DSC \uparrow	ASD \downarrow	$\sum \mathcal{T}' \downarrow$
TotalSegmentator	Fixed	Fine-tune	—	94.0	0.99	40.1
	Fine-tune	Fine-tune	—	94.0	0.97	38.2
	Fixed	EMA update	—	94.1	0.89	38.2
StructSeg19	Fixed	Fine-tune	—	86.2	0.28	27.3
	Fine-tune	Fine-tune	—	85.6	0.31	24.2
	Fixed	EMA update	—	86.4	0.28	24.8
SegTHOR	Fixed	Fine-tune	—	92.9	0.34	1.6
	Fine-tune	Fine-tune	—	92.6	0.33	1.6
	Fixed	EMA update	—	93.3	0.31	1.6
FLARE22	Fixed	Fine-tune	—	89.9	1.16	18.0
	Fine-tune	Fine-tune	—	90.0	1.14	15.2
	Fixed	EMA update	—	90.4	1.05	15.2
KiTS21	Fixed	Fine-tune	—	84.2	1.18	6.0
	Fine-tune	Fine-tune	—	84.6	1.20	2.0
	Fixed	EMA update	—	85.0	1.18	4.0
	Fine-tune	Fine-tune	Channel-wise	85.9	1.17	4.0
	Fixed	Fine-tune	Feature-level	86.3	1.14	2.0
	Fine-tune	EMA update	Channel-wise	86.4	1.14	2.0
	Fixed	EMA update	Feature-level	86.9	1.12	2.0

Table S10 | Impact of fine-tuning GE, EMA update, and feature-level supporting: The GE is pre-trained using SimSiam and later momentum-updated using \mathcal{U}_5 datasets. The training order of the stratified decoders follows ‘Order 1’: TotalSegmentator \rightarrow StructSeg19 \rightarrow FLARE22 \rightarrow SegTHOR \rightarrow KiTS21

	CL-Net ^{C₃₆} _{noFL-Supporting}			CL-Net ^{C₃₆}			CL-Net ^{U₃₆} _{noFL-Supporting}			CL-Net ^{U₃₆}		
	DSC	ASD	\mathcal{T}	DSC	ASD	\mathcal{T}	DSC	ASD	\mathcal{T}	DSC	ASD	\mathcal{T}
HN.LNS_1La	50.8±6.7	1.12±0.38	86.0	52.9±6.7	1.06±0.38	86.0	49.9±6.8	1.10±0.40	86.0	52.2±5.9	1.02±0.41	88.0
HN.LNS_1Lb	78.4±6.9	0.25±0.74		81.3±6.8	0.20±0.74		78.9±7.0	0.28±0.75		80.8±7.7	0.21±0.76	
HN.LNS_1Ra	54.7±6.6	1.26±0.69		55.0±6.6	1.21±0.69		54.5±6.6	1.38±0.68		56.3±5.8	1.31±0.68	
HN.LNS_1Rb	79.9±8.7	1.06±0.83		80.8±8.1	1.00±0.82		80.1±8.6	1.10±0.82		82.0±8.0	1.04±0.83	
HN.LNS_2La	70.1±5.6	1.07±0.98		71.5±5.0	0.99±0.99		70.4±5.8	0.97±0.91		72.1±6.1	0.92±0.92	
HN.LNS_2Lb	72.7±6.5	1.77±0.69		74.6±5.8	1.68±0.70		71.9±6.2	1.68±0.66		74.4±7.2	1.58±0.67	
HN.LNS_2Ra	74.0±7.1	1.96±0.39		76.6±6.7	1.91±0.38		74.3±7.0	1.87±0.38		75.5±6.7	1.78±0.37	
HN.LNS_2Rb	74.9±13.3	1.62±0.57		75.0±14.1	1.53±0.56		74.0±13.5	1.72±0.60		74.9±13.9	1.64±0.60	
HN.LNS_3L	75.6±12.3	1.57±0.76		75.9±12.3	1.52±0.75		75.7±12.4	1.50±0.78		76.1±13.0	1.40±0.78	
HN.LNS_3R	72.0±6.9	1.76±0.64		72.0±7.9	1.68±0.63		72.1±6.7	1.61±0.62		72.3±5.7	1.56±0.62	
HN.LNS_4L	76.4±6.4	1.41±0.50		77.7±5.6	1.31±0.50		76.3±6.1	1.41±0.47		76.5±5.3	1.36±0.47	
HN.LNS_4R	73.4±6.4	1.51±0.47		74.5±6.3	1.43±0.47		72.7±6.7	1.37±0.51		75.7±5.7	1.30±0.50	
HN.LNS_5La	73.0±3.3	0.99±0.56		75.1±3.5	0.90±0.55		73.8±3.4	0.94±0.57		74.2±3.0	0.88±0.57	
HN.LNS_5Lb	75.4±3.7	0.81±0.20		77.5±3.3	0.75±0.19		75.2±3.7	0.88±0.20		76.0±2.8	0.80±0.19	
HN.LNS_5Ra	77.0±3.1	0.97±0.15		78.3±3.3	0.92±0.14		76.5±2.9	0.94±0.13		78.8±3.9	0.87±0.14	
HN.LNS_5Rb	77.7±5.8	1.48±0.09		80.5±6.4	1.45±0.08		77.5±5.8	1.59±0.09		77.9±5.2	1.52±0.09	
HN.LNS_6L	51.2±14.5	1.27±0.97		52.9±15.0	1.24±0.97		51.6±14.8	1.35±0.99		53.1±14.6	1.29±0.99	
HN.LNS_6R	50.2±14.5	1.46±0.96		50.9±14.7	1.39±0.96		50.9±14.5	1.59±0.96		53.1±15.3	1.55±0.95	
Chest.LNS1_L	77.7±8.1	1.56±0.43	90.0	80.9±8.0	1.41±0.43	90.0	78.7±7.9	1.43±0.41	90.0	81.8±8.5	1.32±0.42	90.0
Chest.LNS1_R	77.7±10.1	1.78±0.60		82.0±10.1	1.68±0.60		77.1±10.2	1.85±0.61		80.2±10.2	1.69±0.61	
Chest.LNS2_L	67.2±10.7	1.40±0.48		70.6±10.7	1.22±0.48		66.7±10.7	1.36±0.49		70.6±10.7	1.25±0.49	
Chest.LNS2_R	70.5±15.5	1.48±2.41		74.7±15.5	1.31±2.41		69.9±15.5	1.47±2.27		74.8±15.5	1.34±2.27	
Chest.LNS3_A	77.7±19.7	0.96±3.46		81.3±19.7	0.78±3.46		78.3±19.4	0.95±3.61		82.9±19.4	0.77±3.61	
Chest.LNS3_P	84.7±8.4	0.81±1.14		88.8±8.4	0.62±1.14		85.1±8.3	0.72±1.09		90.1±8.3	0.60±1.09	
Chest.LNS4_L	74.3±10.3	0.96±0.91		78.0±10.3	0.85±0.91		74.7±10.3	1.02±0.92		78.0±10.3	0.86±0.92	
Chest.LNS4_R	73.7±13.4	1.49±1.00		76.8±13.4	1.36±1.00		73.6±13.3	1.58±0.99		77.9±13.3	1.48±0.99	
Chest.LNS5	72.4±12.1	1.28±0.98		71.6±12.5	1.27±0.98		73.3±11.9	1.31±0.97		72.6±12.7	1.31±0.97	
Chest.LNS6	72.5±12.1	0.79±0.95		71.8±11.2	0.79±0.95		72.8±12.2	0.75±0.97		73.6±12.9	0.75±0.97	
Chest.LNS7	85.7±16.3	0.90±1.09		86.1±15.7	0.90±1.10		86.2±16.2	0.96±1.04		86.6±15.5	0.97±1.04	
Chest.LNS8	81.6±14.2	1.67±0.40		82.5±13.7	1.68±0.41		82.5±14.4	1.64±0.42		82.2±14.9	1.64±0.42	
Chest.LNS9	62.8±17.2	1.38±1.43		62.4±16.2	1.37±1.44		62.5±17.2	1.24±1.51		62.0±17.2	1.25±1.50	
Chest.LNS10_L	74.6±19.1	1.53±1.18		78.0±20.0	1.37±1.18		73.6±19.1	1.45±1.16		77.4±19.4	1.32±1.16	
Chest.LNS10_R	73.3±13.6	1.51±1.26		77.2±12.6	1.39±1.26		73.7±13.4	1.40±1.28		77.2±13.2	1.20±1.27	
Mean	72.2	1.30	88.0	74.1	1.22	88.0	72.3	1.29	88.0	74.2	1.21	89.0

Table S11 | Impact of FL-Supporting on head & neck and chest LNS downstream task evaluation: Comparison of DSC (%) and ASD (mm) among CL-Net^{C₃₆}, CL-Net^{C₃₆}_{noFL-Supporting}, CL-Net^{U₃₆}, and CL-Net^{U₃₆}_{noFL-Supporting} for 18 head & neck LNSs and 15 chest LNSs, respectively. Decoder-wise pruning rate (\mathcal{T} , %) are also provided. The supporting structures for the head & neck LNS segmentation are Musc_Cervical_A, Musc_Scalenus, Musc_Scalenus_A, and Musc_Scleido. The supporting structures for the chest LNS segmentation are A_Aorta, Bronchus_L, Bronchus_R, Eso, and Heart³⁶. CL-Net^{C₃₆} and CL-Net^{U₃₆} achieve the best performance, demonstrating their superior segmentation capabilities when using FL-Supporting.

	nnUNet ^{E36}		CL-Net ^{U36} _{unpruned}		CL-Net ^{C36}			CL-Net ^{U36}		
	DSC↑	ASD↓	DSC↑	ASD↓	DSC↑	ASD↓	T↑	DSC↑	ASD↓	T↑
Hippocampus_L	62.4±6.1	1.99±0.25	73.5±5.9	1.27±0.23	71.8±5.9	1.44±0.22	92.0	73.6±5.8	1.25±0.21	92.0
Hippocampus_R	62.2±6.4	1.90±0.15	74.3±6.6	1.25±0.17	72.7±6.4	1.42±0.15		74.3±6.5	1.24±0.16	
TemporalLobe_L	84.4±1.0	2.18±0.06	88.1±1.4	1.53±0.10	86.6±1.4	1.70±0.10	99.0	88.1±1.3	1.51±0.08	99.5
TemporalLobe_R	83.7±1.3	2.26±0.08	87.4±1.6	1.65±0.11	86.0±1.3	1.85±0.08		87.4±1.5	1.64±0.10	
HypoThalamus	60.2±25.7	2.54±2.62	74.1±25.7	0.80±2.56	72.7±25.7	0.76±2.79	96.0	74.1±25.9	0.79±2.65	96.0
BasalGanglia_L	62.7±11.7	2.66±1.28	70.0±11.9	2.24±1.14	69.7±12.1	2.37±1.27	92.0	70.1±11.7	2.24±1.26	90.0
BasalGanglia_R	60.7±12.2	2.78±1.31	70.3±12.1	2.08±1.24	70.1±12.1	2.29±1.29		70.4±12.0	2.07±1.34	
BrainStem	91.2±1.4	0.80±0.08	93.6±1.5	0.69±0.10	93.4±1.6	0.70±0.11	99.5	93.7±1.5	0.69±0.10	99.5
Cerebellum	90.0±3.1	1.20±2.61	90.5±3.0	0.91±2.44	90.2±2.9	1.00±2.59	99.5	90.6±2.8	0.91±2.49	99.7
GlnD_Pineal	60.2±19.3	1.06±0.50	70.7±19.0	0.60±0.48	70.4±19.5	0.60±0.53	90.0	70.6±19.1	0.59±0.49	92.0
Brain	96.7±2.8	0.59±2.02	98.3±2.9	0.27±2.04	98.2±2.9	0.29±1.93	99.5	98.3±2.8	0.26±2.13	99.5
GlnD_Pituitary	75.0±6.3	0.81±0.19	85.1±6.7	0.50±0.24	83.8±6.6	0.52±0.22	98.0	85.1±6.6	0.49±0.22	98.0
Lens_L	78.6±9.7	0.57±0.16	82.4±9.7	0.50±0.17	81.5±9.7	0.53±0.17	99.0	82.5±9.7	0.50±0.16	99.0
Lens_R	80.4±9.4	0.48±0.44	86.3±9.1	0.43±0.41	84.2±9.1	0.40±0.41		86.2±9.2	0.42±0.42	
Chiasm	62.5±12.9	1.42±0.13	74.3±13.0	0.69±0.14	72.7±13.1	0.82±0.14	94.0	74.3±13.0	0.68±0.14	96.0
OpticNerve_L	67.6±8.2	0.78±0.30	78.3±7.9	0.57±0.27	77.7±7.8	0.56±0.27	98.0	78.4±8.0	0.56±0.28	99.0
OpticNerve_R	66.8±6.4	0.81±0.21	79.6±6.4	0.56±0.21	79.2±6.6	0.59±0.23		79.6±6.3	0.55±0.20	
Eye_L	85.7±1.3	0.82±0.08	88.4±1.3	0.61±0.08	86.4±1.3	0.63±0.08	99.5	88.4±1.2	0.61±0.07	99.0
Eye_R	87.7±4.0	0.55±0.09	87.6±4.2	0.56±0.11	86.6±4.4	0.60±0.13		87.7±4.1	0.56±0.10	
GlnD_Lacrimal_L	68.1±12.6	1.05±0.74	72.6±12.7	0.60±0.75	70.8±12.5	0.59±0.72	98.0	72.6±12.6	0.58±0.74	98.0
GlnD_Lacrimal_R	67.1±15.5	1.37±0.88	72.7±15.1	0.65±0.85	70.6±15.3	0.61±0.86		72.7±15.2	0.65±0.86	
Ear_Inner_L	82.8±9.4	0.57±0.36	88.1±9.2	0.59±0.35	86.4±9.3	0.58±0.35	99.5	88.2±9.4	0.58±0.36	99.5
Ear_Inner_R	83.0±9.1	0.58±0.28	86.9±9.0	0.59±0.28	86.5±9.3	0.61±0.30		86.9±9.2	0.58±0.30	
Ear_Mid_L	85.1±3.8	0.97±0.05	91.2±3.6	0.65±0.03	89.1±3.9	0.67±0.05	99.5	91.2±3.6	0.63±0.03	99.5
Ear_Mid_R	85.0±3.4	0.94±0.06	90.3±3.2	0.62±0.04	88.9±3.2	0.60±0.04		90.3±3.2	0.62±0.04	
Ear_Cochlea_L	67.2±10.4	0.47±0.23	73.2±10.2	0.35±0.21	72.4±10.6	0.36±0.24	96.0	73.2±10.4	0.34±0.22	94.0
Ear_Cochlea_R	67.2±11.4	0.47±0.26	71.5±11.2	0.48±0.24	69.5±11.3	0.45±0.25		71.5±11.2	0.46±0.24	
GlnD_Parotid_L	85.6±1.9	1.05±0.16	87.4±1.9	0.97±0.16	85.8±1.9	0.99±0.16	99.0	87.4±2.1	0.97±0.18	99.5
GlnD_Parotid_R	85.7±3.3	1.09±0.51	86.3±3.4	1.11±0.52	85.8±3.6	1.05±0.54		86.4±3.4	1.09±0.52	
GlnD_Submand_L	76.9±7.5	1.24±0.98	82.0±7.5	0.90±0.99	80.3±7.4	0.91±0.99	98.0	81.9±7.5	0.88±0.99	98.0
GlnD_Submand_R	76.1±8.4	1.20±0.44	78.2±8.4	1.01±0.44	77.6±8.4	1.18±0.44		78.1±8.6	1.01±0.46	
GlnD_Thyroid_L	81.2±4.4	0.85±0.26	81.8±4.4	0.78±0.25	81.6±4.8	0.74±0.29	94.0	81.8±4.6	0.77±0.27	94.0
GlnD_Thyroid_R	80.5±4.4	0.97±0.23	83.3±4.2	0.77±0.21	82.2±4.0	0.75±0.19		83.4±4.3	0.75±0.21	
OralCavity	76.3±1.9	2.40±0.15	79.5±1.8	4.35±0.13	77.8±1.9	4.47±0.15	96.0	79.5±1.8	4.33±0.14	96.0
TMJ_L	77.2±9.5	0.65±0.24	78.3±9.5	0.61±0.23	77.6±9.6	0.67±0.24	94.0	78.4±9.6	0.61±0.24	94.0
TMJ_R	75.2±7.7	0.75±0.21	76.6±7.4	0.71±0.18	76.2±7.5	0.70±0.19		76.7±7.4	0.70±0.18	
Bone_ET_L	77.0±12.7	0.43±0.15	82.8±13.1	0.41±0.19	82.5±12.8	0.42±0.16	99.5	82.9±13.0	0.40±0.18	99.5
Bone_ET_R	89.8±10.0	0.37±0.14	95.6±10.1	0.31±0.15	95.3±10.1	0.31±0.15		95.6±10.1	0.31±0.15	
Bone_Mandible_L	90.2±2.0	0.50±0.07	92.1±2.3	0.43±0.09	91.7±2.3	0.40±0.09	99.7	92.1±2.3	0.41±0.09	99.7
Bone_Mandible_R	90.8±2.3	0.45±0.06	91.4±2.5	0.45±0.08	91.1±2.4	0.43±0.07		91.3±2.4	0.44±0.07	
Musc_Masster_L	82.5±6.0	1.15±1.11	84.1±5.9	0.91±1.06	83.5±6.0	1.05±1.19	99.5	84.1±5.8	0.91±1.14	99.5
Musc_Masster_R	81.2±6.4	1.28±1.07	81.9±6.4	1.19±0.97	81.6±6.4	1.25±1.12		81.9±6.3	1.19±1.04	
Epiglottis	68.1±8.9	1.33±6.01	71.1±9.2	1.04±5.85	70.7±9.0	1.25±5.79	99.5	71.0±9.0	1.02±6.17	99.5
Musc_Const_I	70.2±5.9	1.10±0.49	74.8±6.1	0.98±0.50	74.2±5.9	1.03±0.49	99.0	74.7±5.9	0.98±0.49	99.0
Musc_Const_M	63.5±8.4	1.71±0.41	68.1±8.6	1.60±0.43	66.4±8.3	1.63±0.40		68.0±8.7	1.59±0.43	
Musc_Const_S	61.2±7.5	1.86±1.22	62.4±7.7	1.63±1.03	62.0±7.6	1.85±1.15		62.4±7.5	1.63±1.12	
Larynx_Glottic	68.0±3.4	1.67±0.18	70.7±3.3	1.52±0.17	69.4±3.3	1.68±0.17	94.0	70.8±3.3	1.50±0.17	94.0
Larynx_Supraglot	65.3±7.9	1.62±0.39	67.7±8.0	1.44±0.40	65.8±8.0	1.63±0.40		67.7±8.1	1.43±0.42	
Larynx	71.3±5.5	1.46±0.18	75.7±5.6	1.45±0.20	73.8±5.7	1.44±0.21		75.6±5.5	1.45±0.18	
Bone_Skull	83.1±35.4	3.91±0.20	82.2±35.5	1.44±0.22	82.0±35.3	1.34±0.20	99.0	82.5±35.4	3.66±0.21	99.0
Bone_Clavicula_L	94.5±0.8	0.6±0.10	94.9±0.7	0.30±0.09	94.7±0.8	0.30±0.10	99.7	95.2±0.9	0.45±0.11	99.5
Bone_Clavicula_R	98.4±16.1	0.53±0.21	96.8±16.1	0.48±0.21	96.7±15.8	0.51±0.18		98.3±16.0	1.37±0.20	
Mean	76.8	1.15	81.3	0.94	80.3	0.99	97.3	81.3	0.94	97.4

Table S12 | Organ-wise segmentation performance comparison on head & neck region. Comparison of DSC (%) and ASD (mm) among nnUNet^{E36}, CL-Net^{U36}_{unpruned}, CL-Net^{C36}, and CL-Net^{U36} for 52 head & neck structures. Decoder-wise pruning rate (\mathcal{T} , %) of CL-Net^{C36} and CL-Net^{U36} are also provided. CL-Net^{U36} achieves high mean DSC, with only 0.1% gap to top, and the lowest mean ASD, demonstrating its superior performance in the head & neck region.

	nnUNet ^{E₃₆}		CL-Net ^{U₃₆} _{unpruned}		CL-Net ^{C₃₆}			CL-Net ^{U₃₆}		
	DSC↑	ASD↓	DSC↑	ASD↓	DSC↑	ASD↓	T↑	DSC↑	ASD↓	T↑
BrachialPlexus_L	41.7±9.0	3.20±0.71	56.8±8.9	2.83±0.73	56.8±8.9	2.87±0.70	90.0	56.9±8.9	2.81±0.74	90.0
BrachialPlexus_R	40.5±8.3	3.20±0.64	52.9±8.5	2.18±0.68	52.8±8.3	2.27±0.63		53.0±8.4	2.17±0.66	
Bone_Humerus_L	96.9±17.5	0.54±0.20	97.1±17.9	0.53±0.24	97.1±17.9	0.50±0.24	99.7	97.1±17.9	0.52±0.24	99.7
Bone_Humerus_R	93.9±17.2	0.34±0.19	94.0±17.2	0.33±0.19	93.8±17.2	0.33±0.19		94.0±17.2	0.32±0.20	
Bone_Scapula_L	95.3±21.4	0.19±0.18	95.3±21.2	0.17±0.16	95.3±21.2	0.15±0.16	99.0	95.4±21.1	0.16±0.14	99.0
Bone_Scapula_R	93.1±1.8	0.32±0.07	93.4±1.9	0.28±0.08	93.4±1.9	0.27±0.08		93.5±1.8	0.28±0.07	
Eso	86.0±11.9	0.66±4.95	85.9±11.8	0.55±5.07	85.9±11.7	0.53±4.73	96.0	86.0±11.6	0.55±5.21	98.0
A_Aorta_Arch	89.0±5.1	2.13±0.18	91.8±4.7	2.15±0.15	91.8±5.0	2.01±0.17	99.0	91.9±4.9	2.14±0.17	99.0
A_Aorta_Ascending	90.5±2.7	1.80±0.29	91.4±2.5	1.81±0.28	91.4±2.8	1.66±0.30		91.5±2.7	1.79±0.29	
A_Aorta_Descending	94.3±2.9	0.90±0.54	95.6±2.9	0.76±0.55	95.3±3.1	0.75±0.55		95.5±2.9	0.74±0.55	
A_Pulmonary	89.7±2.9	0.94±0.19	94.6±3.4	0.81±0.21	94.5±3.0	0.84±0.20	99.7	94.6±3.3	0.80±0.20	99.7
A_CommonCarotid_L	86.3±7.5	1.00±3.88	88.3±7.7	0.90±3.58	88.2±7.8	0.88±3.74	99.7	88.3±7.6	0.89±3.83	99.7
A_CommonCarotid_R	81.9±9.7	0.69±3.56	86.0±9.3	0.57±3.42	86.0±9.6	0.55±3.47		86.1±9.8	0.55±3.72	
A_Subclavian_L	77.0±8.6	2.75±28.19	78.8±8.7	2.29±24.81	78.6±8.9	2.63±28.08	99.7	78.7±8.7	2.27±26.56	99.7
A_Subclavian_R	83.0±5.8	1.35±6.93	87.2±5.7	1.27±6.16	87.1±5.6	1.20±6.92		87.2±5.8	1.26±6.68	
A_Vertebral_L	57.1±16.7	2.51±2.84	65.5±16.7	1.86±2.68	65.3±16.8	2.11±2.94	99.0	65.4±16.5	1.86±2.93	99.0
A_Vertebral_R	56.4±16.0	2.98±2.35	67.0±16.1	2.30±2.11	66.8±16.3	2.27±2.31		66.9±16.1	2.29±2.15	
A_BrachiocephalicTrunk	89.8±16.2	0.32±0.43	98.3±16.3	0.64±0.44	98.2±16.2	0.61±0.44	99.0	90.8±16.3	0.22±0.44	99.0
V_Azygos	81.3±6.6	1.24±0.49	83.7±6.7	1.25±0.53	83.5±6.8	1.10±0.51	96.0	83.7±6.7	1.23±0.53	96.0
V_Brachiocephalic_L	90.3±5.0	0.45±0.12	92.5±5.2	0.37±0.14	92.4±5.1	0.30±0.13	99.5	92.5±5.2	0.36±0.14	99.5
V_Brachiocephalic_R	88.6±5.9	0.62±0.28	90.0±5.8	0.46±0.25	89.8±5.8	0.50±0.27		90.0±5.8	0.45±0.25	
V_InternalJuguar_L	83.2±13.9	0.75±1.56	83.3±14.1	0.60±1.63	83.2±13.7	0.61±1.64	99.5	83.3±13.9	0.58±1.69	99.5
V_InternalJuguar_R	83.5±12.4	2.83±1.76	87.3±12.1	2.87±1.62	87.2±12.2	2.70±1.77		87.4±12.0	2.86±1.69	
V_Pulmonary	68.9±6.3	2.24±1.16	75.2±6.3	1.37±1.10	75.1±6.3	1.31±1.20	98.0	75.3±6.3	1.36±1.18	99.0
V_Subclavian_L	77.0±14.2	2.75±8.88	81.2±14.2	2.49±8.61	81.1±14.2	2.63±8.93	94.0	81.2±14.2	2.47±8.62	94.0
V_Subclavian_R	83.0±11.9	1.35±8.56	85.1±12.0	1.58±8.51	84.9±12.2	1.25±8.80		85.1±12.1	1.58±8.92	
V_VenaCava_I	83.3±7.5	1.64±0.47	83.8±7.4	1.46±0.49	83.7±7.5	1.53±0.47	99.0	83.9±7.4	1.45±0.48	99.0
V_VenaCava_S	90.2±4.5	0.88±0.26	92.1±4.2	0.76±0.26	91.9±4.4	0.78±0.25	99.0	92.1±4.1	0.75±0.25	99.0
V_Portal_Splenic	86.3±29.0	0.25±0.62	89.2±29.3	0.14±0.63	89.1±29.2	0.14±0.63	98.0	89.2±29.2	0.13±0.62	98.0
Trachea	90.4±2.6	0.78±2.10	92.9±2.3	0.69±2.05	92.7±2.5	0.68±2.02	99.7	92.9±2.5	0.67±2.08	99.7
Bronchus_L	83.4±7.3	0.72±1.13	84.6±6.8	0.61±1.16	84.5±7.1	0.57±1.15		84.7±7.0	0.59±1.19	
Bronchus_R	81.2±11.3	0.98±1.44	84.1±11.4	0.93±1.34	84.0±11.5	0.87±1.36		84.2±11.5	0.92±1.42	
Lung_L	97.5±0.7	0.75±0.33	98.4±0.6	0.63±0.31	98.5±0.7	0.61±0.32	99.5	98.5±0.6	0.61±0.31	99.5
Lung_R	97.9±0.7	0.60±0.12	98.5±0.8	0.51±0.13	98.5±0.4	0.47±0.08		98.5±0.6	0.50±0.11	
ChestWall_L	90.4±2.5	1.40±1.19	95.6±2.7	1.35±1.24	95.3±2.5	1.29±1.25	99.5	95.5±2.6	1.35±1.30	99.5
ChestWall_R	91.8±2.5	0.80±1.05	93.1±2.5	0.63±0.99	93.0±2.5	0.69±1.06		93.1±2.5	0.63±1.09	
Lung_LUL	97.8±3.6	0.31±0.93	98.2±3.8	0.57±0.61	98.2±3.9	0.62±0.64	99.5	97.9±3.7	0.17±0.62	99.7
Lung_LLL	96.5±24.0	0.21±0.98	97.9±2.0	0.46±0.47	98.1±2.0	0.45±0.46		96.5±2.1	0.21±0.47	
Lung_RUL	97.5±20.5	0.79±0.95	96.6±2.4	0.70±0.97	96.6±2.4	0.67±0.98	99.5	97.7±2.4	0.69±0.98	99.5
Lung_RML	92.0±6.2	0.47±1.41	98.6±3.2	0.60±1.41	98.4±3.3	0.61±1.48		92.3±3.3	0.22±1.50	
Lung_RLL	97.4±26.8	0.16±2.45	96.9±3.5	0.47±1.07	96.7±3.5	0.45±1.20		97.2±3.6	0.21±1.19	
Heart	94.2±1.8	1.62±0.22	97.4±1.8	1.35±0.20	97.4±1.7	1.48±0.21	99.0	97.4±1.7	1.34±0.20	99.0
Myocardium	92.5±1.7	1.62±0.21	91.6±1.4	1.59±0.18	91.5±1.6	1.51±0.21	99.7	91.7±1.6	1.58±0.19	99.7
Atrium_L	92.6±1.8	1.70±0.22	95.3±1.9	1.68±0.22	95.2±1.5	1.56±0.19	99.5	95.3±1.8	1.68±0.20	99.5
Ventricle_L	95.2±1.5	1.70±0.20	96.1±1.6	1.47±0.21	96.0±1.6	1.58±0.20		96.2±1.6	1.45±0.21	
Atrium_R	96.0±1.7	1.65±0.21	97.1±1.9	1.29±0.24	96.9±1.6	1.51±0.20		97.1±1.8	1.27±0.23	
Ventricle_R	94.4±1.7	1.69±0.22	94.8±1.9	1.64±0.24	94.6±1.6	1.55±0.20		94.7±1.8	1.62±0.23	
Pericardium	95.6±1.7	1.52±0.21	94.9±1.8	1.49±0.22	94.7±1.9	1.40±0.22	99.0	94.9±1.8	1.48±0.22	99.0
LAA	92.6±3.4	0.46±0.15	93.3±3.4	0.79±0.14	93.2±3.6	0.78±0.18	99.7	91.7±3.3	0.16±0.15	99.5
Musc_Cervical_A	70.0±15.0	1.15±2.70	72.7±15.1	0.99±2.55	72.6±15.0	1.03±2.82	96.0	72.8±15.0	0.97±2.76	96.0
Musc_Scalenus	75.9±4.7	1.09±0.28	76.3±4.3	1.02±0.27	76.2±4.8	0.98±0.29	99.0	76.3±4.5	1.01±0.28	99.0
Musc_Scalenus_A	78.0±5.7	0.95±0.34	81.8±5.9	0.73±0.36	81.5±5.7	0.84±0.34		81.7±5.9	0.72±0.36	
Musc_Scleido	82.4±2.9	0.99±0.21	83.5±2.9	0.79±0.20	83.3±2.6	0.88±0.17	99.5	83.5±2.8	0.79±0.19	99.5
Musc_Autochthon_L	94.2±0.8	0.37±0.11	97.7±0.9	1.84±0.10	97.6±0.8	1.99±0.11	99.0	93.9±0.9	0.32±0.12	99.0
Musc_Autochthon_R	94.6±0.8	0.41±0.12	97.7±0.8	1.79±0.12	97.8±0.8	1.93±0.10		94.8±0.8	0.41±0.11	
SpinalCord	91.7±3.0	0.86±0.25	94.4±3.2	0.68±0.24	94.2±3.3	0.72±0.27	99.7	94.4±3.2	0.67±0.25	99.7
Mean	86.1	1.29	88.6	1.12	88.5	1.13	98.6	88.6	1.11	98.6

Table S13 | Organ-wise segmentation performance comparison on thoracic region. Comparison of DSC (%) and ASD (mm) among nnUNet^{E₃₆}, CL-Net^{U₃₆}_{unpruned}, CL-Net^{C₃₆}, and CL-Net^{U₃₆} for 56 thoracic structures. Decoder-wise pruning rate (\mathcal{T} , %) of CL-Net^{C₃₆} and CL-Net^{U₃₆} are also provided. CL-Net^{U₃₆} achieves the highest mean DSC and the lowest mean ASD, demonstrating its superior performance in the thoracic region.

	nnUNet ^{E₃₆}		CL-Net ^{U₃₆_{unpruned}}		CL-Net ^{C₃₆}		$\mathcal{T}\uparrow$	CL-Net ^{U₃₆}		
	DSC \uparrow	ASD \downarrow	DSC \uparrow	ASD \downarrow	DSC \uparrow	ASD \downarrow		DSC \uparrow	ASD \downarrow	$\mathcal{T}\uparrow$
Kidney_R	93.9 \pm 6.8	1.20 \pm 0.73	95.2 \pm 6.9	0.98 \pm 0.74	95.0 \pm 7.1	1.06 \pm 0.76	99.3	95.2 \pm 7.0	0.97 \pm 0.75	99.7
Kidney_L	95.0 \pm 6.6	1.45 \pm 0.69	94.3 \pm 6.9	1.30 \pm 0.72	94.2 \pm 6.7	1.35 \pm 0.70		94.3 \pm 6.8	1.30 \pm 0.71	
Spleen	97.2 \pm 6.8	0.20 \pm 0.39	98.2 \pm 6.7	0.10 \pm 0.38	98.3 \pm 6.9	0.10 \pm 0.40	99.5	98.2 \pm 6.6	0.10 \pm 0.37	99.5
Liver	97.6 \pm 5.8	0.82 \pm 1.00	97.9 \pm 6.1	0.69 \pm 0.93	97.8 \pm 5.7	0.72 \pm 0.99	99.3	97.9 \pm 5.9	0.67 \pm 0.91	99.5
HepaticVessel	65.3 \pm 9.4	2.40 \pm 3.79	68.1 \pm 9.5	2.24 \pm 3.30	66.5 \pm 9.3	2.25 \pm 3.63	94.0	68.1 \pm 9.5	2.22 \pm 3.46	94.0
GlnD_Adrenal_R	90.2 \pm 13.2	0.22 \pm 0.39	90.5 \pm 13.1	0.10 \pm 0.38	90.4 \pm 13.5	0.09 \pm 0.42	96.0	90.5 \pm 13.3	0.08 \pm 0.39	98.0
GlnD_Adrenal_L	86.5 \pm 12.6	0.36 \pm 0.39	87.8 \pm 12.7	0.21 \pm 0.41	86.0 \pm 12.3	0.21 \pm 0.36		87.8 \pm 12.6	0.20 \pm 0.39	
Pancreas	93.0 \pm 7.1	0.74 \pm 0.39	95.0 \pm 7.0	0.62 \pm 0.38	94.9 \pm 6.8	0.62 \pm 0.36	99.3	95.1 \pm 7.1	0.61 \pm 0.39	99.5
GallBladder	82.2 \pm 8.6	2.13 \pm 0.82	85.7 \pm 8.6	1.87 \pm 0.82	83.7 \pm 8.7	2.02 \pm 0.83	99.3	85.6 \pm 8.6	1.85 \pm 0.82	99.5
Stomach	92.1 \pm 6.5	1.18 \pm 0.68	92.5 \pm 6.1	0.99 \pm 0.65	92.3 \pm 6.3	1.07 \pm 0.67	99.3	92.4 \pm 6.3	0.98 \pm 0.66	99.5
Duodenum	80.8 \pm 15.9	2.40 \pm 1.30	82.8 \pm 16.0	2.10 \pm 1.25	81.8 \pm 15.8	2.30 \pm 1.29	99.5	82.8 \pm 16.2	2.09 \pm 1.28	99.5
SmallBowel	91.7 \pm 16.3	2.32 \pm 2.60	91.3 \pm 16.5	2.08 \pm 2.36	91.2 \pm 16.4	2.17 \pm 2.65	98.0	91.3 \pm 16.5	2.06 \pm 2.62	99.5
Colon	91.6 \pm 15.8	3.01 \pm 1.22	92.9 \pm 15.9	2.65 \pm 1.15	92.7 \pm 15.8	2.87 \pm 1.21	99.0	92.9 \pm 16.0	2.64 \pm 1.27	99.5
Rectum	84.6 \pm 6.8	3.25 \pm 1.48	84.8 \pm 6.7	3.03 \pm 1.56	84.8 \pm 7.0	3.11 \pm 1.55		84.9 \pm 6.7	3.02 \pm 1.57	
UrinaryBladder	92.2 \pm 9.7	1.87 \pm 1.06	94.0 \pm 9.5	1.77 \pm 0.97	93.8 \pm 9.5	1.75 \pm 0.99	98.0	93.9 \pm 9.4	1.75 \pm 1.04	98.0
Prostate	84.3 \pm 18.0	3.65 \pm 1.41	84.8 \pm 17.8	3.42 \pm 1.42	84.6 \pm 17.7	3.52 \pm 1.43	96.0	84.7 \pm 18.0	3.42 \pm 1.43	96.0
A_Iliac_L	94.4 \pm 3.1	0.61 \pm 0.19	91.1 \pm 3.3	0.29 \pm 0.20	90.9 \pm 3.2	0.30 \pm 0.19	99.0	95.1 \pm 3.3	0.50 \pm 0.20	99.5
A_Iliac_R	91.9 \pm 19.5	0.45 \pm 0.15	90.9 \pm 19.4	0.20 \pm 0.16	90.8 \pm 19.5	0.20 \pm 0.17		91.9 \pm 19.6	0.39 \pm 0.18	
V_Iliac_L	92.2 \pm 3.0	0.48 \pm 0.13	93.1 \pm 3.2	0.26 \pm 0.14	93.0 \pm 3.0	0.27 \pm 0.12	99.7	92.9 \pm 3.3	0.43 \pm 0.15	99.0
V_Iliac_R	94.2 \pm 4.9	0.44 \pm 0.31	92.2 \pm 5.0	0.23 \pm 0.29	92.0 \pm 4.9	0.23 \pm 0.28		93.6 \pm 4.8	0.45 \pm 0.27	
Musc_GluteusMax_L	98.9 \pm 5.2	0.84 \pm 1.41	97.2 \pm 5.5	0.40 \pm 1.33	97.2 \pm 5.3	0.44 \pm 1.48	99.5	98.7 \pm 5.4	0.76 \pm 1.50	99.5
Musc_GluteusMax_R	98.1 \pm 2.0	0.93 \pm 0.34	97.8 \pm 1.8	0.38 \pm 0.31	97.9 \pm 2.1	0.39 \pm 0.33		97.9 \pm 2.2	0.71 \pm 0.34	
Musc_GluteusMed_L	98.2 \pm 1.5	0.43 \pm 0.22	97.8 \pm 1.3	0.29 \pm 0.21	97.6 \pm 1.6	0.31 \pm 0.24	99.5	98.4 \pm 1.5	0.45 \pm 0.23	99.7
Musc_GluteusMed_R	97.6 \pm 7.3	0.74 \pm 0.22	97.1 \pm 7.5	0.32 \pm 0.21	96.9 \pm 7.5	0.32 \pm 0.21		97.3 \pm 7.5	0.47 \pm 0.21	
Musc_GluteusMin_L	97.1 \pm 2.3	0.56 \pm 0.16	96.1 \pm 2.5	0.27 \pm 0.18	96.0 \pm 2.3	0.28 \pm 0.16	99.5	97.3 \pm 2.2	0.42 \pm 0.16	99.7
Musc_GluteusMin_R	98.0 \pm 1.1	0.39 \pm 0.08	94.1 \pm 1.2	0.19 \pm 0.11	94.0 \pm 1.3	0.19 \pm 0.11		98.2 \pm 1.1	0.36 \pm 0.10	
Musc_Iliopsoas_L	94.3 \pm 19.7	0.37 \pm 0.18	94.0 \pm 19.5	0.21 \pm 0.18	94.0 \pm 19.5	0.20 \pm 0.18	99.0	93.5 \pm 19.5	0.36 \pm 0.19	99.5
Musc_Iliopsoas_R	95.0 \pm 9.1	0.39 \pm 0.27	94.5 \pm 9.3	0.18 \pm 0.26	94.4 \pm 9.1	0.18 \pm 0.24		94.9 \pm 9.1	0.21 \pm 0.25	
Bone_Hip_L	96.6 \pm 1.6	0.32 \pm 0.13	99.0 \pm 1.9	0.25 \pm 0.14	98.7 \pm 1.8	0.26 \pm 0.12	99.5	97.0 \pm 1.9	0.29 \pm 0.14	99.5
Bone_Hip_R	95.9 \pm 31.6	0.34 \pm 0.10	98.5 \pm 31.7	0.28 \pm 0.09	98.6 \pm 31.6	0.26 \pm 0.08		97.0 \pm 31.9	0.27 \pm 0.11	
Bone_Femur_L	97.4 \pm 15.4	3.51 \pm 0.29	90.2 \pm 0.7	5.51 \pm 0.11	90.1 \pm 0.6	5.66 \pm 0.10	99.5	97.5 \pm 0.7	3.28 \pm 0.11	99.7
Bone_Femur_R	95.8 \pm 0.5	6.85 \pm 0.08	95.2 \pm 0.2	6.32 \pm 0.06	95.2 \pm 0.5	5.77 \pm 0.09		95.3 \pm 0.4	6.26 \pm 0.06	
Body Mask	97.0 \pm 2.9	2.20 \pm 1.31	97.2 \pm 2.8	2.29 \pm 1.11	97.1 \pm 2.7	2.33 \pm 1.27	99.5	97.1 \pm 2.8	2.50 \pm 1.24	99.5
Mean	91.6	1.40	92.5	1.27	92.2	1.30	98.6	92.5	1.27	98.9

Table S14 | Organ-wise segmentation performance comparison on abdomen region. Comparison of DSC (%) and ASD (mm) among nnUNet^{E₃₆}, CL-Net^{U₃₆_{unpruned}}, CL-Net^{C₃₆}, and CL-Net^{U₃₆} for 32 abdomen structures. Decoder-wise pruning rate (\mathcal{T} , %) of CL-Net^{C₃₆} and CL-Net^{U₃₆} are also provided. CL-Net^{U₃₆} achieves the highest mean DSC and the lowest mean ASD, demonstrating its superior performance in the abdomen region.

	nnUNet ^{E36}		CL-Net ^{U36} _{unpruned}		CL-Net ^{C36}			CL-Net ^{U36}		
	DSC↑	ASD↓	DSC↑	ASD↓	DSC↑	ASD↓	T↑	DSC↑	ASD↓	T↑
Bone_Rib1_L	93.6±3.5	0.16±0.23	94.0±3.1	0.15±0.19	93.8±3.1	0.15±0.19	96.0	94.0±3.1	0.15±0.19	96.0
Bone_Rib2_L	89.9±1.6	0.95±0.97	90.8±1.6	0.85±0.90	90.8±1.6	0.91±0.94		90.9±1.7	0.85±0.92	
Bone_Rib3_L	94.7±17.2	0.91±1.04	94.8±17.3	0.84±1.00	94.6±17.0	0.87±1.09		94.7±17.1	0.84±1.05	
Bone_Rib4_L	94.5±18.7	0.76±1.74	95.4±19.0	0.74±1.75	95.3±19.0	0.72±1.79		95.4±18.9	0.73±1.79	
Bone_Rib5_L	94.2±29.3	1.52±4.82	94.1±29.4	1.44±4.49	94.0±29.3	1.48±4.82		94.2±29.3	1.42±4.79	
Bone_Rib6_L	93.2±24.2	1.64±3.35	93.3±24.1	1.47±3.10	93.1±23.9	1.59±3.49		93.3±24.2	1.45±3.20	
Bone_Rib7_L	94.5±20.5	2.71±4.19	95.2±20.9	2.66±3.81	95.1±20.7	2.66±3.96		95.2±20.8	2.64±4.18	
Bone_Rib8_L	94.6±20.8	4.29±4.04	95.1±21.0	4.34±4.16	95.0±21.0	4.27±4.05		95.2±21.0	4.34±4.20	
Bone_Rib9_L	94.0±19.3	2.83±4.83	95.1±19.5	2.95±4.70	95.0±19.4	2.81±4.84		95.1±19.5	2.94±5.17	
Bone_Rib10_L	93.0±13.1	1.51±6.56	93.6±13.2	1.37±6.44	93.5±13.2	1.48±6.60		93.6±13.2	1.35±6.80	
Bone_Rib11_L	93.0±12.1	0.36±8.12	93.0±12.3	0.41±7.70	92.8±12.1	0.34±8.73		92.9±12.3	0.41±8.26	
Bone_Rib12_L	94.2±16.3	0.54±0.40	94.2±16.3	0.52±0.41	94.1±16.4	0.51±0.41		94.2±16.4	0.50±0.42	
Bone_Rib1_R	91.2±5.7	0.11±0.16	91.3±5.9	0.10±0.18	91.2±5.5	0.08±0.15		91.3±5.8	0.08±0.17	
Bone_Rib2_R	94.5±3.4	0.23±0.92	94.3±3.6	0.20±0.93	94.2±3.6	0.19±0.93		94.4±3.6	0.19±0.93	
Bone_Rib3_R	92.8±9.0	0.48±1.13	93.6±9.2	0.48±1.10	93.5±8.9	0.45±1.07		93.7±9.1	0.47±1.13	
Bone_Rib4_R	90.5±18.7	0.83±1.86	90.3±18.7	0.77±1.82	90.3±18.6	0.80±1.89		90.4±18.8	0.77±1.94	
Bone_Rib5_R	90.3±16.4	1.70±2.58	90.7±16.4	1.67±2.38	90.5±16.5	1.69±2.46		90.7±16.3	1.66±2.56	
Bone_Rib6_R	93.4±13.1	1.52±2.43	93.6±13.1	1.38±2.35	93.5±13.1	1.47±2.54		93.6±13.0	1.37±2.52	
Bone_Rib7_R	94.2±21.2	1.56±3.51	95.0±21.1	1.42±3.27	94.9±21.2	1.53±3.33		95.1±21.3	1.41±3.60	
Bone_Rib8_R	95.5±18.1	1.88±4.26	95.9±17.9	1.78±4.08	95.9±18.1	1.83±4.23		96.0±18.1	1.76±4.15	
Bone_Rib9_R	95.9±21.4	2.48±3.21	96.4±21.4	2.46±3.16	96.3±21.3	2.47±3.42		96.5±21.3	2.46±3.48	
Bone_Rib10_R	96.3±23.3	2.50±7.32	96.8±23.4	2.41±7.03	96.6±23.3	2.46±7.19		96.8±23.2	2.41±7.18	
Bone_Rib11_R	96.4±22.9	1.85±6.92	96.5±23.0	1.71±6.64	96.5±22.8	1.81±6.79		96.6±22.9	1.70±6.82	
Bone_Rib12_R	97.1±27.2	0.63±0.08	96.8±27.2	0.63±0.08	96.7±27.1	0.61±0.07		96.8±27.3	0.62±0.09	
Bone_Sternum	94.1±5.7	0.63±0.55	95.1±5.7	0.59±0.55	95.0±5.8	0.62±0.56	99.0	95.2±5.8	0.59±0.56	99.0
Bone_CostalCartilages	88.7±5.0	0.18±0.74	88.3±5.0	0.16±0.74	88.2±5.2	0.14±0.76	99.5	88.4±5.0	0.05±0.75	99.5
Bone_Vert_C1	93.4±14.4	0.25±0.24	93.3±14.3	0.23±0.24	93.2±14.5	0.21±0.25	96.0	93.4±14.2	0.22±0.22	96.0
Bone_Vert_C2	94.5±12.8	0.25±0.14	95.5±13.0	0.25±0.16	95.3±12.8	0.24±0.15		95.5±12.9	0.25±0.16	
Bone_Vert_C3	98.0±0.8	0.31±0.04	98.4±0.9	0.26±0.05	98.2±1.0	0.27±0.06		98.4±0.8	0.26±0.04	
Bone_Vert_C4	98.1±28.0	0.16±0.04	98.6±28.0	0.08±0.05	98.6±28.0	0.11±0.05		98.7±28.0	0.08±0.05	
Bone_Vert_C5	97.0±22.8	0.34±0.37	97.0±22.8	0.31±0.37	96.9±23.0	0.29±0.39		97.0±22.9	0.29±0.38	
Bone_Vert_C6	96.8±8.9	0.22±0.20	96.6±8.9	0.21±0.20	96.5±9.1	0.21±0.22		96.6±8.9	0.20±0.20	
Bone_Vert_C7	95.0±2.4	0.60±0.19	95.4±2.4	0.58±0.19	95.2±2.7	0.56±0.22		95.4±2.4	0.58±0.19	
Bone_Vert_L1	95.2±10.5	0.41±0.94	95.4±10.6	0.27±0.94	95.3±10.3	0.37±0.92		95.4±10.6	0.27±0.94	
Bone_Vert_L2	95.7±17.5	1.27±1.71	95.8±17.5	1.23±1.53	95.6±17.2	1.22±1.69		95.7±17.4	1.22±1.64	
Bone_Vert_L3	94.8±19.4	0.29±3.44	95.1±19.9	0.26±3.13	94.9±19.6	0.25±3.61		95.0±19.7	0.26±3.33	
Bone_Vert_L4	96.0±15.6	0.24±3.49	95.7±15.6	0.21±3.14	95.5±15.3	0.21±3.38		95.6±15.5	0.21±3.19	
Bone_Vert_L5	94.1±10.7	0.43±0.48	94.6±10.6	0.42±0.48	94.6±10.8	0.40±0.49		94.5±10.7	0.40±0.49	
Bone_Vert_T1	92.9±5.2	0.21±0.74	93.1±5.3	0.20±0.75	93.1±5.2	0.20±0.74		93.2±5.4	0.19±0.76	
Bone_Vert_T2	96.3±15.9	0.20±1.37	96.0±16.4	0.19±1.31	95.9±16.0	0.17±1.35		96.0±16.3	0.18±1.39	
Bone_Vert_T3	96.3±12.2	0.15±1.69	97.3±12.2	0.09±1.52	97.3±12.4	0.10±1.62		97.4±12.4	0.08±1.58	
Bone_Vert_T4	97.6±12.9	0.36±1.27	98.4±12.9	0.34±1.24	98.4±13.1	0.32±1.26		98.5±13.0	0.34±1.29	
Bone_Vert_T5	95.1±13.3	0.25±1.36	96.1±13.3	0.18±1.29	96.0±13.4	0.23±1.33		96.2±13.4	0.17±1.32	
Bone_Vert_T6	97.2±19.0	0.32±1.23	97.9±19.1	0.32±1.06	97.8±19.1	0.31±1.22		97.9±19.1	0.31±1.14	
Bone_Vert_T7	98.0±17.3	0.48±1.51	98.6±17.5	0.39±1.36	98.6±17.4	0.44±1.50		98.7±17.5	0.38±1.50	
Bone_Vert_T8	97.0±14.4	0.48±0.43	97.6±14.1	0.41±0.40	97.5±14.4	0.44±0.42		97.6±14.2	0.40±0.41	
Bone_Vert_T9	89.6±16.3	1.12±1.05	90.0±16.1	1.14±1.01	89.9±16.4	1.11±1.06		90.0±16.2	1.13±1.05	
Bone_Vert_T10	90.7±12.3	0.92±0.91	91.1±12.2	0.92±0.91	90.9±12.3	0.90±0.97		91.0±12.1	0.92±0.90	
Bone_Vert_T11	86.3±12.2	1.15±1.00	86.5±12.0	1.13±0.98	86.2±12.2	1.12±0.99		86.4±11.9	1.13±0.97	
Bone_Vert_T12	96.8±13.3	1.58±1.06	97.0±13.4	1.57±0.98	96.9±13.2	1.55±0.97		97.0±13.4	1.56±0.98	
Bone_Vert_S1	91.5±10.2	1.08±0.51	92.6±10.3	1.19±0.52	92.8±10.3	1.23±0.51		92.7±10.5	1.19±0.54	
Bone_Sacrum	94.6±2.0	0.53±0.15	95.3±2.3	0.49±0.18	95.1±2.1	0.48±0.16	99.5	95.3±2.1	0.49±0.16	99.5
Mean	94.4	1.08	94.7	1.05	94.6	1.05	98.0	94.8	1.04	98.0

Table S15 | Organ-wise segmentation performance comparison on costovertebral bones. Comparison of DSC (%) and ASD (mm) among nnUNet^{E36}, CL-Net^{U36}_{unpruned}, CL-Net^{C36}, and CL-Net^{U36} for 52 costovertebral bones. Decoder-wise pruning rate (T , %) of CL-Net^{C36} and CL-Net^{U36} are also provided. CL-Net^{U36} achieves the highest mean DSC and the lowest mean ASD, demonstrating its superior performance in costovertebral bones.

	nnUNet ^{E₃₆}		CL-Net ^{U₃₆_{unpruned}}		CL-Net ^{C₃₆}			CL-Net ^{U₃₆}				
	DSC↑	ASD↓	DSC↑	ASD↓	DSC↑	ASD↓	\mathcal{T} ↑	DSC↑	ASD↓	\mathcal{T} ↑		
HN_LNS_1La	51.3±6.7	1.06±0.38	52.6±6.2	1.05±0.39	52.9±6.7	1.06±0.38	86.0	52.2±5.9	1.02±0.41	88.0		
HN_LNS_1Lb	78.6±7.1	0.28±0.76	80.2±6.1	0.18±0.77	81.3±6.8	0.20±0.74		80.8±7.7	0.21±0.76			
HN_LNS_1Ra	54.1±6.6	1.39±0.69	57.0±6.1	1.36±0.66	55.0±6.6	1.21±0.69		56.3±5.8	1.31±0.68			
HN_LNS_1Rb	80.5±8.3	1.04±0.80	81.3±9.7	1.02±0.85	80.8±8.1	1.00±0.82		82.0±8.0	1.04±0.83			
HN_LNS_2La	69.2±5.7	1.00±0.99	72.8±5.2	0.89±0.93	71.5±5.0	0.99±0.99		72.1±6.1	0.92±0.92			
HN_LNS_2Lb	73.4±6.5	1.93±0.69	74.2±5.9	1.60±0.66	74.6±5.8	1.68±0.70		74.4±7.2	1.58±0.67			
HN_LNS_2Ra	73.7±7.1	2.11±0.39	75.7±8.1	1.77±0.40	76.6±6.7	1.91±0.38		75.5±6.7	1.78±0.37			
HN_LNS_2Rb	75.0±13.4	1.75±0.58	75.2±14.1	1.68±0.61	75.0±14.1	1.53±0.56		74.9±13.9	1.64±0.60			
HN_LNS_3L	76.3±12.6	1.51±0.79	76.5±12.3	1.40±0.77	75.9±12.3	1.52±0.75		76.1±13.0	1.40±0.78			
HN_LNS_3R	72.0±6.8	1.83±0.63	72.4±7.1	1.57±0.60	72.0±7.9	1.68±0.63		72.3±5.7	1.56±0.62			
HN_LNS_4L	77.0±6.3	1.56±0.49	76.8±6.4	1.35±0.47	77.7±5.6	1.31±0.50		76.5±5.3	1.36±0.47			
HN_LNS_4R	72.6±6.5	1.56±0.49	73.9±5.8	1.31±0.51	74.5±6.3	1.43±0.47		75.7±5.7	1.30±0.50			
HN_LNS_5La	72.9±3.2	0.90±0.54	74.3±3.0	0.91±0.59	75.1±3.5	0.90±0.55		74.2±3.0	0.88±0.57			
HN_LNS_5Lb	75.8±3.5	0.92±0.18	76.2±4.5	0.85±0.18	77.5±3.3	0.75±0.19		76.0±2.8	0.80±0.19			
HN_LNS_5Ra	76.6±2.8	1.00±0.12	78.7±3.5	0.91±0.12	78.3±3.3	0.92±0.14		78.8±3.9	0.87±0.14			
HN_LNS_5Rb	77.5±5.8	1.51±0.09	79.3±6.2	1.50±0.08	80.5±6.4	1.45±0.08		77.9±5.2	1.52±0.09			
HN_LNS_6L	50.4±14.5	1.38±0.96	51.7±14.0	1.27±0.97	52.9±15.0	1.24±0.97		53.1±14.6	1.29±0.99			
HN_LNS_6R	49.8±14.7	1.42±0.98	53.6±14.1	1.55±0.94	50.9±14.7	1.39±0.96		53.1±15.3	1.55±0.95			
Chest_LNS1_L	78.1±8.1	1.48±0.43	82.9±7.7	1.23±0.42	80.9±8.0	1.41±0.43		90.0	81.8±8.5		1.32±0.42	90.0
Chest_LNS1_R	76.8±10.4	1.66±0.63	81.9±10.0	1.71±0.59	82.0±10.1	1.68±0.60			80.2±10.2		1.69±0.61	
Chest_LNS2_L	66.9±10.5	1.55±0.47	71.1±10.9	1.23±0.50	70.6±10.7	1.22±0.48			70.6±10.7		1.25±0.49	
Chest_LNS2_R	70.7±15.5	1.67±2.44	74.1±15.5	1.35±2.17	74.7±15.5	1.31±2.41			74.8±15.5		1.34±2.27	
Chest_LNS3_A	77.4±19.7	1.09±3.26	82.1±19.6	0.82±3.37	81.3±19.7	0.78±3.46			82.9±19.4		0.77±3.61	
Chest_LNS3_P	84.6±8.2	0.86±1.19	90.0±8.3	0.63±1.07	88.8±8.4	0.62±1.14			90.1±8.3		0.60±1.09	
Chest_LNS4_L	74.1±10.4	0.96±0.92	79.4±10.4	0.88±0.92	78.0±10.3	0.85±0.91	78.0±10.3		0.86±0.92			
Chest_LNS4_R	73.8±13.4	1.65±1.06	77.0±13.4	1.40±0.98	76.8±13.4	1.36±1.00	77.9±13.3		1.48±0.99			
Chest_LNS5	72.6±12.1	1.28±0.98	72.6±11.9	1.30±0.96	71.6±12.5	1.27±0.98	72.6±12.7		1.31±0.97			
Chest_LNS6	72.4±12.2	0.88±0.91	75.1±13.2	0.76±0.96	71.8±11.2	0.79±0.95	73.6±12.9		0.75±0.97			
Chest_LNS7	85.0±16.0	1.00±1.06	86.7±15.3	0.95±0.99	86.1±15.7	0.90±1.10	86.6±15.5		0.97±1.04			
Chest_LNS8	80.9±14.1	1.66±0.40	81.8±13.9	1.65±0.42	82.5±13.7	1.68±0.41	82.2±14.9		1.64±0.42			
Chest_LNS9	62.7±17.6	1.39±1.39	62.1±17.8	1.26±1.48	62.4±16.2	1.37±1.44	62.0±17.2		1.25±1.50			
Chest_LNS10_L	74.1±19.1	1.69±1.19	77.4±19.4	1.30±1.11	78.0±20.0	1.37±1.18	77.4±19.4		1.32±1.16			
Chest_LNS10_R	72.8±13.5	1.52±1.37	76.9±13.5	1.21±1.15	77.2±12.6	1.39±1.26	77.2±13.2		1.20±1.27			
Mean	72.1	1.35	74.4	1.21	74.1	1.22	88.0		74.2	1.21	89.0	

Table S16 | Organ-wise segmentation performance comparison on lymph node stations (LNS). Comparison of DSC (%) and ASD (mm) among nnUNet^{E₃₆}, CL-Net^{U₃₆_{unpruned}}, CL-Net^{C₃₆}, and CL-Net^{U₃₆} for 33 lymph node stations. Decoder-wise pruning rate (\mathcal{T} , %) of CL-Net^{C₃₆} and CL-Net^{U₃₆} are also provided. CL-Net^{U₃₆} achieves the highest mean DSC and the lowest mean ASD, demonstrating its superior performance in the LNS group.

	nnUNet ^{E₃₆}		CL-Net ^{U₃₆_{unpruned}}		CL-Net ^{C₃₆}			CL-Net ^{U₃₆}		
	DSC↑	ASD↓	DSC↑	ASD↓	DSC↑	ASD↓	T↑	DSC↑	ASD↓	T↑
Eso_Lesion	73.2±10.9	3.70±2.23	73.6±10.9	3.73±2.09	73.3±11.0	3.93±2.03	92.0	73.4±11.0	3.56±2.19	92.0
Lung_Lesion	78.2±10.9	1.07±2.17	78.2±11.0	1.16±2.12	78.0±11.0	1.17±2.20	92.0	79.1±11.0	1.07±2.21	92.0
Liver_Lesion	63.4±8.4	3.80±2.15	63.9±8.4	3.75±2.09	63.6±8.3	3.60±2.15	92.0	63.8±8.5	3.48±2.10	92.0
Kidney_Lesion	83.7±9.2	1.10±1.08	84.0±9.1	1.23±1.00	83.8±9.3	1.10±1.02	94.0	83.9±9.0	1.18±1.04	94.0
Colon_Lesion	58.8±8.9	3.62±3.60	60.8±8.8	3.50±3.57	61.2±8.8	3.81±3.28	94.0	61.3±8.9	3.40±3.59	94.0
Pancreas_Lesion	62.2±8.5	3.75±2.02	62.8±8.4	3.74±2.09	62.7±8.5	3.75±2.10	94.0	62.8±8.3	3.62±1.89	94.0
NPC_Lesion	72.5±12.4	2.40±2.09	72.9±12.4	2.06±1.95	72.7±12.4	2.36±1.92	92.0	72.8±12.6	2.23±2.02	92.0
HN_LN	71.8±13.2	2.58±2.19	71.9±13.6	2.51±2.05	71.8±13.3	2.72±2.15	92.0	71.8±13.2	2.57±2.10	92.0
Chest_LN	56.2±18.8	12.70±4.91	56.8±19.1	13.62±4.59	56.4±18.7	12.97±4.50	88.0	56.6±18.9	12.58±4.61	88.0
Mean	70.3	3.60	70.8	3.65	70.7	3.67	90.6	70.9	3.48	92.6

Table S17 | Organ-wise segmentation performance comparison on lesions. Comparison of DSC (%) and ASD (mm) among nnUNet^{E₃₆}, CL-Net^{U₃₆_{unpruned}}, CL-Net^{C₃₆}, and CL-Net^{U₃₆} for 10 lesions. Decoder-wise pruning rate (\mathcal{T} , %) of CL-Net^{C₃₆} and CL-Net^{U₃₆} are also provided. CL-Net^{U₃₆} achieves the highest mean DSC and the lowest mean ASD, demonstrating its superior performance in the lesion group.

	nnUNet ^{E5}		MultiTalent		CL-Net ^{U5}		
	DSC↑	ASD↓	DSC↑	ASD↓	DSC↑	ASD↓	\mathcal{T} ↑
Spleen	97.6±15.6	1.95±0.40	96.6±3.2	0.36±0.44	97.1±6.8	1.65±0.39	99.7
Kidney_R	95.9±16.9	0.19±0.73	95.7±4.7	0.29±0.30	96.1±7.1	0.21±0.76	99.7
Kidney_L	96.1±26.7	1.15±6.45	91.9±17.5	1.72±8.64	97.2±6.9	1.00±0.72	
GallBladder	92.2±24.4	1.14±0.82	86.0±19.3	1.42±2.67	93.2±8.7	0.95±0.83	99.7
Liver	97.3±14.9	0.57±0.93	97.8±1.5	0.52±0.65	97.5±5.8	0.54±0.93	99.5
Stomach	95.9±16.2	1.18±0.66	94.2±8.2	0.66±0.68	96.5±6.2	1.11±0.66	99.5
Pancreas	91.8±17.0	1.06±0.67	90.3±6.8	0.79±1.53	92.0±6.9	0.84±0.37	99.5
GlnD_Adrenal_R	83.0±13.5	0.55±1.17	87.8±11.2	0.50±1.60	84.2±13.3	0.43±0.39	94.0
GlnD_Adrenal_L	84.2±12.2	1.03±0.36	85.4±13.5	0.31±0.26	84.8±12.5	0.87±0.39	
Lung_LUL	97.8±3.6	0.31±0.93	97.3±4.5	1.15±4.41	97.9±3.7	0.17±0.62	99.7
Lung_LLL	96.5±24.0	0.21±0.98	95.7±8.5	0.72±1.68	96.5±2.1	0.21±0.47	
Lung_RUL	97.5±20.5	0.30±1.48	92.0±19.5	0.77±1.37	97.7±2.5	0.20±0.98	99.5
Lung_RML	92.0±6.2	0.47±1.41	94.8±6.5	0.83±1.31	92.3±3.3	0.22±1.50	
Lung_RLL	97.4±26.8	0.16±2.45	97.2±5.9	0.43±0.83	97.2±3.6	0.21±1.19	
Eso	94.8±2.9	0.61±0.15	94.1±2.1	0.24±0.24	94.4±3.1	0.45±0.16	99.7
Trachea	96.7±5.8	0.36±0.12	96.0±5.0	0.27±0.47	97.1±6.1	0.27±0.12	99.5
GlnD_Thyroid	91.7±14.7	0.41±0.96	90.2±9.2	0.37±0.45	92.6±14.5	0.28±0.96	99.7
SmallBowel	91.2±26.4	1.63±2.53	87.4±14.0	1.56±1.77	91.2±16.6	1.55±2.62	99.7
Duodenum	87.3±26.0	1.87±1.26	82.9±18.3	1.02±1.08	88.8±16.1	1.81±1.26	99.5
Colon	90.2±16.0	2.54±1.21	89.9±7.9	1.55±1.90	90.4±15.8	2.36±1.23	99.5
UrinaryBladder	89.1±9.5	2.98±1.08	92.5±7.6	1.27±1.97	89.2±9.6	2.85±1.03	99.5
Prostate	81.7±38.0	0.52±2.06	72.8±33.5	1.45±1.72	83.3±17.9	0.35±1.47	99.5
Mean	92.6	0.96	91.3	0.83	93.1	0.84	99.3

Table S18 | Organ-wise performance comparison of nnUNet^{E5}, MultiTalent, and CL-Net^{U5} on TotalSegmentator V2 ‘Organ’ subgroup. Organ-wise DSC (%) and ASD (mm) of nnUNet^{E5}, MultiTalent and CL-Net^{U5} are evaluated on TotalSegmentator V2 ‘Organ’ subgroup. CL-Net^{U5} achieves the best mean DSC.

	nnUNet ^{E5}		MultiTalent		CL-Net ^{U5}		
	DSC↑	ASD↓	DSC↑	ASD↓	DSC↑	ASD↓	\mathcal{T} ↑
Heart	95.2±14.7	0.42±0.20	95.9±1.4	1.10±3.24	94.9±14.7	0.43±0.18	99.7
A_Aorta	96.0±16.7	0.44±0.95	96.7±4.7	0.30±0.57	96.5±16.7	0.41±0.85	99.7
V_Pulmonary	89.8±15.5	0.47±0.14	93.1±3.1	0.23±0.13	91.3±15.5	0.31±0.16	99.0
A_BrachiocephalicTrunk	89.8±16.2	0.32±0.43	93.8±3.0	0.22±0.18	90.8±16.3	0.22±0.44	99.0
A_Subclavian_L	94.6±3.5	0.44±0.28	91.6±3.5	0.33±0.47	94.9±3.6	0.27±0.29	99.7
A_Subclavian_R	94.1±3.3	0.23±0.17	91.5±3.4	0.22±0.15	93.3±3.4	0.17±0.18	
A_CommonCarotid_L	91.2±5.4	0.35±0.28	90.3±4.8	0.23±0.22	91.1±5.4	0.24±0.28	99.5
A_CommonCarotid_R	96.6±3.3	0.28±0.99	93.2±2.4	0.15±0.13	97.4±3.3	0.26±1.02	
V_Brachiocephalic_L	90.4±26.2	0.37±1.97	91.5±15.7	0.44±1.59	91.2±16.1	0.31±2.11	99.5
V_Brachiocephalic_R	88.7±15.0	0.32±0.81	89.8±11.4	0.37±0.57	89.1±15.3	0.24±0.84	
LAA	92.6±3.4	0.46±0.15	93.2±2.7	0.20±0.11	91.7±3.3	0.16±0.15	99.5
V_VenaCava_S	93.8±21.4	0.23±2.35	88.4±24.2	0.42±0.83	93.7±21.4	0.18±2.44	99.5
V_VenaCava_I	93.9±9.8	1.03±1.05	92.3±6.3	0.47±0.38	95.2±9.8	0.77±1.00	99.5
V_Portal_Splenic	85.5±29.3	1.29±0.62	85.1±12.1	0.67±0.72	86.7±29.1	1.12±0.63	99.0
A_Iliac_L	94.4±3.1	0.61±0.19	93.2±3.0	0.25±0.38	95.1±3.3	0.50±0.20	99.5
A_Iliac_R	91.9±19.5	0.45±0.15	93.5±3.8	0.19±0.26	91.9±19.6	0.39±0.18	
V_Iliac_L	92.2±3.0	0.48±0.13	94.1±2.8	0.18±0.10	92.9±3.3	0.43±0.15	99.0
V_Iliac_R	94.2±4.9	0.44±0.31	92.9±5.6	0.22±0.20	93.6±4.8	0.45±0.27	
Mean	92.5	0.48	92.2	0.34	92.9	0.38	99.4

Table S19 | Organ-wise performance comparison of nnUNet^{E5}, MultiTalent, and CL-Net^{U5} on TotalSegmentator V2 ‘Cardiac’ subgroup. Organ-wise DSC (%) and ASD (mm) of nnUNet^{E5}, MultiTalent and CL-Net^{U5} are evaluated on TotalSegmentator V2 ‘Cardiac’ subgroup. CL-Net^{U5} achieves the best mean DSC.

	nnUNet ^{E5}		MultiTalent		CL-Net ^{U5}		
	DSC↑	ASD↓	DSC↑	ASD↓	DSC↑	ASD↓	\mathcal{T} ↑
Bone_Humerus_L	96.9±17.5	2.84±0.20	93.5±7.1	0.57±0.97	97.1±17.6	2.77±0.21	99.5
Bone_Humerus_R	96.6±17.3	4.31±0.17	96.5±2.0	5.20±12.27	97.1±17.0	3.88±0.17	
Bone_Scapula_L	94.1±21.1	1.16±0.18	94.8±1.9	0.49±1.16	93.8±21.4	0.97±0.17	99.5
Bone_Scapula_R	95.1±1.7	1.95±0.07	95.2±2.1	0.35±0.59	94.4±1.9	1.63±0.08	
Bone_Clavicula_L	94.5±0.8	0.60±0.10	96.6±1.8	1.76±7.40	95.2±0.9	0.45±0.11	99.5
Bone_Clavicula_R	98.4±16.1	1.52±0.19	95.5±3.2	1.72±9.22	98.3±16.0	1.37±0.20	
Bone_Femur_L	97.4±15.4	3.51±0.29	94.6±14.3	9.92±40.53	97.5±0.7	3.28±0.11	99.7
Bone_Femur_R	95.8±0.5	6.85±0.08	98.4±0.4	0.52±1.08	96.3±0.2	6.26±0.06	
Bone_Hip_L	96.6±1.6	0.32±0.13	97.3±1.5	0.44±0.89	97.0±1.9	0.29±0.14	99.5
Bone_Hip_R	95.9±31.6	0.34±0.10	98.0±0.3	0.20±0.45	97.0±31.9	0.27±0.11	
SpinalCord	92.7±16.8	0.27±0.24	94.5±3.7	0.20±0.13	92.7±16.5	0.26±0.24	99.5
Musc_GluteusMax_L	98.9±5.2	0.84±1.41	93.8±7.7	3.56±10.31	98.7±5.4	0.76±1.50	99.5
Musc_GluteusMax_R	98.1±2.0	0.93±0.34	95.2±4.0	2.29±4.92	97.9±2.2	0.71±0.34	
Musc_GluteusMed_L	98.2±1.5	0.43±0.22	94.0±3.0	0.93±1.57	98.4±1.5	0.45±0.23	99.7
Musc_GluteusMed_R	97.6±7.3	0.74±0.22	93.7±3.8	0.76±0.73	97.3±7.5	0.47±0.21	
Musc_GluteusMin_L	97.1±2.3	0.56±0.16	91.9±3.0	0.93±1.75	97.3±2.2	0.42±0.16	99.7
Musc_GluteusMin_R	98.0±1.1	0.39±0.08	93.0±1.7	0.41±0.16	98.2±1.1	0.36±0.10	
Musc_Autochthon_L	94.2±0.8	0.37±0.11	95.8±1.3	0.38±0.15	93.9±0.9	0.32±0.12	99.7
Musc_Autochthon_R	94.6±0.8	0.41±0.12	95.8±1.2	0.37±0.12	94.8±0.8	0.41±0.11	
Musc_Iliopsoas_L	94.3±19.7	0.37±0.18	90.3±9.0	0.50±0.86	93.5±19.6	0.36±0.19	99.5
Musc_Iliopsoas_R	95.0±9.1	0.39±0.27	90.0±9.5	0.44±0.57	94.9±9.1	0.32±0.25	
Brain	97.9±36.4	0.56±1.01	88.3±28.0	7.85±24.00	98.2±16.3	0.51±1.07	99.5
Skull	83.1±35.4	3.91±0.20	79.5±21.0	1.07±2.79	82.5±35.4	3.66±0.21	99.7
Mean	96.1	1.46	94.2	1.78	96.2	1.31	99.6

Table S20 | Organ-wise performance comparison of nnUNet^{E5}, MultiTalent, and CL-Net^{U5} on TotalSegmentator V2 ‘Muscle’ subgroup. Organ-wise DSC (%) and ASD (mm) of nnUNet^{E5}, MultiTalent and CL-Net^{U5} are evaluated on TotalSegmentator V2 ‘Muscle’ subgroup. CL-Net^{U5} achieves the best mean DSC and ASD.

	nnUNet ^{E5}		MultiTalent		CL-Net ^{U5}		
	DSC↑	ASD↓	DSC↑	ASD↓	DSC↑	ASD↓	\mathcal{T} ↑
Bone_Rib1_L	93.6±3.3	0.16±0.23	92.4±8.9	0.15±0.13	93.3±3.3	0.14±0.21	96.0
Bone_Rib2_L	89.9±1.7	0.95±0.95	95.4±1.5	0.19±0.76	90.2±1.5	0.74±1.02	
Bone_Rib3_L	94.7±17.0	0.91±1.06	94.9±3.0	0.13±0.20	94.9±17.0	0.85±1.08	
Bone_Rib4_L	94.5±18.9	0.76±1.82	94.9±3.8	0.20±0.48	93.9±18.7	0.63±1.77	
Bone_Rib5_L	94.2±29.7	1.52±4.61	91.5±15.6	0.42±1.23	94.3±29.6	1.06±4.53	
Bone_Rib6_L	93.2±23.9	1.64±3.32	93.0±11.4	0.37±0.97	92.8±24.1	1.51±3.35	
Bone_Rib7_L	94.5±20.7	2.71±4.08	93.9±5.4	0.33±0.50	95.8±20.8	2.36±4.01	
Bone_Rib8_L	94.6±21.1	4.29±4.00	90.4±15.0	0.89±2.41	95.2±21.1	4.15±4.04	
Bone_Rib9_L	94.0±19.4	2.83±5.21	89.9±16.2	1.32±3.61	94.5±19.3	2.74±4.83	
Bone_Rib10_L	93.0±22.9	1.51±6.63	87.5±23.7	2.24±5.96	91.9±13.2	1.48±6.45	
Bone_Rib11_L	93.0±22.4	0.36±8.01	87.5±23.4	2.55±7.91	92.1±12.1	0.34±8.12	
Bone_Rib12_L	94.2±26.2	0.54±0.41	91.5±8.3	1.02±4.36	94.7±16.3	0.33±0.41	
Bone_Rib1_R	91.2±5.6	0.11±0.17	94.0±2.6	0.15±0.17	91.8±5.6	0.14±0.15	
Bone_Rib2_R	94.5±3.5	0.23±0.94	95.1±3.4	0.14±0.41	94.6±3.4	0.09±0.91	
Bone_Rib3_R	92.8±9.1	0.48±0.75	93.7±5.8	0.20±0.38	93.7±9.1	0.34±1.14	
Bone_Rib4_R	90.5±18.8	0.83±2.02	94.4±7.4	0.10±0.10	90.4±18.6	0.73±1.92	
Bone_Rib5_R	90.3±26.5	1.70±2.42	89.7±20.6	0.72±2.36	90.7±16.4	1.49±2.51	
Bone_Rib6_R	93.4±18.9	1.52±2.45	89.6±18.0	1.05±3.01	93.4±13.0	1.38±2.54	
Bone_Rib7_R	94.2±21.0	1.56±3.51	90.7±16.5	0.77±1.61	95.5±21.3	1.57±3.36	
Bone_Rib8_R	95.5±18.3	1.88±4.08	91.8±10.0	0.81±1.83	95.0±18.0	1.78±4.22	
Bone_Rib9_R	95.9±21.4	2.48±5.16	91.7±11.6	1.21±2.97	96.3±21.6	2.25±3.18	
Bone_Rib10_R	96.3±23.3	2.50±7.23	90.6±18.4	1.33±4.17	95.9±23.3	2.30±7.41	
Bone_Rib11_R	96.4±22.8	1.85±6.95	90.4±18.2	1.50±5.23	97.5±22.7	1.71±6.70	
Bone_Rib12_R	97.1±27.5	0.63±0.07	89.5±13.9	1.32±3.03	97.4±27.5	0.46±0.10	
Bone_Sternum	94.1±5.8	0.63±0.55	94.9±2.7	0.36±0.91	95.5±5.7	0.35±0.55	99.7
Bone_CostalCartilages	88.7±5.0	0.18±0.74	91.2±3.2	0.44±0.59	88.6±5.0	0.16±0.74	99.5
Mean	93.6	1.34	91.9	0.77	93.8	1.20	98.4

Table S21 | Organ-wise performance comparison of nnUNet^{E5}, MultiTalent, and CL-Net^{U5} on TotalSegmentator V2 ‘Rib’ subgroup. Organ-wise DSC (%) and ASD (mm) of nnUNet^{E5}, MultiTalent and CL-Net^{U5} are evaluated on TotalSegmentator V2 ‘Rib’ subgroup. CL-Net^{U5} achieves the best mean DSC.

	nnUNet ^{E5}		MultiTalent		CL-Net ^{U5}		
	DSC↑	ASD↓	DSC↑	ASD↓	DSC↑	ASD↓	\mathcal{T} ↑
Bone_Sacrum	93.4±1.8	0.25±0.13	95.0±2.2	0.48±0.27	93.9±1.9	0.19±0.14	99.0
Bone_Vert_C1	94.5±20.3	0.25±0.53	94.3±4.2	0.42±0.53	95.3±10.2	0.23±0.50	96.0
Bone_Vert_C2	98.0±20.7	0.31±3.04	93.2±20.1	0.09±0.08	97.9±10.5	0.14±0.47	
Bone_Vert_C3	98.1±23.4	0.16±3.22	94.8±10.3	0.28±0.64	98.0±15.5	0.16±3.18	
Bone_Vert_C4	97.0±23.4	0.34±3.60	92.1±20.0	0.60±1.99	96.6±19.6	0.30±3.54	
Bone_Vert_C5	96.8±17.5	0.22±1.62	88.7±22.3	0.26±0.62	97.8±17.4	0.21±1.63	
Bone_Vert_C6	95.0±10.6	0.60±0.93	96.9±4.6	0.16±0.33	96.0±10.5	0.45±0.93	
Bone_Vert_C7	95.2±17.5	0.41±0.86	96.5±5.8	0.19±0.45	95.3±13.1	0.18±1.00	
Bone_Vert_L1	95.7±12.1	1.27±0.98	97.1±3.1	0.14±0.30	94.9±12.1	1.19±0.98	
Bone_Vert_L2	94.8±18.2	0.29±1.09	97.4±1.7	0.11±0.21	93.7±12.3	0.18±0.95	
Bone_Vert_L3	96.0±16.1	0.24±1.09	97.0±1.8	0.13±0.16	96.9±16.2	0.18±1.06	
Bone_Vert_L4	94.1±14.3	0.43±0.41	95.7±6.4	0.22±0.39	94.2±14.2	0.23±0.41	
Bone_Vert_L5	92.9±17.3	0.21±1.49	94.6±9.5	0.31±0.70	93.9±17.4	0.19±1.43	
Bone_Vert_S1	96.3±23.8	0.20±2.10	92.0±14.2	0.42±0.96	97.3±18.9	0.19±1.22	
Bone_Vert_T1	96.3±23.5	0.15±1.28	92.5±13.0	0.41±0.94	95.9±13.5	0.15±1.37	
Bone_Vert_T2	98.0±5.2	0.48±0.74	88.6±22.0	0.59±1.38	97.7±5.4	0.32±0.76	
Bone_Vert_T3	97.0±2.7	0.48±0.20	90.4±17.1	0.64±1.58	97.9±2.6	0.46±0.21	
Bone_Vert_T4	89.6±17.0	1.12±0.21	91.2±16.9	0.51±1.50	90.5±8.9	1.05±0.20	
Bone_Vert_T5	90.7±22.9	0.92±0.38	93.6±15.8	0.42±1.73	90.4±23.1	0.88±0.39	
Bone_Vert_T6	86.3±28.3	1.15±0.07	92.8±15.8	0.48±2.13	85.4±28.1	1.04±0.06	
Bone_Vert_T7	96.8±1.0	1.58±0.04	89.9±17.5	0.37±1.00	97.1±1.0	1.48±0.06	
Bone_Vert_T8	91.5±13.0	1.08±0.40	84.9±24.3	0.18±0.22	91.6±13.0	0.93±0.16	
Bone_Vert_T9	94.6±44.2	0.53±0.23	94.4±4.6	0.08±0.03	94.3±14.4	0.42±0.24	
Bone_Vert_T10	97.6±29.9	0.36±2.18	95.8±0.9	0.10±0.07	97.5±13.0	0.38±1.32	
Bone_Vert_T11	95.1±19.4	0.25±1.64	94.7±5.5	0.22±0.46	95.1±12.4	0.22±1.67	
Bone_Vert_T12	97.2±16.3	0.32±1.30	84.3±27.3	0.24±0.34	97.5±16.0	0.26±1.35	
Mean	94.9	0.52	93.0	0.31	95.1	0.45	97.5

Table S22 | Organ-wise performance comparison of nnUNet^{E5}, MultiTalent, and CL-Net^{U5} on TotalSegmentator V2 ‘Vertebrae’ subgroup. Organ-wise DSC (%) and ASD (mm) of nnUNet^{E5}, MultiTalent and CL-Net^{U5} are evaluated on TotalSegmentator V2 ‘Vertebrae’ subgroup. CL-Net^{U5} achieves the best mean DSC.

	nnUNet ^{E5}		MultiTalent		CL-Net ^{U5}		
	DSC↑	ASD↓	DSC↑	ASD↓	DSC↑	ASD↓	\mathcal{T} ↑
BrainStem	93.7±1.5	0.32±0.10	87.2±2.5	0.84±0.26	92.9±1.6	0.23±0.11	99.5
Eye_L	94.8±1.3	0.17±0.08	89.5±2.9	0.40±0.12	93.6±1.3	0.14±0.08	99.0
Eye_R	93.2±4.2	0.24±0.28	90.0±2.5	1.43±2.58	95.3±4.3	0.28±0.29	
Lens_L	80.1±9.8	0.25±0.18	77.9±6.3	0.23±0.14	80.4±9.8	0.21±0.17	96.0
Lens_R	79.7±9.2	0.33±0.43	80.3±5.6	0.21±0.09	82.0±9.3	0.41±0.43	
OpticNerve_L	80.3±8.0	0.29±0.28	67.3±8.7	1.11±1.78	81.7±8.1	0.31±0.30	99.0
OpticNerve_R	84.1±6.4	0.20±0.21	68.1±7.0	0.52±0.15	86.5±6.2	0.17±0.20	
Chiasm	71.6±12.9	0.26±0.13	42.9±18.6	23.27±47.95	71.9±13.1	0.23±0.15	96.0
TemporalLobe_L	94.7±1.2	0.24±0.08	85.6±7.0	1.93±0.94	95.3±1.3	0.22±0.09	99.5
TemporalLobe_R	94.8±1.4	0.26±0.09	84.1±6.0	2.02±0.83	93.5±1.6	0.23±0.11	
GlnD_Pituitary	84.5±6.4	0.22±0.21	52.6±23.3	1.04±0.65	85.6±6.4	0.16±0.21	99.0
GlnD_Parotid_L	93.3±1.9	0.35±0.16	83.0±5.6	1.19±0.58	91.7±1.7	0.29±0.15	99.5
GlnD_Parotid_R	92.5±3.4	0.50±0.52	84.3±4.4	1.20±0.55	96.0±1.3	0.42±0.50	
Ear_Inner_L	67.0±9.5	0.66±0.37	83.1±2.7	0.50±0.12	69.3±9.4	0.61±0.36	99.5
Ear_Inner_R	64.3±9.3	0.66±0.30	86.8±2.7	0.33±0.11	63.8±9.4	0.75±0.31	
Ear_Mid_L	90.4±3.7	0.07±0.04	75.2±15.7	1.30±1.14	90.6±3.6	0.07±0.03	99.5
Ear_Mid_R	90.2±3.3	0.08±0.06	81.2±7.0	1.69±2.60	92.1±3.4	0.07±0.06	
TMJ_L	84.4±9.5	0.31±0.23	78.1±6.8	0.79±0.34	82.5±9.3	0.24±0.22	98.0
TMJ_R	84.1±7.6	0.33±0.20	75.8±6.7	1.55±2.24	84.3±7.7	0.33±0.21	
SpinalCord	91.5±2.9	0.36±0.19	81.4±3.2	0.61±0.14	90.8±3.1	0.33±0.21	99.0
Bone_Mandible_L	95.7±2.1	0.17±0.08	91.4±1.9	0.37±0.13	97.5±2.0	0.15±0.07	99.7
Bone_Mandible_R	95.7±2.5	0.17±0.08	91.3±1.1	0.36±0.10	95.6±2.6	0.13±0.09	
Mean	86.4	0.29	79.0	1.95	87.0	0.27	98.7

Table S23 | Organ-wise performance comparison of nnUNet^{E5}, MultiTalent, and CL-Net^{U5} on StructSeg19. Organ-wise DSC (%) and ASD (mm) of nnUNet^{E5}, MultiTalent and CL-Net^{U5} are evaluated on StructSeg19. CL-Net^{U5} achieves the best mean DSC and ASD.

	nnUNet ^{E₅}		MultiTalent		CL-Net ^{U₅}		
	DSC↑	ASD↓	DSC↑	ASD↓	DSC↑	ASD↓	\mathcal{T} ↑
Eso	88.2±3.2	0.35±0.16	83.1±8.5	1.17±0.98	90.4±3.0	0.31±0.14	99.5
Heart	94.7±14.9	0.39±0.20	94.3±1.0	3.44±3.79	94.5±14.6	0.37±0.17	99.0
Trachea	92.2±5.8	0.30±0.09	90.7±3.5	0.67±0.39	93.8±5.9	0.28±0.10	99.5
A_Aorta	95.2±16.6	0.32±0.84	94.6±0.8	0.47±0.11	96.2±16.6	0.31±0.84	99.7
Mean	92.6	0.34	90.7	1.44	93.7	0.32	99.4

Table S24 | Organ-wise performance comparison of nnUNet^{E₅}, MultiTalent, and CL-Net^{U₅} on SegThor. Organ-wise DSC (%) and ASD (mm) of nnUNet^{E₅}, MultiTalent and CL-Net^{U₅} are evaluated on SegThor. CL-Net^{U₅} achieves the best mean DSC and ASD.

	nnUNet ^{E5}		MultiTalent		CL-Net ^{U5}		
	DSC↑	ASD↓	DSC↑	ASD↓	DSC↑	ASD↓	\mathcal{T} ↑
Liver	98.1±14.5	0.83±0.98	97.3±3.4	0.74±1.11	98.3±5.8	0.81±1.00	99.5
Kidney_R	92.4±16.9	1.81±0.74	94.3±9.2	3.40±9.09	94.3±7.1	1.44±0.76	99.7
Kidney_L	92.8±16.9	1.27±0.74	94.2±9.6	4.22±8.64	92.9±6.7	1.18±0.69	
Spleen	97.9±15.6	0.30±0.37	97.1±3.4	0.45±0.89	98.0±6.6	0.19±0.37	99.5
Pancreas	91.6±17.2	0.80±0.69	89.0±4.8	0.98±0.68	92.4±7.0	0.72±0.38	99.5
A_Aorta	96.7±16.5	0.21±0.95	94.5±8.0	1.58±3.43	97.1±16.5	0.18±0.83	99.7
V_VenaCava_I	88.8±10.1	1.08±1.03	90.3±10.2	0.83±1.11	88.6±9.9	1.12±0.98	99.0
GlnD_Adrenal_R	85.9±12.3	0.39±0.37	84.3±7.0	0.44±0.53	87.9±13.2	0.35±0.39	96.0
GlnD_Adrenal_L	88.0±13.3	0.26±1.16	85.9±6.1	0.34±0.19	87.7±12.5	0.21±0.38	
GallBladder	80.2±24.7	2.16±0.83	81.0±23.4	2.06±2.84	83.1±8.7	2.12±0.83	99.5
Eso	84.4±3.1	1.70±0.15	84.1±15.4	1.93±3.34	86.0±3.0	1.61±0.14	99.7
Stomach	91.7±16.4	1.24±0.67	89.8±19.8	2.09±4.22	92.4±6.5	1.17±0.69	99.5
Duodenum	79.8±25.9	2.71±1.29	79.0±16.9	4.77±8.97	81.0±16.1	2.39±1.18	99.5
Mean	89.9	1.14	89.3	1.83	90.7	1.04	99.2

Table S25 | Organ-wise performance comparison of nnUNet^{E5}, MultiTalent, and CL-Net^{U5} on FLARE22. Organ-wise DSC (%) and ASD (mm) of nnUNet^{E5}, MultiTalent and CL-Net^{U5} are evaluated on FLARE22. CL-Net^{U5} achieves the best mean DSC and ASD.

	nnUNet ^{E₅}		MultiTalent		CL-Net ^{U₅}		
	DSC↑	ASD↓	DSC↑	ASD↓	DSC↑	ASD↓	\mathcal{T} ↑
Kidney_Lesion	86.7±9.0	1.18±1.06	79.6±20.8	9.94±17.66	87.2±9.0	1.03±0.98	96.0

Table S26 | Organ-wise performance comparison of nnUNet^{E₅}, MultiTalent, and CL-Net^{U₅} on KiTS21. Organ-wise DSC (%) and ASD (mm) of nnUNet^{E₅}, MultiTalent and CL-Net^{U₅} are evaluated on KiTS21. CL-Net^{U₅} achieves the best mean DSC and ASD.

	SAT-pro		Vista3D		MultiTalent		nnUNet ^{L36}		CL-Net ^{L36}		CL-Net ^{L36}	
	DSC↑	ASD↓	DSC↑	ASD↓	DSC↑	ASD↓	DSC↑	ASD↓	DSC↑	ASD↓	DSC↑	ASD↓
BrainStem	62.1±20.8	—	—	—	83.0±5.2	1.12±0.39	85.3±4.6	1.20±0.49	85.1±4.1	1.02±0.53	85.7±3.6	0.96±0.50
Eye_L	76.5±13.5	—	—	—	84.2±9.4	0.61±0.46	89.2±5.2	0.71±0.40	89.5±2.7	0.46±0.16	89.2±2.8	0.48±0.17
Eye_R	76.7±9.9	—	—	—	82.2±12.1	0.62±0.19	89.3±3.6	0.69±0.29	88.7±2.7	0.53±0.18	89.1±2.5	0.50±0.17
Lens_L	54.3±28.3	—	—	—	71.3±14.5	0.63±0.31	74.5±7.9	0.48±0.24	75.1±10.1	0.57±0.39	75.8±8.6	0.53±0.32
Lens_R	60.3±16.7	—	—	—	68.9±15.5	0.66±0.23	72.7±10.1	0.52±0.31	75.0±11.6	0.60±0.39	75.4±8.7	0.52±0.33
Chiasm	7.8±18.2	—	—	—	39.8±18.5	2.15±0.95	50.5±13.1	1.42±0.66	54.6±12.3	0.82±0.59	54.6±12.2	0.82±0.63
OpticNerve_L	27.9±30.6	—	—	—	65.6±13.9	0.74±0.28	68.0±9.3	0.79±0.38	68.2±10.4	0.56±0.34	69.7±9.7	0.58±0.35
OpticNerve_R	24.8±26.1	—	—	—	67.6±13.5	0.63±0.26	67.4±11.1	0.84±0.48	69.4±8.7	0.59±0.41	69.2±7.9	0.61±0.47
GlnD_Parotid_L	62.3±21.6	—	—	—	85.3±6.4	1.17±0.52	84.2±5.8	1.23±0.73	85.6±3.9	1.05±0.35	85.8±3.5	0.99±0.29
GlnD_Parotid_R	73.4±11.6	—	—	—	86.4±6.5	1.24±0.42	83.9±5.6	1.27±0.53	85.7±3.5	1.09±0.39	85.8±3.5	1.05±0.39
TMJ_L	17.6±27.9	—	—	—	71.9±16.2	0.91±0.76	69.8±11.5	1.07±0.53	72.2±12.0	0.89±0.57	72.4±9.3	0.63±0.48
TMJ_R	9.1±20.3	—	—	—	71.1±7.5	0.99±0.26	69.6±12.3	1.10±0.58	71.5±12.6	0.94±0.58	71.9±10.7	0.67±0.52
Mean	46.1	—	—	—	73.1	0.96	75.4	0.94	76.7	0.76	77.1	0.70

Table S27 | External testing: organ-wise segmentation performance comparison on 268 patients head & neck dataset. The organ-wise DSC (%) and ASD (mm) are evaluated for comparison. Note that structures excluded from the officially released Vista3D model are indicated with a '-'. Furthermore, the SAT-pro inference framework removes image metadata headers during inference, making it impossible to calculate ASD. CL-Net^{L36} achieves the best mean DSC and ASD.

	SAT-pro		Vista3D		MultiTalent		nnUNet ^{L36}		CL-Net ^{L36}		CL-Net ^{L96}	
	DSC↑	ASD↓	DSC↑	ASD↓	DSC↑	ASD↓	DSC↑	ASD↓	DSC↑	ASD↓	DSC↑	ASD↓
BrachialPlex	—	—	—	—	—	—	40.5±11.8	3.35±3.69	49.0±8.8	2.52±2.88	49.9±8.8	2.54±2.09
Eso	80.5±7.5	—	81.2±6.3	0.74±0.56	81.6±7.8	0.97±0.53	84.3±6.6	1.12±0.68	88.3±5.8	0.68±0.68	88.3±5.3	0.70±0.70
Lung_L	97.1±0.6	—	97.2±0.6	0.60±0.22	98.0±0.0	0.64±0.05	98.0±0.4	0.85±1.07	98.1±0.4	0.84±0.99	98.2±0.6	0.68±1.35
Lung_R	94.7±0.4	—	95.4±3.2	1.63±0.62	96.7±2.3	0.67±0.43	97.0±0.4	0.80±1.02	97.1±0.3	0.80±0.54	97.8±0.6	0.60±1.10
Pericardium	83.7±6.1	—	73.6±4.1	3.00±1.36	87.6±2.4	39.75±6.56	92.2±1.8	1.62±3.84	92.2±1.4	1.62±3.69	92.4±1.8	1.54±4.45
SpinalCord	77.9±5.5	—	75.5±5.6	3.08±2.37	54.9±4.3	102.08±13.70	89.5±3.4	1.13±1.16	91.8±2.5	0.90±0.85	92.2±2.3	0.85±0.86
ProximalBronchi	13.6±3.3	—	91.0±2.3	0.89±0.75	70.1±4.7	57.36±7.23	91.0±2.3	0.89±0.75	91.1±1.9	0.89±0.70	91.5±2.0	0.88±0.67
A_Aorta	—	—	86.9±0.9	2.18±0.49	87.7±1.3	1.54±0.08	92.0±7.5	1.34±4.42	92.8±7.7	1.11±4.63	92.9±8.0	1.03±4.65
A_Pulmonary	80.4±4.0	—	—	—	—	—	87.8±4.0	1.12±1.47	87.8±4.0	1.10±1.09	89.0±3.8	0.88±1.44
V_Pulmonary	62.2±6.2	—	66.0±6.4	1.29±0.62	67.4±5.9	54.81±9.14	69.7±9.5	2.21±1.24	71.2±8.0	1.94±0.99	73.3±8.2	1.80±1.43
V_Venacava_I	—	—	41.6±9.7	8.16±1.07	42.5±10.0	41.78±3.19	88.0±7.6	1.22±1.10	86.3±7.5	1.16±1.10	88.6±8.1	0.95±1.15
V_Venacava_S	81.8±4.1	—	83.0±3.3	1.15±0.40	84.9±2.8	79.27±8.22	86.2±4.1	1.09±0.87	87.8±4.2	0.88±0.52	87.9±4.4	0.86±0.68
ChestWall_L	—	—	—	—	—	—	90.2±2.3	1.45±0.98	90.4±2.2	1.03±0.99	90.9±2.6	1.23±1.20
ChestWall_R	—	—	—	—	—	—	90.3±2.0	1.13±0.89	90.9±2.0	0.99±0.88	90.8±2.1	0.64±0.50
Mean	—	—	—	—	—	—	85.5	1.38	86.8	1.18	87.4	1.08

Table S28 | External testing: organ-wise segmentation performance comparison on 60 patients chest dataset. The organ-wise DSC (%) and ASD (mm) are evaluated for comparison. Note that structures excluded from the officially released SAT-pro, Vista3D, and MultiTalent (trained on C_5 datasets) models are indicated with a ‘-’. Furthermore, the SAT-pro inference framework removes image metadata headers during inference, making it impossible to calculate ASD. The CL-Net^{L36} achieves the best mean DSC and ASD.

	SAT-pro		Vista3D		MultiTalent		nnUNet ^{C₃₆}		CL-Net ^{C₃₆}		CL-Net ^{U₃₆}	
	DSC↑	ASD↓	DSC↑	ASD↓	DSC↑	ASD↓	DSC↑	ASD↓	DSC↑	ASD↓	DSC↑	ASD↓
Spleen	—	—	95.0±1.9	0.63±0.77	92.9±8.4	0.68±0.99	93.4±6.9	0.74±0.49	94.7±7.7	0.71±0.51	94.3±6.0	0.57±0.54
Kidney_R	—	—	91.3±15.4	2.14±9.28	91.3±14.2	0.69±0.52	91.0±7.0	0.62±0.74	91.2±6.7	0.78±0.85	91.3±6.5	0.73±0.62
Kidney_L	—	—	92.9±6.2	0.79±1.63	91.9±13.9	0.63±0.38	91.2±6.8	0.83±0.77	91.0±7.6	1.11±0.62	91.7±8.3	0.73±0.75
Gallbladder	—	—	78.1±24.2	0.56±0.46	71.0±30.2	4.11±11.93	77.3±8.7	1.90±0.82	78.0±9.6	0.63±0.79	78.8±8.7	0.61±0.79
Eso	—	—	78.6±6.3	1.13±1.15	78.9±7.7	1.44±0.96	79.0±9.6	1.68±1.33	80.1±10.5	1.38±1.41	81.1±10.6	1.26±1.36
Liver	—	—	96.7±0.8	0.46±0.17	96.8±0.7	0.85±0.35	97.0±0.5	0.79±1.03	96.4±0.4	0.41±0.10	97.3±0.7	0.44±0.09
Stomach	—	—	93.0±2.2	0.79±0.94	90.7±6.0	1.18±0.95	89.6±8.6	1.26±0.99	86.8±9.6	1.53±0.98	87.8±9.5	1.48±0.95
A_Aorta	—	—	91.7±2.2	0.81±0.94	92.5±2.3	0.76±0.81	91.1±3.6	1.51±0.36	92.2±4.2	0.61±0.34	92.5±4.2	0.61±0.28
V_VenaCava_I	—	—	86.9±5.2	1.38±1.97	87.6±5.8	1.22±0.50	88.0±7.0	2.03±0.49	86.8±6.4	1.22±0.56	86.3±6.4	1.21±0.53
V_Portal_Splenic	—	—	74.8±7.3	0.57±0.48	76.5±11.3	2.19±2.29	77.0±19.0	1.48±0.79	75.9±19.9	0.71±0.73	75.8±19.2	0.74±0.74
Pancreas	—	—	83.9±4.6	0.77±0.99	81.4±7.2	1.61±1.71	83.4±9.2	1.53±0.37	82.2±10.1	0.56±0.33	81.9±7.3	0.48±0.38
GlnD_Adrenal_R	—	—	72.0±5.7	0.60±0.30	73.0±5.2	0.88±0.31	72.1±14.2	1.30±0.43	75.1±14.9	0.69±0.46	76.0±16.0	0.66±0.50
GlnD_Adrenal_L	—	—	72.3±12.7	0.48±0.14	69.9±18.0	1.80±3.13	72.0±16.4	1.67±0.45	75.0±17.3	0.69±0.46	75.4±17.1	0.65±0.51
Mean	—	—	85.2	0.85	84.1	1.39	84.8	1.33	85.0	0.85	85.4	0.78

Table S29 | External testing: Organ-wise segmentation performance comparison on 30 patients BTCV ⁶⁷ abdomen dataset. The organ-wise DSC (%) and ASD (mm) are evaluated for comparison. Note that structures not included in the officially released SAT-pro model and MultiTalent (trained on C_5 datasets) are indicated with a '-'. CL-Net^{U₃₆} achieves the best mean DSC and ASD.

*Note: BTCV is used for SAT-Pro training, therefore, it's not available for SAT-Pro external testing and no result is provided in the table.

	SAT-pro		Vista3D		MultiTalent		nnUNet ^{U36}		CL-Net ^{U36}		CL-Net ^{U36}	
	DSC↑	ASD↓	DSC↑	ASD↓	DSC↑	ASD↓	DSC↑	ASD↓	DSC↑	ASD↓	DSC↑	ASD↓
NPC_lesion	64.9±13.3	—	—	—	—	—	70.3±13.1	2.02±1.46	70.5±14.2	2.01±1.59	70.3±9.9	1.98±1.58
Eso_lesion	—	—	—	—	—	—	75.0±18.4	8.85±14.23	74.9±16.7	8.87±12.24	75.1±18.8	8.67±14.50
Liver_lesion	33.7±33.3	—	—	—	—	—	69.9±16.3	8.41±4.31	69.9±20.9	8.43±6.42	70.4±18.1	7.53±4.74
Kidney_lesion	—	—	—	—	81.3±11.4	7.22±10.62	83.6±18.1	2.20±1.64	86.6±12.6	1.01±0.99	86.7±11.0	1.00±0.99
Mean	—	—	—	—	—	—	74.7	5.37	75.5	5.08	75.6	4.80

Table S30 | External testing: Organ-wise segmentation performance comparison on external 319 NPC lesion patients, 148 Eso lesion patients, 176 Liver lesion patients, and 978 Kidney lesion patients. The organ-wise DSC (%) and ASD (mm) are evaluated for comparison. Note that structures not included in the officially released SAT-pro model and MultiTalent (trained on \mathcal{C}_5 datasets) are indicated with a ‘-’. Furthermore, the SAT-pro inference framework removes image metadata headers during inference, making it impossible to calculate ASD. The CL-Net^{U36} achieves the best mean DSC and ASD.

	CL-Net \mathcal{U}_{36}			CL-Net $\mathcal{U}_{36}^{\text{fine-tune}}$		
	DSC \uparrow	ASD \downarrow	$\mathcal{T}\uparrow$	DSC \uparrow	ASD \downarrow	$\mathcal{T}\uparrow$
Spleen	97.8 \pm 6.9	0.29 \pm 0.41	99.5	97.2 \pm 6.8	1.67 \pm 0.40	99.5
Kidney_R	94.9 \pm 7.1	1.07 \pm 0.76	99.7	97.1 \pm 7.2	0.21 \pm 0.78	99.7
Kidney_L	94.2 \pm 6.9	1.46 \pm 0.72		97.1 \pm 7.0	0.92 \pm 0.73	
GallBladder	86.6 \pm 8.8	1.96 \pm 0.84	99.5	93.9 \pm 8.9	0.91 \pm 0.85	99.0
Liver	97.8 \pm 5.9	0.77 \pm 0.94	99.5	97.6 \pm 5.8	0.58 \pm 0.93	99.7
Stomach	92.4 \pm 6.2	1.07 \pm 0.65	99.5	96.1 \pm 6.1	1.08 \pm 0.64	99.5
Pancreas	94.6 \pm 6.9	0.66 \pm 0.37	99.5	92.5 \pm 7.0	0.89 \pm 0.37	99.5
GlnD_Adrenal_R	90.6 \pm 13.1	0.22 \pm 0.38	98.0	85.2 \pm 13.5	0.43 \pm 0.41	98.0
GlnD_Adrenal_L	88.3 \pm 12.5	0.40 \pm 0.39		85.0 \pm 12.6	0.93 \pm 0.39	
Lung_LUL	97.9 \pm 3.7	0.17 \pm 0.62	99.5	97.8 \pm 3.6	0.16 \pm 0.61	99.5
Lung_LLL	96.5 \pm 2.1	0.21 \pm 0.47		97.4 \pm 2.0	0.19 \pm 0.46	
Lung_RUL	97.7 \pm 2.5	0.20 \pm 0.98	99.5	97.8 \pm 2.6	0.21 \pm 1.00	99.5
Lung_RML	92.3 \pm 3.3	0.22 \pm 1.50		93.1 \pm 3.3	0.23 \pm 1.37	
Lung_RLL	97.2 \pm 3.6	0.21 \pm 1.19		97.0 \pm 3.7	0.21 \pm 1.10	
Eso	85.4 \pm 3.0	0.64 \pm 0.15	98.0	94.5 \pm 3.1	0.46 \pm 0.16	99.0
Trachea	92.9 \pm 6.1	0.86 \pm 0.12	99.7	97.2 \pm 6.0	0.27 \pm 0.11	99.7
GlnD_Thyroid	82.7 \pm 14.5	0.95 \pm 0.96	94.0	93.3 \pm 14.6	0.26 \pm 0.97	99.0
SmallBowel	91.2 \pm 16.4	2.22 \pm 2.54	99.5	91.1 \pm 16.6	1.52 \pm 2.41	99.5
Duodenum	82.9 \pm 16.0	2.29 \pm 1.18	99.5	89.4 \pm 15.9	1.74 \pm 1.19	99.5
Colon	92.9 \pm 15.9	2.72 \pm 1.13	99.5	90.7 \pm 15.7	2.49 \pm 1.13	99.7
UrinaryBladder	93.6 \pm 9.7	1.82 \pm 0.94	98.0	89.7 \pm 9.5	2.99 \pm 0.96	99.5
Prostate	85.5 \pm 17.7	3.62 \pm 1.36	96.0	83.8 \pm 17.9	0.33 \pm 1.44	99.5
Mean	92.3	1.20	98.7	93.4	0.85	99.4

Table S31 | Performance comparison of CL-Net \mathcal{U}_{36} and CL-Net $\mathcal{U}_{36}^{\text{fine-tune}}$ on TotalSegmentator V2 ‘Organ’ subgroup. Organ-wise DSC (%), ASD (mm), and decoder-wise pruning rate \mathcal{T} (%) of CL-Net \mathcal{U}_{36} and CL-Net $\mathcal{U}_{36}^{\text{fine-tune}}$ are evaluated on TotalSegmentator V2 ‘Organ’ subgroup. After fine-tuning, CL-Net $\mathcal{U}_{36}^{\text{fine-tune}}$ achieves improved mean DSC and ASD, indicating that CL-Net \mathcal{U}_{36} can further overfit its general label style learned from \mathcal{U}_{36} datasets to the distinct label style of TotalSegmentator V2 ‘Organ’ subgroup.

	CL-Net \mathcal{U}_{36}			CL-Net $\mathcal{U}_{36}^{\text{fine-tune}}$		
	DSC \uparrow	ASD \downarrow	$\mathcal{T}\uparrow$	DSC \uparrow	ASD \downarrow	$\mathcal{T}\uparrow$
Heart	97.1 \pm 14.7	1.64 \pm 0.19	99.0	94.8 \pm 14.8	0.46 \pm 0.20	99.5
A_Aorta	95.0 \pm 16.9	0.75 \pm 0.86	99.0	96.0 \pm 16.8	0.42 \pm 0.86	99.7
V_Pulmonary	75.5 \pm 15.3	1.37 \pm 0.14	99.0	90.7 \pm 15.4	0.30 \pm 0.14	99.0
A_BrachiocephalicTrunk	98.2 \pm 16.2	0.62 \pm 0.43	99.0	90.5 \pm 16.3	0.22 \pm 0.44	99.5
A_Subclavian_L	82.4 \pm 3.5	2.69 \pm 0.28	94.0	95.3 \pm 3.6	0.27 \pm 0.29	99.7
A_Subclavian_R	85.5 \pm 3.3	1.45 \pm 0.16		93.0 \pm 3.3	0.17 \pm 0.17	
A_CommonCarotid_L	88.3 \pm 7.6	0.89 \pm 3.83	99.7	89.6 \pm 5.5	0.23 \pm 0.29	99.7
A_CommonCarotid_R	86.1 \pm 9.4	0.55 \pm 3.72		87.2 \pm 3.5	0.26 \pm 1.01	
V_Brachiocephalic_L	92.5 \pm 5.2	0.36 \pm 0.14	99.5	92.2 \pm 6.2	0.33 \pm 1.91	99.5
V_Brachiocephalic_R	90.0 \pm 5.8	0.45 \pm 0.25		90.0 \pm 5.3	0.24 \pm 0.83	
LAA	91.7 \pm 3.3	0.16 \pm 0.15	99.7	92.5 \pm 3.4	0.18 \pm 0.16	99.7
V_VenaCava_S	92.0 \pm 21.4	0.83 \pm 2.23	99.0	93.7 \pm 21.5	0.17 \pm 2.23	99.5
V_VenaCava_I	84.5 \pm 9.7	1.72 \pm 0.99	99.0	95.8 \pm 9.7	0.77 \pm 0.99	99.7
V_Portal_Splenic	86.7 \pm 29.1	1.12 \pm 0.63	98.0	89.0 \pm 27.1	0.18 \pm 0.63	98.0
A_Iliac_L	95.1 \pm 3.3	0.50 \pm 0.20	99.0	96.0 \pm 3.3	0.50 \pm 0.20	99.7
A_Iliac_R	91.9 \pm 19.6	0.39 \pm 0.18		91.1 \pm 19.7	0.36 \pm 0.19	
V_Iliac_L	92.9 \pm 3.3	0.43 \pm 0.15	99.7	92.6 \pm 3.3	0.45 \pm 0.15	99.0
V_Iliac_R	93.6 \pm 4.8	0.45 \pm 0.27		94.4 \pm 4.9	0.47 \pm 0.28	
Mean	89.8	0.84	98.7	92.5	0.33	99.4

Table S32 | Performance comparison of CL-Net \mathcal{U}_{36} and CL-Net $\mathcal{U}_{36}^{\text{fine-tune}}$ on TotalSegmentator V2 ‘Cardiac’ subgroup. Organ-wise DSC (%), ASD (mm), and decoder-wise pruning rate \mathcal{T} (%) of CL-Net \mathcal{U}_{36} and CL-Net $\mathcal{U}_{36}^{\text{fine-tune}}$ are evaluated on TotalSegmentator V2 ‘Cardiac’ subgroup. After fine-tuning, CL-Net $\mathcal{U}_{36}^{\text{fine-tune}}$ achieves improved mean DSC and ASD, indicating that CL-Net \mathcal{U}_{36} can further overfit its general label style learned from \mathcal{U}_{36} datasets to the distinct label style of TotalSegmentator V2 ‘Cardiac’ subgroup.

	CL-Net \mathcal{U}_{36}			CL-Net $\mathcal{U}_{36}^{\text{fine-tune}}$		
	DSC \uparrow	ASD \downarrow	$\mathcal{T}\uparrow$	DSC \uparrow	ASD \downarrow	$\mathcal{T}\uparrow$
Bone_Humerus_L	97.1 \pm 17.6	2.77 \pm 0.21	99.7	97.3 \pm 17.4	0.97 \pm 0.29	99.5
Bone_Humerus_R	97.1 \pm 17.0	3.88 \pm 0.17		97.2 \pm 17.0	0.19 \pm 0.17	
Bone_Scapula_L	93.8 \pm 21.4	0.97 \pm 0.17	99.7	94.0 \pm 21.5	0.98 \pm 0.19	99.5
Bone_Scapula_R	94.4 \pm 1.9	1.63 \pm 0.08		93.9 \pm 12.1	1.48 \pm 0.10	
Bone_Clavicula_L	95.2 \pm 0.9	0.45 \pm 0.11	99.7	96.0 \pm 1.0	0.36 \pm 0.13	99.5
Bone_Clavicula_R	98.3 \pm 16.0	1.37 \pm 0.20		98.4 \pm 15.8	0.29 \pm 0.18	
Bone_Femur_L	92.0 \pm 0.6	5.77 \pm 0.10	99.5	97.6 \pm 0.7	3.06 \pm 0.11	99.5
Bone_Femur_R	94.6 \pm 0.2	5.95 \pm 0.06		96.9 \pm 0.3	5.96 \pm 0.07	
Bone_Hip_L	97.0 \pm 1.9	0.29 \pm 0.14	99.5	97.1 \pm 2.0	0.31 \pm 0.14	99.7
Bone_Hip_R	97.0 \pm 31.9	0.27 \pm 0.11		96.5 \pm 31.8	0.30 \pm 0.10	
SpinalCord	94.1 \pm 16.7	0.84 \pm 0.26	99.7	93.1 \pm 16.4	0.27 \pm 0.23	99.5
Musc_GluteusMax_L	98.7 \pm 5.4	0.76 \pm 1.50	99.5	98.8 \pm 5.5	0.75 \pm 1.45	99.7
Musc_GluteusMax_R	97.9 \pm 2.2	0.71 \pm 0.34		97.7 \pm 2.3	0.66 \pm 0.35	
Musc_GluteusMed_L	98.4 \pm 1.5	0.45 \pm 0.23	99.5	98.3 \pm 1.5	0.47 \pm 0.23	99.5
Musc_GluteusMed_R	97.3 \pm 7.5	0.47 \pm 0.21		97.5 \pm 7.4	0.50 \pm 0.19	
Musc_GluteusMin_L	97.3 \pm 2.2	0.42 \pm 0.16	99.5	97.4 \pm 2.1	0.43 \pm 0.15	99.7
Musc_GluteusMin_R	98.2 \pm 1.1	0.36 \pm 0.10		98.3 \pm 1.0	0.34 \pm 0.09	
Musc_Autochthon_L	93.9 \pm 0.9	0.32 \pm 0.12	99.0	94.3 \pm 1.1	0.29 \pm 0.14	99.0
Musc_Autochthon_R	94.8 \pm 0.8	0.41 \pm 0.11		95.1 \pm 0.9	0.39 \pm 0.12	
Musc_Iliopsoas_L	93.5 \pm 19.6	0.36 \pm 0.19	99.0	92.5 \pm 19.8	0.33 \pm 0.20	99.0
Musc_Iliopsoas_R	94.9 \pm 9.1	0.32 \pm 0.25		95.6 \pm 9.2	0.30 \pm 0.26	
Brain	98.2 \pm 16.3	0.51 \pm 1.07	99.5	98.2 \pm 16.4	0.51 \pm 1.04	99.5
Skull	82.5 \pm 35.4	3.66 \pm 0.21	99.0	82.0 \pm 35.5	1.45 \pm 0.21	99.5
Mean	95.4	0.98	99.4	95.8	0.90	99.5

Table S33 | Performance comparison of CL-Net \mathcal{U}_{36} and CL-Net $\mathcal{U}_{36}^{\text{fine-tune}}$ on TotalSegmentator V2 ‘Muscles’ subgroup. Organ-wise DSC (%), ASD (mm), and decoder-wise pruning rate \mathcal{T} (%) of CL-Net \mathcal{U}_{36} and CL-Net $\mathcal{U}_{36}^{\text{fine-tune}}$ are evaluated on TotalSegmentator V2 ‘Muscles’ subgroup. After fine-tuning, CL-Net $\mathcal{U}_{36}^{\text{fine-tune}}$ achieves improved mean DSC, indicating that CL-Net \mathcal{U}_{36} can further overfit its general label style learned from \mathcal{U}_{36} datasets to the distinct label style of TotalSegmentator V2 ‘Muscles’ subgroup.

	CL-Net \mathcal{U}_{36}			CL-Net $\mathcal{U}_{36}^{\text{fine-tune}}$		
	DSC \uparrow	ASD \downarrow	$\mathcal{T}\uparrow$	DSC \uparrow	ASD \downarrow	$\mathcal{T}\uparrow$
Bone_Rib1_L	93.3 \pm 3.3	0.14 \pm 0.21	96.0	92.4 \pm 3.1	0.14 \pm 0.19	98.0
Bone_Rib2_L	90.2 \pm 1.5	0.74 \pm 1.05		91.5 \pm 1.6	0.59 \pm 0.92	
Bone_Rib3_L	94.9 \pm 17.0	0.85 \pm 1.08		94.5 \pm 17.0	0.90 \pm 1.04	
Bone_Rib4_L	93.9 \pm 18.7	0.63 \pm 1.77		94.1 \pm 18.8	0.61 \pm 1.67	
Bone_Rib5_L	94.3 \pm 29.6	1.18 \pm 4.53		91.4 \pm 29.4	1.11 \pm 4.29	
Bone_Rib6_L	92.8 \pm 24.1	1.51 \pm 3.35		92.8 \pm 24.3	1.55 \pm 3.15	
Bone_Rib7_L	95.8 \pm 20.8	2.36 \pm 4.01		95.6 \pm 20.8	2.25 \pm 3.69	
Bone_Rib8_L	95.2 \pm 21.1	4.15 \pm 4.04		95.5 \pm 20.9	3.82 \pm 3.80	
Bone_Rib9_L	94.5 \pm 19.3	2.74 \pm 4.83		95.0 \pm 19.5	2.57 \pm 4.40	
Bone_Rib10_L	91.9 \pm 13.2	1.48 \pm 6.45		91.5 \pm 13.1	1.46 \pm 6.42	
Bone_Rib11_L	92.1 \pm 12.1	0.34 \pm 8.12		92.7 \pm 12.1	0.32 \pm 7.51	
Bone_Rib12_L	94.7 \pm 16.3	0.33 \pm 0.41		94.5 \pm 16.3	0.31 \pm 0.40	
Bone_Rib1_R	91.8 \pm 5.6	0.14 \pm 0.15		91.9 \pm 5.5	0.15 \pm 0.14	
Bone_Rib2_R	94.6 \pm 3.4	0.09 \pm 0.91		94.7 \pm 3.2	0.09 \pm 0.89	
Bone_Rib3_R	93.7 \pm 9.1	0.34 \pm 1.14		93.9 \pm 9.3	0.38 \pm 1.11	
Bone_Rib4_R	90.4 \pm 18.6	0.73 \pm 1.92		91.1 \pm 18.4	0.73 \pm 1.85	
Bone_Rib5_R	90.7 \pm 16.4	1.49 \pm 2.51		91.4 \pm 16.5	1.43 \pm 2.31	
Bone_Rib6_R	93.4 \pm 13.0	1.38 \pm 2.54		93.0 \pm 13.1	1.46 \pm 2.45	
Bone_Rib7_R	95.5 \pm 21.3	1.57 \pm 3.36		94.6 \pm 21.3	1.62 \pm 3.08	
Bone_Rib8_R	95.0 \pm 18.0	1.78 \pm 4.22		95.5 \pm 17.9	1.67 \pm 4.06	
Bone_Rib9_R	96.3 \pm 21.6	2.25 \pm 3.18		95.5 \pm 21.7	2.05 \pm 3.06	
Bone_Rib10_R	95.9 \pm 23.3	2.30 \pm 7.41		95.9 \pm 23.4	2.27 \pm 7.24	
Bone_Rib11_R	97.5 \pm 22.7	1.71 \pm 6.70		97.6 \pm 22.9	1.60 \pm 6.06	
Bone_Rib12_R	97.4 \pm 27.5	0.46 \pm 0.10		97.2 \pm 27.6	0.41 \pm 0.12	
Bone_Sternum	95.5 \pm 5.7	0.35 \pm 0.55	99.7	95.7 \pm 5.5	0.36 \pm 0.53	99.7
Bone_CostalCartilages	88.6 \pm 5.0	0.16 \pm 0.74	99.7	89.0 \pm 5.0	0.16 \pm 0.75	99.5
Mean	93.8	1.20	98.4	93.8	1.16	99.1

Table S34 | Performance comparison of CL-Net \mathcal{U}_{36} and CL-Net $\mathcal{U}_{36}^{\text{fine-tune}}$ on TotalSegmentator V2 ‘Ribs’ subgroup. Organ-wise DSC (%), ASD (mm), and decoder-wise pruning rate \mathcal{T} (%) of CL-Net \mathcal{U}_{36} and CL-Net $\mathcal{U}_{36}^{\text{fine-tune}}$ are evaluated on TotalSegmentator V2 ‘Ribs’ subgroup. After fine-tuning, CL-Net $\mathcal{U}_{36}^{\text{fine-tune}}$ achieves improved mean DSC, indicating that CL-Net \mathcal{U}_{36} can further overfit its general label style learned from \mathcal{U}_{36} datasets to the distinct label style of TotalSegmentator V2 ‘Ribs’ subgroup.

	CL-Net \mathcal{U}_{36}			CL-Net $\mathcal{U}_{36}^{\text{fine-tune}}$		
	DSC \uparrow	ASD \downarrow	$\mathcal{T}\uparrow$	DSC \uparrow	ASD \downarrow	$\mathcal{T}\uparrow$
Bone_Sacrum	93.9 \pm 1.9	0.19 \pm 0.14	99.5	93.8 \pm 2.1	0.20 \pm 0.16	99.5
Bone_Vert_C1	95.3 \pm 10.2	0.23 \pm 0.50	96.0	94.6 \pm 10.0	0.24 \pm 0.49	96.0
Bone_Vert_C2	97.9 \pm 10.5	0.14 \pm 0.47		98.0 \pm 10.7	0.15 \pm 0.49	
Bone_Vert_C3	98.0 \pm 15.5	0.16 \pm 3.18		98.2 \pm 15.4	0.15 \pm 2.86	
Bone_Vert_C4	96.6 \pm 19.6	0.30 \pm 3.54		95.9 \pm 19.5	0.27 \pm 3.36	
Bone_Vert_C5	97.8 \pm 17.4	0.21 \pm 1.63		97.8 \pm 17.3	0.19 \pm 1.49	
Bone_Vert_C6	96.0 \pm 10.5	0.45 \pm 0.93		95.1 \pm 10.5	0.44 \pm 0.93	
Bone_Vert_C7	95.3 \pm 13.1	0.18 \pm 1.00		96.1 \pm 13.0	0.19 \pm 0.98	
Bone_Vert_L1	94.9 \pm 12.1	1.19 \pm 0.98		94.4 \pm 12.0	1.13 \pm 0.97	
Bone_Vert_L2	93.7 \pm 12.3	0.18 \pm 0.95		92.8 \pm 12.1	0.18 \pm 0.93	
Bone_Vert_L3	96.9 \pm 16.2	0.18 \pm 1.06		97.3 \pm 16.3	0.20 \pm 0.96	
Bone_Vert_L4	94.2 \pm 14.2	0.23 \pm 0.41		94.6 \pm 14.0	0.24 \pm 0.39	
Bone_Vert_L5	93.9 \pm 17.4	0.19 \pm 1.43		93.9 \pm 17.2	0.18 \pm 1.40	
Bone_Vert_S1	97.3 \pm 18.9	0.19 \pm 1.22		97.3 \pm 19.0	0.18 \pm 1.12	
Bone_Vert_T1	95.9 \pm 13.5	0.15 \pm 1.37		96.8 \pm 13.6	0.14 \pm 1.25	
Bone_Vert_T2	97.7 \pm 5.4	0.32 \pm 0.76		97.5 \pm 5.6	0.32 \pm 0.77	
Bone_Vert_T3	97.9 \pm 2.6	0.46 \pm 0.21		97.9 \pm 2.5	0.44 \pm 0.20	
Bone_Vert_T4	90.5 \pm 8.9	1.05 \pm 0.20		91.4 \pm 8.9	0.95 \pm 0.20	
Bone_Vert_T5	90.4 \pm 23.1	0.88 \pm 0.39		91.0 \pm 22.9	0.97 \pm 0.37	
Bone_Vert_T6	85.4 \pm 28.1	1.04 \pm 0.06		85.4 \pm 28.2	0.94 \pm 0.06	
Bone_Vert_T7	97.1 \pm 1.0	1.48 \pm 0.06		97.0 \pm 1.2	1.62 \pm 0.08	
Bone_Vert_T8	91.6 \pm 13.0	0.93 \pm 0.16		91.9 \pm 13.0	1.00 \pm 0.17	
Bone_Vert_T9	94.3 \pm 14.4	0.42 \pm 0.24		93.3 \pm 14.4	0.46 \pm 0.25	
Bone_Vert_T10	97.5 \pm 13.0	0.38 \pm 1.32		97.4 \pm 13.0	0.37 \pm 1.21	
Bone_Vert_T11	95.1 \pm 12.4	0.22 \pm 1.67		95.6 \pm 12.4	0.23 \pm 1.64	
Bone_Vert_T12	97.5 \pm 16.0	0.26 \pm 1.35		97.7 \pm 16.1	0.24 \pm 1.26	
Mean	95.1	0.45	97.8	95.1	0.45	97.8

Table S35 | Performance comparison of CL-Net \mathcal{U}_{36} and CL-Net $\mathcal{U}_{36}^{\text{fine-tune}}$ on TotalSegmentator V2 ‘Vertebrae’ subgroup. Organ-wise DSC (%), ASD (mm), and decoder-wise pruning rate \mathcal{T} (%) of CL-Net \mathcal{U}_{36} and CL-Net $\mathcal{U}_{36}^{\text{fine-tune}}$ are evaluated on TotalSegmentator V2 ‘Vertebrae’ subgroup. After fine-tuning, CL-Net $\mathcal{U}_{36}^{\text{fine-tune}}$ achieves improved mean DSC and ASD, indicating that CL-Net \mathcal{U}_{36} can further overfit its general label style learned from \mathcal{U}_{36} datasets to the distinct label style of TotalSegmentator V2 ‘Vertebrae’ subgroup.

	CL-Net \mathcal{U}_{36}			CL-Net $\mathcal{U}_{36}^{\text{fine-tune}}$		
	DSC \uparrow	ASD \downarrow	$\mathcal{T}\uparrow$	DSC \uparrow	ASD \downarrow	$\mathcal{T}\uparrow$
BrainStem	93.6 \pm 1.7	0.76 \pm 0.11	99.5	93.1 \pm 1.7	0.24 \pm 0.12	99.0
Eye_L	86.6 \pm 1.4	0.69 \pm 0.09	99.0	93.7 \pm 1.3	0.13 \pm 0.08	99.0
Eye_R	86.7 \pm 4.3	0.57 \pm 0.29		95.4 \pm 4.3	0.25 \pm 0.29	
Lens_L	81.6 \pm 9.9	0.56 \pm 0.18	99.0	82.5 \pm 9.9	0.22 \pm 0.19	98.0
Lens_R	84.3 \pm 9.4	0.37 \pm 0.44		82.1 \pm 9.3	0.43 \pm 0.43	
OpticNerve_L	77.8 \pm 8.0	0.60 \pm 0.28	99.0	80.8 \pm 8.0	0.33 \pm 0.29	99.5
OpticNerve_R	79.3 \pm 6.1	0.59 \pm 0.19		81.6 \pm 6.2	0.19 \pm 0.20	
Chiasm	74.5 \pm 13.0	0.62 \pm 0.14	96.0	69.1 \pm 13.3	0.29 \pm 0.16	99.5
TemporalLobe_L	88.2 \pm 1.3	1.41 \pm 0.09	99.5	95.5 \pm 1.1	0.20 \pm 0.07	99.7
TemporalLobe_R	87.6 \pm 1.7	1.73 \pm 0.13		95.7 \pm 1.5	0.25 \pm 0.10	
GlnD_Pituitary	85.2 \pm 6.5	0.49 \pm 0.21	98.0	88.7 \pm 6.3	0.15 \pm 0.20	99.5
GlnD_Parotid_L	87.6 \pm 1.7	1.06 \pm 0.14	99.5	95.9 \pm 1.9	0.30 \pm 0.16	99.5
GlnD_Parotid_R	86.6 \pm 1.4	1.09 \pm 0.51		96.1 \pm 1.4	0.41 \pm 0.52	
Ear_Inner_L	58.3 \pm 9.5	0.60 \pm 0.37	99.5	65.5 \pm 9.3	0.61 \pm 0.35	98.0
Ear_Inner_R	57.1 \pm 9.4	0.57 \pm 0.32		65.0 \pm 9.4	0.79 \pm 0.32	
Ear_Mid_L	91.3 \pm 3.7	0.57 \pm 0.04	99.5	90.7 \pm 3.6	0.07 \pm 0.02	99.7
Ear_Mid_R	90.4 \pm 3.4	0.64 \pm 0.06		89.2 \pm 3.3	0.07 \pm 0.05	
TMJ_L	78.6 \pm 9.4	0.65 \pm 0.23	94.0	78.7 \pm 9.5	0.36 \pm 0.23	96.0
TMJ_R	76.8 \pm 7.9	0.71 \pm 0.23		80.5 \pm 7.5	0.37 \pm 0.20	
SpinalCord	94.4 \pm 3.0	0.67 \pm 0.20	99.7	94.9 \pm 3.2	0.35 \pm 0.22	99.0
Bone_Mandible_L	92.2 \pm 1.8	0.43 \pm 0.05	99.7	97.7 \pm 2.2	0.16 \pm 0.08	99.7
Bone_Mandible_R	91.5 \pm 2.4	0.47 \pm 0.07		97.7 \pm 2.6	0.14 \pm 0.09	
Mean	83.2	0.72	98.6	86.8	0.29	98.9

Table S36 | Performance comparison of CL-Net \mathcal{U}_{36} and CL-Net $\mathcal{U}_{36}^{\text{fine-tune}}$ on StructSeg19. Organ-wise DSC (%), ASD (mm), and decoder-wise pruning rate \mathcal{T} (%) of CL-Net \mathcal{U}_{36} and CL-Net $\mathcal{U}_{36}^{\text{fine-tune}}$ are evaluated on StructSeg19. After fine-tuning, CL-Net $\mathcal{U}_{36}^{\text{fine-tune}}$ achieves improved mean DSC, ASD and pruning rate, indicating that CL-Net \mathcal{U}_{36} can further overfit its general label style learned from \mathcal{U}_{36} datasets to the distinct label style of StructSeg19.

	CL-Net \mathcal{U}_{36}			CL-Net $\mathcal{U}_{36}^{\text{fine-tune}}$		
	DSC \uparrow	ASD \downarrow	$\mathcal{T}\uparrow$	DSC \uparrow	ASD \downarrow	$\mathcal{T}\uparrow$
Eso	89.9 \pm 2.8	0.53 \pm 0.12	98.0	90.5 \pm 2.9	0.32 \pm 0.13	99.5
Heart	91.4 \pm 14.8	1.48 \pm 0.19	99.0	94.6 \pm 14.6	0.37 \pm 0.18	99.0
Trachea	92.7 \pm 6.1	0.68 \pm 0.12	99.7	92.9 \pm 5.8	0.31 \pm 0.09	99.5
A_Aorta	95.3 \pm 16.8	0.75 \pm 0.86	99.0	95.9 \pm 16.7	0.34 \pm 0.85	99.5
Mean	92.3	0.86	98.9	93.5	0.34	99.4

Table S37 | Performance comparison of CL-Net \mathcal{U}_{36} and CL-Net $\mathcal{U}_{36}^{\text{fine-tune}}$ on SegThor. Organ-wise DSC (%), ASD (mm), and decoder-wise pruning rate \mathcal{T} (%) of CL-Net \mathcal{U}_{36} and CL-Net $\mathcal{U}_{36}^{\text{fine-tune}}$ are evaluated on SegThor. After fine-tuning, CL-Net $\mathcal{U}_{36}^{\text{fine-tune}}$ achieves improved mean DSC, ASD and pruning rate, indicating that CL-Net \mathcal{U}_{36} can further overfit its general label style learned from \mathcal{U}_{36} datasets to the distinct label style of SegThor.

	CL-Net \mathcal{U}_{36}			CL-Net $\mathcal{U}_{36}^{\text{fine-tune}}$		
	DSC \uparrow	ASD \downarrow	$\mathcal{T}\uparrow$	DSC \uparrow	ASD \downarrow	$\mathcal{T}\uparrow$
Liver	93.7 \pm 5.9	0.81 \pm 0.95	99.5	97.9 \pm 5.6	0.79 \pm 0.99	99.5
Kidney_R	95.0 \pm 7.0	1.78 \pm 0.75	99.7	94.4 \pm 7.0	1.36 \pm 0.75	99.7
Kidney_L	91.1 \pm 6.7	1.29 \pm 0.70		94.3 \pm 6.9	1.06 \pm 0.72	
Spleen	98.0 \pm 6.7	0.32 \pm 0.39	99.5	98.1 \pm 6.9	0.20 \pm 0.40	99.5
Pancreas	94.9 \pm 7.0	0.86 \pm 0.38	99.5	92.6 \pm 7.0	0.74 \pm 0.38	99.5
A_Aorta	92.2 \pm 16.7	0.23 \pm 0.85	99.0	97.1 \pm 16.6	0.18 \pm 0.84	99.5
V_VenaCava_I	78.5 \pm 10.0	1.17 \pm 1.02	99.0	88.8 \pm 9.9	1.08 \pm 0.97	99.0
GlnD_Adrenal_R	90.3 \pm 13.4	0.43 \pm 0.41	98.0	89.0 \pm 13.2	0.33 \pm 0.39	99.0
GlnD_Adrenal_L	87.6 \pm 12.5	0.28 \pm 0.39		89.9 \pm 12.6	0.22 \pm 0.39	
GallBladder	85.5 \pm 8.4	2.15 \pm 0.80	99.5	83.2 \pm 8.5	2.27 \pm 0.82	99.5
Eso	81.8 \pm 3.2	1.66 \pm 0.16	98.0	86.1 \pm 2.8	1.50 \pm 0.13	99.5
Stomach	92.3 \pm 6.5	1.17 \pm 0.68	99.5	92.5 \pm 6.2	1.05 \pm 0.65	99.5
Duodenum	82.6 \pm 15.9	2.60 \pm 1.26	99.5	83.2 \pm 15.8	2.36 \pm 1.19	99.5
Mean	89.5	1.13	99.2	91.3	1.01	99.4

Table S38 | Performance comparison of CL-Net \mathcal{U}_{36} and CL-Net $\mathcal{U}_{36}^{\text{fine-tune}}$ on FLARE22. Organ-wise DSC (%), ASD (mm), and decoder-wise pruning rate \mathcal{T} (%) of CL-Net \mathcal{U}_{36} and CL-Net $\mathcal{U}_{36}^{\text{fine-tune}}$ are evaluated on FLARE22. After fine-tuning, CL-Net $\mathcal{U}_{36}^{\text{fine-tune}}$ achieves improved mean DSC, ASD and pruning rate, indicating that CL-Net \mathcal{U}_{36} can further overfit its general label style learned from \mathcal{U}_{36} datasets to the distinct label style of FLARE22.

	CL-Net \mathcal{U}_{36}			CL-Net $\mathcal{U}_{36}^{\text{fine-tune}}$		
	DSC \uparrow	ASD \downarrow	$\mathcal{T}\uparrow$	DSC \uparrow	ASD \downarrow	$\mathcal{T}\uparrow$
Kidney_Lesion	83.9 \pm 9.0	1.18 \pm 1.04	90.0	87.1 \pm 9.4	1.28 \pm 1.05	96.0

Table S39 | Performance comparison of CL-Net \mathcal{U}_{36} and CL-Net $\mathcal{U}_{36}^{\text{fine-tune}}$ on KiTS21. Organ-wise DSC (%), ASD (mm), and decoder-wise pruning rate \mathcal{T} (%) of CL-Net \mathcal{U}_{36} and CL-Net $\mathcal{U}_{36}^{\text{fine-tune}}$ are evaluated on KiTS21. After fine-tuning, CL-Net $\mathcal{U}_{36}^{\text{fine-tune}}$ achieves improved DSC and pruning rate, indicating that CL-Net \mathcal{U}_{36} can further overfit its general label style learned from \mathcal{U}_{36} datasets to the distinct label style of KiTS21.

	nnUNet		Order 1			Order 2			Order 3			Order 4		
	DSC↑	ASD↓	DSC↑	ASD↓	\mathcal{T} ↑	DSC↑	ASD↓	\mathcal{T} ↑	DSC↑	ASD↓	\mathcal{T} ↑	DSC↑	ASD↓	\mathcal{T} ↑
Spleen	97.6±15.6	1.95±0.40	97.6±6.8	1.87±0.40	99.5	98.4±6.9	1.81±0.41	99.7	97.1±7.0	1.87±0.41	99.0	97.6±6.8	1.87±0.40	99.5
Kidney_R	95.9±16.9	0.19±0.73	96.8±7.0	0.25±0.75	99.7	95.4±6.9	0.17±0.74	99.7	96.0±7.1	0.22±0.76	99.0	96.8±7.0	0.25±0.75	99.7
Kidney_L	96.1±26.7	1.15±6.45	95.9±6.8	1.07±0.71		94.3±6.8	1.17±0.71		97.2±6.6	1.10±0.69		95.9±6.8	1.07±0.71	
GallBladder	92.2±24.4	1.14±0.82	93.1±8.7	1.05±0.83	99.7	90.2±8.4	1.23±0.80	99.7	93.0±8.4	1.22±0.80	99.0	93.1±8.7	1.05±0.83	99.7
Liver	97.3±14.9	0.57±0.93	97.3±5.7	0.61±0.99	99.7	97.6±5.9	0.57±0.91	99.5	97.6±5.7	0.62±0.99	99.0	97.3±5.7	0.61±0.99	99.7
Stomach	95.9±16.2	1.18±0.66	95.2±6.4	1.22±0.68	99.5	97.0±6.5	1.20±0.68	99.5	96.3±6.4	1.24±0.67	99.0	95.2±6.4	1.22±0.68	99.5
Pancreas	91.8±17.0	1.06±0.67	92.7±7.0	0.78±0.38	99.7	92.7±6.9	1.09±0.36	99.5	91.9±6.9	1.04±0.37	99.0	92.7±7.0	0.78±0.38	99.7
GlnD_Adrenal_R	83.0±13.5	0.55±1.17	82.1±13.2	0.42±0.39	99.0	83.2±13.4	0.59±0.41	94.0	82.9±13.5	0.43±0.42	96.0	82.1±13.2	0.42±0.39	99.0
GlnD_Adrenal_L	84.2±12.2	1.03±0.36	85.1±12.5	0.96±0.38		84.4±12.3	0.93±0.37		84.4±12.3	1.01±0.36		85.1±12.5	0.96±0.38	
Lung_LUL	97.8±3.6	0.31±0.93	97.7±4.0	0.19±0.64	99.5	99.3±3.8	0.34±0.63	99.5	98.0±3.7	0.27±0.62	99.0	97.7±4.0	0.19±0.64	99.5
Lung_LLL	96.5±24.0	0.21±0.98	96.7±2.2	0.19±0.48		97.1±2.3	0.22±0.50		96.4±2.1	0.22±0.47		96.7±2.2	0.19±0.48	
Lung_RUL	97.5±20.5	0.30±1.48	97.5±2.5	0.22±0.99	99.5	98.4±2.4	0.32±0.98	99.0	97.8±2.7	0.22±0.96	99.0	97.5±2.5	0.22±0.99	99.5
Lung_RML	92.0±6.2	0.47±1.41	92.0±3.3	0.21±1.45		92.0±3.0	0.48±1.47		92.1±3.2	0.21±1.40		92.0±3.3	0.21±1.45	
Lung_RLL	97.4±26.8	0.16±2.45	97.5±3.6	0.22±1.21		96.9±3.7	0.15±1.18		97.2±3.8	0.26±1.22		97.5±3.6	0.22±1.21	
Eso	94.8±2.9	0.61±0.15	94.4±2.9	0.50±0.13	99.7	95.4±2.9	0.64±0.13	99.5	94.2±3.0	0.66±0.14	98.0	94.4±2.9	0.50±0.13	99.7
Trachea	96.7±5.8	0.36±0.12	96.9±6.1	0.30±0.12	99.5	95.9±5.9	0.33±0.10	99.0	97.2±6.0	0.30±0.11	99.0	96.9±6.1	0.30±0.12	99.5
GlnD_Thyroid	91.7±14.7	0.41±0.96	92.4±14.8	0.32±0.99	99.0	90.6±14.6	0.40±0.97	99.0	92.5±14.8	0.42±0.99	99.7	92.4±14.8	0.32±0.99	99.0
SmallBowel	91.2±26.4	1.63±2.53	90.7±16.5	1.55±2.77	99.7	93.0±16.2	1.66±2.61	99.5	91.1±16.3	1.82±2.71	98.0	90.7±16.5	1.55±2.77	99.7
Duodenum	87.3±26.0	1.87±1.26	87.0±16.2	1.94±1.20	99.0	87.0±16.0	2.04±1.26	98.0	87.4±15.9	2.29±1.20	98.0	87.0±16.2	1.94±1.20	99.0
Colon	90.2±16.0	2.54±1.21	89.7±16.2	2.28±1.26	99.7	92.7±16.1	2.50±1.29	99.7	90.3±15.8	2.66±1.17	98.0	89.7±16.2	2.28±1.26	99.7
UrinaryBladder	89.1±9.5	2.98±1.08	89.2±9.4	2.91±1.04	99.0	87.9±9.8	2.99±1.05	99.5	89.2±9.6	2.84±1.00	98.0	89.2±9.4	2.91±1.04	99.0
Prostate	81.7±38.0	0.52±2.06	81.7±17.8	0.36±1.42	94.0	83.4±17.8	0.54±1.43	94.0	81.5±18.0	0.36±1.53	96.0	81.7±17.8	0.36±1.42	94.0
Mean	92.6	0.96	92.7	0.88	99.1	92.9	0.97	98.7	92.8	0.97	98.4	92.7	0.88	99.1

Table S40 | CSS order-wise performance details of CL-Net^{C5} on TotalSegmentator V2 ‘Organ’ subgroup. Organ-wise DSC (%), ASD (mm), and decoder-wise pruning rate \mathcal{T} (%) of CL-Net^{C5} on TotalSegmentator V2 ‘Organ’ subgroup are evaluated across all CSS orders. Notably, CL-Net^{C5} achieves mean DSC and ASD comparable to nnUNet upper bound and the average decoder pruning rates exceed 98% across all orders, demonstrating high efficiency without compromising segmentation performance.

	nnUNet		Order 1			Order 2			Order 3			Order 4		
	DSC \uparrow	ASD \downarrow	DSC \uparrow	ASD \downarrow	$\mathcal{T}\uparrow$	DSC \uparrow	ASD \downarrow	$\mathcal{T}\uparrow$	DSC \uparrow	ASD \downarrow	$\mathcal{T}\uparrow$	DSC \uparrow	ASD \downarrow	$\mathcal{T}\uparrow$
Heart	95.2 \pm 14.7	0.42 \pm 0.20	95.1 \pm 14.6	0.44 \pm 0.17	99.5	96.0 \pm 14.8	0.40 \pm 0.19	99.5	94.8 \pm 14.6	0.54 \pm 0.18	99.0	95.1 \pm 14.6	0.44 \pm 0.17	99.5
A_Aorta	96.0 \pm 16.7	0.44 \pm 0.95	96.6 \pm 16.5	0.43 \pm 0.82	99.7	93.7 \pm 16.7	0.45 \pm 0.85	99.0	96.4 \pm 16.7	0.46 \pm 0.85	99.0	96.6 \pm 16.5	0.43 \pm 0.82	99.7
V_Pulmonary	89.8 \pm 15.5	0.47 \pm 0.14	89.2 \pm 15.4	0.36 \pm 0.14	99.7	89.0 \pm 15.5	0.44 \pm 0.15	99.0	89.4 \pm 15.5	0.43 \pm 0.16	99.0	89.2 \pm 15.4	0.36 \pm 0.14	99.7
A_BrachiocephalicTrunk	89.8 \pm 16.2	0.32 \pm 0.43	89.8 \pm 16.1	0.22 \pm 0.42	99.7	89.5 \pm 16.1	0.32 \pm 0.43	99.0	89.2 \pm 16.0	0.23 \pm 0.42	99.0	89.8 \pm 16.1	0.22 \pm 0.42	99.7
A_Subclavian_L	94.6 \pm 3.5	0.44 \pm 0.28	94.9 \pm 3.4	0.29 \pm 0.27	99.7	94.6 \pm 3.3	0.47 \pm 0.26	98.0	94.8 \pm 3.5	0.59 \pm 0.28	98.0	94.9 \pm 3.4	0.29 \pm 0.27	99.7
A_Subclavian_R	94.1 \pm 3.3	0.23 \pm 0.17	93.7 \pm 3.4	0.19 \pm 0.18		95.5 \pm 3.2	0.25 \pm 0.16		93.1 \pm 3.3	0.20 \pm 0.17		93.7 \pm 3.4	0.19 \pm 0.18	
A_CommonCarotid_L	91.2 \pm 5.4	0.35 \pm 0.28	91.6 \pm 5.7	0.25 \pm 0.31	99.7	90.4 \pm 5.4	0.38 \pm 0.28	99.0	90.9 \pm 5.4	0.24 \pm 0.28	99.0	91.6 \pm 5.7	0.25 \pm 0.31	99.7
A_CommonCarotid_R	96.6 \pm 3.3	0.28 \pm 0.99	96.9 \pm 3.1	0.25 \pm 1.00		97.2 \pm 3.3	0.28 \pm 1.07		97.4 \pm 3.3	0.32 \pm 1.04		96.9 \pm 3.1	0.25 \pm 1.00	
V_Brachiocephalic_L	90.4 \pm 26.2	0.37 \pm 1.97	91.2 \pm 15.9	0.34 \pm 1.94	99.5	89.6 \pm 15.8	0.34 \pm 1.96	98.0	89.4 \pm 15.9	0.31 \pm 1.92	99.0	91.2 \pm 15.9	0.34 \pm 1.94	99.5
V_Brachiocephalic_R	88.7 \pm 15.0	0.32 \pm 0.81	88.1 \pm 15.1	0.24 \pm 0.82		88.9 \pm 15.2	0.35 \pm 0.83		88.6 \pm 15.2	0.38 \pm 0.83		88.1 \pm 15.1	0.24 \pm 0.82	
LAA	92.6 \pm 3.4	0.46 \pm 0.15	92.6 \pm 3.6	0.18 \pm 0.18	99.7	92.1 \pm 3.3	0.41 \pm 0.15	99.0	91.6 \pm 3.4	0.49 \pm 0.16	99.0	92.6 \pm 3.6	0.18 \pm 0.18	99.7
V_VenaCava_S	93.8 \pm 21.4	0.23 \pm 2.35	93.8 \pm 21.4	0.19 \pm 2.31	99.7	95.6 \pm 21.4	0.23 \pm 2.47	99.0	93.6 \pm 21.5	0.16 \pm 2.49	98.0	93.8 \pm 21.4	0.19 \pm 2.31	99.7
V_VenaCava_I	93.9 \pm 9.8	1.03 \pm 1.05	94.5 \pm 9.9	0.87 \pm 0.96	99.5	95.5 \pm 10.1	1.13 \pm 1.04	99.0	95.1 \pm 10.0	0.88 \pm 0.95	99.0	94.5 \pm 9.9	0.87 \pm 0.96	99.5
V_Portal_Splenic	85.5 \pm 29.3	1.29 \pm 0.62	86.1 \pm 29.3	1.28 \pm 0.65	99.0	86.8 \pm 29.0	1.27 \pm 0.62	98.0	85.7 \pm 29.3	1.28 \pm 0.64	98.0	86.1 \pm 29.3	1.28 \pm 0.65	99.0
A_Iliac_L	94.4 \pm 3.1	0.61 \pm 0.19	94.1 \pm 3.1	0.52 \pm 0.18	99.0	94.5 \pm 3.3	0.59 \pm 0.20	99.0	94.9 \pm 3.2	0.62 \pm 0.20	99.0	94.1 \pm 3.1	0.52 \pm 0.18	99.0
A_Iliac_R	91.9 \pm 19.5	0.45 \pm 0.15	91.0 \pm 19.5	0.40 \pm 0.18		93.2 \pm 19.4	0.45 \pm 0.16		91.7 \pm 19.3	0.45 \pm 0.16		91.0 \pm 19.5	0.40 \pm 0.18	
V_Iliac_L	92.2 \pm 3.0	0.48 \pm 0.13	91.7 \pm 3.4	0.47 \pm 0.16	99.7	91.7 \pm 3.1	0.47 \pm 0.14	99.7	92.8 \pm 3.3	0.59 \pm 0.15	99.0	91.7 \pm 3.4	0.47 \pm 0.16	99.7
V_Iliac_R	94.2 \pm 4.9	0.44 \pm 0.31	93.4 \pm 5.1	0.46 \pm 0.30		95.3 \pm 4.8	0.43 \pm 0.27		93.5 \pm 4.9	0.69 \pm 0.28		93.4 \pm 5.1	0.46 \pm 0.30	
Mean	92.5	0.48	92.5	0.41	99.6	92.7	0.48	98.9	92.4	0.49	98.8	92.5	0.41	99.6

Table S41 | CSS order-wise performance details of CL-Net^{C5} on TotalSegmentator V2 ‘Cardiac’ subgroup. Organ-wise DSC (%), ASD (mm), and decoder-wise pruning rate \mathcal{T} (%) of CL-Net^{C5} on TotalSegmentator V2 ‘Cardiac’ subgroup are evaluated across all CSS orders. Notably, CL-Net^{C5} achieves mean DSC and ASD comparable to nnUNet upper bound and the average decoder pruning rates exceed 98% across all orders, demonstrating high efficiency without compromising segmentation performance.

	nnUNet		Order 1				Order 2			Order 3			Order 4		
	DSC \uparrow	ASD \downarrow	DSC \uparrow	ASD \downarrow	$\mathcal{T}\uparrow$	DSC \uparrow	ASD \downarrow	$\mathcal{T}\uparrow$	DSC \uparrow	ASD \downarrow	$\mathcal{T}\uparrow$	DSC \uparrow	ASD \downarrow	$\mathcal{T}\uparrow$	
Bone_Humerus_L	96.9 \pm 17.5	2.84 \pm 0.20	97.0 \pm 17.7	2.80 \pm 0.21	99.5	96.8 \pm 17.9	3.00 \pm 0.23	99.5	97.1 \pm 17.8	2.85 \pm 0.23	99.0	97.0 \pm 17.7	2.80 \pm 0.21	99.5	
Bone_Humerus_R	96.6 \pm 17.3	4.31 \pm 0.17	97.2 \pm 17.2	4.23 \pm 0.19		97.4 \pm 17.2	4.44 \pm 0.20		97.2 \pm 17.2	4.57 \pm 0.19		97.2 \pm 17.2	4.23 \pm 0.19		
Bone_Scapula_L	94.1 \pm 21.1	1.16 \pm 0.18	94.6 \pm 21.1	1.05 \pm 0.15	99.7	92.7 \pm 21.1	1.25 \pm 0.14	99.0	93.6 \pm 21.4	1.16 \pm 0.17	99.0	94.6 \pm 21.1	1.05 \pm 0.15	99.7	
Bone_Scapula_R	95.1 \pm 1.7	1.95 \pm 0.07	95.2 \pm 1.9	1.67 \pm 0.08		93.5 \pm 1.6	1.78 \pm 0.05		94.2 \pm 1.6	2.12 \pm 0.05		95.2 \pm 1.9	1.67 \pm 0.08		
Bone_Clavicula_L	94.5 \pm 0.8	0.60 \pm 0.10	94.9 \pm 0.8	0.46 \pm 0.10	99.5	95.2 \pm 1.0	0.55 \pm 0.12	99.0	95.0 \pm 0.9	0.48 \pm 0.12	99.0	94.9 \pm 0.8	0.46 \pm 0.10	99.5	
Bone_Clavicula_R	98.4 \pm 16.1	1.52 \pm 0.19	98.6 \pm 16.1	1.43 \pm 0.21		97.5 \pm 16.1	1.50 \pm 0.21		98.3 \pm 15.8	1.60 \pm 0.18		98.6 \pm 16.1	1.43 \pm 0.21		
Bone_Femur_L	97.4 \pm 15.4	3.51 \pm 0.29	97.4 \pm 0.5	3.39 \pm 0.09	99.5	98.7 \pm 0.6	3.82 \pm 0.10	99.0	97.5 \pm 0.4	3.17 \pm 0.08	99.0	97.4 \pm 0.5	3.39 \pm 0.09	99.5	
Bone_Femur_R	95.8 \pm 0.5	6.85 \pm 0.08	96.3 \pm 0.3	6.22 \pm 0.06		96.0 \pm 0.5	6.53 \pm 0.09		96.1 \pm 0.3	7.59 \pm 0.06		96.3 \pm 0.3	6.22 \pm 0.06		
Bone_Hip_L	96.6 \pm 1.6	0.32 \pm 1.13	97.0 \pm 1.9	0.28 \pm 0.13	99.7	96.7 \pm 1.8	0.32 \pm 0.12	99.0	96.9 \pm 1.9	0.34 \pm 0.13	99.0	97.0 \pm 1.9	0.28 \pm 0.13	99.7	
Bone_Hip_R	95.9 \pm 31.6	0.34 \pm 0.10	95.6 \pm 31.8	0.29 \pm 0.10		97.3 \pm 31.6	0.32 \pm 0.08		96.8 \pm 31.9	0.44 \pm 0.11		95.6 \pm 31.8	0.29 \pm 0.10		
SpinalCord	92.7 \pm 16.8	0.27 \pm 0.24	91.9 \pm 16.8	0.25 \pm 0.27	99.7	94.8 \pm 16.5	0.28 \pm 0.24	99.0	92.6 \pm 16.9	0.31 \pm 0.27	99.0	91.9 \pm 16.8	0.25 \pm 0.27	99.7	
Musc_GluteusMax_L	98.9 \pm 5.2	0.84 \pm 1.41	99.0 \pm 5.6	0.80 \pm 1.44	99.7	98.3 \pm 5.5	0.87 \pm 1.41	99.7	98.7 \pm 5.3	0.85 \pm 1.40	99.0	99.0 \pm 5.6	0.80 \pm 1.44	99.7	
Musc_GluteusMax_R	98.1 \pm 2.0	0.93 \pm 0.34	97.9 \pm 2.0	0.74 \pm 0.33		98.3 \pm 1.8	0.92 \pm 0.31		97.8 \pm 2.2	0.78 \pm 0.34		97.9 \pm 2.0	0.74 \pm 0.33		
Musc_GluteusMed_L	98.2 \pm 1.5	0.43 \pm 0.22	98.2 \pm 1.2	0.45 \pm 0.20	99.7	98.6 \pm 1.6	0.38 \pm 0.23	99.7	98.4 \pm 1.3	0.48 \pm 0.21	99.0	98.2 \pm 1.2	0.45 \pm 0.20	99.7	
Musc_GluteusMed_R	97.6 \pm 7.3	0.74 \pm 0.22	97.4 \pm 7.6	0.44 \pm 0.22		96.5 \pm 7.6	0.81 \pm 0.22		97.4 \pm 7.4	0.55 \pm 0.20		97.4 \pm 7.6	0.44 \pm 0.22		
Musc_GluteusMin_L	97.1 \pm 2.3	0.56 \pm 0.16	97.3 \pm 2.2	0.40 \pm 0.16	99.7	95.6 \pm 2.5	0.59 \pm 0.19	99.5	97.2 \pm 2.2	0.61 \pm 0.16	99.5	97.3 \pm 2.2	0.40 \pm 0.16	99.7	
Musc_GluteusMin_R	98.0 \pm 1.1	0.39 \pm 0.08	97.9 \pm 1.2	0.38 \pm 0.11		97.1 \pm 1.0	0.39 \pm 0.09		98.2 \pm 1.1	0.51 \pm 0.10		97.9 \pm 1.2	0.38 \pm 0.11		
Musc_Autochthon_L	94.2 \pm 0.8	0.37 \pm 0.11	95.1 \pm 1.1	0.31 \pm 0.14	99.0	94.1 \pm 1.0	0.40 \pm 0.12	99.5	93.8 \pm 0.9	0.46 \pm 0.12	99.0	95.1 \pm 1.1	0.31 \pm 0.14	99.0	
Musc_Autochthon_R	94.6 \pm 0.8	0.41 \pm 0.12	94.2 \pm 0.7	0.39 \pm 0.10		93.8 \pm 0.9	0.42 \pm 0.12		94.6 \pm 0.8	0.56 \pm 0.11		94.2 \pm 0.7	0.39 \pm 0.10		
Musc_Iliopsoas_L	94.3 \pm 19.7	0.37 \pm 0.18	94.9 \pm 19.7	0.35 \pm 0.20	99.7	93.4 \pm 19.7	0.36 \pm 0.20	98.0	93.3 \pm 19.6	0.67 \pm 0.19	99.0	94.9 \pm 19.7	0.35 \pm 0.20	99.7	
Musc_Iliopsoas_R	95.0 \pm 9.1	0.39 \pm 0.27	95.8 \pm 9.0	0.35 \pm 0.24		93.4 \pm 9.1	0.40 \pm 0.25		94.8 \pm 9.1	0.36 \pm 0.25		95.8 \pm 9.0	0.35 \pm 0.24		
Brain	97.9 \pm 36.4	0.56 \pm 1.01	97.9 \pm 16.5	0.58 \pm 1.06	99.5	98.5 \pm 16.2	0.59 \pm 1.08	98.0	98.2 \pm 16.3	0.58 \pm 1.07	99.5	97.9 \pm 16.5	0.58 \pm 1.06	99.5	
Skull	93.1 \pm 35.4	3.91 \pm 0.20	92.3 \pm 35.5	3.59 \pm 0.21	99.7	93.0 \pm 35.5	3.86 \pm 0.21	99.0	92.4 \pm 35.3	3.96 \pm 0.20	99.0	92.3 \pm 35.5	3.59 \pm 0.21	99.7	
Mean	96.1	1.46	96.2	1.34	99.6	96.0	1.47	99.1	96.1	1.52	99.1	96.2	1.34	99.6	

Table S42 | CSS order-wise performance details of CL-Net^{C5} on TotalSegmentator V2 ‘Muscles’ subgroup. Organ-wise DSC (%), ASD (mm), and decoder-wise pruning rate \mathcal{T} (%) of CL-Net^{C5} on TotalSegmentator V2 ‘Muscles’ subgroup are evaluated across all CSS orders. Notably, CL-Net^{C5} achieves mean DSC and ASD comparable to nnUNet upper bound and the average decoder pruning rates exceed 99% across all orders, demonstrating high efficiency without compromising segmentation performance.

	nnUNet		Order 1			Order 2			Order 3			Order 4		
	DSC \uparrow	ASD \downarrow	DSC \uparrow	ASD \downarrow	$\mathcal{T}\uparrow$	DSC \uparrow	ASD \downarrow	$\mathcal{T}\uparrow$	DSC \uparrow	ASD \downarrow	$\mathcal{T}\uparrow$	DSC \uparrow	ASD \downarrow	$\mathcal{T}\uparrow$
Bone_Rib1_L	93.6 \pm 3.3	0.16 \pm 0.23	93.8 \pm 3.4	0.15 \pm 0.22	96.0	96.0 \pm 3.3	0.17 \pm 0.21	94.0	93.1 \pm 3.4	0.27 \pm 0.22	96.0	93.8 \pm 3.4	0.15 \pm 0.22	96.0
Bone_Rib2_L	89.9 \pm 1.7	0.95 \pm 0.95	89.5 \pm 1.7	0.88 \pm 0.96		89.7 \pm 1.4	0.85 \pm 0.99		89.6 \pm 1.5	0.84 \pm 0.97		89.5 \pm 1.7	0.88 \pm 0.96	
Bone_Rib3_L	94.7 \pm 17.0	0.91 \pm 1.06	95.0 \pm 17.2	0.90 \pm 1.06		96.3 \pm 17.0	0.87 \pm 1.04		94.8 \pm 16.9	0.81 \pm 1.04		95.0 \pm 17.2	0.90 \pm 1.06	
Bone_Rib4_L	94.5 \pm 18.9	0.76 \pm 1.82	94.8 \pm 19.0	0.67 \pm 1.80		94.6 \pm 18.9	0.69 \pm 1.89		93.8 \pm 18.9	0.66 \pm 1.89		94.8 \pm 19.0	0.67 \pm 1.80	
Bone_Rib5_L	94.2 \pm 29.7	1.52 \pm 4.61	94.8 \pm 29.3	1.18 \pm 4.70		94.3 \pm 29.3	1.49 \pm 4.41		94.2 \pm 29.4	1.08 \pm 4.49		94.8 \pm 29.3	1.18 \pm 4.70	
Bone_Rib6_L	93.2 \pm 23.9	1.64 \pm 3.32	92.7 \pm 23.9	1.42 \pm 3.24		93.8 \pm 23.8	1.59 \pm 3.35		92.6 \pm 24.2	1.75 \pm 3.23		92.7 \pm 23.9	1.42 \pm 3.24	
Bone_Rib7_L	94.5 \pm 20.7	2.71 \pm 4.08	93.6 \pm 20.6	2.68 \pm 3.98		96.6 \pm 20.7	2.47 \pm 4.10		95.6 \pm 20.8	2.72 \pm 4.11		93.6 \pm 20.6	2.68 \pm 3.98	
Bone_Rib8_L	94.6 \pm 21.1	4.29 \pm 4.00	95.3 \pm 20.9	4.59 \pm 3.81		94.0 \pm 20.8	4.08 \pm 3.82		95.1 \pm 21.0	4.12 \pm 4.10		95.3 \pm 20.9	4.59 \pm 3.81	
Bone_Rib9_L	94.0 \pm 19.4	2.83 \pm 5.21	93.5 \pm 19.4	2.93 \pm 5.24		95.4 \pm 19.2	2.59 \pm 5.01		94.3 \pm 19.4	2.73 \pm 4.94		93.5 \pm 19.4	2.93 \pm 5.24	
Bone_Rib10_L	93.0 \pm 22.9	1.51 \pm 6.63	92.8 \pm 12.9	1.38 \pm 6.61		92.4 \pm 13.2	1.61 \pm 6.77		91.8 \pm 13.0	1.41 \pm 7.00		92.8 \pm 12.9	1.38 \pm 6.61	
Bone_Rib11_L	93.0 \pm 22.4	0.36 \pm 8.01	92.8 \pm 12.5	0.31 \pm 8.12		95.2 \pm 12.4	0.34 \pm 7.89		92.0 \pm 12.4	0.39 \pm 8.20		92.8 \pm 12.5	0.31 \pm 8.12	
Bone_Rib12_L	94.2 \pm 26.2	0.54 \pm 0.41	93.5 \pm 16.3	0.34 \pm 0.41		93.3 \pm 16.1	0.54 \pm 0.39		94.5 \pm 16.2	0.34 \pm 0.39		93.5 \pm 16.3	0.34 \pm 0.41	
Bone_Rib1_R	91.2 \pm 5.6	0.11 \pm 0.17	91.0 \pm 5.8	0.13 \pm 0.17		92.7 \pm 5.6	0.11 \pm 0.15		91.7 \pm 5.7	0.21 \pm 0.16		91.0 \pm 5.8	0.13 \pm 0.17	
Bone_Rib2_R	94.5 \pm 3.5	0.23 \pm 0.94	93.6 \pm 3.4	0.09 \pm 0.91		94.1 \pm 3.6	0.22 \pm 0.93		94.4 \pm 3.6	0.15 \pm 0.93		93.6 \pm 3.4	0.09 \pm 0.91	
Bone_Rib3_R	92.8 \pm 9.1	0.48 \pm 0.75	92.9 \pm 9.0	0.34 \pm 1.05		92.5 \pm 9.1	0.47 \pm 1.05		93.6 \pm 9.1	0.38 \pm 1.14		92.9 \pm 9.0	0.34 \pm 1.05	
Bone_Rib4_R	90.5 \pm 18.8	0.83 \pm 2.02	91.3 \pm 18.8	0.69 \pm 1.88		88.3 \pm 18.6	0.83 \pm 2.02		90.3 \pm 18.8	0.77 \pm 1.82		91.3 \pm 18.8	0.69 \pm 1.88	
Bone_Rib5_R	90.3 \pm 26.5	1.70 \pm 2.42	90.5 \pm 16.5	1.64 \pm 2.53		89.5 \pm 16.4	1.84 \pm 2.61		90.6 \pm 16.6	1.98 \pm 2.52		90.5 \pm 16.5	1.64 \pm 2.53	
Bone_Rib6_R	93.4 \pm 18.9	1.52 \pm 2.45	93.4 \pm 13.0	1.65 \pm 2.32		93.0 \pm 13.0	1.48 \pm 2.54		93.3 \pm 13.0	1.74 \pm 2.42		93.4 \pm 13.0	1.65 \pm 2.32	
Bone_Rib7_R	94.2 \pm 21.0	1.56 \pm 3.51	93.8 \pm 21.2	1.61 \pm 3.66		92.5 \pm 21.1	1.56 \pm 3.36		95.4 \pm 21.2	1.70 \pm 3.40		93.8 \pm 21.2	1.61 \pm 3.66	
Bone_Rib8_R	95.5 \pm 18.3	1.88 \pm 4.08	95.4 \pm 18.1	1.81 \pm 4.16		95.4 \pm 18.2	1.79 \pm 3.92		94.8 \pm 18.2	1.72 \pm 4.08		95.4 \pm 18.1	1.81 \pm 4.16	
Bone_Rib9_R	95.9 \pm 21.4	2.48 \pm 5.16	95.1 \pm 21.6	2.31 \pm 3.20		96.8 \pm 21.4	2.58 \pm 3.35		96.2 \pm 21.3	2.93 \pm 3.41		95.1 \pm 21.6	2.31 \pm 3.20	
Bone_Rib10_R	96.3 \pm 23.3	2.50 \pm 7.23	97.1 \pm 23.1	2.56 \pm 7.10		97.0 \pm 23.3	2.60 \pm 7.30		95.8 \pm 23.3	2.67 \pm 7.41		97.1 \pm 23.1	2.56 \pm 7.10	
Bone_Rib11_R	96.4 \pm 22.8	1.85 \pm 6.95	96.1 \pm 22.7	1.88 \pm 7.02		97.0 \pm 23.0	1.90 \pm 7.27		97.5 \pm 23.0	1.82 \pm 6.86		96.1 \pm 22.7	1.88 \pm 7.02	
Bone_Rib12_R	97.1 \pm 27.5	0.63 \pm 0.07	97.2 \pm 27.4	0.45 \pm 0.10		97.6 \pm 27.2	0.57 \pm 0.08		97.3 \pm 27.2	0.51 \pm 0.08		97.2 \pm 27.4	0.45 \pm 0.10	
Bone_Sternum	94.1 \pm 5.8	0.63 \pm 0.55	94.8 \pm 5.9	0.38 \pm 0.57	99.0	95.6 \pm 5.7	0.64 \pm 0.55	99.0	95.3 \pm 5.9	0.39 \pm 0.57	99.5	94.8 \pm 5.9	0.38 \pm 0.57	99.0
Bone_CostalCartilages	88.7 \pm 5.0	0.18 \pm 0.74	89.6 \pm 5.1	0.18 \pm 0.76	99.0	89.4 \pm 5.3	0.16 \pm 0.77	98.0	88.3 \pm 5.1	0.17 \pm 0.75	98.0	89.6 \pm 5.1	0.18 \pm 0.76	99.0
Mean	93.6	1.34	93.6	1.28	98.0	94.0	1.31	97.0	93.7	1.32	97.8	93.6	1.28	98.0

Table S43 | CSS order-wise performance details of CL-Net^{C5} on TotalSegmentator V2 ‘Ribs’ subgroup. Organ-wise DSC (%), ASD (mm), and decoder-wise pruning rate \mathcal{T} (%) of CL-Net^{C5} on TotalSegmentator V2 ‘Ribs’ subgroup are evaluated across all CSS orders. Notably, CL-Net^{C5} achieves higher mean DSC and ASD than nnUNet upper bound and the average decoder pruning rates exceed 97% across all orders, demonstrating both high segmentation performance and efficiency.

	nnUNet		Order 1			Order 2			Order 3			Order 4		
	DSC \uparrow	ASD \downarrow	DSC \uparrow	ASD \downarrow	$\mathcal{T}\uparrow$	DSC \uparrow	ASD \downarrow	$\mathcal{T}\uparrow$	DSC \uparrow	ASD \downarrow	$\mathcal{T}\uparrow$	DSC \uparrow	ASD \downarrow	$\mathcal{T}\uparrow$
Bone_Sacrum	93.4 \pm 1.8	0.25 \pm 0.13	94.4 \pm 2.1	0.22 \pm 0.16	99.7	93.4 \pm 1.9	0.26 \pm 0.14	99.0	93.8 \pm 2.0	0.30 \pm 0.15	99.0	94.4 \pm 2.1	0.22 \pm 0.16	99.7
Bone_Vert_C1	94.5 \pm 20.3	0.25 \pm 0.53	94.5 \pm 10.4	0.24 \pm 0.53	94.0	93.2 \pm 10.5	0.23 \pm 0.54	94.0	95.1 \pm 10.5	0.29 \pm 0.53	94.0	94.5 \pm 10.4	0.24 \pm 0.53	94.0
Bone_Vert_C2	98.0 \pm 20.7	0.31 \pm 3.04	97.8 \pm 10.9	0.16 \pm 0.50		98.9 \pm 10.8	0.29 \pm 0.50		97.8 \pm 10.7	0.19 \pm 0.49		97.8 \pm 10.9	0.16 \pm 0.50	
Bone_Vert_C3	98.1 \pm 23.4	0.16 \pm 3.22	98.2 \pm 15.4	0.17 \pm 3.38		98.1 \pm 15.7	0.15 \pm 3.42		97.9 \pm 15.6	0.23 \pm 3.40		98.2 \pm 15.4	0.17 \pm 3.38	
Bone_Vert_C4	97.0 \pm 23.4	0.34 \pm 3.60	96.8 \pm 19.5	0.34 \pm 3.55		95.2 \pm 19.4	0.34 \pm 3.61		96.5 \pm 19.5	0.41 \pm 3.42		96.8 \pm 19.5	0.34 \pm 3.55	
Bone_Vert_C5	96.8 \pm 17.5	0.22 \pm 1.62	96.3 \pm 17.4	0.21 \pm 1.65		97.6 \pm 17.5	0.22 \pm 1.67		97.9 \pm 17.6	0.48 \pm 1.69		96.3 \pm 17.4	0.21 \pm 1.65	
Bone_Vert_C6	95.0 \pm 10.6	0.60 \pm 0.93	96.0 \pm 10.3	0.50 \pm 0.91		95.9 \pm 10.5	0.64 \pm 0.94		95.8 \pm 10.4	0.45 \pm 0.92		96.0 \pm 10.3	0.50 \pm 0.91	
Bone_Vert_C7	95.2 \pm 17.5	0.41 \pm 0.86	95.0 \pm 13.3	0.19 \pm 0.97		95.1 \pm 13.4	0.42 \pm 1.00		95.2 \pm 13.1	0.46 \pm 0.99		95.0 \pm 13.3	0.19 \pm 0.97	
Bone_Vert_L1	95.7 \pm 12.1	1.27 \pm 0.98	96.1 \pm 12.3	1.18 \pm 0.91		97.2 \pm 12.1	1.21 \pm 0.99		94.8 \pm 12.0	1.40 \pm 0.98		96.1 \pm 12.3	1.18 \pm 0.91	
Bone_Vert_L2	94.8 \pm 18.2	0.29 \pm 1.09	94.8 \pm 12.2	0.18 \pm 0.91		94.8 \pm 12.0	0.32 \pm 1.00		93.6 \pm 12.3	0.19 \pm 0.95		94.8 \pm 12.2	0.18 \pm 0.91	
Bone_Vert_L3	96.0 \pm 16.1	0.24 \pm 1.09	95.3 \pm 16.3	0.20 \pm 1.01		95.1 \pm 16.2	0.26 \pm 1.03		96.7 \pm 16.2	0.39 \pm 1.07		95.3 \pm 16.3	0.20 \pm 1.01	
Bone_Vert_L4	94.1 \pm 14.3	0.43 \pm 0.41	94.2 \pm 14.4	0.25 \pm 0.43		94.4 \pm 14.2	0.43 \pm 0.41		94.0 \pm 14.2	0.18 \pm 0.41		94.2 \pm 14.4	0.25 \pm 0.43	
Bone_Vert_L5	92.9 \pm 17.3	0.21 \pm 1.49	93.1 \pm 17.3	0.21 \pm 1.49		94.4 \pm 17.3	0.21 \pm 1.46		93.7 \pm 17.4	0.32 \pm 1.50		93.1 \pm 17.3	0.21 \pm 1.49	
Bone_Vert_S1	96.3 \pm 23.8	0.20 \pm 2.10	96.8 \pm 19.0	0.22 \pm 1.22		97.6 \pm 19.1	0.19 \pm 1.22		97.2 \pm 18.9	0.23 \pm 1.11		96.8 \pm 19.0	0.22 \pm 1.22	
Bone_Vert_T1	96.3 \pm 23.5	0.15 \pm 1.28	96.4 \pm 13.6	0.17 \pm 1.30		97.6 \pm 13.5	0.15 \pm 1.27		95.7 \pm 13.6	0.23 \pm 1.31		96.4 \pm 13.6	0.17 \pm 1.30	
Bone_Vert_T2	98.0 \pm 5.2	0.48 \pm 0.74	98.0 \pm 5.1	0.34 \pm 0.73		97.3 \pm 5.2	0.52 \pm 0.73		97.6 \pm 5.4	0.38 \pm 0.75		98.0 \pm 5.1	0.34 \pm 0.73	
Bone_Vert_T3	97.0 \pm 2.7	0.48 \pm 0.20	97.5 \pm 2.6	0.43 \pm 0.21		95.3 \pm 2.5	0.44 \pm 0.20		97.8 \pm 2.4	0.64 \pm 0.19		97.5 \pm 2.6	0.43 \pm 0.21	
Bone_Vert_T4	89.6 \pm 17.0	1.12 \pm 0.21	88.7 \pm 8.9	1.02 \pm 0.20		90.3 \pm 9.1	1.09 \pm 0.22		90.4 \pm 8.9	1.19 \pm 0.20		88.7 \pm 8.9	1.02 \pm 0.20	
Bone_Vert_T5	90.7 \pm 22.9	0.92 \pm 0.38	91.0 \pm 22.8	0.91 \pm 0.36		91.7 \pm 22.7	0.92 \pm 0.35		90.3 \pm 22.9	0.86 \pm 0.37		91.0 \pm 22.8	0.91 \pm 0.36	
Bone_Vert_T6	86.3 \pm 28.3	1.15 \pm 0.07	85.9 \pm 28.2	1.00 \pm 0.07		84.9 \pm 28.3	1.14 \pm 0.07		85.2 \pm 28.2	1.08 \pm 0.06		85.9 \pm 28.2	1.00 \pm 0.07	
Bone_Vert_T7	96.8 \pm 1.0	1.58 \pm 0.04	97.4 \pm 1.0	1.46 \pm 0.05		95.9 \pm 0.7	1.53 \pm 0.03		97.0 \pm 0.8	1.72 \pm 0.04		97.4 \pm 1.0	1.46 \pm 0.05	
Bone_Vert_T8	91.5 \pm 13.0	1.08 \pm 0.40	91.8 \pm 12.8	1.06 \pm 0.15		91.2 \pm 12.6	0.99 \pm 0.13		91.4 \pm 12.7	0.99 \pm 0.13		91.8 \pm 12.8	1.06 \pm 0.15	
Bone_Vert_T9	94.6 \pm 44.2	0.53 \pm 0.23	94.1 \pm 14.4	0.46 \pm 0.24		95.2 \pm 14.5	0.48 \pm 0.25		94.2 \pm 14.2	0.77 \pm 0.23		94.1 \pm 14.4	0.46 \pm 0.24	
Bone_Vert_T10	97.6 \pm 29.9	0.36 \pm 2.18	97.8 \pm 13.2	0.36 \pm 1.32		99.0 \pm 13.0	0.39 \pm 1.23		97.4 \pm 13.2	0.64 \pm 1.28		97.8 \pm 13.2	0.36 \pm 1.32	
Bone_Vert_T11	95.1 \pm 19.4	0.25 \pm 1.64	95.2 \pm 12.4	0.22 \pm 1.64		93.6 \pm 12.5	0.27 \pm 1.59		94.9 \pm 12.5	0.32 \pm 1.70		95.2 \pm 12.4	0.22 \pm 1.64	
Bone_Vert_T12	97.2 \pm 16.3	0.32 \pm 1.30	97.3 \pm 16.2	0.27 \pm 1.29		97.1 \pm 16.2	0.33 \pm 1.29		97.6 \pm 16.1	0.20 \pm 1.34		97.3 \pm 16.2	0.27 \pm 1.29	
Mean	94.9	0.52	95.0	0.46	96.9	95.0	0.52	96.5	95.0	0.56	96.5	95.0	0.46	96.9

Table S44 | CSS order-wise performance details of CL-Net^{C5} on TotalSegmentator V2 ‘Vertebrae’ subgroup. Organ-wise DSC (%), ASD (mm), and decoder-wise pruning rate \mathcal{T} (%) of CL-Net^{C5} on TotalSegmentator V2 ‘Vertebrae’ subgroup are evaluated across all CSS orders. Notably, CL-Net^{C5} achieves mean DSC and ASD comparable to nnUNet upper bound and the average decoder pruning rates exceed 96.5% across all orders, demonstrating high efficiency without compromising segmentation performance.

	nnUNet		Order 1			Order 2			Order 3			Order 4		
	DSC \uparrow	ASD \downarrow	DSC \uparrow	ASD \downarrow	$\mathcal{T}\uparrow$	DSC \uparrow	ASD \downarrow	$\mathcal{T}\uparrow$	DSC \uparrow	ASD \downarrow	$\mathcal{T}\uparrow$	DSC \uparrow	ASD \downarrow	$\mathcal{T}\uparrow$
BrainStem	93.7 \pm 1.5	0.32 \pm 0.10	92.9 \pm 1.4	0.28 \pm 0.09	99.0	92.2 \pm 1.5	0.25 \pm 0.10	98.0	92.8 \pm 1.4	0.25 \pm 0.09	99.0	92.9 \pm 1.4	0.28 \pm 0.09	99.0
Eye_L	94.8 \pm 1.3	0.17 \pm 0.08	94.8 \pm 1.3	0.15 \pm 0.08	98.0	94.3 \pm 1.4	0.16 \pm 0.09	99.0	93.5 \pm 1.4	0.15 \pm 0.09	99.0	94.8 \pm 1.3	0.15 \pm 0.08	98.0
Eye_R	93.2 \pm 4.2	0.24 \pm 0.28	94.1 \pm 4.1	0.28 \pm 0.28		91.8 \pm 4.4	0.31 \pm 0.30		95.2 \pm 4.3	0.30 \pm 0.29		94.1 \pm 4.1	0.28 \pm 0.28	
Lens_L	80.1 \pm 9.8	0.25 \pm 0.18	79.6 \pm 10.0	0.23 \pm 0.20	98.0	78.7 \pm 9.9	0.24 \pm 0.18	99.0	80.2 \pm 9.6	0.21 \pm 0.16	98.0	79.6 \pm 10.0	0.23 \pm 0.20	98.0
Lens_R	79.7 \pm 9.2	0.33 \pm 0.43	78.0 \pm 9.1	0.35 \pm 0.41		78.6 \pm 9.0	0.40 \pm 0.41		80.4 \pm 9.3	0.42 \pm 0.43		78.0 \pm 9.1	0.35 \pm 0.41	
OpticNerve_L	80.3 \pm 8.0	0.29 \pm 0.28	80.9 \pm 8.0	0.29 \pm 0.28	94.0	81.1 \pm 8.0	0.31 \pm 0.28	98.0	81.0 \pm 7.9	0.33 \pm 0.27	96.0	80.9 \pm 8.0	0.29 \pm 0.28	94.0
OpticNerve_R	84.1 \pm 6.4	0.20 \pm 0.21	85.0 \pm 6.5	0.17 \pm 0.22		85.2 \pm 6.4	0.17 \pm 0.21		85.6 \pm 6.3	0.18 \pm 0.20		85.0 \pm 6.5	0.17 \pm 0.22	
Chiasm	71.6 \pm 12.9	0.26 \pm 0.13	69.6 \pm 13.1	0.26 \pm 0.15	94.0	73.3 \pm 12.7	0.25 \pm 0.11	94.0	71.0 \pm 13.0	0.25 \pm 0.13	94.0	69.6 \pm 13.1	0.26 \pm 0.15	94.0
TemporalLobe_L	94.7 \pm 1.2	0.24 \pm 0.08	93.7 \pm 1.2	0.21 \pm 0.08	99.7	93.2 \pm 1.3	0.22 \pm 0.08	98.0	95.1 \pm 1.2	0.23 \pm 0.08	99.0	93.7 \pm 1.2	0.21 \pm 0.08	99.7
TemporalLobe_R	94.8 \pm 1.4	0.26 \pm 0.09	93.2 \pm 1.4	0.24 \pm 0.09		94.4 \pm 1.6	0.24 \pm 0.11		93.4 \pm 1.6	0.25 \pm 0.11		93.2 \pm 1.4	0.24 \pm 0.09	
GlnD_Pituitary	84.5 \pm 6.4	0.22 \pm 0.21	84.5 \pm 6.3	0.21 \pm 0.19	99.5	83.5 \pm 6.5	0.19 \pm 0.22	98.0	83.7 \pm 6.5	0.18 \pm 0.22	99.5	84.5 \pm 6.3	0.21 \pm 0.19	99.5
GlnD_Parotid_L	93.3 \pm 1.9	0.35 \pm 0.16	94.9 \pm 1.9	0.32 \pm 0.16	96.0	95.3 \pm 2.0	0.34 \pm 0.17	96.0	91.5 \pm 2.0	0.32 \pm 0.17	94.0	94.9 \pm 1.9	0.32 \pm 0.16	96.0
GlnD_Parotid_R	92.5 \pm 3.4	0.50 \pm 0.52	95.3 \pm 1.6	0.40 \pm 0.54		95.1 \pm 1.6	0.46 \pm 0.54		95.9 \pm 1.4	0.44 \pm 0.52		95.3 \pm 1.6	0.40 \pm 0.54	
Ear_Inner_L	67.0 \pm 9.5	0.66 \pm 0.37	67.5 \pm 9.5	0.59 \pm 0.37	99.0	65.6 \pm 9.6	0.58 \pm 0.38	99.0	68.8 \pm 9.4	0.65 \pm 0.37	96.0	67.5 \pm 9.5	0.59 \pm 0.37	99.0
Ear_Inner_R	64.3 \pm 9.3	0.66 \pm 0.30	65.6 \pm 9.3	0.67 \pm 0.31		62.9 \pm 9.4	0.81 \pm 0.31		63.7 \pm 9.4	0.83 \pm 0.31		65.6 \pm 9.3	0.67 \pm 0.31	
Ear_Mid_L	90.4 \pm 3.7	0.07 \pm 0.04	90.0 \pm 3.9	0.07 \pm 0.05	99.5	91.4 \pm 3.7	0.07 \pm 0.04	99.0	88.6 \pm 3.9	0.07 \pm 0.06	98.0	90.0 \pm 3.9	0.07 \pm 0.05	99.5
Ear_Mid_R	90.2 \pm 3.3	0.08 \pm 0.06	90.2 \pm 3.2	0.08 \pm 0.04		90.0 \pm 3.4	0.07 \pm 0.06		91.9 \pm 3.4	0.07 \pm 0.06		90.2 \pm 3.2	0.08 \pm 0.04	
TMJ_L	84.4 \pm 9.5	0.31 \pm 0.23	86.1 \pm 9.5	0.30 \pm 0.24	99.5	83.6 \pm 9.6	0.26 \pm 0.24	96.0	82.5 \pm 9.6	0.24 \pm 0.24	98.0	86.1 \pm 9.5	0.30 \pm 0.24	99.5
TMJ_R	84.1 \pm 7.6	0.33 \pm 0.20	83.4 \pm 7.4	0.33 \pm 0.18		82.5 \pm 7.4	0.33 \pm 0.19		82.9 \pm 7.6	0.34 \pm 0.20		83.4 \pm 7.4	0.33 \pm 0.18	
SpinalCord	91.5 \pm 2.9	0.36 \pm 0.19	90.1 \pm 2.8	0.33 \pm 0.17	99.5	93.7 \pm 2.9	0.33 \pm 0.19	99.0	90.6 \pm 2.9	0.35 \pm 0.19	98.0	90.1 \pm 2.8	0.33 \pm 0.17	99.5
Bone_Mandible_L	95.7 \pm 2.1	0.17 \pm 0.08	96.6 \pm 2.1	0.17 \pm 0.08	99.5	94.0 \pm 2.3	0.16 \pm 0.09	99.7	97.5 \pm 2.2	0.15 \pm 0.09	99.5	96.6 \pm 2.1	0.17 \pm 0.08	99.5
Bone_Mandible_R	95.7 \pm 2.5	0.17 \pm 0.08	94.8 \pm 2.7	0.14 \pm 0.10		94.2 \pm 2.4	0.13 \pm 0.07		95.5 \pm 2.4	0.13 \pm 0.07		94.8 \pm 2.7	0.14 \pm 0.10	
Mean	86.4	0.29	86.4	0.28	98.1	86.1	0.29	97.9	86.4	0.29	97.5	86.4	0.28	98.1

Table S45 | CSS order-wise performance details of CL-Net^{C5} on StructSeg19. Organ-wise DSC (%), ASD (mm), and decoder-wise pruning rate \mathcal{T} (%) of CL-Net^{C5} on StructSeg19 are evaluated across all CSS orders. Notably, CL-Net^{C5} achieves mean DSC and ASD comparable to nnUNet upper bound and the average decoder pruning rates exceed 97.5% across all orders, demonstrating high efficiency without compromising segmentation performance.

	nnUNet		Order 1			Order 2			Order 3			Order 4		
	DSC \uparrow	ASD \downarrow	DSC \uparrow	ASD \downarrow	$\mathcal{T}\uparrow$	DSC \uparrow	ASD \downarrow	$\mathcal{T}\uparrow$	DSC \uparrow	ASD \downarrow	$\mathcal{T}\uparrow$	DSC \uparrow	ASD \downarrow	$\mathcal{T}\uparrow$
Liver	98.1 \pm 14.5	0.83 \pm 0.98	97.6 \pm 5.6	0.85 \pm 0.98	99.5	98.3 \pm 5.8	0.75 \pm 0.98	99.5	97.4 \pm 5.7	0.90 \pm 0.99	99.7	97.9 \pm 5.6	0.81 \pm 0.98	99.7
Kidney_R	92.4 \pm 16.9	1.81 \pm 0.74	93.7 \pm 7.1	1.56 \pm 0.76	99.7	94.6 \pm 7.1	1.74 \pm 0.76	99.7	91.4 \pm 6.8	1.98 \pm 0.73	99.5	94.3 \pm 7.1	1.30 \pm 0.76	99.5
Kidney_L	92.8 \pm 16.9	1.27 \pm 0.74	92.9 \pm 7.0	1.19 \pm 0.72		94.0 \pm 6.8	1.27 \pm 0.70		92.1 \pm 6.9	1.36 \pm 0.72		92.2 \pm 6.7	1.26 \pm 0.69	
Spleen	97.9 \pm 15.6	0.30 \pm 0.37	97.3 \pm 6.7	0.20 \pm 0.38	99.7	98.2 \pm 6.6	0.22 \pm 0.38	99.5	97.2 \pm 6.8	0.45 \pm 0.39	99.5	97.8 \pm 6.9	0.21 \pm 0.40	99.5
Pancreas	91.6 \pm 17.2	0.80 \pm 0.69	92.4 \pm 7.0	0.80 \pm 0.38	99.7	92.8 \pm 7.2	0.69 \pm 0.39	99.7	88.8 \pm 7.2	0.95 \pm 0.40	98.0	93.1 \pm 7.0	0.72 \pm 0.38	99.0
A_Aorta	96.7 \pm 16.5	0.21 \pm 0.95	97.9 \pm 16.7	0.19 \pm 0.85	99.7	97.0 \pm 16.6	0.18 \pm 0.84	99.5	96.4 \pm 16.5	0.37 \pm 0.82	99.7	97.2 \pm 16.8	0.22 \pm 0.86	99.7
V_VenaCava_I	89.8 \pm 10.1	1.08 \pm 1.03	88.4 \pm 10.0	1.03 \pm 1.03	99.0	87.9 \pm 9.8	1.18 \pm 1.04	98.0	90.5 \pm 10.0	1.25 \pm 0.99	99.0	88.1 \pm 9.9	1.14 \pm 0.96	99.5
GlnD_Adrenal_R	85.9 \pm 12.3	0.39 \pm 0.37	86.4 \pm 13.5	0.39 \pm 0.42	99.0	87.0 \pm 13.4	0.35 \pm 0.41	98.0	85.2 \pm 13.2	0.62 \pm 0.39	96.0	86.8 \pm 13.4	0.42 \pm 0.41	98.0
GlnD_Adrenal_L	88.0 \pm 13.3	0.26 \pm 1.16	89.9 \pm 12.5	0.21 \pm 0.39		93.2 \pm 12.4	0.30 \pm 0.38		87.8 \pm 12.4	0.37 \pm 0.37		90.0 \pm 12.5	0.18 \pm 0.39	
GallBladder	80.2 \pm 24.7	2.16 \pm 0.83	81.8 \pm 8.4	2.07 \pm 0.80	94.0	82.3 \pm 8.5	2.03 \pm 0.81	98.0	81.2 \pm 8.5	2.33 \pm 0.81	99.0	82.1 \pm 8.4	2.29 \pm 0.80	94.0
Eso	84.4 \pm 3.1	1.70 \pm 0.15	82.7 \pm 3.1	1.48 \pm 0.15	99.0	83.5 \pm 3.1	1.46 \pm 0.15	96.0	85.0 \pm 3.1	1.70 \pm 0.15	98.0	84.6 \pm 3.0	1.55 \pm 0.15	99.0
Stomach	91.7 \pm 16.4	1.24 \pm 0.67	93.0 \pm 6.5	1.14 \pm 0.69	99.5	94.9 \pm 6.4	1.29 \pm 0.67	99.0	91.0 \pm 6.2	1.47 \pm 0.66	99.7	92.9 \pm 6.3	1.29 \pm 0.66	99.5
Duodenum	79.8 \pm 25.9	2.71 \pm 1.29	81.5 \pm 16.1	2.55 \pm 1.20	96.0	82.9 \pm 16.2	2.81 \pm 1.19	94.0	79.7 \pm 15.8	2.86 \pm 1.28	94.0	80.9 \pm 15.8	2.39 \pm 1.24	96.0
Mean	90.0	1.14	90.4	1.05	98.6	91.3	1.10	98.3	89.5	1.28	98.4	90.6	1.1	98.5

Table S46 | CSS order-wise performance details of CL-Net^{C5} on FLARE22. Organ-wise DSC (%), ASD (mm), and decoder pruning rate \mathcal{T} (%) of CL-Net^{C5} on FLARE22 are evaluated across all CSS orders. Notably, CL-Net^{C5} achieves mean DSC and ASD comparable to nnUNet upper bound and the average decoder pruning rates exceed 98% across all orders, demonstrating both high segmentation performance and efficiency.

	nnUNet		Order 1			Order 2			Order 3			Order 4		
	DSC \uparrow	ASD \downarrow	DSC \uparrow	ASD \downarrow	$\mathcal{T}\uparrow$	DSC \uparrow	ASD \downarrow	$\mathcal{T}\uparrow$	DSC \uparrow	ASD \downarrow	$\mathcal{T}\uparrow$	DSC \uparrow	ASD \downarrow	$\mathcal{T}\uparrow$
Eso	88.2 \pm 3.2	0.35 \pm 0.16	89.2 \pm 3.1	0.34 \pm 0.16	99.7	89.1 \pm 2.8	0.48 \pm 0.12	99.5	90.0 \pm 3.0	0.33 \pm 0.15	99.7	88.6 \pm 2.9	0.33 \pm 0.14	98.0
Heart	94.7 \pm 14.9	0.39 \pm 0.20	95.9 \pm 14.6	0.40 \pm 0.17	99.5	94.6 \pm 14.5	0.53 \pm 0.16	99.7	95.5 \pm 14.8	0.36 \pm 0.19	99.0	94.4 \pm 14.5	0.37 \pm 0.17	99.5
Trachea	92.2 \pm 5.8	0.30 \pm 0.09	92.6 \pm 6.1	0.28 \pm 0.12	99.5	92.8 \pm 5.7	0.48 \pm 0.08	99.7	93.2 \pm 5.9	0.30 \pm 0.10	99.7	93.7 \pm 5.9	0.30 \pm 0.10	99.7
A_Aorta	95.2 \pm 16.6	0.32 \pm 0.84	95.2 \pm 16.4	0.30 \pm 0.82	99.7	95.7 \pm 16.6	0.43 \pm 0.83	99.7	95.1 \pm 16.7	0.30 \pm 0.85	99.7	96.0 \pm 16.5	0.32 \pm 0.83	99.7
Mean	92.6	0.34	93.3	0.33	99.6	93.1	0.48	99.7	93.5	0.32	99.5	93.1	0.33	99.2

Table S47 | CSS order-wise performance details of CL-Net^{C5} on SegThor. Organ-wise DSC (%), ASD (mm), and decoder-wise pruning rate \mathcal{T} (%) of CL-Net^{C5} on SegThor are evaluated across all CSS orders. Notably, CL-Net^{C5} achieves higher mean DSC and ASD than nnUNet upper bound and the average decoder pruning rates exceed 98% across all orders, demonstrating high efficiency without compromising segmentation performance.

	nnUNet		Order 1			Order 2			Order 3			Order 4		
	DSC \uparrow	ASD \downarrow	DSC \uparrow	ASD \downarrow	$\mathcal{T}\uparrow$	DSC \uparrow	ASD \downarrow	$\mathcal{T}\uparrow$	DSC \uparrow	ASD \downarrow	$\mathcal{T}\uparrow$	DSC \uparrow	ASD \downarrow	$\mathcal{T}\uparrow$
Kidney_Lesion	86.7 \pm 9.0	1.18 \pm 1.06	86.9 \pm 9.4	1.32 \pm 1.06	98.0	87.1 \pm 9.3	0.92 \pm 1.01	94.0	86.6 \pm 9.1	1.13 \pm 1.07	94.0	86.9 \pm 9.4	1.32 \pm 1.06	98.0

Table S48 | CSS order-wise performance details of CL-Net^{C5} on KiTS21. Organ-wise DSC (%), ASD (mm), and decoder-wise pruning rate \mathcal{T} (%) of CL-Net^{C5} on KiTS21 are evaluated across all CSS orders. Notably, CL-Net^{C5} achieves DSC and ASD comparable to nnUNet upper bound and the average decoder pruning rate exceeds 94% across all orders, demonstrating high efficiency without compromising segmentation performance.